

ABSTRACT

Title of dissertation: 3D MAGNETIC IMAGING USING
SQUIDS AND SPIN-VALVE SENSORS

Alex D. E. Jeffers, Doctor of Philosophy, 2016

Dissertation directed by: Professor Frederick C. Wellstood
Department of Physics

We have used 2 μm by 4 μm thin-film Cu-Mn-Ir spin-valve sensors and high T_c $\text{YBa}_2\text{Cu}_3\text{O}_{7-x}$ dc SQUIDS to take magnetic images of test samples with current paths that meander between 1 and 5 metallization layers separated by 1 μm to 10 μm vertically. I describe the development and performance of a 3D magnetic inverse for reconstructing current paths from a magnetic image. I present results from this inverse technique that demonstrate the reconstruction of the 3D current paths from magnetic images of samples. This technique not only maps active current paths in the sample but also extracts key parameters such as the layer-to-layer separations. When imaging with 2 μm by 4 μm spin-valve sensors I typically applied currents of 1 mA at 95 kHz and achieved system noise of about 200 nT for a 3 ms averaging time per pixel. This enabled a vertical resolution of 1 μm and a lateral resolution of 1 μm in the top layers and 3 μm in the bottom layer. For our roughly 30 μm square SQUID sensors, I typically applied currents of 1 mA at 5.3 kHz, and achieved system noise of about 200 pT for a 3 ms averaging time per pixel. The higher sensitivity compared to the spin-valve sensor allowed me to resolve more deeply buried current paths.

3D MAGNETIC IMAGING USING
SQUIDS AND SPIN-VALVE SENSORS

by

Alex David Eugene Jeffers

Dissertation submitted to the Faculty of the Graduate School of the
University of Maryland, College Park in partial fulfillment
of the requirements for the degree of
Doctor of Philosophy
2016

Advisory Committee:
Professor Frederick C. Wellstood, Chair/Advisor
Doctor Antonio Orozco
Doctor Richard L. Greene
Doctor Christopher J. Lobb
Doctor Ichiro Takeuchi

If I have seen further, it is by standing on the shoulders of giants.

– Isaac Newton, 1676

Dedication

To my parents

Acknowledgments

I thank my advisor, Fred Wellstood for the incredible help and support he gave me while I was working on this project. I'd also like to thank the other members of the project at the University of Maryland, namely Ben Cheng, Hyeok Shin Kwan, and Keyvan Torkashvan. This project was a collaboration with Neocera, and I received tremendous support from their team, in particular from Antonio Orozco, Fred Cawthorne, Steve Garrahan, Vladimir Talanov, Nick Gagliogio, Chris rowlett, Nesco Lettsome, Enoch Wong and Anurag Moghe.

I thank my fellow students and postdocs in the Physics Department at the University of Maryland for their comraderie, interesting conversations and moral support. Graduate school is challenge which is better faced together. Thanks to Rangga Budoyo, Ben Cooper, Cody Ballard, Sudeep Dutta, David Angelaszek, Chris Anelli and Kristen Voigt. I'd like to thank the graduate students which I spent time writing with for their moral support and encouragement: Xuan Wang, Raymond Williams, Deniz Cil, Caitlin McCulloch, Auvil Elise, Zhao Feng, and Stephanie Chang. I'd like to thank the staff at the graduate writing center, and in particular Linda Macri, for their help when I was having difficulty writing. I'd like to thank Mary Sutton, Bryan Straughn, Doug Bensen and Jane Hessian for their help. I'd like to thank Paul Syers and J.P. Paglione for their help with the PPMS system. I'd like to thank Dave and Bruce for their help in the machine shop with using the lathe and mill. I'd like to thank Bob for helping with the coil winder. This work was supported by IARPA, Neocera, and the Center for Nanophysics and Nanomaterials at the University of Maryland, College Park.

I thank my thesis committee for their help and interesting discussions. I thank all the

people at INESC who helped me there when i was training on spin-valve sensors, including Susanna de Freitas and Filipe Cardoso.

Finally, I thank my family: my sisters Kimberly and Jessica, and my parents, Derek and Esther Jeffers, to whom I dedicate this thesis.

Table of Contents

List of Tables	ix
List of Figures	x
List of Abbreviations	xi
1 Introduction	1
1.1 What is a magnetic microscope?	1
1.2 Applications of magnetic imaging	2
1.3 Failure analysis & circuit analysis	5
1.4 The Standard Inverse	6
1.5 Vertical and lateral resolution	7
1.6 Overview of the thesis	8
2 Standard FFT Magnetic Inverse	10
2.1 Introduction	10
2.2 Derivation of the Standard Inverse	11
2.2.1 Inverse of B_x and B_y	11
2.2.2 Inverse of B_z	15
2.3 Tilted Standard Inverse	18
2.4 Noise and spatial resolution	20
2.5 Advantages and limitations	28
2.6 Conclusions	31
3 A 3D Inverse Technique	33
3.1 Introduction	33
3.2 Need for constraints	34
3.3 Reasonable constraints for semiconductor circuits	35
3.4 3D technique overview	37
3.5 Uniqueness of solution	41
3.6 3D Inverse signal-to-noise-ratio and current rings	46
3.7 Spatial resolution and least resolvable rings	53
3.8 Conclusions	68

4	Implementing the 3D Solver	69
4.1	Introduction	69
4.2	Z-search algorithm	70
4.3	Corner search algorithm	76
4.4	Infeeds and outfeeds	80
4.5	Noise and goodness of fit	83
4.6	Parameter search	86
4.7	Multiple wires	88
4.8	Cropping and region of interest searches	90
4.9	Conclusions	92
5	Running the 3D Solver	93
5.1	Introduction	93
5.2	Main graphical user interface	93
5.3	Order of operations	99
5.4	Drawing and re-drawing paths	104
5.4.1	Automatic routines	104
5.4.2	Drawing a path manually	110
5.5	Using Wirization techniques	113
5.6	Parameter search	114
5.7	Grid size	118
5.8	Conclusions	119
6	MAGMA System	120
6.1	Introduction	120
6.2	Overview of the system	120
6.3	SQUID sensor	126
6.4	Comb contact pads	130
6.5	Magnetometer or gradiometer?	136
6.6	Conclusions	139
7	Spin-Valve Sensor Fabrication and Characterization	140
7.1	Introduction	140
7.2	Theory	140
7.3	Sensor stack and fabrication	145
7.4	Sensor characterization	148
7.5	Spin-valve advantages and disadvantages compared to a SQUID	150
7.6	Sensor integration into the MAGMA system	155
7.7	Spin-valve sensor tilt	157
7.8	Conclusion	162
8	Select Magnetic Images	163
8.1	Introduction	163
8.2	SU8 three-layer sample	163
8.3	3DiS five-layer sample	169

8.4	Modified 3DiS five-layer samples	176
8.5	Fraunhofer sample	190
8.6	Conclusions	199
9	Future Work and Conclusions	201
9.1	Future work	201
9.2	Conclusions	208
A	3D Solver code	211
A.1	Wire class	211
A.2	Wirization Schemes: LVC wirization	212
A.3	Parameter Search	214
B	Ultimate limits on spatial resolution, J. Matthew <i>et. al.</i>	219
C	Run sheet detailing steps for spin-valve sensor fabrication	239
	Bibliography	248

List of Tables

5.1	Table of search parameters	115
7.1	Magnetoresistance of INESC spin-valves	148
7.2	Table of tilt scan parameters	156
8.1	Best fit parameters obtained for scan of sample 1 (3 layer LVC)	167
8.2	Parameters for scan of sample 2 (5-layer meander) in Fig. 8.3 (a)	174
8.3	Best fit parameters for sample 3 – modified 5-layer 3DiS sample with added short and 1 μm layer-to-layer separation.	183
8.4	Best fit parameters for sample 4 – modified 10 μm sample with added short.	188

List of Figures

1.1	Overview of scanning magnetic microscopy	3
2.1	Sensor tilt convention	19
2.2	Noise from a single pixel	23
2.3	Noise from a single pixel	24
2.4	Summary diagram of how the Fourier inverse works	26
3.1	Simple path difference	42
3.2	Modifying a path	48
3.3	Magnetic dipole vs. quadrupole field strength	54
3.4	2-ring signal vs. ring distance	56
3.5	Multipole ring combinations	58
3.6	Multipole ring signal strength, $z = 120 \mu\text{m}$	62
3.7	Multipole ring signal strength, $z = 120 \mu\text{m}$	63
3.8	Multipole ring signal strength, $z = 80 \mu\text{m}$	64
3.9	Multipole ring signal strength, $z = 60 \mu\text{m}$	65
3.10	Multipole rings signal strength, $z = 40 \mu\text{m}$	66
3.11	Multipole rings signal strength, $z = 20 \mu\text{m}$	67
4.1	Basic path search algorithm	71
4.2	Results from a z -search	75
4.3	Corner search algorithm ring pattern	77
4.4	Corner search algorithm example (simulation)	79
4.5	Infeed/outfeed automatic routine simulation	82
4.6	Example of choosing noise	84
4.7	Multiwire simulation showing infeed routines	89
4.8	Multiwire simulation showing fully resolved difference image after fitting.	90
4.9	Crop2 region	92
5.1	Main 3D Solver interface	94
5.2	3D Solver scan interface	96
5.3	3D Solver main search window	102
5.4	3D Solver Tools	105

5.5	CEA-LETI scan	108
6.1	MAGMA System	121
6.2	MAGMA scanning stages	122
6.3	MAGMA System software	125
6.4	SQUID scan close-up	128
6.5	Signal due to contact pads	132
6.5	Signal due to contact pads	133
6.6	Comb Contact Pads Design	134
6.7	Photograph of SQUID sensor	135
7.1	Spin-valve sensor mechanism	141
7.2	Magnetoresistance curves of spin-valves I built at INESC	143
7.3	Spin-valve sensor stack	144
7.4	Spin-valve sensor photograph	146
7.5	Spin-valve calibration by fitting magnetoresistance curve	149
7.6	Noise estimation of a spin-valve sensor	151
7.7	Tilt scans show we aren't getting z component	152
7.8	Schematics of Spin-valve cantilever	154
7.9	θ angle in tilt scan data set	159
7.10	Parameters in tilt scan data set	160
7.11	Spin-valve tilt model	161
8.1	Sample 1 analysis (3 layer SU8)	164
8.2	SEM image of sample similar to sample 2	170
8.3	Analysis of sample 2, a 5 layer meander	172
8.4	Sample 2 (5-layer meander) best fit path	173
8.5	3DiS 5-layer meander samples SEM pictures	177
8.6	Analysis of sample 3 (shorted sample)	179
8.7	Analysis of sample 3 (shorted sample)	181
8.8	Analysis of sample 4 (10 μ m shorted sample)	184
8.9	Analysis of sample 4 (10 μ m shorted sample)	186
8.10	Sample 5 scan	191
8.11	Sample 5 scan y-channel	192
8.12	Sample 5 scan with adjusted phase	193
8.13	Sample 5 scan out-of-phase signal	194
8.14	Sample 5 model	197
8.15	Sample 5 zoom	198

List of Acronyms, symbols and Abbreviations

SQUID	Superconducting quantum interference device
SVS	Spin-valve sensor
GMR	Giant magnetoresistance effect
IARPA	Intelligence Advanced Research Projects Activity
FA	Failure analysis
SSM	Scanning SQUID microscope
MFI	Magnetic field imaging
CAT	Circuit analysis tools
FT or FFT	Fourier transform
FWHM	Full width at half maximum
CIP (SV)	Current-in-plane (spin-valve)
CPP (SV)	Current perpendicular to the plane (spin-valve)
SU8	An epoxy-based negative photoresist
TSV	Through silicon via
LVC	Linear via chain
FIB	Focused ion beam
SEM	Scanning electron microscope
S/N	Signal-to-noise ratio

Imaging parameter abbreviations

z	sensor-sample distance
g	sensor gain
I	current through the sample
θ and ϕ	sensor tilt angles
θ_S	sample in-plane rotation
w , w_x and w_y	lateral grid spacings
h_{i-j}	layer i to layer j separation
b	trace width (wire width)
B_0	constant (ac) B field offset

Chapter 1: Introduction

1.1 What is a magnetic microscope?

The ongoing development of 3D integrated circuits [1–5] using through silicon vias (TSVs) [6–8] raises the question of how one can do failure analysis [9–11] on these novel structures. Failure analysis or fault analysis is particularly useful during the development of a new circuit fabrication process, such as that currently underway for through-silicon vias [1, 12, 13]. Information about the location and underlying cause of device failures can be used to guide modifications to the fabrication process to improve the yield of working devices. 3D integrated structures present particular challenges because of the presence of buried or hidden layers that are inaccessible to many techniques used in conventional fault analysis [14], including optical inspection or scanning electron microscopy [15].

Magnetic field imaging [16–18] presents a potentially useful tool for fault analysis in 3D samples because low frequency magnetic fields can penetrate through metallic, semiconducting and insulating layers. In addition, magnetic imaging is nondestructive, contactless, and does not require the removal of overlayers.

Figure 1.1 shows an overview of how a near-field scanning magnetic microscope works. A small, very sensitive magnetic sensor is brought as close as possible to the surface of the sample. Electrical power is applied to produce currents that flow through the sample

and produce a magnetic field that varies spatially over the sample. The sensor is raster scanned close above the surface of the sample, typically collecting the z-component of the magnetic field, as shown in Fig. 1.1. This field is then used to reconstruct the spatial distribution of the currents in the sample. From the resulting current map, one can identify the possible locations of shorts, opens, and other defects in the sample [19–21]. Prior to the work described in this thesis, Fourier transform based techniques were the state of the art for extracting a current map from a magnetic image [21, 22]. These Fourier techniques are discussed in detail in Chapter 2. While very powerful, Fourier inverses require an assumption that all the currents are in a single plane, and therefore they cannot reconstruct 3D currents [22].

In this thesis I describe a method to convert magnetic images of technologically interesting microelectronic circuits into three dimensional current distributions. To demonstrate this new approach, we used a spin-valve sensor and a superconducting quantum interference device (SQUID) to acquire magnetic images of samples in which the current path meandered between 3 and 5 metallization layers. I then describe how I used a custom 3D Solver algorithm I built to reconstruct the currents in the samples from the 2D magnetic images.

1.2 Applications of magnetic imaging

Perhaps the most well-known examples of magnetic imaging are in bioimaging. Because magnetic imaging is non-invasive, it is particularly attractive for imaging people. Without a doubt the best known type of magnetic imaging is Magnetic Resonance Imaging (MRI) [23, 24]. In MRI, a strong magnetic field and various gradients are applied to the

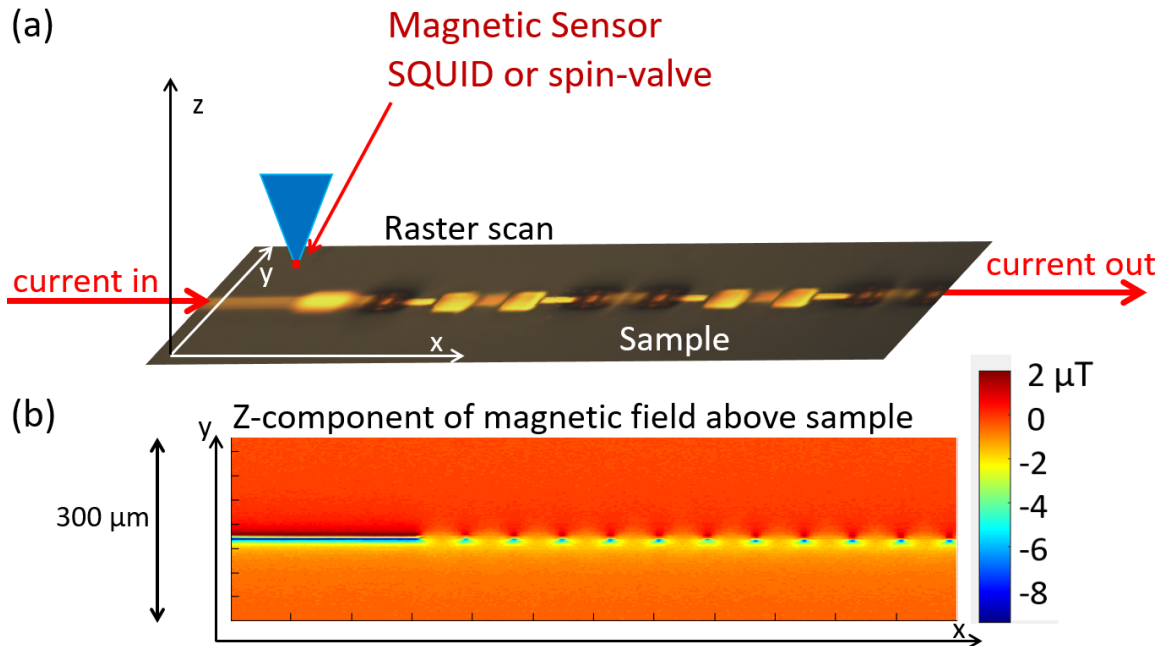


Fig. 1.1. Overview of scanning magnetic microscopy. (a) A magnetic sensor is brought as close as possible to the surface of a semiconductor sample. The sensor is then raster scanned above the sample, with the sensor collecting magnetic field measurements as a function of its position. Using AC current in the sample, a lock-in amplifier is used to detect the sensor output with a good signal-to-noise ratio even in an unshielded environment. Typically the sensor only measures one component of the magnetic field. (b) Resulting false color magnetic image. Red represents positive field, while blue represents negative field along the z-axis.

subject, which is typically a live person. Nuclei with magnetic moments (mainly hydrogen) align along the applied field and precess at a frequency that depends on the local field strength. By measuring the strength of the rf field emitted by the precessing nuclei as a function of the frequency, one can generate spatially resolved images with contrast between different tissues.

A lesser-known type of bio-imaging involves using SQUIDs to detect weak magnetic fields produced by biological activity in living organisms. Magnetoencephalography involves using arrays of SQUIDs to image neural activity by directly measuring the field due to currents produced by neural activity in the brain [25, 26]. A similar technique, magnetocardiography, uses SQUIDs to image the heart [27–30].

Scanning SQUID microscopy was invented at the University of Maryland in the 1990's [31, 32]. The technique has been used to find defects in metallic parts, such as cracks or inclusions [33, 34], and in superconducting wires [35], as well as for semiconductor failure analysis, as discussed below, and for imaging the behavior of high- T_c superconductors [36–38].

Single SQUID sensors have been fairly widely used to measure magnetic properties of a wide variety of samples since at least the 1970's. For example, SQUIDs are used in Quantum Design's Magnetic Property Measurement Systems (MPMS) [39, 40] to measure the magnetic properties of samples as a function of magnetic field strength and temperature. In geophysics, SQUIDs have been used to measure the properties and composition of rocks [39, 41], search for oil [39, 42, 43], and profile the conductivity of the ground as a function of depth [44].

Many other types of magnetic field sensors are widely used. AMR and GMR sensors

are commonly used in hard drives thanks to their low cost, small size and high speed [45]. Spin exchange relaxation-free (SERF) magnetometers [46] are seeing considerable recent interest, as are Nitrogen-vacancy centers in diamonds [47,48]. For an in depth overview of magnetic sensors, see the SQUID Handbook [21].

1.3 Failure analysis & circuit analysis

There are two broad types of failure analysis techniques. The first involves directly imaging a sample, and then trying to distinguish the physical characteristics (metal, insulator, thickness, *etc*) or composition of the sample (Al, Cu, SiO₂, *etc*). Optical imaging using a conventional lens-based microscope has a spatial resolution limited by diffraction [49] to about 500 nm for visible light. While optical images can resolve depth information and see through transparent overlayers, metal layers can typically only be imaged on the surface. Scanning Electron Microscopy (SEM) has a much finer resolution, routinely imaging at 20 nm and often better [50], but can only image the surface of samples. Focused Ion Beam (FIB) is particularly useful as it can image a sample layer by layer and produce cross-section images [51]. However, the sample is destroyed in the process.

Unfortunately, while these techniques may give a very good image of a sample, defects that cause electrical problems may not be detectable. Cracks in a metallization layer may be buried or too small to resolve. Electrical shorts may be similarly hard to spot. In order to deal with these shortcomings, failure localization techniques are used. The aim of failure localization is to locate the defects that are causing a specific failure, rather than trying to determine the precise physical nature of the failure. Once the defect location is found,

tools such as FIB can be applied effectively to examine the defect at high resolution. For example, voltage contrast imaging [52,53] has been used to identify the location of leakages or shorts. Another example is thermal imaging which takes advantage of the heat generated by currents to reveal the location of shorts [54–57]. Finally, scanning magnetic microscopy detects the field produced by the currents in the device and can locate electrical shorts or opens [10,58,59].

In 3D integrated circuits, localizing failures is much more difficult than in conventional integrated circuits because there are multiple layers the failure could be in, the layers are relatively thick (tens of μm), and the devices tend to be large, densely packed and complex. Techniques that can provide vertical resolution for fault localization in die stacks are particularly important. Unfortunately, existing failure localization techniques have typically focused on 2D devices. With the rising use of Through Silicon Vias (TSVs), identifying which layer a defect is in has become more urgent for companies pursuing this technology.

1.4 The Standard Inverse

Given a current path, it is easy to find the magnetic field it produces by applying the Biot-Savart law [60]. We can think of the Biot-Savart law as a function that converts current distributions to magnetic field images. If instead one finds the current path from a measured magnetic field, this is called finding the “magnetic inverse,” since one is trying to apply the inverse of the Biot-Savart law.

Techniques that can convert a magnetic image into an image of current density have

been widely used for more than two decades [31, 32, 61]. Much of this work has been done using a Fourier based approach that is so ubiquitous it is called the “standard inverse.” An intrinsic feature of the standard inverse is that it is restricted to two dimensions. In other words it cannot resolve into separate layers currents that are flowing on different layers. For many samples, two dimensions is a good assumption, and this has made the standard inverse a very useful and powerful technique. For example, most conventional silicon chips are built with many different layers, but these layers are so thin that they can be treated as being at the same height for many purposes. On the other hand, three-dimensional integrated circuits utilizing TSVs have currents that are flowing on well-separated layers, typically 20-100 μm from one layer to the next. Although the standard inverse can be applied to magnetic images of such samples, the resulting current density images do not provide an accurate representation of the 3D current flow in such samples.

1.5 Vertical and lateral resolution

Unlike the Fourier based standard inverse, the 3D Solver technique I describe in this thesis in [Chapter 3](#) and [Chapter 4](#) allowed me to resolve current paths in 3D and achieve sub-micron vertical resolution. I was also able to achieve sub-micron lateral resolution (see [Chapter 8](#)) and this also represented a significant improvement over what the standard inverse could achieve with the same starting magnetic image. How this is achieved and why the spatial resolution is better is discussed in [Chapter 3](#).

I should emphasize here that the exact definition of spatial resolution is not obvious, and many different definitions can be used. At first sight, the most straightforward definition,

in analogy with optical images, would involve some measure of the spatial sharpness of the imaged magnetic field. However, what we care about most are the currents in the sample, and it is the ability to spatially resolve currents in the sample that is important. Even so, defining spatial resolution is not simple, as I discuss in [Chapter 3](#).

1.6 Overview of the thesis

In this thesis I present the results from my research on 3D magnetic imaging. This research was supported by a subcontract from Neocera, LLC., and was part of a project funded by the Intelligence Advanced Research Projects Activity (IARPA). The goal of the project was to develop 3D magnetic imaging capability and use it to identify and locate electrical defects in semiconductor such as shorts devices. Our research was specifically aimed at imaging 3D integrated semiconductor chips that use TSVs, and identifying which layer a defect was located on – that is, obtaining vertical information about the location of the defect.

My work was mainly focused on developing the 3D inverse – creating a 3D current map from a magnetic image of a sample. The physical systems that we used for collecting magnetic images, the magnetic microscopes, were mainly located at Neocera. The analysis of magnetic images, as well as improved understanding of magnetic inverses, informed design decisions that influenced the microscope development and also let us identify shortcomings or errors in the magnetic scanning.

In [Chapter 2](#), I describe the standard magnetic inverse. This was the state of the art approach before I started on this project, and I discuss its advantages and shortcomings. In

[Chapter 3](#), I discuss the theoretical underpinnings of our new inverse technique. I discuss the basic approach as well as the practical algorithms that the inverse uses.

In [Chapter 4](#) I discuss the algorithms I implemented to make an actual 3D Solver program that could be used to analyze real magnetic images. In [Chapter 5](#), I discuss the operation of the 3D Solver from a user perspective instead of a development perspective.

In [Chapter 6](#), I discuss the MAGMA magnetic microscope system we used to acquire magnetic images. This system was a new design that was developed at Neocera specifically for the 3D imaging project. [Chapter 7](#) looks specifically at the spin-valve sensor used in the MAGMA system. These sensors exhibited some unusual properties, which are still not completely understood. In particular, we were surprised by the component of field that the spin-valve sensors detected, and this is discussed in detail in [Chapter 7](#).

In [Chapter 8](#) I demonstrate the capabilities of the 3D Solver by describing results on select magnetic images. Over the course of my work we acquired hundreds of magnetic scans and then ran these through various versions of the 3D Solver to understand how different samples and parameters affect our inverse technique. I present a representative set of interesting scans and use these to illustrate the capabilities of the microscope and solver. Finally, in [Chapter 9](#) I examine possible future work and conclude with a brief summary of my main results.

Chapter 2: Standard FFT Magnetic Inverse

2.1 Introduction

In this chapter I discuss a well-known fast Fourier transform (FFT) algorithm [62] for converting a 2D magnetic image into a 2D current density image. This FFT approach is so widely it is referred to simply as “the standard inverse.” It has been the norm for transforming scanned magnetic images of circuits into current maps for at least the last decade [63, 64]. The ability to quickly and easily generate a current density image is a critical step in the magnetic imaging process for failure analysis because a current map can directly reveal the location of shorts, leakage, and other defects in a sample. The FFT inverse has two key advantages: it is extremely fast and it requires very few input parameters from the operator – usually just the sensor-to-sample distance and a k-space window cut-off parameter. As I discuss below, it also has some very significant limitations.

Given a current path, it is easy to find the magnetic field it produces by applying the Biot-Savart law [65]. The Biot-Savart law can be thought of as a function that converts a current distribution into a magnetic field image. A process that instead finds the current path from a measured magnetic field is called a “magnetic inverse,” since one is trying to apply the inverse of the Biot-Savart law. Prior to our work, Fourier transform based magnetic inverse techniques were the state of the art for performing a magnetic inverse on scanned

magnetic images of circuits. Although very powerful, the FFT approach is only valid if all the currents are in a single plane [22]. In particular, the standard inverse cannot reconstruct 3D currents. If one nevertheless applies the technique to samples with 3D currents, by assuming that all of the currents are at a distance z from the image plane, then one obtains a 2D current image that is physically incorrect. Typically one finds that any currents that are further away than z appear out of focus or blurrier, while currents that are closer than z show strong “ringing” or overshoot effects (see Section 2.5). In order to reconstruct the correct current flow in multi-layer samples, one clearly needs an inversion technique that is not limited to current flow in two dimensions.

In this Chapter, I review the derivation of the standard inverse. I next discuss the extension of this technique to include the case of a sensor tilted with respect to the imaging plane. Then I discuss the signal-to-noise ratio and spatial resolution of the standard inverse, following the discussion in Ref. [59]. Finally, I look at the advantages and disadvantages of the standard inverse, and explain why we decided to develop our own technique for solving the magnetic inverse for 3D current paths.

2.2 Derivation of the Standard Inverse

2.2.1 Inverse of B_x and B_y

The following derivation of the standard inverse is based on the discussion found in Chapter 6 of Chatrathorn’s thesis [59]. Given a magnetic field image $B(\vec{r})$ that covers a finite area, we want to find the current density $\vec{J}(\vec{r}')$ that produced the field. This is

equivalent to finding the inverse of the Biot-Savart law,

$$\vec{B}(\vec{r}) = \frac{\mu_0}{4\pi} \int \frac{\vec{J}(\vec{r}') \times (\vec{r} - \vec{r}')}{|\vec{r} - \vec{r}'|^3} d^3\vec{r}'. \quad (2.1)$$

In Eq. (2.1), $\mu_0 = 4\pi \times 10^{-7}$ T m/A is the permeability of free space, $\vec{J}(\vec{r}')$ is the current density in space at location \vec{r}' , and $\vec{B}(\vec{r})$ is the resulting magnetic field at \vec{r} . Typically, only one component of the field (B_x , B_y or B_z) is measured. I first look at how to invert B_x and B_y , and then look at B_z .

For the standard inverse to be valid, the current \vec{J} must be the only source of the measured magnetic field. In addition, I assume the current is contained in a two-dimensional plane called the sample plane, which I define as the x-y plane. In other words, the vertical component of the current distribution is 0 at all locations:

$$J_z = 0. \quad (2.2)$$

Thus the standard inverse solves for a current flow on a flat surface $\vec{J} = (J_x, J_y, 0)$.

I will assume the sensor-to-sample distance z_0 is constant so that the sensor imaging plane and the current plane are parallel. z_0 must be known to apply the standard inverse and obtain the correct solution for \vec{J} . I define the z axis so that $z = 0$ for the sample plane. Therefore, points on the current plane are of the form $\vec{r}' = (x', y', 0)$, while the position of the sensor is $\vec{r} = (x, y, z_0)$.

Next, I assume that the current is quasistatic, and therefore

$$\nabla \cdot \vec{J} = 0. \quad (2.3)$$

From Eq. (2.1), one can explicitly calculate the x -component of \vec{B} at position \vec{r} :

$$B_x(\vec{r}) = \frac{\mu_0}{4\pi} \int \frac{J_y(\vec{r}') * (z_0 - z') - J_z(\vec{r}') * (y - y')}{|\vec{r} - \vec{r}'|^3} d^3\vec{r}' \quad (2.4)$$

Since $J_z = 0$, this yields:

$$B_x(x, y, z_0) = \frac{\mu_0 d}{4\pi} \int_{-\infty}^{+\infty} \int_{-\infty}^{+\infty} \frac{J_y(x', y', 0) * z_0}{[(x - x')^2 + (y - y')^2 + z_0^2]^{3/2}} dx' dy' \quad (2.5)$$

where I integrated over z' and used the assumption that the current density is contained in the sample plane in a layer of thickness $d \ll z_0$. Similarly, for B_y we get

$$B_y(x, y, z_0) = \frac{\mu_0 d}{4\pi} \int_{-\infty}^{+\infty} \int_{-\infty}^{+\infty} \frac{-J_x(x', y', 0) * z_0}{[(x - x')^2 + (y - y')^2 + z_0^2]^{3/2}} dx' dy' . \quad (2.6)$$

Note from Eqs. (2.5) and (2.6) that when the vertical component of the current is zero, the magnetic field in the x and y directions is solely generated by the current in the y and x directions, respectively. The expression for B_z is slightly more complicated:

$$B_z(x, y, z_0) = \frac{\mu_0 d}{4\pi} \int_{-\infty}^{+\infty} \int_{-\infty}^{+\infty} \frac{J_x(\vec{r}') * (y - y') - J_y(\vec{r}') * (x - x')}{[(x - x')^2 + (y - y')^2 + z_0^2]^{3/2}} dx' dy' . \quad (2.7)$$

To proceed, I now define the 2D Fourier transforms of the x -component of the field with respect to x and y only, *i.e.*

$$b_x(k_x, k_y, z) = \mathcal{F}(B_x) = \int_{-\infty}^{+\infty} \int_{-\infty}^{+\infty} B_x(x, y, z) e^{-i(k_x x + k_y y)} dx dy . \quad (2.8)$$

Throughout this thesis I will use lowercase letters to represent the 2D Fourier transforms of uppercase functions. The inverse Fourier transform of b_x gives B_x :

$$B_x(x, y, z) = \mathcal{F}^{-1}(b_x) = \frac{1}{(2\pi)^2} \int_{-\infty}^{+\infty} \int_{-\infty}^{+\infty} b_x(k_x, k_y, z) e^{i(k_x x + k_y y)} dk_x dk_y . \quad (2.9)$$

The convolution theorem [66] states that if H is the convolution of two functions $F, G : \mathbb{R}^n \rightarrow \mathbb{R}$, *i.e.*:

$$H(\vec{r}) = \int_{\mathbb{R}^n} F(\vec{r}') * G(\vec{r} - \vec{r}') d^n \vec{r}' , \quad (2.10)$$

Then $h(\vec{k}) = f(\vec{k})g(\vec{k})$, where f , g and h are Fourier transforms of F , G and H , respectively.

I can now define three Green's functions:

$$G_x(x, y, z) = \frac{\mu_0 d}{4\pi} \frac{x}{|\vec{r}|^3} \quad (2.11)$$

$$G_y(x, y, z) = \frac{\mu_0 d}{4\pi} \frac{y}{|\vec{r}|^3} \quad (2.12)$$

$$G_z(x, y, z) = \frac{\mu_0 d}{4\pi} \frac{z}{|\vec{r}|^3} \quad (2.13)$$

The Fourier transforms of functions G_x , G_y and G_z can be obtained analytically (see [59]

Appendix C), and one finds:

$$g_x(k_x, k_y, z_0) = \frac{i\mu_0 d}{2} \frac{k_x}{k} e^{-kz} \quad (2.14)$$

$$g_y(k_x, k_y, z_0) = \frac{i\mu_0 d}{2} \frac{k_y}{k} e^{-kz} \quad (2.15)$$

$$g_z(k_x, k_y, z_0) = \frac{\mu_0 d}{2} e^{-kz} \quad (2.16)$$

where $k = \sqrt{k_x^2 + k_y^2}$.

Examining Eq. (2.5) reveals that B_x is a convolution of G_z and J_y with respect to x and y and I can write

$$B_x(x, y, z_0) = \int_{-\infty}^{+\infty} \int_{-\infty}^{+\infty} J_y(x', y', 0) G_z(x - x', y - y', z_0) dx' dy'. \quad (2.17)$$

Therefore from the convolution theorem

$$b_x(k_x, k_y, z_0) = j_y(k_x, k_y, 0) g_z(k_x, k_y, z_0). \quad (2.18)$$

Our way forward is now clear. From Eqs. (2.16) and (2.18) we can write

$$j_y = \frac{b_x}{g_z} = \frac{2}{\mu_0 d} e^{kz_0} b_x. \quad (2.19)$$

A similar calculation can be done to find j_x . Starting from Eq. (2.6) we see that B_y is a convolution of J_x and G_z :

$$B_y(x, y, z_0) = - \int_{-\infty}^{+\infty} \int_{-\infty}^{+\infty} J_x(x', y', 0) G_z(x - x', y - y', z_0) dx' dy'. \quad (2.20)$$

Applying the convolution theorem again gives

$$b_y(k_x, k_y, z_0) = -j_x(k_x, k_y, 0) g_z(k_x, k_y, z_0). \quad (2.21)$$

Rearranging, and using Eq. (2.14) gives

$$j_x = -\frac{2}{\mu_0 d} e^{kz} b_y. \quad (2.22)$$

2.2.2 Inverse of B_z

So far we have seen that we can obtain J_x from B_y and J_y from B_x . In fact, as we will see presently we can obtain J_x and J_y from any one component of the field. The idea is that Eq. (2.3) ($\nabla \cdot \vec{J} = 0$) gives us a relationship between j_x and j_y . Taking the Fourier transform of (2.3) gives

$$\int_{-\infty}^{+\infty} \int_{-\infty}^{+\infty} e^{-2\pi i \vec{k} \cdot \vec{r}} \nabla \cdot \vec{J} dx dy = 0. \quad (2.23)$$

Note that $\partial J_z / \partial z = 0$ since $J_z = 0$ and we can rewrite Eq. (2.23) as

$$\int_{-\infty}^{+\infty} \int_{-\infty}^{+\infty} e^{-2\pi i \vec{k} \cdot \vec{r}} \left(\frac{\partial}{\partial x} J_y + \frac{\partial}{\partial y} J_x \right) dx dy = 0. \quad (2.24)$$

Integrating by parts gives:

$$\left[e^{-2\pi i \vec{k} \cdot \vec{r}} (J_x + J_y) \right]_{-\infty}^{+\infty} - \int_{-\infty}^{+\infty} \int_{-\infty}^{+\infty} (J_x \partial_x + J_y \partial_y) e^{-2\pi i \vec{k} \cdot \vec{r}} dx dy = 0. \quad (2.25)$$

We can eliminate the first term by assuming that \vec{J} vanishes outside of some finite region.

Thus

$$-\int_{-\infty}^{+\infty} \int_{-\infty}^{+\infty} [-2\pi i k_x J_x - 2\pi i k_y J_y] e^{-2\pi i \vec{k} \cdot \vec{r}} dx dy = 0. \quad (2.26)$$

From the definition of j_x and j_y , this gives

$$i k_x j_x + i k_y j_y = 0, \quad (2.27)$$

and thus

$$k_x j_x = -k_y j_y. \quad (2.28)$$

Equation (2.28) is a key result: from conservation of current, knowing J_x automatically gives us J_y , and vice-versa. This means that measuring either B_x or B_y is enough to determine both J_x and J_y . As we will see presently, it also allows us to obtain them from B_z . To see how, start from (2.7):

$$B_z(x, y, z_0) = \int_{-\infty}^{+\infty} \int_{-\infty}^{+\infty} J_x(\vec{r}') * G_y(\vec{r} - \vec{r}') - J_y(\vec{r}') * G_x(\vec{r} - \vec{r}') dx' dy' \quad (2.29)$$

Since Fourier transforms are linear operations, we can apply the convolution theorem to each term in Eq. (2.29), and we get:

$$b_z(k_x, k_y, z) = j_x(k_x, k_y, z) g_y(k_x, k_y, z) - j_y(k_x, k_y, z) g_x(k_x, k_y, z). \quad (2.30)$$

Now using Eqs. (2.14) and (2.15), we get

$$b_z = \frac{i\mu_0 d}{2k} e^{-kz} (j_x k_y - j_y k_x). \quad (2.31)$$

Combining (2.28) with (2.19), (2.22) and (2.31) we can now obtain relationships between the currents from any one component of the field:

$$\begin{cases} j_x = -\frac{2}{\mu_0 d} \frac{k_y}{k_x} e^{kz_0} b_x \\ j_y = +\frac{2}{\mu_0 d} e^{kz_0} b_x \end{cases} \quad (2.32)$$

$$\begin{cases} j_x = -\frac{2}{\mu_0 d} e^{kz_0} b_y \\ j_y = +\frac{2}{\mu_0 d} \frac{k_x}{k_y} e^{kz_0} b_y \end{cases} \quad (2.33)$$

$$\begin{cases} j_x = -\frac{2i}{\mu_0 d} \frac{k_y}{k} e^{kz_0} b_z \\ j_y = +\frac{2i}{\mu_0 d} \frac{k_x}{k} e^{kz_0} b_z \end{cases} \quad (2.34)$$

$$\begin{cases} j_x = -\frac{2i}{\mu_0 d} \frac{k_y}{k} e^{kz_0} b_z \\ j_y = +\frac{2i}{\mu_0 d} \frac{k_x}{k} e^{kz_0} b_z \end{cases} \quad (2.35)$$

$$\begin{cases} j_x = -\frac{2i}{\mu_0 d} \frac{k_y}{k} e^{kz_0} b_z \\ j_y = +\frac{2i}{\mu_0 d} \frac{k_x}{k} e^{kz_0} b_z \end{cases} \quad (2.36)$$

$$\begin{cases} j_x = -\frac{2i}{\mu_0 d} \frac{k_y}{k} e^{kz_0} b_z \\ j_y = +\frac{2i}{\mu_0 d} \frac{k_x}{k} e^{kz_0} b_z \end{cases} \quad (2.37)$$

Eqs. (2.32 - 2.37) are expressed in terms of the Fourier transforms of the magnetic field and current. To express these in terms of the magnetic field and current directly, we can use the definition of the inverse Fourier transform (Eq. (2.9)). For example, this turns Eq. (2.32) into

$$J_x(x, y, 0) = \frac{-2}{\mu_0 d (2\pi)^2} \int_{-\infty}^{+\infty} \int_{-\infty}^{+\infty} dk_x dk_y \left[\frac{k_y}{k_x} e^{kz_0} \int_{-\infty}^{+\infty} \int_{-\infty}^{+\infty} dx dy B_x(x, y, z) e^{-i(k_x x + k_y y)} \right]. \quad (2.38)$$

Note that in practice, the integral over real space (dx and dy) is limited by the area covered by the magnetic scan. For noise reasons discussed in Section 2.4, the integral over frequency space (dk_x and dk_y) must be cut off at high frequencies with a noise cutoff k_w . If a square cutoff is used, I can rewrite Eq. (2.38) as

$$J_x(x, y, 0) = \frac{-2}{\mu_0 d (2\pi)^2} \int_0^{k_w} \int_0^{2\pi} dk d\theta_k \left[k \tan \theta_k e^{kz_0} \iint_{scan} dx dy B_x(x, y, z) e^{-i(k_x x + k_y y)} \right]. \quad (2.39)$$

Other cutoffs, such as Gaussian or Hanning have been used and tend to produce less ringing artifacts [10].

2.3 Tilted Standard Inverse

As part of the IARPA 3D magnetic imaging project, we collected scans with spin-valve sensors that had significant sensor tilt. Instead of collecting the magnetic field along the z axis as intended, these sensors measured the field at a significant angle θ from the z axis, sometimes as large as 40° (see Chapter 7 for examples). In Section 2.2, I described how the standard inverse uses the field component along the x , y or z axes to find the current density. A slight modification allows the inverse to work for a measurement of the magnetic field in an arbitrary direction. Using such a modified inverse is preferable to trying to precisely align the sensor in a particular direction. Of course one needs to input the tilt angles to use the inverse. It turns out that we can easily measure the sensor orientation via a calibration scan – ideally an L-shaped or T-shaped current path, and use the angles measured for subsequent scans.

To modify, the standard inverse to take tilt into account, I again assume the currents in the sample are confined to the x - y plane (see Fig. 2.1), and that the sensor imaging plane is parallel to the sample plane, a distance z away. However instead of measuring B_z , the sensor measures $B_m = B_x \sin \theta \cos \phi + B_y \sin \theta \sin \phi + B_z \cos \theta$. The idea is to now find modified versions of Eqs. (2.32 – 2.37) that give j_x and j_y in terms of b_m rather than in terms of b_z .

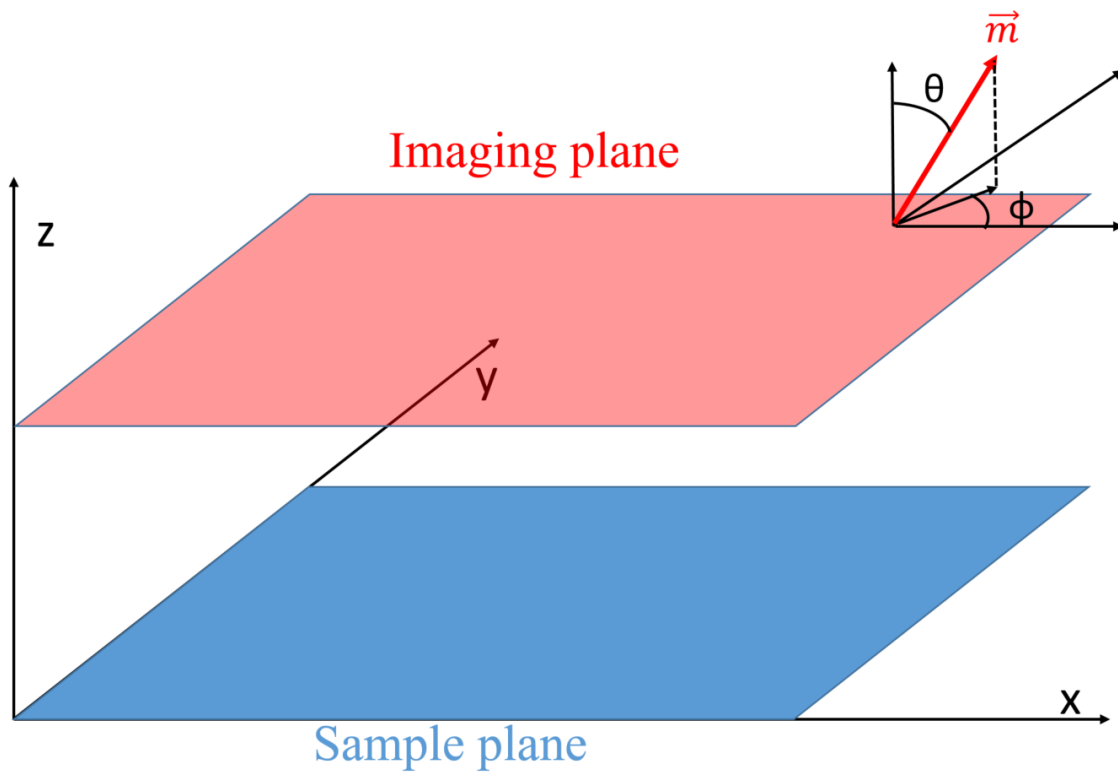


Fig. 2.1. The sensor tilt angles θ and ϕ follow the conventional definition for spherical coordinates and determine which component of the magnetic field the sensor detects. Note that the imaging plane and the current carrying plane are parallel and independent from the sensor angles.

Since Fourier transforms are linear, we can immediately write

$$b_m = b_x \sin \theta \cos \phi + b_y \sin \theta \sin \phi + b_z \cos \theta . \quad (2.40)$$

From Eqs. (2.32), (2.34) and (2.36) we can then write

$$b_m = \sin \theta \cos \phi j_x \left(-\frac{\mu_0 k_x}{2 k_y} e^{-kz_0} \right) + \sin \theta \sin \phi j_x \left(-\frac{\mu_0}{2} e^{-kz_0} \right) + \cos \theta j_x \left(\frac{i \mu_0 k}{2 k_y} e^{-kz_0} \right) \quad (2.41)$$

which simplifies to

$$j_x = \frac{2}{\mu_0} k_y e^{kz_0} \frac{1}{(-k_x \sin \theta \cos \phi - k_y \sin \theta \sin \phi + ik \cos \theta)} b_m . \quad (2.42)$$

Similarly, I can use Eq. (2.28) to obtain

$$j_y = -\frac{2}{\mu_0} k_x e^{kz_0} \frac{1}{(-k_x \sin \theta \cos \phi - k_y \sin \theta \sin \phi + ik \cos \theta)} b_m . \quad (2.43)$$

We can check that Eqs. (2.42) and (2.43) make sense by verifying that they reduce to Eqs. (2.32 - 2.37) when $\theta = 0$ ($B_m = B_z$), $\theta = \pi/2$ and $\phi = 0$ ($B_m = B_x$), and $\theta = \pi/2$ and $\phi = \pi/2$ ($B_m = B_y$).

2.4 Noise and spatial resolution

In this section I review how the spatial resolution of the standard inverse is determined by the noise in the original magnetic image. The key point is that Eqs. (2.32 – 2.39) contain an exponential e^{kz_0} term. This means that noise at high spatial frequencies ($kz_0 \gg 1$) will be amplified exponentially with the size of Fourier k-space included in the inverse. Therefore we must use a low-pass k-space filter to cut out high spatial frequency noise.

We call the filter cut-off spatial frequency k_w . To understand how noise limits the spatial resolution, one needs to understand how the cutoff frequency affects both the signal and the noise. We look at both of these in turn.

To start, consider the case where there is a single pixel of noise in an otherwise blank image:

$$B_z(x, y) = B_0 \delta^2(x, y) A \quad (2.44)$$

where B_0 is the noise in the pixel and A is its area. I now calculate what current the standard inverse would assign to this magnetic image. Following the derivation in [67], one obtains

$$b_z(k_x, k_y) = \mathcal{F}(B_z(x, y)) = B_0 A. \quad (2.45)$$

Using Eq. (2.36),

$$j_x(k_x, k_y) = -\frac{2i}{\mu_0 d} e^{k_z z_0} \frac{k_y}{k} B_0 A \quad (2.46)$$

and according to [59] this yields:

$$J_x(x, y) = -\frac{B_0 A}{\pi \mu_0 d} \frac{y}{r} \int_0^{k_w} k e^{kz} J_1(kr) dk \quad (2.47)$$

and one finds

$$J_x(x, y) \approx -\frac{B_0 A}{\pi \mu_0 d} \frac{y}{r} J_1(k_w r) \left[\frac{e^{k_w z} (k_w z - 1) + 1}{z^2} \right] \quad (2.48)$$

with the approximation holding for $k_w r \ll 1$, where $r = \sqrt{x^2 + y^2}$, and J_1 is the Bessel function of the first kind of order 1. Similarly, the y component of the current density can be reconstructed as:

$$J_y(x, y) \approx +\frac{B_0 A}{\pi \mu_0 d} \frac{x}{r} J_1(k_w r) \left[\frac{e^{k_w z} (k_w z - 1) + 1}{z^2} \right]. \quad (2.49)$$

The resulting squared current density is

$$|J(x, y)|^2 \approx \left(\frac{B_0 A}{\pi \mu_0 d} \right)^2 J_1^2(k_w r) \left[\frac{e^{k_w z}(k_w z - 1) + 1}{z^2} \right]^2. \quad (2.50)$$

The only spatial dependence in Eq. (2.50) comes from the Bessel function argument, $k_w r$. Thus we know that the current noise will be azimuthally symmetric for one pixel of field noise, with a radial dependence similar to J_1 . That is, it will resemble concentric rings of current. The radius of the first and highest ring will be located at the maximum of $J_1(k_w r)$, which depends on the cutoff frequency k_w . For example, Fig. 2.2 (a) - (e) show plots from applying Eqs. (2.48 – 2.50). Figures 2.2 (b), (c) and (d) show the overall shape of the noise in the image. Figure 2.2 (e) shows that the cross-section of J_y along the x axis has the shape of J_1 . Figure 2.2 (b) shows the noise in J_x , Fig. 2.2 (c) shows the noise in J_y , and Fig. 2.2 (d) shows the noise in J^2 . I note specifically from Fig. 2.2 (d) that the noise is azimuthally symmetric and consists of one main ring (corresponding to the max of J_1), and a series of smaller “ripples”. Figure 2.3 shows a perspective view of the plots in Fig. 2.2; these plots make it easier to judge relative heights. For this simulation, I used reasonable imaging parameters: $B_0 = 100$ nT, $z = 100$ μm , $A = 100$ μm^2 , $k_w = 2\pi \cdot 4.7\text{mm}^{-1}$.

I can use the single pixel noise result to find what happens when there is magnetic noise in each pixel of the entire image. Since Fourier transforms are linear operations, one can simply add up the current density noise in k-space due to each pixel’s magnetic noise. A reasonable assumption is that the magnetic noise follows an uncorrelated Gaussian distribution. In [68] Chatrathorn calculates the standard deviation of the current density noise resulting from this magnetic noise and finds:

$$\Delta J^2 = \frac{1}{2\pi} \left(\frac{\Delta x \Delta B}{\mu_0 dz} \right)^2 \left[e^{2k_w z}(2k_w z - 1) + 1 \right]. \quad (2.51)$$

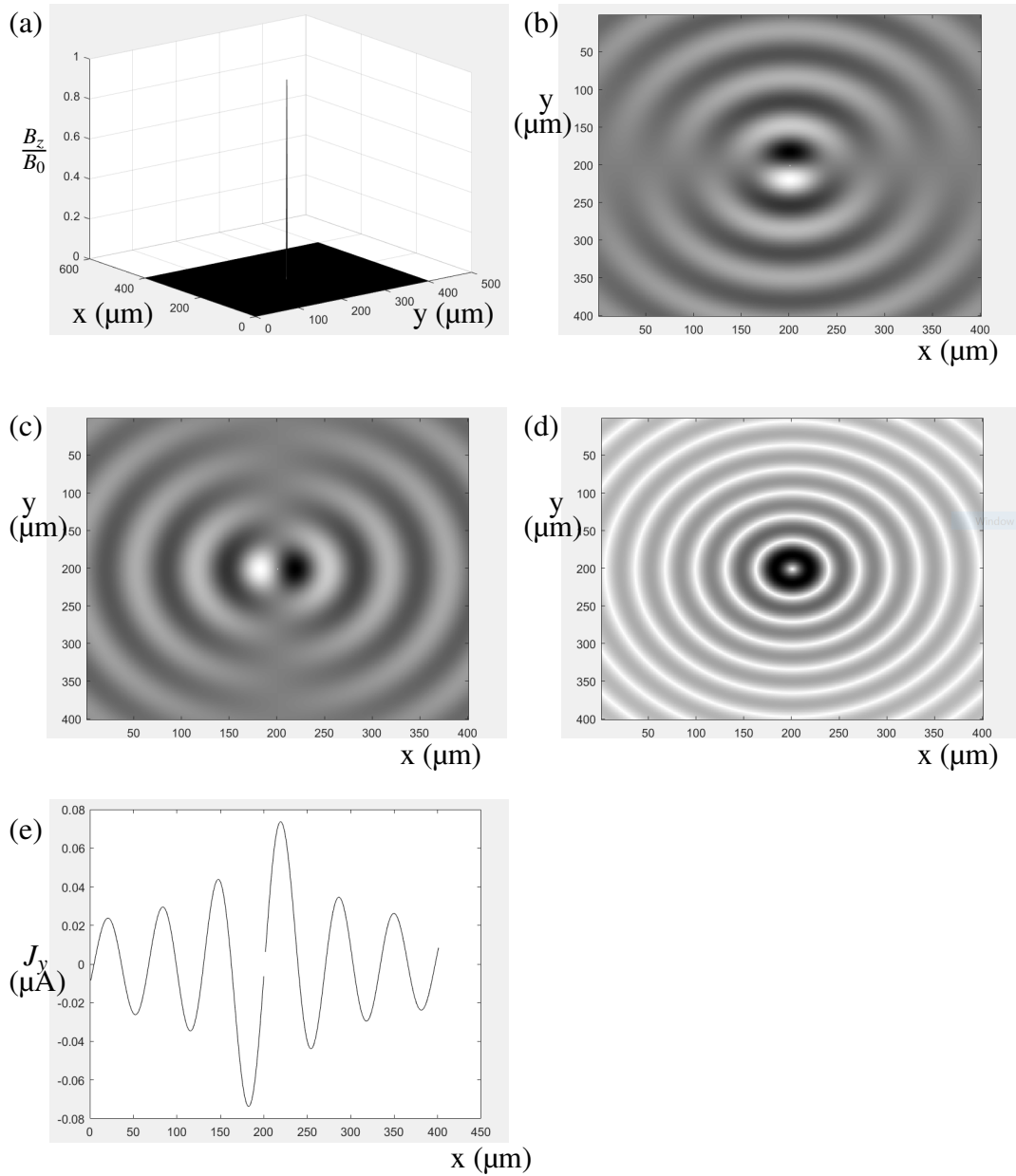


Fig. 2.2. (a) Perspective view of a single pixel of noise B_0 in a magnetic scan measuring B_z . (b) Current density noise in J_x due to magnetic noise in (a). (c) Current density noise in J_y due to magnetic noise in (a). (d) Current noise power density in J^2 due to magnetic noise in (a). (e) Line cut in (c) along the x axis shows that the noise in (a) closely follows the profile of the bessel function J_1 . For these plots, $B_0 = 100$ nT, $z = 100$ μm , $A = 100$ μm^2 , $k_w = 2 \cdot \pi 4.7 \text{mm}^{-1}$.

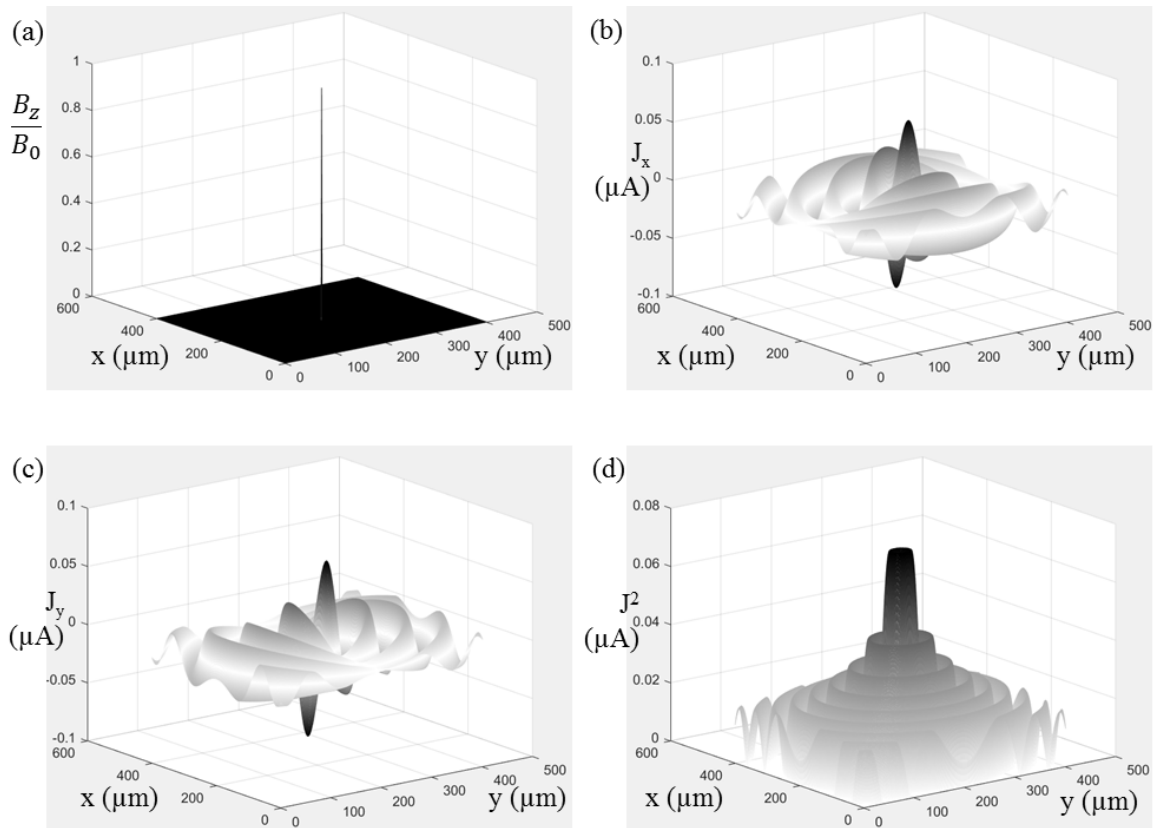


Fig. 2.3. Perspective view of Figure 2.2 (a) - (d). (a) Perspective view of a single pixel of noise in a magnetic scan measuring B_z . (b) Current density noise in J_x due to magnetic noise in (a). (c) Current density noise in J_y due to magnetic noise in (a). (d) Current density noise in J^2 due to magnetic noise in (a).

Here, ΔB is the standard deviation of the noise in the image, Δx is the pixel-to-pixel distance, and ΔJ^2 is the variance of the current density. I note that in fact the resulting current density noise is correlated spatially in the current density image. Qualitatively, it will not look fully random, but like a superposition of rings that circle the pixels with highest magnetic noise.

To proceed to find the spatial resolution, I next consider the case of a straight wire, carrying a current I along the x axis. While there are many ways one can define “spatial resolution,” here I define the spatial resolution as the full width at half maximum (FWHM) of the peak in a current density squared image of an infinitely thin wire. This is the separation at which the J^2 image of two wires would merge together and look like only one wire. There are other definitions of spatial resolution that we could pick, but this definition makes the analysis straightforward and the need to resolve adjacent long wires is a common situation that is important to understand. For a single long wire carrying current I along the x -axis, the current density is

$$\vec{J}(x, y) = \left(0, \frac{I}{d} * \delta(y), 0 \right) \quad (2.52)$$

where d is the nominal thickness of the wire. I now assume that the imaging system measures magnetic field $B_z(x, y)$ due to \vec{J} . This image is then transformed into Fourier space, processed and then transformed back into real space to find the current (see Fig. 2.4).

In the Fourier transform step from $\vec{B}(x, y)$ to $\vec{J}(x, y)$, we must cut off the integration over real space to include just the area scanned. Theoretically, we should be integrating over all space, but in practice we only scan a finite area in a region near the sample. Provided the area we scan is large, this approximation is good because magnetic fields drop off as they get further from their source — but it introduces artifacts which can cause distortion.

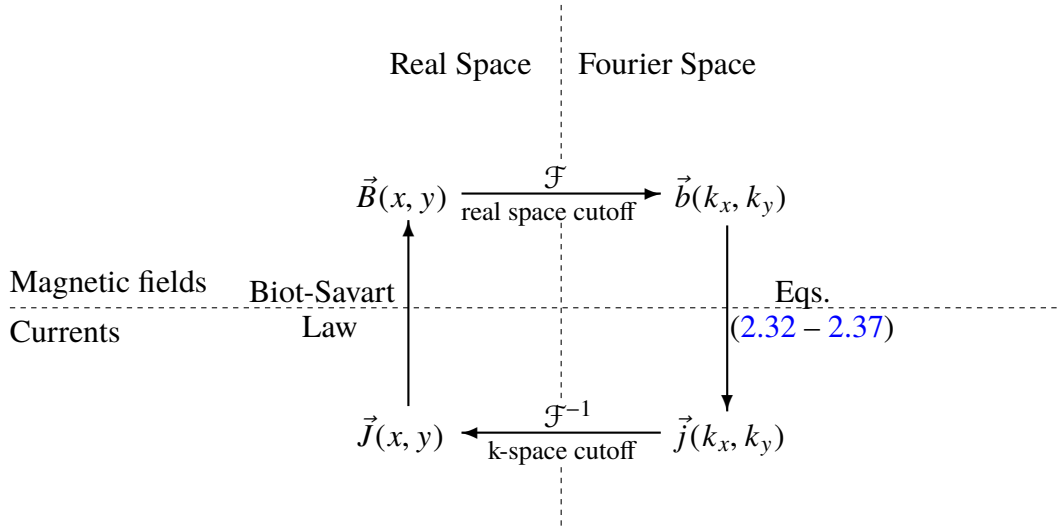


Fig. 2.4. Diagram of how the Fourier inverse works. We assume a current distribution \vec{J} (bottom left) has generated a magnetic image \vec{B} (top left). For the inverse, we measure the magnetic image \vec{B} , then transform it into Fourier space to get \vec{b} (top right). This introduces some defects since we can only image a finite area. We then use Eqs. (2.32 – 2.37) to reconstruct the currents \vec{j} in k-space (bottom right). Finally, we transform the currents back into real space (bottom left) to obtain \vec{J} . This time, noise forces us to introduce a k-space cutoff, limiting the spatial resolution and introducing windowing artifacts.

Similarly, in the inverse Fourier transform step, we must cut off the integration in k-space at k_w due to noise. This is what limits the spatial resolution.

To understand the effects of a k-space cutoff k_w , ignoring any effects from real-space

cutoff or noise, we first note that with no cutoff in k-space that

$$j_y(k_x, k_y) = \int_{-\infty}^{+\infty} \int_{-\infty}^{+\infty} J_y(x, y) e^{-i(k_x x + k_y y)} dx dy \quad (2.53)$$

$$= \int_{-\infty}^{+\infty} \int_{-\infty}^{+\infty} \frac{I}{d} \delta(y) e^{-i(k_x x + k_y y)} dx dy \quad (2.54)$$

$$= \frac{I}{d} \delta(k_x) \quad (2.55)$$

If we did an inverse Fourier transform over all k-space, this would yield an infinitely sharp feature, and the spatial resolution $s = 0$. However, instead of a true inverse Fourier transform, we must use a hard cut-off in k-space and find

$$J_y(x, y) = \frac{1}{2\pi} \int_{-k_w}^{k_w} \frac{I}{d} e^{-ik_x x} dk \quad (2.56)$$

This integral can be solved analytically. From [68], we get

$$J_y^2(x, y) = \left(\frac{Ik_w}{\pi d} \right)^2 \left(\frac{\sin(k_w x)}{k_w x} \right)^2 \quad (2.57)$$

and a FWHM of

$$s = \frac{2.783}{k_w} \quad (2.58)$$

With different window choices, one finds somewhat different relationships between s and k_w .

Equations (2.51) and (2.57) can now be combined to get the dependence of the spatial resolution s on the noise ΔB in the sample. The peak current density given by the inverse will occur right above the wire, when $x = 0$. At $x = 0$, one finds for $S/N = 1$ that

$$1 = \frac{J_{max}^2}{\Delta J^2} = 2\pi \left(\frac{\mu_0 z I k_w}{\pi \Delta x \Delta B} \right)^2 \frac{1}{[e^{2k_w z} (2k_w z - 1) + 1]} \quad (2.59)$$

We can use (2.58) and rearrange as in [68] to find a transcendental equation for z/s :

$$\frac{z}{s} = \frac{1}{2 * 2.783} \ln \left\{ \frac{\frac{2\pi}{(S/N)} \left[\frac{2.783\mu_0 I}{\pi\Delta x\Delta B} \left(\frac{z}{s} \right) \right]^2 - 1}{2 * 2.783(z/s) - 1} \right\}. \quad (2.60)$$

Where S/N is an arbitrary threshold that there is enough signal in the image (typically, one would set $S/N = 1$). This implies that the spatial resolution is linear in the sensor-to-sample distance z . With typical SQUID imaging parameters, a $z/s = 5$ is achievable [68]. However, the logarithmic dependence in (2.60) means that improving on this performance will require logarithmic improvements in the magnetic noise or the sampling distance.

2.5 Advantages and limitations

The standard inverse has several advantages that have made it a popular choice as an inverse technique. First, it is a fast algorithm to run, giving a nearly instant solution. This is in part because the solution can be written in a closed mathematical form (see Eqs. (2.32-2.37)) and because computers can run an FFT very efficiently. Having a closed mathematical form also makes the code for running the algorithm simple to write, test and debug. Second, the inverse requires few parameters to run; the algorithm only needs a magnetic scan, the sensor to sample distance z_0 , and a value for the k-space cut-off k_w . Optionally, the user may specify a custom Fourier space filter. Otherwise, a default can be used (typically a Hanning filter). If there is a possibility the sensor is tilted, then the user would have to specify values for the sensor angles as well. This is a very small and intuitive set of parameters — and only the sensor-sample distance z_0 is truly required. This simplicity leads to the possibility of a simple user interface and less effort by the user. This is an important advantage when considering commercial applications.

It is also interesting to note that the output of the standard inverse is two current density images (of J_x and J_y) that are sampled on the same spatial grid as the original magnetic scan. Often, the two images can be combined by mapping the sum squared of the two values, $J^2 = J_x^2 + J_y^2$. Because of current conservation, J^2 images can show the path taken by a current and these images tend to be much more easily understood by people than the magnetic images or the individual J_x and J_y images. These advantages have made the standard inverse the main inverse method for at least the last 15 years for semiconductor imaging.

The standard inverse also has some serious limitations. The most important one is that it assumes that the currents in the sample are limited to a single plane. That is, the inverse cannot correctly resolve currents in three dimensions or currents that flow in more than one layer. Trying to apply these techniques to samples with 3D currents, by assuming that all of the currents are at a distance z_0 from the image plane, results in a 2D current image that is physically incorrect. This limitation of the standard inverse is a major motivation for my work on developing an alternative inverse.

Because the Fourier method requires a high spatial frequency cutoff k_w to achieve a fine spatial resolution s , it has difficulty with sharply spatially defined fields or currents. k_w is limited by the noise in the system and in practice it does not go higher than $k_w \approx 2\pi \cdot 10 \text{ mm}^{-1}$. From Eq. (2.58) this means that the effective resolution in the reconstructed current image is limited to about $45 \mu\text{m}$ regardless of the magnetic scan resolution. This limitation is due to the exponential amplification of the high-frequency noise in eqs. (2.32 – 2.39). There is no fundamental reason the high-frequency noise should limit the spatial resolution in this way and other inverse techniques do not have this limitation. Other

methods can realistically provide much higher current resolution from a lower resolution magnetic image. Due to the Fourier nature of the inverse, high-frequency contributions are also limited by the Nyquist sampling frequency. However, since magnetic scans are often sampled at $1\ \mu\text{m}$, and could be sampled at even finer resolution, the noise usually limits k_w well before Nyquist sampling rate does.

Another problem with the standard inverse is that the reconstructed currents include noise and artifacts. This is particularly a problem at the edges of the magnetic image, which typically produce a sudden cutoff in the magnetic field. This leads to artifacts such as Gibbs overshoot and ringing. Indeed, we see the same ringing effects that plague other Fourier based method with high-frequency cutoffs, such as jpeg image compression [69] or audio mp3 compression [70]. Different cutoffs, such as Gaussian or Hanning, can be used to eliminate ringing due to a square cutoff [10, 71]. However the artifacts cannot be fully eliminated because they are also caused by the missing high-frequency terms. Therefore in order to get artifact-free current densities image of a sample, one must take a magnetic field image much larger than the section one is actually interested in. In practice, this means one needs to spend more time taking images, and most of the area one is imaging will not be of interest.

A related problem is that the Fourier method applied to B_z to date assumes continuity of current and does not deal appropriately with currents that run off the boundary of the image. If currents run off the image, the inverse produces compensation currents that run back into the image. In addition, if the boundary of the image occurs in a region where B_z or its gradient are non-negligible, the inverse tends to generate large artifacts. The exponential factor in k-space amplifies any abrupt features, including the edges of an image.

Another potential problem with the standard inverse is that any vertical currents in the sample will lead to unphysical artifacts in the current density since the inverse assumes there are no vertical currents. Vertical infeeds and outfeeds are particularly problematic because the current entirely disappears, effectively creating a current sink or a current source. Since the standard inverse assumes conservation of current in 2D, this results in introducing currents that do not exist and the answer will be unphysical.

I should also note that the standard inverse generates a current density image with noise that depends exponentially on the cutoff k_w or equivalently the spatial resolutions (see Eq. 2.58). This makes it very hard to get significantly better spatial resolution by reducing the noise in the system. Averaging longer or building lower noise SQUIDs will yield very small improvements in the spatial resolution, as the resolution's dependence on the noise is logarithmic. In practice, this means SQUID systems using the standard inverse will be stuck at a spatial resolution of $s \approx z/5$ at best [68].

Finally, it is difficult to incorporate information about the current flow or other known constraints into the standard inverse solution, such as the location and strength of the infeed and outfeed currents. The inverse will give a false solution when wrong parameters (such as z_0 or the sensor tilts) are used, and there is no metric for measuring how good the obtained solution is.

2.6 Conclusions

In this chapter I derived the standard Fourier magnetic inverse from the Biot-Savart law. I also showed how the standard inverse can be modified to account for sensor tilts

– a very useful extension for practical applications. We also saw that while the Fourier inverse’s simplicity has made it successful in scientific and commercial applications, it also has significant drawbacks. Most importantly, the Fourier inverse cannot be used to find 3D currents distributions.

I note that there is a fundamental trade-off between assumptions and results. Making more assumptions about your sample lets you perform a magnetic inverse which would otherwise not be possible. On the other hand, the more assumptions are made, the fewer samples can be successfully “inverted” because fewer samples will meet the constraints. It appears to be quite difficult to introduce new constraints in the Fourier approach, which makes it difficult to tailor the inverse even when additional information is available about a sample. For 3D applications, we specifically need to relax the requirement that the sample have 2D currents and must introduce new constraints. Doing so required us to abandon the standard inverse and develop the new approach described in Chapter 3.

Chapter 3: A 3D Inverse Technique

3.1 Introduction

In [Chapter 2](#) I examined the standard FFT magnetic inverse and discussed its advantages and disadvantages. In particular I emphasized why it wasn't suitable for multilayer samples. Here, I introduce a new inverse technique we developed to reconstruct current paths from magnetic images. Unlike the standard FFT magnetic inverse, this new technique was designed to handle current paths on multiple layers and we call it the "3D inverse" to distinguish it from the standard inverse.

In [Section 3.2](#) I show why a general inverse isn't possible for the Biot-Savart law, and why any inverse must incorporate constraints on the possible solutions for the currents. In [Section 3.3](#) I present the constraints we chose for the 3D inverse, which are suited for imaging 3D circuits. In [Section 3.4](#) I give an overview of the search process, which is explained in detail in [Chapter 4](#). In [Section 3.5](#) I show that the constraints that we use for the 3D inverse are sufficient to guarantee a unique solution. In [Section 3.6](#) I introduce the concepts of current rings and the least resolvable rings. The least resolvable ring patterns limit the spatial resolution of the inverse, and are also a critical concept in the inversion algorithms I describe in [Chapter 4](#). In [Section 3.7](#) I examine the signal-to-noise ratio expected for these least resolvable rings and from this find the spatial resolution achievable

with the 3D inverse. I briefly compare the performance of the 3D inverse to the spatial resolution obtained via the FFT routine, and to the ultimate limits on spatial resolution that can be obtained using any magnetic inverse technique. Finally, I conclude in [Section 3.8](#).

3.2 Need for constraints

The fundamental difficulty in reconstructing a 3D current path from a 2D magnetic image is that the Biot-Savart law, which calculates magnetic fields from a current distribution, does not have a unique mathematical inverse because it is not one-to-one. That is, two different 3D current distributions can give exactly the same magnetic field image. For example, consider the following two cases involving a long coaxial cable. In the first case, current flows axially down the outer cylindrical sheath of the cable. In the second, current flows through the central wire of the cable. Both current distributions produce the same magnetic field outside of the cable. This makes it impossible to distinguish which current distribution is present from just a magnetic field image outside the cable. In order to eliminate incorrect current distributions, one needs to apply a sufficient number of constraints on the allowed current distributions to get a unique solution.

I note that a key characteristic of the complete set of constraints is that it must exclude all current distributions that produce no external magnetic field. For example, all magnetic inverses need to exclude coaxial cable geometries in which there is current flowing in the inner conductor and equal but opposite current flowing in the outer conductor, as this produces no net magnetic field outside the cable. In fact, excluding all non-zero current distributions producing zero magnetic field is a sufficient condition to guarantee that the

inverse has unique solutions. To see this, consider an inverse whose image range (output) contains no current distributions producing no magnetic field except the trivial case, *i.e.* only the $\vec{J} = 0$ distribution produces zero field. Now suppose there are two distinct current distributions, \vec{J}_1 and \vec{J}_2 , that produce the same magnetic field. The difference, $\vec{J}_2 - \vec{J}_1$, must produce zero magnetic field, because the Biot-Savart law is a linear transformation. Since only the $\vec{J} = 0$ distribution can produce zero magnetic field, $\vec{J}_2 - \vec{J}_1 = 0$. However, by assumption \vec{J}_1 and \vec{J}_2 are distinct. By this contradiction we see that excluding such fields guarantees a unique inverse.

3.3 Reasonable constraints for semiconductor circuits

For computer chips, multilayer modules [72, 73] and 3D integrated circuits built using through silicon via (TSV) there are natural constraints which we can apply. Typical semiconductor devices are fabricated according to well-known rules which restrict the possible flow of currents. By taking these restrictions into account, we developed a set of constraints on the set of possible current paths that are sufficiently powerful that the inverse will yield a unique solution.

The first assumption is that the current can only flow in wires on a finite-sized 3D orthogonal grid-like pattern, *i.e.* along short segments that are along the x , y and z directions. We assume that these segments have a well-defined width and are formed from thin films with a thickness d that is negligible compared to all other dimensions in the problem. In this sense we discretize the problem into a lattice – current can only flow through straight segments between adjacent lattice points. I note that this is not consistent

with some structures found in microelectronics such as ground planes.

Second, I assume that the grid only has a finite number of layers (typically no more than 5) in the z -direction (depth) and is of finite extent in the x and y dimensions. Since the grid is orthogonal, all current flow between the layers is vertical, *i.e.* along the z direction. For computational reasons, our grid has uniform spacing in x (w_x) and in y (w_y), although $w_x = w_y$ is not required. In z , each current carrying layer can be separated by an arbitrary distance h_i , where h_1 represents the distance between layers 1 and 2, and so on. We will refer to this as a 3D Manhattan lattice.

Third, I assume that all currents outside of the finite 3D grid region of the sample are known and that we are only concerned with finding currents in the grid region. Naturally, I assume that the input leads and output leads supplying current to the sample must connect with a path inside the sample. If any other sources of magnetic field are present (*e.g.* currents outside the imaging region) the assumption is that they are known and their magnetic field contribution can be subtracted from the magnetic image so that we are left only with the magnetic field from currents inside the sample.

Fourth, I assume that we can apply Kirchoff's current conservation law: the net current through any lattice point is zero. That is, all current going into a lattice point must come out. Fifth, I assume that the current in a given wire will follow a single connected path, so that at every point the current in a wire is the same. That is, current does not branch at the vertex of lattice points. Since current is conserved, each segment that is part of the wire carries the same current I and all other segments carry zero current. In practice, the 3D solver will allow for more than one wire and this introduces some complications, as we will see in [Chapter 4](#). It turns out the situation is manageable, even if the wires

carry different currents, provided there aren't too many wires, and this allows for a limited number of branching points by splitting one wire into two separate wires. For the purpose of understanding uniqueness, I will assume here that there is only one wire. Sixth, I assume we are measuring a component of the magnetic field – typically the z component. Seventh, I assume that the sensor is a fixed distance z above the top surface of the sample. Eighth, I assume all current carrying layers are parallel to each other and to the imaging plane. Ninth, I assume that each wire has uniform width b . Tenth, I assume that a wire cannot overlap or intersect itself. In addition to preventing branching, this means that there are no current sinks or sources, such as batteries, embedded in our circuit. Note that assumption four and ten imply that the only currents present in the sample are supplied by means of input and output leads attached to the boundary of the sample, and the boundary conditions are known.

The use of a regular 3D Manhattan lattice is mostly for convenience and it appears this approach can be extended to include 45° segments, for example. Constraints five and ten greatly simplify the types of paths that need to be considered and also ensure that there are no branches of a path that have arbitrarily small current flow and no sections of paths that exactly overlap with segments of the path carrying the opposite current.

3.4 3D technique overview

In our 3D technique, we resort to a search over possible current paths that meet the constraints laid out in [Section 3.3](#). We can think of this as a highly restricted search in the phase space of current distributions. During the search, we make a small variation in an

existing or starting path, calculate the field it would produce, compare this to the measured field, and select for paths that produce a closer & closer match to the measured field. By choosing paths that minimize the difference between the observed field and the fitted field, we obtain a best fit path.

The first step in such a path search is to find a reasonable starting path, ideally one that is close to the actual solution. We call the process of generating a starting path “wirization.” We use a variety of custom made algorithms to obtain starting paths, including inputting a path known from CAD, hand-drawing a suspected path, and using the Hosaka-Cohen transform [74], which uses the field derivatives to find an approximation to the current density. As another example, one could start with the solution provided by the 2-dimensional FFT inverse and discretize it to create a path in 3D. Although the initial path would be incorrect, in favorable cases it could be similar enough to the true path to allow an iterative search algorithm to go from the initial solution to the correct solution.

The actual path search is composed of two parts. The first part of the search starts with the initial path and then makes a series of relatively small changes in the geometrical path the current takes through the lattice so as to minimize χ^2 (see Eq. 3.13) between the measured magnetic field image and the magnetic field calculated from the test path. Given typical lattice sizes of a few layers and about 20,000 x - y vertices, a typical current path may be thousands of segments long, and thus go through thousands of lattice points. In this case the search algorithm will typically search through millions of combinations to produce a best fit. Since it takes far too long to test all possible paths, I devised a few routines which make a few simple types of restricted path changes. For example, the “ z -search” part of the routine tries moving a designated number of segments up or down in different layers. All

the path search algorithms rely on continuity of current, so that when the path is varied, the routine does so in a manner which maintains a connected path.

The second part of the search relates to optimizing the imaging and sample parameters. In many cases, important sample parameters will be unknown or only roughly known. For example, the layer-to-layer spacing h in the sample and the trace width b of the current carrying path need to be known quite accurately to accurately calculate the magnetic field from a current path. In some cases, these parameters might be known, but not to sufficient precision to allow a good match between a simulated path and the data. For example, in many samples our images are sensitive to sub- μm differences in the layer-to-layer separations. As part of our path search process, we must optimize both the sample parameters and the geometrical distribution of current.

In addition to the sample parameters, the search process must also find accurate values for several scanning parameters, including the sensor gain g , the sensor-to-sample distance z , the sensor tilt and alignment (θ and ϕ), the noise level σ_B in each pixel, and whether an (ac) offset field is present. Although we can determine some of these parameters from independent measurements on test samples, we typically need to know them quite accurately and in practice try to find best fit values along with the sample parameters and the path. For example, since we control the input current to our sample, we may know with a precision of 1% what the input current I is. However, as we apply the inversion algorithm to the scan, we may need to know I to better than one part in one thousand. Also, since there can be leakage currents outside of the range of the image, we can't assume the input current we feed into the sample is known with certainty, and we must use the image to fit for it. Similarly, we typically know the sample has been aligned with the x - y scan directions (in-plane rotation)

to better than 1° . However, our inverse is typically sensitive to rotations on the order of 0.01° . Fortunately, such global parameters as the gain, currents, rotation angles, and sensor rotation can usually be fit very well from the data.

The main difficulty of the path search approach is that it is susceptible to becoming trapped in local minima of χ^2 , *i.e.* stuck with a path that produces a minimum in χ^2 compared to “nearby” paths, but which isn’t the global minimum. This is a reflection of the underlying physics of the situation – there can be many distinct current distributions that produce nearly the same magnetic field image but have current paths that look quite different. In addition, some samples have paths that are more prone to getting trapped in local minima than others. As a rule of thumb, the more complex the circuit and the poorer the signal-to-noise ratio, the more susceptible the search is to getting trapped in a local minima. Also, the parameter and path search tend to be heavily correlated. In particular, mistakes in the parameters make it difficult to find the correct path, and *vice versa*. On the other hand, if one possesses good information about key parameters such as the gain g and layer separation z and a good guess for a starting path, and the path is not too complex, the routine can work remarkably well. In practice, we usually start with best guesses for the parameters and do a series of automated and hand-drawn searches on the path. We then go back and try re-optimizing the parameters, and again search on the path, going through this iterative cycle until the fit has converged. Depending on the complexity of the sample and the image, and the amount of information known about the image, this process of analysis can take a few hours to many days of patient work.

3.5 Uniqueness of solution

Given a magnetic field image produced by currents in a sample that obeys our constraints, I now examine whether there is a unique solution for the source currents that produced the field. For this discussion, I assume that the current I in the path, the number of layers n_L , the grid sizes w_x and w_y , the layer spacings h_i , and the sensor-to-sample distance z are known and that the true path that produced the image exists and obeys the constraints. I assume that each trial path and the true path consist of only one wire, although the approach is generalizable to multiple wires.

In the following argument I will suppose the contrary and establish that this causes a contradiction. That is, I start by assuming that there is a solution path P_1 that produces a magnetic field $B_1(x, y, z_0)$ but this solution is not unique. Thus there is a second path P_2 which differs from the first path but produces a magnetic image $B_2(x, y, z_0)$ that is equal to $B_1(x, y, z_0)$. The constraint on boundary conditions ensures that both paths start at the same location and end at the same location, so for the paths to be distinct there must be one or more segments inside the sample region that are on one path but not on the other. The segments that differ must lie on the 3D Manhattan lattice, since they are just a subset of segments from two paths that obey the constraints.

I construct the difference between the two paths $\Delta P = P_2 - P_1$. Segments where the two paths are the same will cancel out, *i.e.* contribute nothing to the difference image, and thus can be effectively erased from the difference path as well. The resulting difference path must form one or more closed loops on the 3D Manhattan lattice corresponding to sections where the two paths diverged from each other. To see why ΔP must form a closed

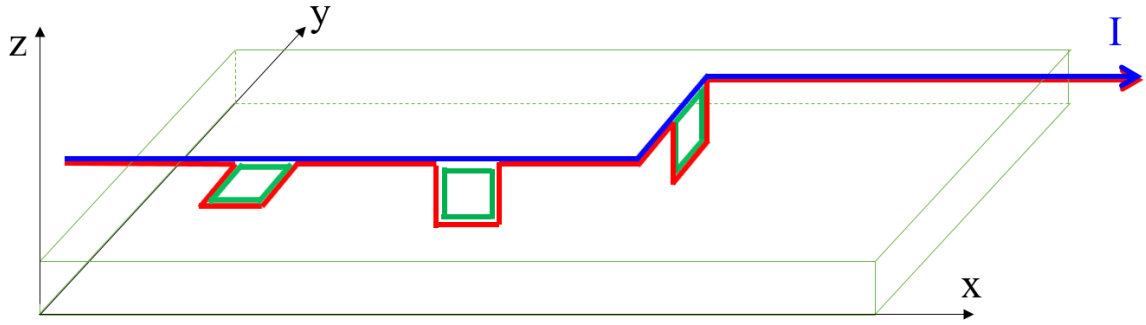


Fig. 3.1. A blue and red path go through a sample grid. The red and blue paths are very similar but differ in three areas. The difference between the paths forms closed rings of current shown in green. These rings are the smallest geometrical differences which can occur between different paths on the sample grid and are therefore fundamental units of path difference. On the left, an “ xy ring” is shown, in the middle an xz ring, and on the right a yz ring.

loop, we first note that ΔP must have at least one segment since by assumption $P_1 \neq P_2$. Furthermore, note from constraint four that current is conserved for P_1 and P_2 ; therefore current is also conserved in ΔP . But since the infeed and outfeed currents are the same for P_1 and P_2 , and we know there is at least one segment in ΔP , it must be that the current in ΔP forms one or more closed loops. The smallest possible closed loop is formed by a single rectangular ring of current oriented in the xy , xz or yz plane (see Fig. 3.1).

I proceed by noting that any closed loop, or set of closed loops, created by taking the difference between two paths on a 3D Manhattan lattice can be constructed by superposing x , y and z segments in appropriate locations with appropriate orientations. Furthermore, any closed loop difference path formed from paths that meet our constraints must have at least two x or two y segments in it, *i.e.* a closed loop must be constructed from at least one

xy , xz or yz ring. Thus ΔB_z , the z -component of the magnetic field of ΔP , can always be written as the sum of the field produced by x and y segments on a 3D lattice and there are always contributions from at least two x segments or two y segments when P_1 and P_2 differ (the z segments contribute no field in the z direction).

Note that ΔB_z can also be written as the difference between the z -component of the field from P_1 and P_2 :

$$\Delta B_z(x, y, z) = B_{2,z}(x, y, z) - B_{1,z}(x, y, z) = 0. \quad (3.1)$$

As stated above, I can also write ΔB_z as a sum of the fields due to the x and y segments in the difference path:

$$\Delta B_z(x, y, z_0) = \sum_{n=1}^{N_x} \alpha_n B_z^{xseg}(x-x_n, y-y_n, z_0+p_n h) + \sum_{n=1}^{N_y} \beta_n B_z^{yseg}(x-x'_n, y-y'_n, z_0+q_n h) \quad (3.2)$$

where $B_z^{xseg}(x, y, z)$ is the z -component of magnetic field at location (x, y, z) from an x -oriented segment with current I that starts at position $(0,0,0)$ and ends at $(w,0,0)$, N_x is the total number of x -segments in the difference path, the n -th x -segment in the difference path extends from $(x_n, y_n, p_n h)$ to $(x_n + w, y_n, p_n h)$, and $\alpha_n = \pm 1$ for current flowing in the $\pm x$ direction in the n -th x -segment. Similarly, $B_z^{yseg}(x, y, z)$ is the z component of the magnetic field from a y -oriented segment with current I that starts at $(0,0,0)$ and ends at $(0,w,0)$, N_y is the total number of y -segments in the difference path, the n -th y -segment in the difference path extends from $(x'_n, y'_n, q_n h)$ to $(x'_n, y'_n + w, q_n h)$ and $\beta_n = \pm 1$ for current flowing in the $\pm y$ direction in the n -th y -segment. Finally, p_n is the layer depth number of the n -th x -segment and q_n is the layer depth number of the n -th y segment. Possible values

for p_n and q_n range from zero for a segment in the top layer to $N_L - 1$ for a segment in the lowest of the N_L layers.

To proceed, I take the Fourier transform of Eq. (3.2) to find:

$$\begin{aligned} \Delta b_z(k_x, k_y, z_0) &= \sum_{n=1}^{N_x} \alpha_n \int_{-\infty}^{+\infty} \int_{-\infty}^{+\infty} B_z^{xseg}(x - x_n, y - y_n, z_0 + p_n h) e^{-i(k_x x + k_y y)} dx dy \\ &+ \sum_{n=1}^{N_y} \beta_n \int_{-\infty}^{+\infty} \int_{-\infty}^{+\infty} B_z^{yseg}(x - x'_n, y - y'_n, z_0 + q_n h) e^{-i(k_x x + k_y y)} dx dy \end{aligned} \quad (3.3)$$

$$\begin{aligned} &= \sum_{n=1}^{N_x} \alpha_n e^{-i(k_x x_n + k_y y_n)} b_z^{xseg}(k_x, k_y, z_0 + p_n h) \\ &+ \sum_{n=1}^{N_y} \beta_n e^{-i(k_x x'_n + k_y y'_n)} b_z^{yseg}(k_x, k_y, z_0 + q_n h) \end{aligned} \quad (3.4)$$

And using Eqs. (2.36) and (2.37),

$$\begin{aligned} \Delta b_z(k_x, k_y, z_0) &= \frac{\mu_0 d}{2i} \left[- \sum_{n=1}^{N_x} \alpha_n e^{-i(k_x x_n + k_y y_n)} \frac{k}{k_y} j_0 x e^{-k(z_0 + p_n h)} \right. \\ &\quad \left. + \sum_{n=1}^{N_y} \beta_n e^{-i(k_x x'_n + k_y y'_n)} \frac{k}{k_x} j_0 y e^{-k(z_0 + q_n h)} \right] \end{aligned} \quad (3.5)$$

where $k = \sqrt{k_x^2 + k_y^2}$ and $j_0 x$ and $j_0 y$ are the fourier transforms of a single $+x$ and $+y$ segment starting at the origin and of length w , respectively.

$$j_0 x(k_x, k_y) = \int_{-\infty}^{+\infty} \int_{-\infty}^{+\infty} J_0 x(x, y) e^{-i(k_x x + k_y y)} dx dy \quad (3.6)$$

$$= \int_0^w dx \int_{-\infty}^{+\infty} \frac{I}{d} \delta(y) e^{-i(k_x x + k_y y)} dy \quad (3.7)$$

$$= \frac{I}{d} \int_0^w e^{-ik_x x} dx \quad (3.8)$$

$$= \frac{I}{d} \frac{e^{-ik_x w} - 1}{-ik_x} \quad (3.9)$$

$$= \frac{iI}{dk_x} (e^{-ik_x w} - 1). \quad (3.10)$$

Similarly,

$$j_0 y(k_x, k_y) = \frac{iI}{dk_y} (e^{-ik_y w} - 1). \quad (3.11)$$

We can plug Eqs. (3.10) and (3.11) into Eq. (3.5) and simplify to find

$$\Delta b_z = \mu_0 I \frac{k e^{-kz_0}}{k_x k_y} \left[- \sum_{n=1}^{N_x} \alpha_n e^{-i(k_x x_n + k_y y_n)} (e^{-ik_x w} - 1) e^{-kp_n h} + \sum_{n=1}^{N_y} \beta_n e^{-i(k_x x'_n + k_y y'_n)} (e^{-ik_y w} - 1) e^{-kq_n h} \right] \quad (3.12)$$

Equation (3.12) must be true for all (k_x, k_y) . Notice that I have separated the exponents in the brackets into their real and imaginary components, with the real components being $-q_n h k$ and $-p_n h k$. Thus for large values of k , all the terms will be suppressed except for the contribution from segments on the topmost layer for which $q_1 h = p_1 h = 0$. Thus we can consider just the segments on the first layer and the total field from all those segments must vanish for Eq. (3.12) to be satisfied for all values of k .

We can similarly “peel away” each subsequent layer, one by one, by noting that the field from each lower layer is negligible at large k . Thus, each layer must have currents that produce zero net field.

However, from the discussion on the standard inverse in [Chapter 2](#) we know that if all the currents are in a single plane and produce zero field, the only current distribution that creates this situation is the zero current distribution. Thus we find that if $B_1 = B_2$, then $P_1 = P_2$. In other words, if two paths produce the same magnetic field then they must be the same path. Therefore each magnetic field has a unique inverse, we have a contradiction and our original assumption that there are two distinct paths that obey the constraints and produce the same magnetic field must be incorrect. We conclude that any given path (call it

path 1) that obeys the constraints produces a magnetic field $B_1(x, y, z)$ that is unique to the path, *i.e.* there is no path 2 that generates the same field as path 1, meets the constraints, and differs from path 1 in the location or orientation of any segments.

3.6 3D Inverse signal-to-noise-ratio and current rings

An important consideration in applying the 3D inverse is to understand the minimum grid spacing w that can be used. If too small of a grid spacing is chosen, then there will be configurations that cannot be distinguished from each other due to noise in the image and the technique will not be able to generate a unique solution. Furthermore, the number of possible paths grows rapidly as the grid spacing is reduced in size. In practice, even if the path is resolvable in principle at a fine grid spacing, it may take a prohibitive amount of time to find the solution. Here I examine how the noise limits the minimum grid spacing but ignore possible practical limitations to finding it, which are addressed in [Chapter 4](#) where I discuss actual inversion algorithms.

To understand what limits the grid size, I consider one of the simplest types of paths, a linear via chain (see [Fig. 3.2](#)). In this case I assume a simple trial path with N lateral segments oriented along the x -axis and 2 layers. Note that we can ignore the presence of any layer-to-layer z segments since they contribute nothing to the z -component of the magnetic field. This trial path may be an initial guess that was chosen based on the data collected or from some other information. It is always possible to create such a trial path (see [Section 5.4](#) for practical details).

Once an initial path is selected, we then calculate the expected magnetic field

$B_{z,i}^{theory}(I, x_i, y_i)$ from this path at the N_m points where the data was measured and compare this field to the measured field $B_{z,i}^{data}$ using χ^2 :

$$\chi^2 = \frac{1}{\sigma_B^2} \sum_{i=1}^{N_m} [B_{z,i}^{data} - B_{z,i}^{theory}]^2. \quad (3.13)$$

The next step is to vary the path until one finds the path with the lowest χ^2 . By adding one or more closed square current rings (see Fig. 3.2 (a)) to the trial path, we can obtain any other valid linear chain path, including the true path. For a linear via chain, the rings lie in the x - z plane and have height h along the z -axis and length w along the x -axis. To maintain a fixed current in a single current path, only certain rings or combination of rings will be allowed to be added to an existing path. Determining which rings can be added is somewhat complicated, but the rule of thumb is to cancel some existing segment in the path while adding others to maintain continuity of current. For example, in Fig. 3.2 (a), I added a $+y$ ring to raise a bottom segment, and then a $-y$ ring to lower a top segment. The resulting path is shown in Fig. 3.2 (b). These rings represent the difference between the paths in Fig. 3.2 (a) and (b). Because the Biot-Savart law is linear, the magnetic field produced by these rings is equal to the difference between the magnetic fields of the two paths.

To find the minimum grid size w , we must find the minimum value for w at which we can distinguish between the magnetic fields of any two paths in the presence of noise. Since two paths always differ by some set of closed rings, this problem reduces to finding the value of w for which the signal of any combination of rings is detectable over the noise in the image. To proceed, I will first examine the noise in the image. Next, I examine which ring combinations give the smallest signal and use the S/N to find the minimum grid size w .

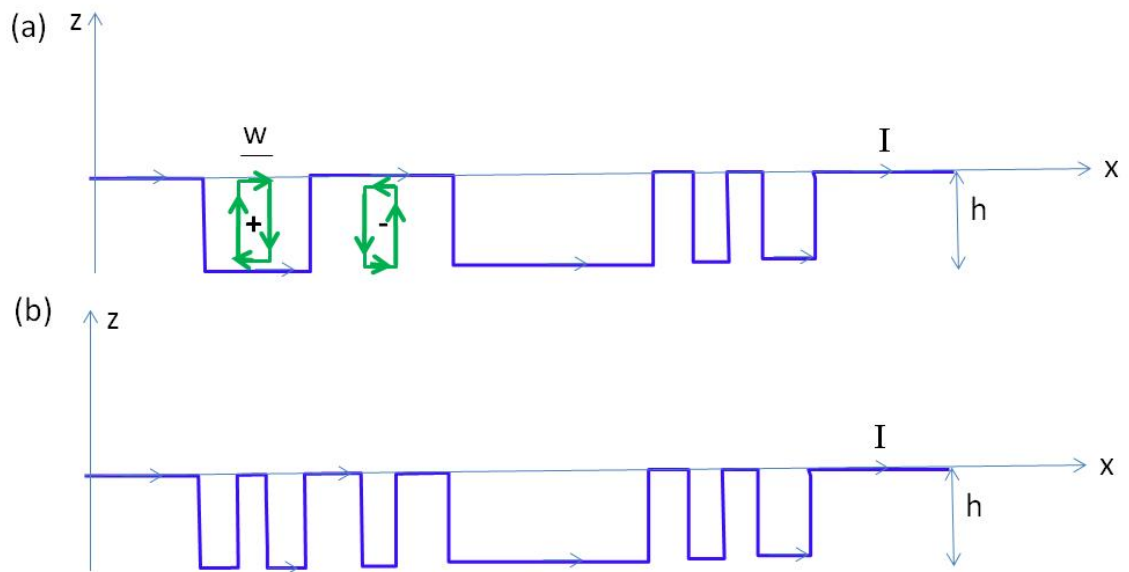


Fig. 3.2. (a) Two rectangular current rings (green), a +y ring and a -y ring, are added to a linear via current path (blue curve). The +y ring raises a current segment from the lower layer to the upper layer and produces a magnetic moment oriented in the +y direction. The -y ring produces a magnetic moment oriented in the -y direction and lowers a current segment on the upper layer to the lower layer. (b) The current path resulting from adding the two rings to the blue current path shown in (a).

I now consider two paths P_1 and P_2 with corresponding magnetic fields $B_{z,i}^{theory,1}$ and $B_{z,i}^{theory,2}$ for $i = 1$ to N_m . I assume that the first path is in fact the true path and the second path differs by a set of rings ΔP with magnetic field $B_{z,i}^{rings}$. Obviously,

$$B_{z,i}^{theory,2} = B_{z,i}^{theory,1} + B_{z,i}^{rings} \quad (3.14)$$

The χ^2 for the first path is then

$$\chi_1^2 = \frac{1}{\sigma_B^2} \sum_{i=1}^{N_m} [B_{z,i}^{data} - B_{z,i}^{theory,1}]^2 \quad (3.15)$$

and for the second path,

$$\chi_2^2 = \frac{1}{\sigma_B^2} \sum_{i=1}^{N_m} [B_{z,i}^{data} - B_{z,i}^{theory,2}]^2. \quad (3.16)$$

Since P_1 is actually the true path, the difference between the data and $B_{z,i}^{theory,1}$ will just be due to random error and we can write:

$$B_{z,i}^{data} - B_{z,i}^{theory,1} = \Delta B_i \quad (3.17)$$

where I assume that the ΔB_i are randomly distributed with standard deviation σ_B . Thus I can write:

$$\chi_1^2 = \frac{1}{\sigma_B^2} \sum_{i=1}^{N_m} [B_{z,i}^{data} - B_{z,i}^{theory,1}]^2 = \frac{1}{\sigma_B^2} \sum_{i=1}^{N_m} [\Delta B_{z,i}]^2 \approx N_m. \quad (3.18)$$

The difference between the two values of χ^2 is

$$\Delta\chi^2 = \chi_2^2 - \chi_1^2 \quad (3.19)$$

$$= \frac{1}{\sigma_B^2} \sum_{i=1}^{N_m} [B_{z,i}^{data} - B_{z,i}^{theory,2}]^2 - \frac{1}{\sigma_B^2} \sum_{i=1}^{N_m} [B_{z,i}^{data} - B_{z,i}^{theory,1}]^2. \quad (3.20)$$

Expanding and simplifying, I find

$$\Delta\chi^2 = \frac{1}{\sigma_B^2} \sum_{i=1}^{N_m} \left\{ [B_{z,i}^{rings}]^2 - 2B_{z,i}^{data} B_{z,i}^{rings} + 2B_{z,i}^{theory,1} B_{z,i}^{rings} \right\}. \quad (3.21)$$

Since P_1 is the true path, we expect $\chi_2^2 > \chi_1^2$ and so $\Delta\chi^2 > 0$. Of course the value of χ^2 will vary from one image to the next by about $\pm\sqrt{N_m}$ because of noise in the measurement. The key question we need to answer is whether or not this difference is statistically significant. If the difference is statistically significant, then we can say that the two paths are resolvable and we will find $\Delta\chi^2 > 0$.

To proceed, we note that the value of χ^2 has some uncertainty because the values $B_{z,i}^{data}$ are uncertain, *i.e.* if we repeat the measurements of the field, we will get values that differ by about $\pm\sigma_B$ from the original values. We can find $\Delta\chi^2$, the uncertainty in χ^2 , using propagation of errors:

$$\sigma_{\Delta\chi^2}^2 = \sum_{i=1}^{N_m} \left\{ \left(\frac{\partial (\Delta\chi^2)}{\partial B_{z,i}^{data}} \right)^2 \sigma_B^2 \right\}. \quad (3.22)$$

Substituting, we find

$$\sigma_{\Delta\chi^2}^2 = \sigma_B^2 \sum_{i=1}^{N_m} \left\{ \frac{\partial}{\partial B_{z,i}^{data}} \left(\frac{1}{\sigma_B^2} \sum_{i=1}^{N_m} \left\{ [B_{z,i}^{rings}]^2 - 2B_{z,i}^{data} B_{z,i}^{rings} + 2B_{z,i}^{theory,1} B_{z,i}^{rings} \right\} \right)^2 \right\} \quad (3.23)$$

$$= \frac{1}{\sigma_B^2} \sum_{i=1}^{N_m} \left\{ \frac{\partial}{\partial B_{z,i}^{data}} \left([B_{z,i}^{rings}]^2 - 2B_{z,i}^{data} B_{z,i}^{rings} + 2B_{z,i}^{theory,1} B_{z,i}^{rings} \right)^2 \right\} \quad (3.24)$$

$$= \frac{1}{\sigma_B^2} \sum_{i=1}^{N_m} \left\{ -2B_{z,i}^{rings} \right\}^2 = \frac{4}{\sigma_B^2} \sum_{i=1}^{N_m} (B_{z,i}^{rings})^2. \quad (3.25)$$

It is informative at this point to find the uncertainty in the individual χ^2 . For example,

we find:

$$\sigma_{\chi_1^2}^2 = \sum_{i=1}^{N_m} \left\{ \left(\frac{\partial (\chi_1^2)}{\partial B_{z,i}^{data}} \right)^2 \sigma_B^2 \right\} \quad (3.26)$$

$$= \sigma_B^2 \sum_{i=1}^{N_m} \left(\frac{\partial}{\partial B_{z,i}^{data}} \left\{ 1/\sigma_B^2 \sum_{i=1}^{N_m} [B_{z,i}^{data} - B_{z,i}^{theory,1}]^2 \right\} \right)^2 \quad (3.27)$$

$$= \frac{4}{\sigma_B^2} \sum_{i=1}^{N_m} [B_{z,i}^{data} - B_{z,i}^{theory,1}]^2 \quad (3.28)$$

$$= 4\chi_1^2. \quad (3.29)$$

Since P_1 is the true path we expect $\chi_1^2 = N_m$ and this reduces to simply

$$\sigma_{\chi_1^2} = 2\sqrt{N_m} \quad (3.30)$$

and thus

$$\frac{\sigma_{\chi_1^2}}{\chi_1^2} = \frac{2\sqrt{N_m}}{N_m} = \frac{2}{\sqrt{N_m}}. \quad (3.31)$$

Examination of these expressions reveals that the factor of two or four arises simply because B_z enters as a square in the definition of χ^2 .

In order for the path to be resolvable, we require:

$$\sigma_{\Delta\chi^2} = \sqrt{\sigma_{\Delta\chi^2}^2} \leq \Delta\chi^2. \quad (3.32)$$

Substituting, we find the resolvability condition becomes:

$$\sqrt{\frac{4}{\sigma_B^2} \sum_{i=1}^{N_m} (B_{z,i}^{rings})^2} \leq \frac{1}{\sigma_B^2} \sum_{i=1}^{N_m} \left\{ [B_{z,i}^{rings}]^2 - 2(B_{z,i}^{data} - B_{z,i}^{theory,1}) B_{z,i}^{rings} \right\} \quad (3.33)$$

Simplifying, we find:

$$2\sqrt{\sum_{i=1}^{N_m} (B_{z,i}^{rings})^2} \leq \frac{1}{\sigma_B} \sum_{i=1}^{N_m} \left\{ [B_{z,i}^{rings}]^2 - 2(B_{z,i}^{data} - B_{z,i}^{theory,1}) B_{z,i}^{rings} \right\} \quad (3.34)$$

$$2\sqrt{\sum_{i=1}^{N_m} (B_{z,i}^{rings})^2} \leq \frac{1}{\sigma_B} \sum_{i=1}^{N_m} \left\{ [B_{z,i}^{rings}]^2 - 2B_i^n B_{z,i}^{rings} \right\} \quad (3.35)$$

$$\leq \frac{1}{\sigma_B} \sum_{i=1}^{N_m} [B_{z,i}^{rings}]^2 - \frac{2}{\sigma_B} \sum_{i=1}^{N_m} \{B_i^n B_{z,i}^{rings}\}. \quad (3.36)$$

Now if we sample heavily, then the second term on the right in Eq. (3.36) will on average tend to zero since the B_i^n are randomly distributed errors with mean of zero. Thus we can write the resolvability condition as:

$$\sqrt{\sum_{i=1}^{N_m} (B_{z,i}^{rings})^2} \leq \frac{1}{2\sigma_B} \sum_{i=1}^{N_m} [B_{z,i}^{rings}]^2 \quad (3.37)$$

or

$$\sqrt{\sum_{i=1}^{N_m} (B_{z,i}^{rings})^2} \geq 2\sigma_B. \quad (3.38)$$

This is a key result, and we can write it in an equivalent form. Assuming that the average field produced by the ring is zero, we can define

$$B_{rms}^{rings} = \sqrt{\langle [B_{z,i}^{rings}] \rangle} = \sqrt{\frac{1}{N_m} \sum_{i=1}^{N_m} [B_{z,i}^{rings}]^2}. \quad (3.39)$$

Then the resolvability condition becomes simply

$$B_{rms}^{rings} \geq \frac{2\sigma_B}{\sqrt{N_m}} \quad (3.40)$$

where N_m is the number of points the field was measured at.

From the above discussion, I can now define the signal-to-noise ratio for detecting a set of rings. I define the effective ring signal S in the magnetic image to be:

$$S = \sum_{i=1}^{N_m} [B_{z,i}^{rings}]^2 \quad (3.41)$$

and the effective noise in the image to be:

$$N = 4\sigma_B^2 \quad (3.42)$$

where σ_B is the RMS magnetic field noise in each pixel. Notice that this is not the total noise from all the pixels, and it is not the noise in one pixel, but an effective noise that we have defined in an *ad hoc* fashion based on the χ^2 analysis. The signal-to-noise ratio for detecting a set of rings then becomes

$$S/N = \frac{\sum_{i=1}^{N_m} [B_{z,i}^{rings}]^2}{4\sigma_B^2}. \quad (3.43)$$

If we define the minimal detectable signal to be when $S/N = 1$, then I recover Eq. (3.38).

3.7 Spatial resolution and least resolvable rings

Naively, one might think that paths that differ by just one ring have the closest magnetic fields. However, this is not the case because the field from different rings can partially, although not completely, cancel each other out. This means that typically two paths with almost the same magnetic image will differ by many current rings.

To gain some insight, the best way to think about the rings is to treat them as magnetic dipoles. Two opposite dipoles (*i.e.* two rings) stacked next to each other form a magnetic quadrupole, whose far-field signal is fainter than the signal of a single dipole. Similarly, the signal of two quadrupoles, an octupole, is smaller in the far-field, and so on. These are the higher magnetic multipoles, and the χ^2 of some of these ring patterns can be much less than the χ^2 of single ring defects.

Figure 3.3 illustrates this problem. Figure 3.3 (a) shows the field of a single ring of current, a magnetic dipole. Figure 3.3 (b) shows the field due to two rings that are placed

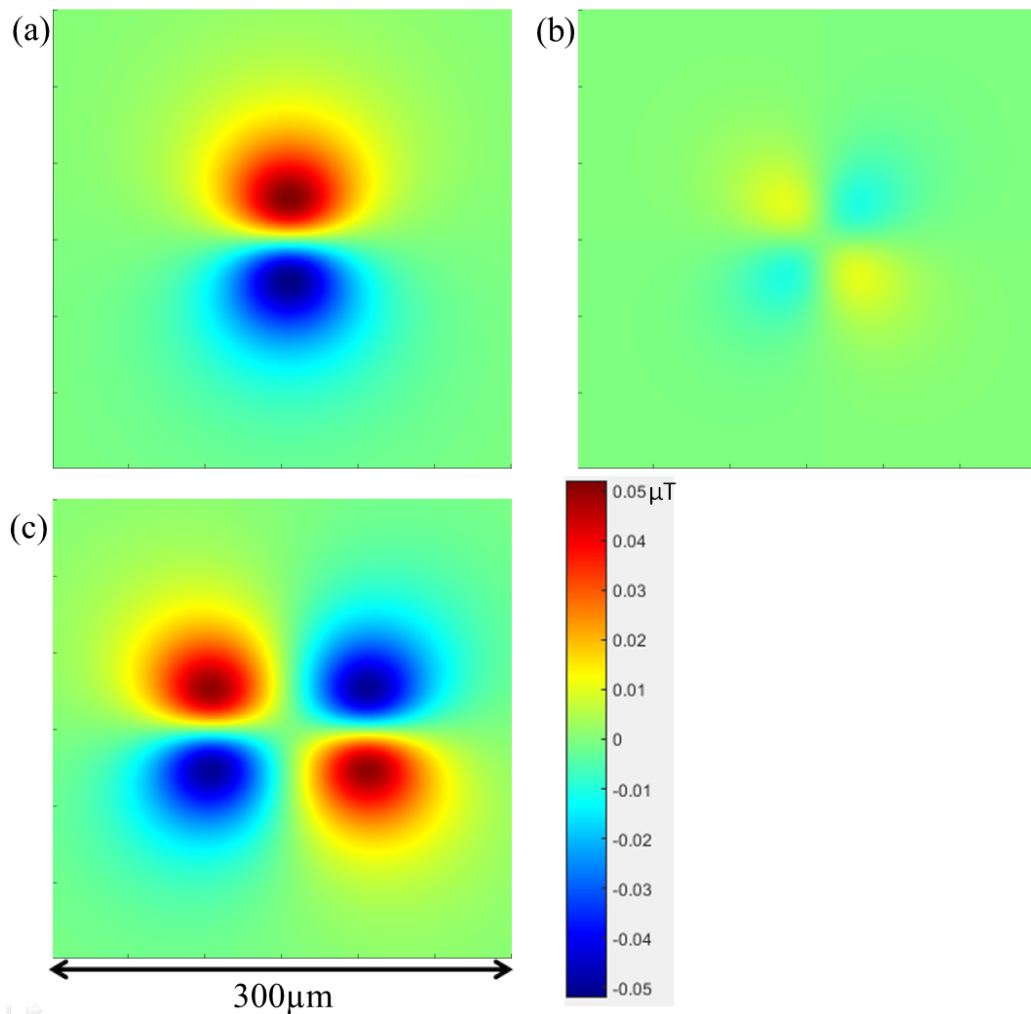


Fig. 3.3. (a) z component of the magnetic field (B_z) from a single square ring of current in the x - z plane. The ring produces a magnetic dipole pattern. (b) B_z from two adjacent (center-to-center $10\ \mu\text{m}$) x - z rings with opposing current. The two rings produce a magnetic quadrupole pattern. This field is very faint compared to the field in (a). (c) Field of two rings of current separated by the correlation length, $100\ \mu\text{m}$ (center-to-center is twice the imaging distance). The fields do not overlap and the image behaves as two dipoles rather than a single quadrupole. All images have same color scale. $z = 50\ \mu\text{m}$, square rings are $10\ \mu\text{m}$ long and $10\ \mu\text{m}$ high and scan has 1 by $1\ \mu\text{m}$ resolution.

adjacent to each other, with current flowing in opposite directions. The field from these opposing rings partially cancel. The two figures use the same color scale for the magnetic field, and we can see that the field in Fig. 3.3 (b) is much smaller than in 3.3 (a).

Strictly speaking, the field pattern is only approximately a quadrupole, the approximation being good when the imaging distance z is much larger than the distance between the dipoles and the layer-to-layer separation. In Fig. 3.3 (c) we have moved the dipoles so that they are separated by their correlation length of $\Delta x = 2z = 100 \mu\text{m}$. When the two rings are separated by Δx we see that the image resembles that from two independent full strength dipoles rather than the weak quadrupole field as in 3.3 (b). Note that the maximum value for B_z in 3.3 (c) is almost as strong as the maximum value for B_z in 3.3 (a).

Figure 3.3 illustrates the significance of the multipole expansion [60]. Just as the field of a quadrupole is fainter than the field of a dipole, the field of the quadrupole is fainter than that of an octupole, all other things being equal. At first sight, this is worrisome because it suggests that the field of higher and higher order n -ring multipoles will be fainter and fainter.

Thankfully, we are saved by the physical size of the structure. An n -ring multipole produces a structure that grows linearly in size as nw , where w is the length of an x segment. However when $nw \approx 2z$, which is the correlation length of the rings, the multipole no longer behaves as a multipole but instead its field appears as that of independent ring combinations. Roughly speaking, the correlation length is the distance between two rings at which the field from the rings stop melding together and instead appear as independent rings. A more rigorous definition is that it is the separation between two rings at which the power of the signal integrated over the image from the structure is smaller than the power from one ring

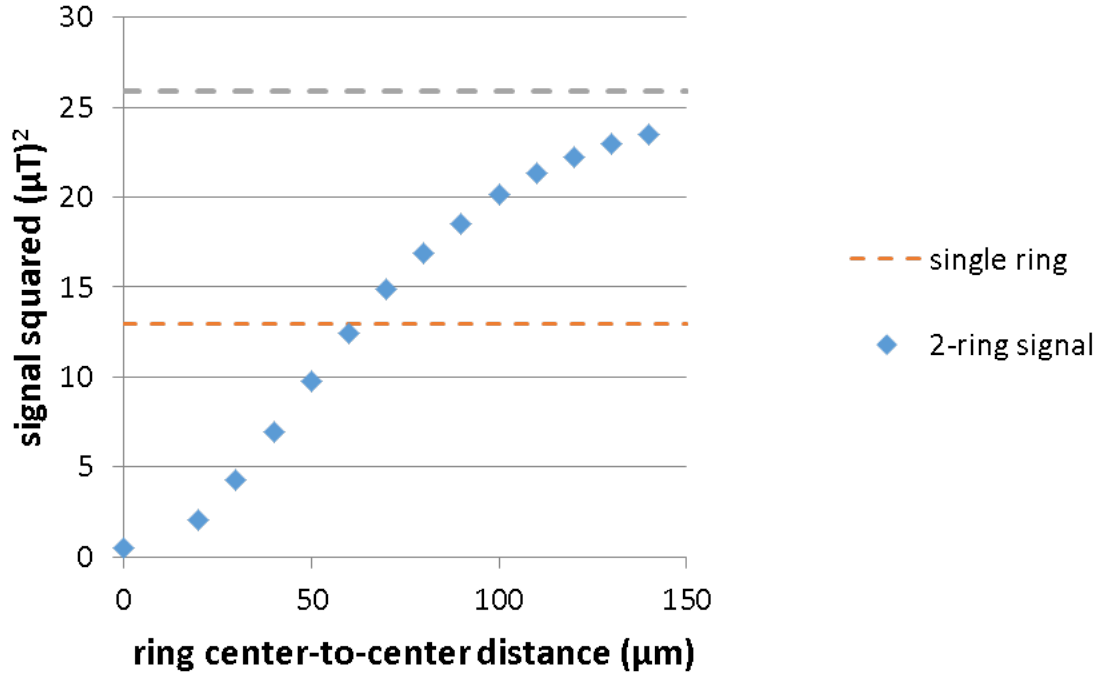


Fig. 3.4. The blue losanges show the integrated signal power S^2 in a 2-ring quadrupole vs. the ring center-to-center distance d . For $d < z$, S^2 is smaller than the signal for a single ring. S^2 approaches the signal of two distinct rings around $d = 2z$. For this simulation, $z = 50 \mu\text{m}$, $g = 1$, rings are $(10 \mu\text{m})^2$, simulation is $(300 \mu\text{m})^2$ with $(1 \mu\text{m})^2$ pixel size.

(*i.e.*, at what ring separation does power from the 2-ring multipole become stronger than the 1-ring dipole). Figure 3.4 plots the integrated power signal S^2 of two rings vs. the distance between the rings for a scan distance z of $50 \mu\text{m}$. As we can see, S^2 becomes greater than the signal due to a single ring when the separation between the rings $d \approx 1.2z$, and S^2 approaches 90% of the signal of 2 independent rings when $d \approx 2.2z$. Thus for segment lengths $w \ll z$, the correlation length is $\approx 2z$.

Figure 3.5 shows some of the lowest order multi-ring patterns that occur in a linear via chain. In bold I show “pure” multipoles such as the 2-, 4-, 8-, and 16-ring multipoles. Some

ring patterns also have components from multiple n-poles, such as the 6-ring which is the sum of a 2-ring and 8-ring pattern. In practice we do not search for multipoles with more than 16 rings (a 32-pole) for two reasons. First, for typical imaging parameters 6-10 ring poles tend to produce the weakest signal. Second, the computational difficulty of searching for higher order multipoles grows exponentially. This is almost never an issue because our grid size w is limited by sensor noise before we reach w/z ratios where these higher order multipoles have the lowest signal.

For a single ring (dipole), I present the S/N analysis analytically. For higher order multipoles, I present a numerical analysis using typical imaging parameters. For a single ring with magnetic moment m , we can write the magnetic field as [60]

$$\vec{B}(\vec{r}) = \frac{\mu_0}{4\pi} \frac{3\vec{r}(\vec{r} \cdot \vec{m}) - r^2\vec{m}}{r^5}. \quad (3.44)$$

With a magnetic moment oriented in the $-y$ direction, the z -component of the magnetic field is

$$B_z = \frac{\mu_0}{4\pi} \frac{\vec{r} \cdot \hat{k} (-3\vec{r} \cdot m\hat{j})}{r^5} \quad (3.45)$$

$$= -\frac{\mu_0}{4\pi} \frac{3myz}{r^5} \quad (3.46)$$

$$= -\frac{\mu_0}{4\pi} \frac{3myz}{(x^2 + y^2 + z^2)^{5/2}} \quad (3.47)$$

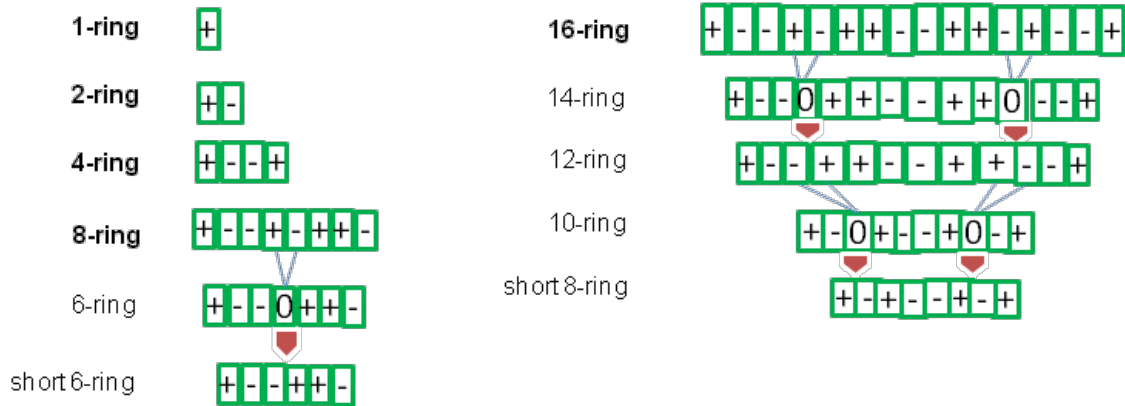


Fig. 3.5. Various low-order y -ring combinations used for the calculations of the S/N ratio versus grid spacing. The 1, 2, 4, 8, 16-ring configurations are “pure” multi-poles. The 6 ring combination is formed from the 8-ring combination by pushing the left and right four rings together, overlapping a + and -y ring to produce a zero in the center cell. The 6-ring pattern (also can be called a 7-ring pattern with the central ring being zero) is a pure 16-pole configuration, with a smaller moment than the 8-ring combination it was spawned from. The short 6-ring combination is spawned from the 6-ring configuration by deleting the central zero and pushing the remaining cells together, and it is not a pure multipole configuration. The 16-ring spawns 14-ring, 12-ring, 10-ring and a short 8-ring configuration as shown. The 14-ring can also be thought of as + and - 7-ring configuration and is a pure 32-pole configuration, with a lower moment and longitudinal extent than the 16-ring that spawned it. The 12 ring, 10-ring and short 8 combinations are not pure multipoles.

To proceed, we now write the signal as

$$S = \sum_{i=1}^{N_m} [B_{z,i}^{ring}] \quad (3.48)$$

$$= N_m [B_{rms}^{ring}] \quad (3.49)$$

$$= N_m \langle [B_{z,i}^{ring}] \rangle \quad (3.50)$$

$$\approx \frac{N_m}{L} \int_{-\infty}^{+\infty} \int_{-\infty}^{+\infty} \left(\frac{\mu_0}{4\pi} \frac{3myz}{(x^2 + y^2 + z^2)^{5/2}} \right) dx dy \quad (3.51)$$

In the last step I have replaced the sum by an integral (normalized by the area L^2 of the picture) and extended the limits of the integration to infinity. This should be a good approximation for relatively large pictures ($L \gg z$) since the field falls rapidly with distance from the dipole. We can simplify this expression to get

$$S \approx \frac{N_m}{L^2} \left(\frac{m\mu_0}{4\pi} \right)^2 \frac{3\pi}{8} \frac{1}{z^4} \quad (3.52)$$

and we find

$$\frac{S}{N} = \frac{N_m}{L^2} \left(\frac{m\mu_0}{4\pi} \right)^2 \frac{3\pi}{8} \frac{1}{z^4} \frac{1}{4\sigma_B^2}. \quad (3.53)$$

Substituting $Iwh = m$ for a current ring of height h , width w and current I we find:

$$\frac{S}{N} = \frac{N_m}{L^2} \left(\frac{\mu_0 I}{4\pi\sigma_B} \right)^2 \frac{3\pi}{32} \frac{w^2 h^2}{z^4} \quad (3.54)$$

Setting $S/N = 1$ we find the minimum resolvable grid spacing for a single xz or yz ring in a linear via chain is:

$$w_{min} = \frac{z^2}{h} \left(\frac{4\pi\sigma_B L}{\mu_0 I} \right) \sqrt{\left(\frac{32}{3\pi} \right) \frac{1}{N_m}} \quad (3.55)$$

In the standard magnetic inverse, the ratio z/s of the separation z to spatial resolution s can typically be about as large as $z/s = 4$ or 5 , but not much larger. With this in mind,

we also can write the above result in the suggestive form:

$$\frac{z}{w_{min}} = \sqrt{N_m \left(\frac{3\pi}{2} \right) \frac{h}{4zL} \left(\frac{\mu_0 I}{4\pi\sigma_B} \right)} \quad (3.56)$$

This ratio can be substantially larger than 4 or 5, and the scaling with I and Δx is much stronger than the logarithmic dependence found for the standard magnetic inverse [58, 75].

Consider for example an image with a field noise in each pixel of $\sigma_B = 20$ pT, data measured on a square grid with $\Delta x = 10$ μm , $L = 1$ mm, $h = 20$ μm , $N_m = 10^4$, the current carried in the path is $I = 10$ μA and the sample was imaged at a distance of $z = 100$ μm . One finds from Eq. (3.56) that the minimum resolvable grid size for one ring variations is: $w_{min} = 0.184$ μm , and thus $z/w_{min} = 540$. Note that this result only holds for single ring variations. As noted above, for higher order multipole this ratio gets significantly worse.

For a given lattice size w and distance z , we expect there will be a ring arrangement that is least resolvable, and it is the signal produced by this arrangement that ultimately determines whether the path is or is not resolvable at length scale w . From numerical simulations, I have found the ring patterns presented in Fig. 3.5 to be the least resolvable for linear via chain paths with typical parameters found in our samples. For different parameters, and specifically if the z/w ratio were much increased, we would expect even larger patterns to also be important. Note also that this analysis is conducted on a 2-layer linear via chain. For multi-layer and more complex 3D paths the analysis is more complicated because the resulting 3D ring patterns are more numerous and rings buried deeper in the structure contribute less to the field, and multiple rings buried deep can cancel out a single top-layer dipole.

Figure 3.6 shows a plot of the S/N ratio for 1-ring, 2-ring, 4-ring, 8-ring and 16-

ring multi-pole configurations as a function of the grid spacing w with $h = 20 \mu\text{m}$ and $z = 100 \mu\text{m}$. Notice that $S/N = 1$ along the horizontal dashed red line. Examining this line we see that the least resolvable ring configuration at $S/N = 1$ for this subset of all possible configurations is the 8-ring configuration, which requires a grid spacing of about $9 \mu\text{m}$ or larger in order to be resolvable. Notice that all other ring combinations hit $S/N = 1$ at a smaller grid spacing, although the 4-ring and the 8-ring are almost equally difficult to resolve. Note also that the 16-ring configuration is easier to resolve than the 8-ring, and the 1-ring and 2-ring are the most easily resolved. It is also interesting to see that at a grid spacing of $10 \mu\text{m}$, the 4-ring is still the most difficult to resolve, with a signal-to-noise ratio of about 3.6, while the 8-ring has a nearly identical S/N ratio. Finally, notice that the curve for the dipole intersects $S/N = 1$ at $w = 0.2 \mu\text{m}$. This is consistent with the dipole analysis above which gave $S/N = 1$ at about $w = 0.18 \mu\text{m}$.

Figures 3.7 to 3.11 show similar plots of the S/N ratio for $z = 120 \mu\text{m}$, $80 \mu\text{m}$, $60 \mu\text{m}$, $40 \mu\text{m}$, and $20 \mu\text{m}$ for multi-pole ring configurations as a function of the grid spacing w with $h = 20 \mu\text{m}$. Notice that in each case the least resolvable ring configuration is the 6-ring configuration (see Fig. 3.5). Notice also that the minimum grid spacing shrinks steadily as z decreases, from $w_{min} = 11 \mu\text{m}$ at $z = 120 \mu\text{m}$, to $w_{min} = 1.3 \mu\text{m}$ at $z = 20 \mu\text{m}$. In this range of z , the z/w_{min} ratio stays relatively constant from around $z/w_{min} = 11$ at $z = 120 \mu\text{m}$ to about 15 at $z = 20 \mu\text{m}$.

For these plots, I used typical SQUID imaging parameters as listed in each figure caption. Note that if the current were raised from $10 \mu\text{A}$ to $100 \mu\text{A}$, the S/N would increase by 100 (all of the curves would be displaced upward on the S/N axis by a factor of 100). For example, in Fig. 3.6, this would yield a new minimum grid spacing of about $5 \mu\text{m}$

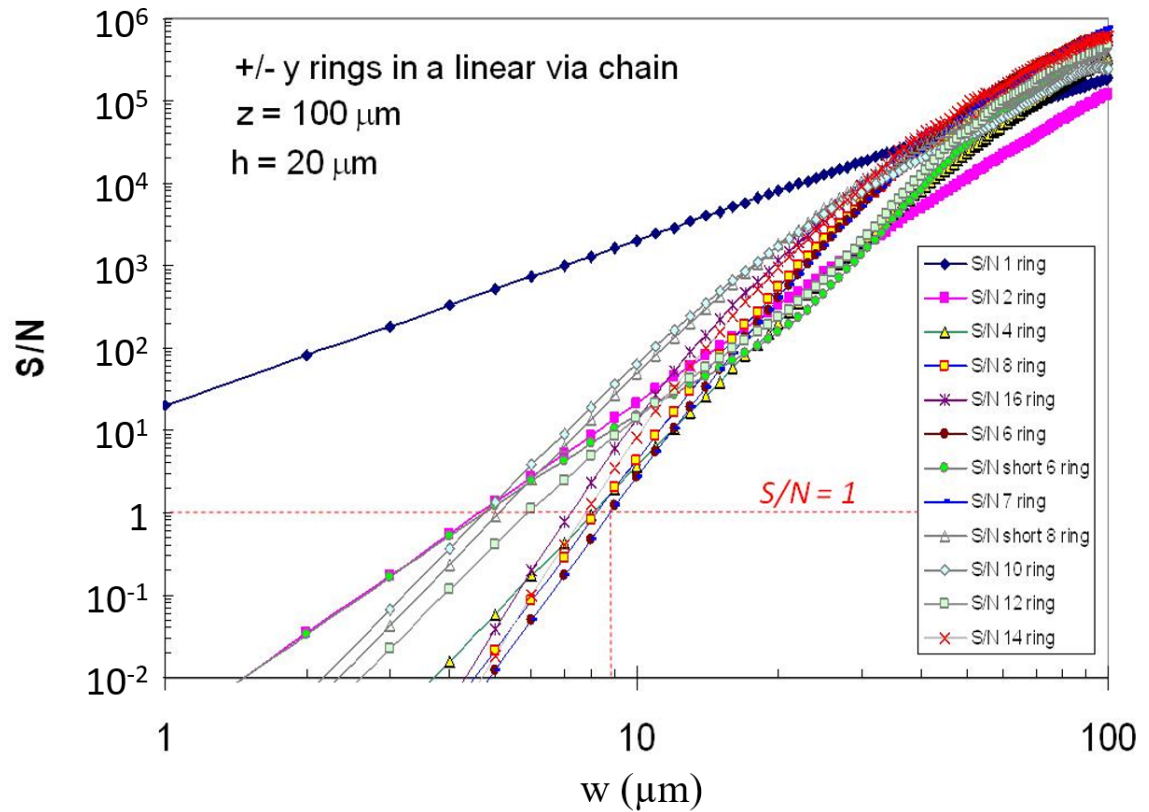


Fig. 3.6. S/N for the y-ring configurations shown in Fig. 3.5. The 6-ring is least resolvable, requiring a grid spacing of about $9 \mu\text{m}$ to produce a S/N ratio of 1. The next least resolvable are the 8 and 4-ring. For this plot $z = 100 \mu\text{m}$, $I = 10 \mu\text{A}$, $\sigma_B = 20 \text{ pT}$ per pixel, $N_m = 10^4$, $L = 1 \text{ mm}$, and the layer separation was fixed at $h = 20 \mu\text{m}$.

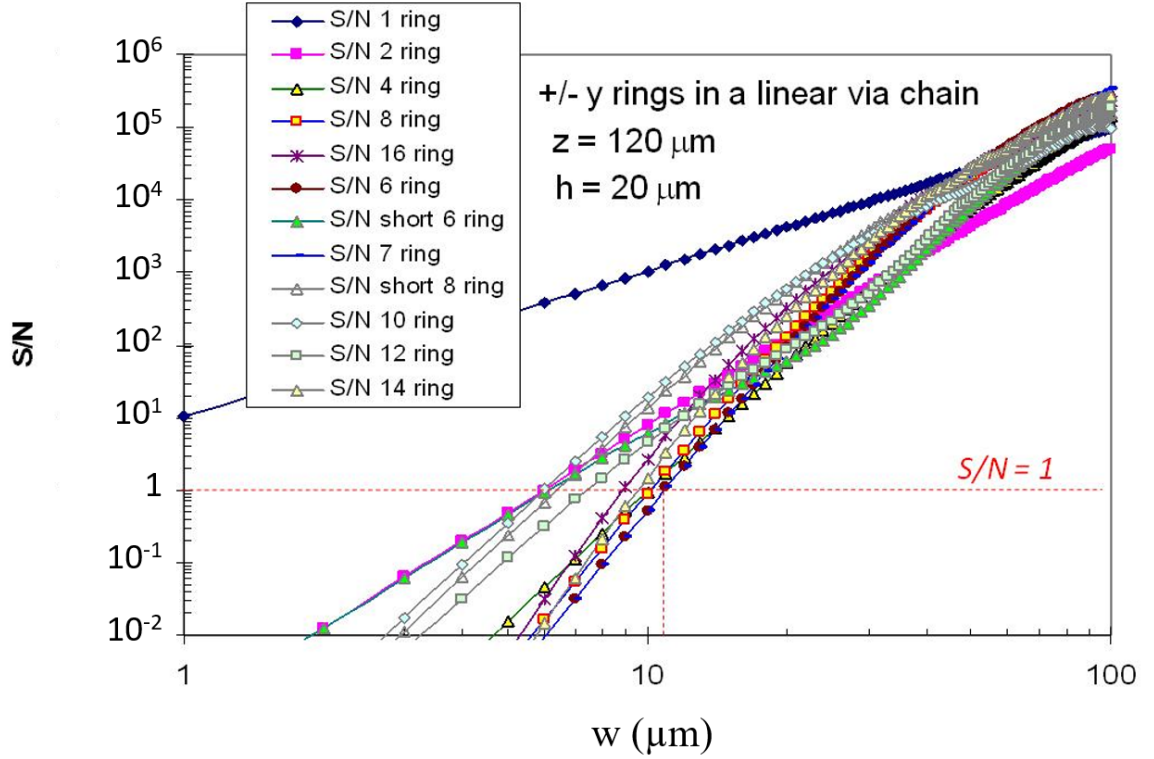


Fig. 3.7. S/N for rectangular y-ring configurations shown in Fig. 3.5. For this plot $z = 120 \mu\text{m}$. The 6-ring combination is the least resolvable, requiring a grid spacing of about $11 \mu\text{m}$ to produce a S/N ratio of 1. Here $I = 10 \mu\text{A}$, $\sigma_B = 20 \text{ pT}$ per pixel, $N_m = 10^4$, $L = 1 \text{ mm}$, and the layer separation was fixed at $h = 20 \mu\text{m}$.

instead of $9 \mu\text{m}$. While the dependence of the minimum grid spacing on the current (or noise amplitude) is fairly weak, it is much stronger than the logarithmic dependence found in the standard magnetic inverse. Also, it generally will not be possible to achieve good inversions at $S/N = 1$, but rather at a somewhat higher S/N . Thus improving the S/N is important because the higher the S/N ratio, the easier it will be to work at a given grid size.

Based on the above signal-to-noise analysis, we see that the 3D inverse's resolution can achieve $z/w_{min} \leq 11$ for typical samples and typical SQUID imaging parameters and

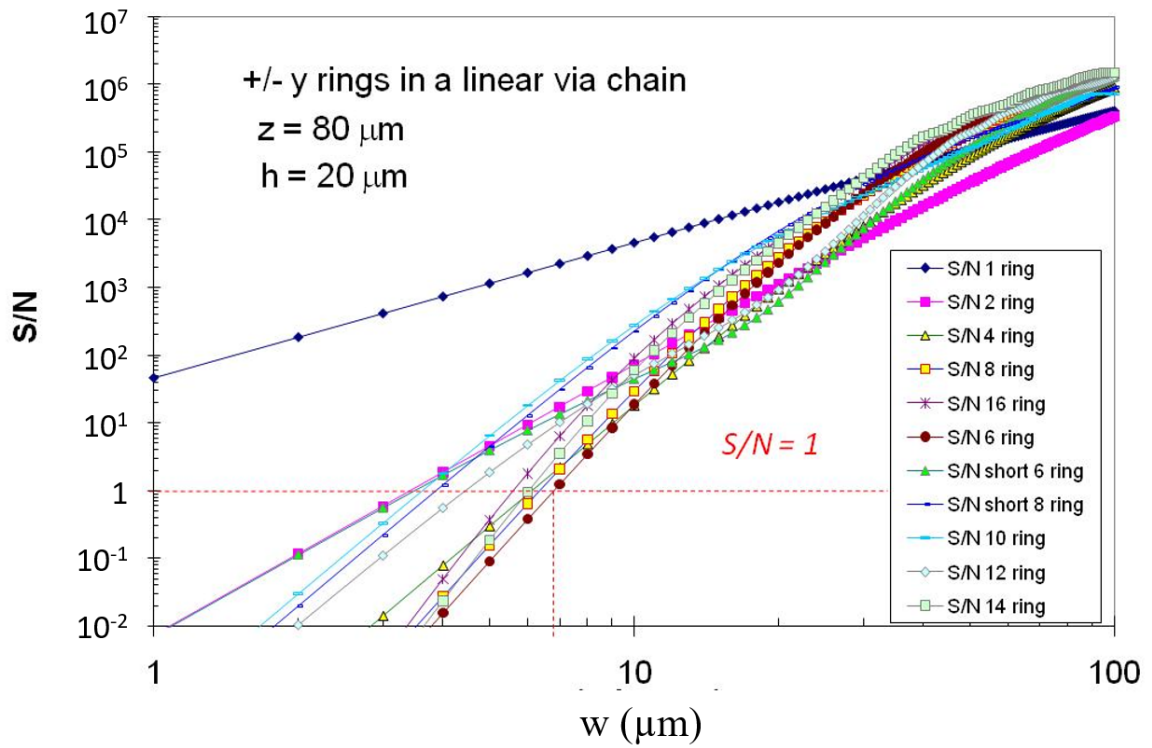


Fig. 3.8. S/N for a single rectangular y-ring, as well as multi-poles built from 2, 4, 8, 16 rings and a few other combinations of +y and -y rings. For this plot $z = 80 \mu\text{m}$ and $h = 20 \mu\text{m}$. The 6-ring combination is the least resolvable, requiring a grid spacing of about $6.8 \mu\text{m}$ to produce a S/N of 1.

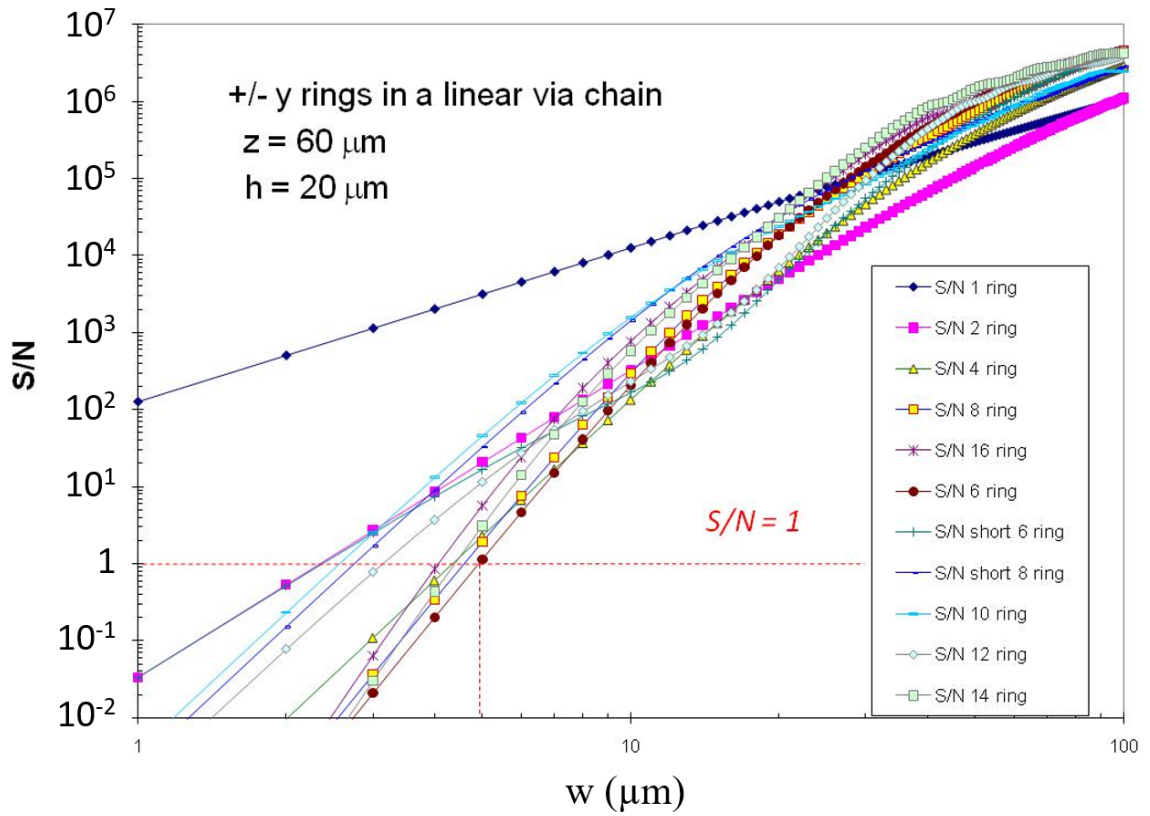


Fig. 3.9. S/N for a single rectangular y -ring, as well as multi-poles built from 2, 4, 8, and 16 rings and a few other combinations of $+y$ and $-y$ rings. For this plot $z = 60 \mu\text{m}$ and $h = 20 \mu\text{m}$. The 6-ring combination is the least resolvable, requiring a grid spacing of about $5.0 \mu\text{m}$ to produce a S/N of 1.

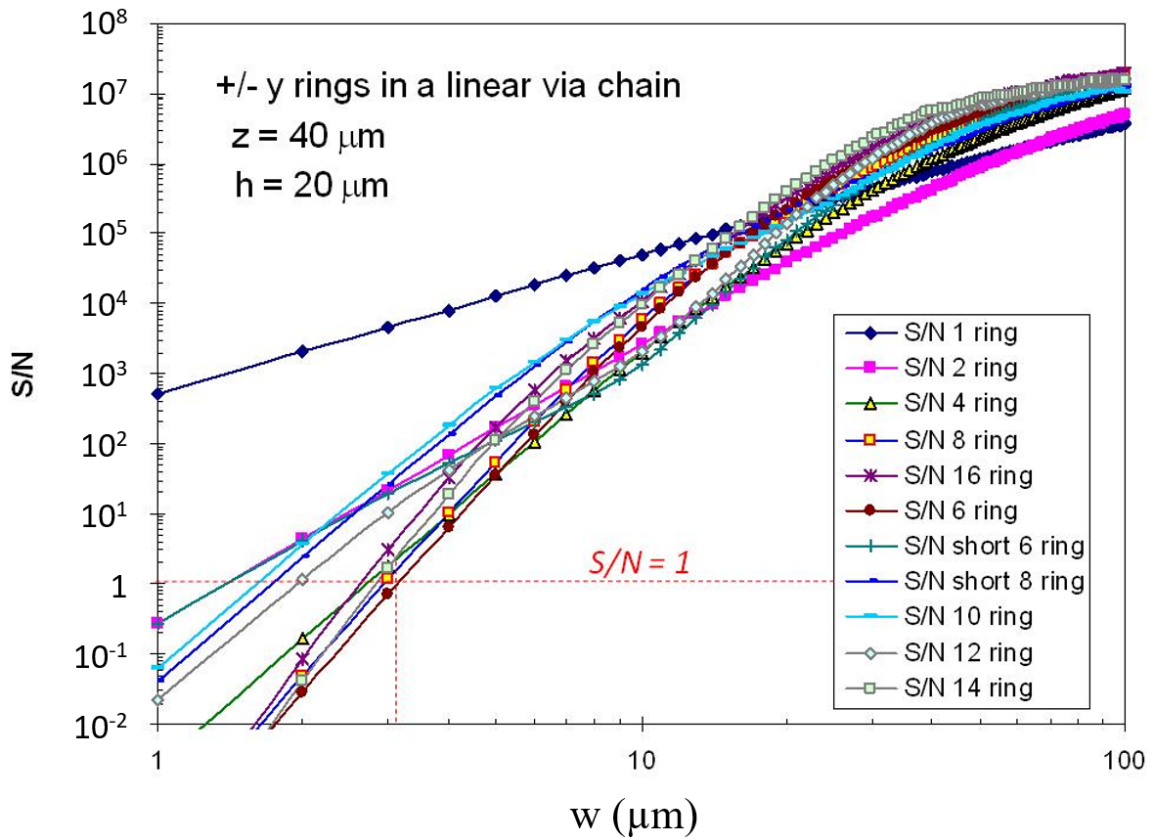


Fig. 3.10. S/N for a single rectangular y-ring, as well as multi-poles built from 2, 4, 8, and 16 rings and a few other combinations of +y and -y rings. For this plot $z = 40 \mu\text{m}$ and $h = 20 \mu\text{m}$. The 6-ring combination is the least resolvable, requiring a grid spacing of about $3.1 \mu\text{m}$ to produce a S/N of 1.

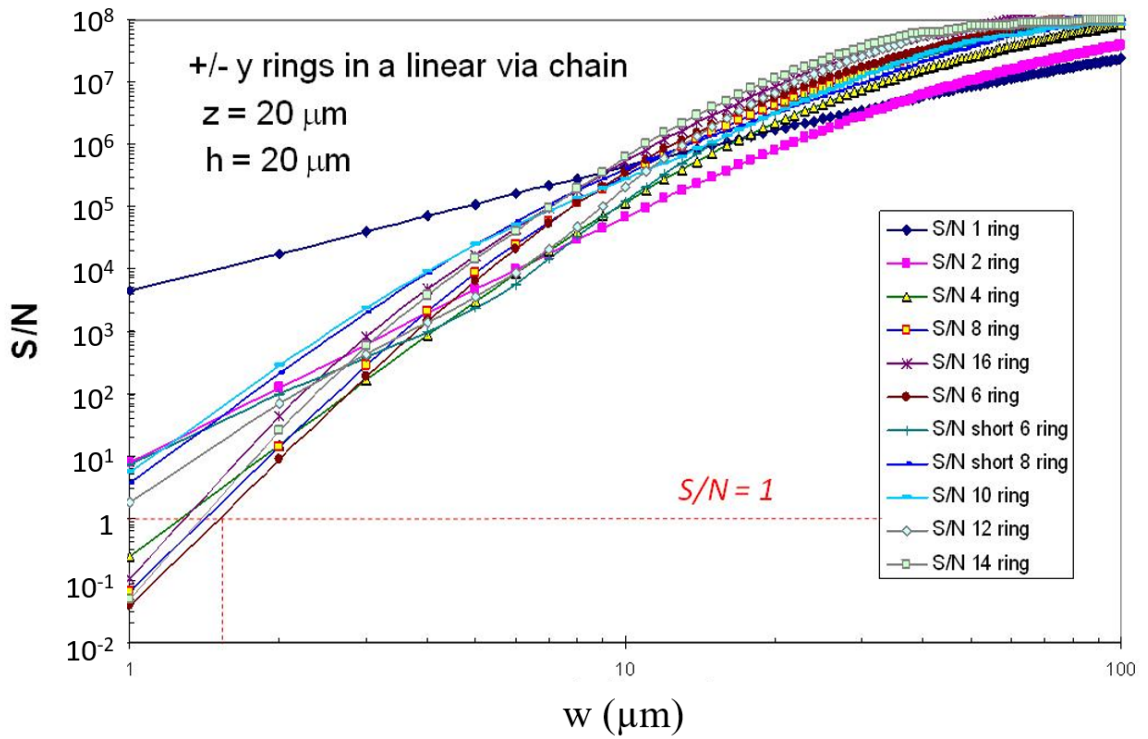


Fig. 3.11. S/N for a single rectangular y -ring, as well as multi-poles built from 2, 4, 8, and 16 rings and a few other combinations of $+y$ and $-y$ rings. For this plot $z = 20 \mu\text{m}$ and $h = 20 \mu\text{m}$. The 6-ring combination is the least resolvable, requiring a grid spacing of about $1.5 \mu\text{m}$ to produce a S/N of 1.

for imaging distances from $z = 20 \mu\text{m}$ to $z = 120 \mu\text{m}$. This is significantly better than $z/w \approx 4.5$ which is what the standard inverse can achieve. In his paper on the ultimate limits of magnetic field imaging resolution (see [Appendix B](#)), John Matthews finds that the ultimate spatial resolution for a SQUID microscope is about $0.5 \mu\text{m}$ for $z = 100 \mu\text{m}$. This is much better resolution than the 3D Solver can achieve under the same conditions. The implication is that the addition of more constraints could in principle lead to as much as a factor of 200 further improvement in the spatial resolution by eliminating difficult to resolve ring patterns.

3.8 Conclusions

In Chapter 3, I described a new approach to obtaining a 3D magnetic inverse that uses grid-based constraints. These constraints are an appropriate way to discretize the magnetic inverse and are consistent with many real samples. I showed that these constraints guarantee a unique solution for the current path. I also analyzed this inverse's noise performance and showed that we can expect a best case resolution of $z/w_{min} = 11$, about a factor of two better than the standard inverse for typical imaging and sample parameters. In the next Chapter, I introduce the algorithms that I used to run the 3D inverse in practice.

Chapter 4: Implementing the 3D Solver

4.1 Introduction

In this chapter I discuss the search algorithms that I developed for the 3D Solver. In [Section 4.2](#) I present the z -search algorithm, which is the main search function we use to place segments in the correct layer. In [Section 4.3](#), I present the corner search algorithm, which we use to search the path laterally but does not change the layer assignment of segments. These are the core routines that power the 3D Solver and allow it to reconstruct the geometrical path that the current takes through a sample. Both the z -search algorithm and the corner search algorithm are essentially a series of local searches that concern the details of the path taken by the current.

The third critical search algorithm we use is the parameter search, which runs completely independently from the segment searches. The parameter search is used to determine the parameters of the sample and of the scanning process, including the input current I , the sample-sensor distance z , the spacing between different layers of the sample h_i , the sensor tilts θ and ϕ and the gain g . These parameters are global parameters in the sense that changing any of them affects our model of the entire image instead of a small localized region. The parameter search is covered in [Section 4.6](#).

Finally, I present some important but secondary algorithms that are critical to obtain-

ing a good fit. In [Section 4.4](#) I cover how I take into account the infeeds and outfeeds of samples. In [Section 4.5](#) I explain how I use a χ^2 statistical test to know when we have arrived at an acceptable solution for the inverse. In [Section 4.7](#) I cover the use of multiple wires in the inverse, and in [Section 4.8](#) I cover the use of cropping to conduct region of interest searches on small parts of the image.

4.2 Z-search algorithm

To simplify the discussion of path search algorithms, I start by considering linear via chains (LVCs), which are some of the simplest paths. LVCs are paths that can meander over two or more layers in z but do not meander in x or y . To make things even simpler, I first consider LVC paths that are built from x segments that are on only two layers. That is, each lateral ($+x$) segment can either be in the top layer or the bottom layer. [Fig. 4.1 \(a\)](#) shows an example of such a path in blue.

LVCs are drawn from a very restricted set of 3D paths, and this greatly simplifies the path search. First, an LVC has no y segments or $-x$ segments. Moreover, it has a fixed number of $+x$ segments, which is a great advantage. For a two-layer LVC, the only variation in the path is that $+x$ segments may be in the top layer or the bottom layer. Of course, z segments will need to be incorporated into the path in order to keep top layer and bottom layer segments connected.

In [Fig. 4.1 \(a\)](#), the initial test path (red) is a straight line that is completely in the top layer. The true path (blue) is different and has some $+x$ segments in the lower layer. Given a test path, the routine calculates the corresponding magnetic field and the difference

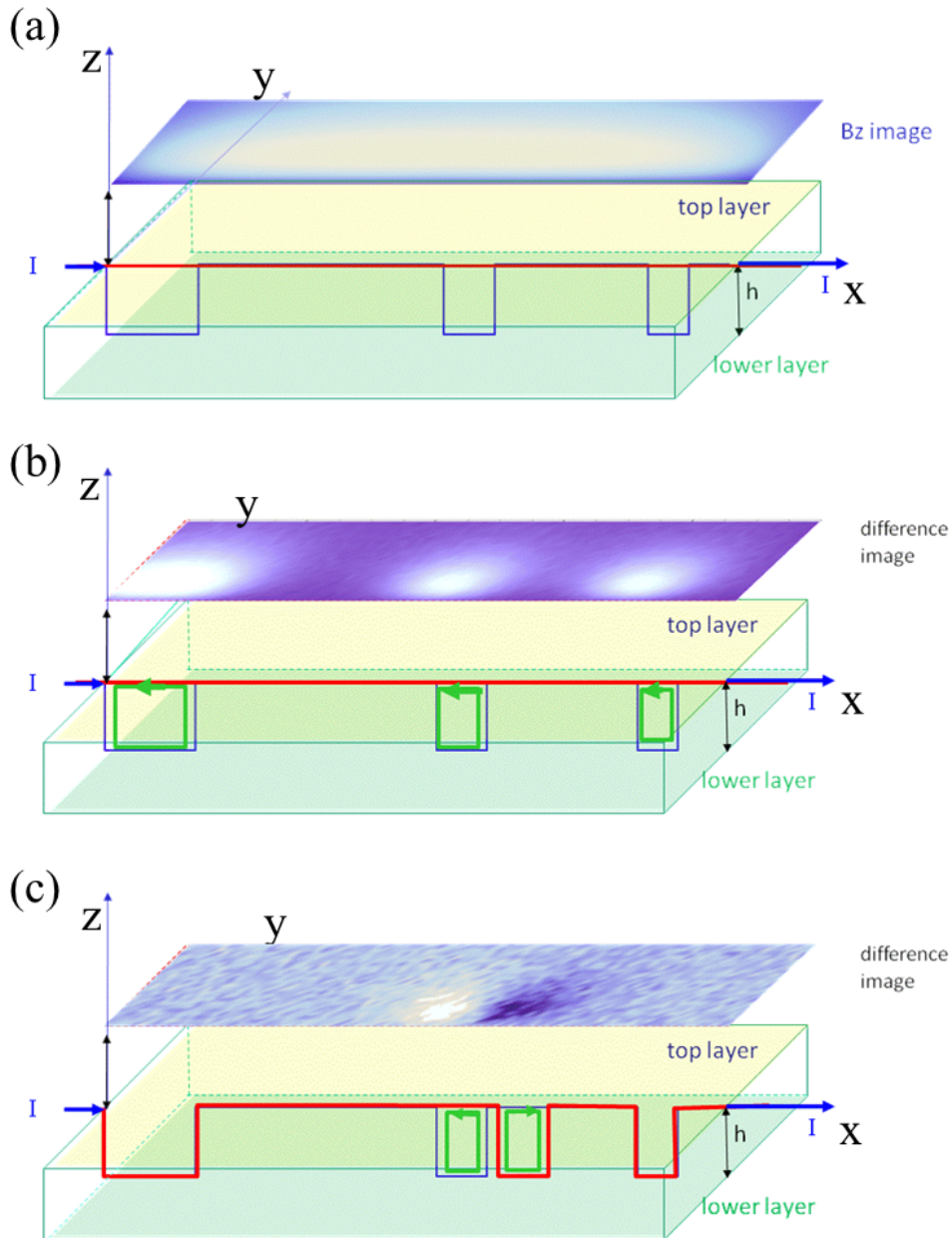


Fig. 4.1. Basic path search algorithm approach. (a) starting path (red) is superposed on true path (blue), with B_z shown above. (b) Difference image above the paths shows areas of discrepancy. These correspond to discrepancies in path shown by the green current rings. (c) Vary the starting path to lower the χ^2 . As the search progresses, we eliminate discrepancies and our test path gets closer to the starting path.

between the magnetic field from the data and from the test path. As seen in Fig. 4.1 (b), the difference image shows discrepancies that correspond to the errors in the path. The difference image is precisely the magnetic field due to just the difference in path between the true path and the test path. The path difference can be thought of as composed of rings of current, as described in Section 3.6 (see Fig. 3.2). Moreover, the field produced by the rings increases the χ^2 of the difference field above the value it would have if it were just due to noise and the test path was the same as the true path.

The object of the path search is to get rid of these rings of discrepancy. For example, suppose there are 100 $+x$ segments in a 2 layer LVC. The good news is that there are only 100 rings of current possible – one for each $+x$ segment, sandwiched between the top and bottom layers. A naive search would simply go through the test path, trying to add each ring one at a time. In each case, if the addition improved the χ^2 ,

$$\chi^2 = \sum_{i=1}^N \left(\frac{B_i^{data} - B_i^{fit}}{\sigma_{B_i}} \right)^2, \quad (4.1)$$

you would keep the ring. If it didn't improve the χ^2 , you would remove the ring. The problem with this approach is that, as we saw in Section 3.7, some combinations of rings have magnetic fields that almost cancel (see Fig. 3.3). Thus, adding a single ring of current may not improve the χ^2 , and the search would be stuck in a local minima.

To get around this, another naive approach would be to try every possible combination of rings. This would guarantee that we find the combination with the lowest χ^2 . Unfortunately, for an LVC with 100 $+x$ segments, which is quite a short path, this would require $2^{100} \approx 10^{30}$ trial paths, which is not computationally feasible.

There is a middle ground between these two approaches. Considering adding a single

ring at a time to the path is very fast but leaves us susceptible to local minima. Considering every possible ring simultaneously gives us too many ring combinations to compute and is not feasible practically. This suggests that we should consider a small number of rings simultaneously, enough to avoid local minima but not so many that the combinatorics of the problem become intractable. In this manner, we search for small multipole combinations such as 2-ring, 4-ring or 6-ring combinations, but avoid the largest ring combinations which are the most time consuming but not necessary for the search. From [Section 3.7](#), given the scanning distance z and our desired segment length w we can compute the correlation length to know how many rings we need to search over. For example, for typical SQUID imaging parameters ($z = 60 \mu\text{m}$, $h = 20 \mu\text{m}$, $w = 5 \mu\text{m}$), we need to search over 6 segments, which is no issue computationally. Note that for deeper layers, the distance to the layer itself must be taken into account. Note also that while the minimum value for w will typically be limited by noise, it could be limited by our computational capacity if the noise were low enough. On the desktop computer I used, 12-ring combinations were the computational limit for a reasonable search timeframe of a few hours. The algorithm for the z search is as follows.

(1) First, the z search function captures inputs such as the area of the image to calculate the χ^2 over, the number of rings to search over n_r (dictated by the correlation length), and which segments to search over.

(2) It identifies all of the x and y segments in current wire being searched. Note that the number of x and y segments stays constant but that the number of z segments may change.

(3) It calculates the χ^2 of the current best fit magnetic image, χ_{test}^2 .

(4) Starting at the beginning of the path, the search calculates the field of every ring combination that can be added to the first n_r segments (*i.e.* lateral segments 1 to n_r). Each segment can be raised by a + ring, lowered by a - ring or not moved at all (see Fig. 3.2). Thus, the routine calculates the field of 3^{n_r} ring combinations. For each ring combination, it adds the field generated to the current best fit magnetic image and computes the χ^2 , keeping track of the lowest computed χ^2 .

(5) At the end of step (4), the routine selects the path with the lowest computed χ^2 as the new best fit path. The set of segments to be varied increments by 1 (*i.e.* the new set of lateral segments are number 2 through $n_r + 1$).

(6) Steps (4) and (5) are repeated until the end of the wire is reached.

(7) If multiple wires are being searched on, the search (steps (1) through (6)) is executed on the next wire.

(8) The search outputs the results to the main GUI interface.

Compared to the two “naive” approaches described above, our z -search algorithm represents a middle ground. It searches over enough ring combinations to capture correlated rings, but not so many that the problem is computationally intractable. This may still involve a very large number of possible paths, but it is far fewer than all possible paths.

In Figure 4.2, I show the results of applying the z search algorithm to a real magnetic image. Figure 4.2 (a) shows a magnetic image (taken by spin-valve) of sample 1, a 3-layer LVC. After applying a straight line initial path, we end up with a path with 1200 + x segments. All these segments are assigned to the top layer. We then do an initial fit to the parameters (see Section 4.6). Next we apply the z -search algorithm. Fig. 4.2 shows the reconstructed field from our algorithm. The difference between the data and simulated image is shown in

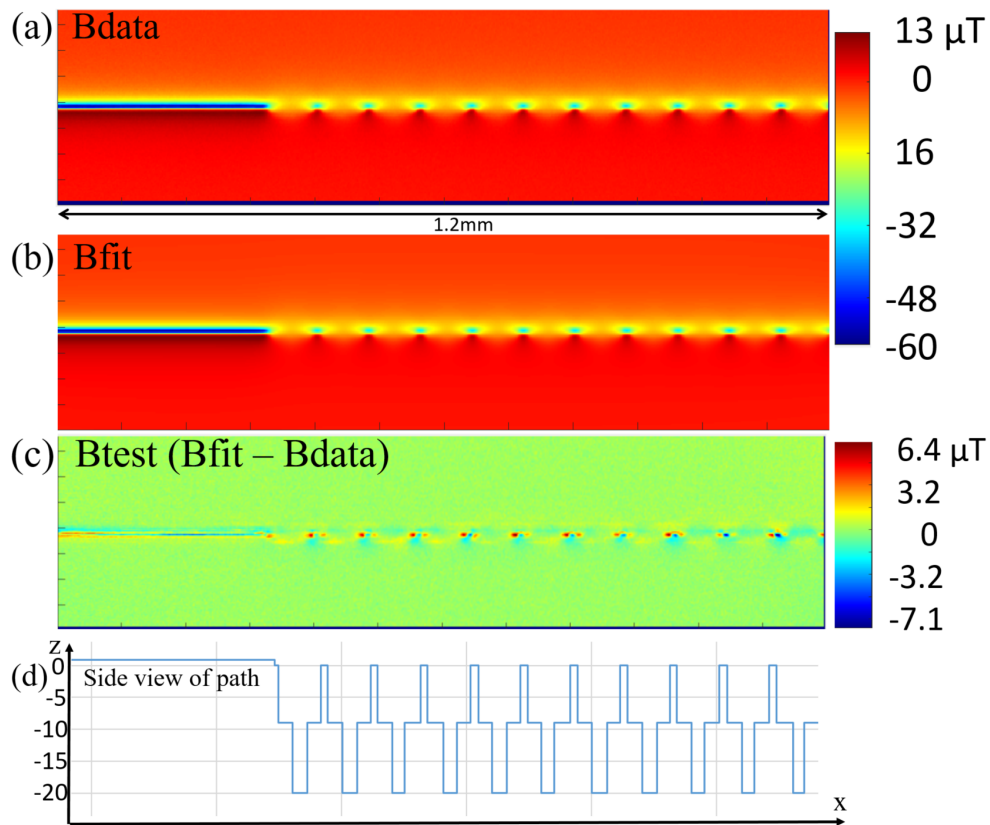


Fig. 4.2. Results from a z -search on a magnetic image from a 3 layer test sample. (a) The original magnetic image of sample 01, a 3-layer linear via chain. (b) The fit after running the search and optimizing parameters. (c) Agreement between the data and fit are good except at the ends of some of the top-layer segments. (d) Side view of reconstructed path matches what we know from optical imaging of the sample.

Fig. 4.2 (c). As we can see, the difference is small and thus the fit and the data are very similar. As is typical of real data, there are still some discrepancies in the data, particularly close to the path. This may be from errors in the path or that the model does not exactly replicate the distribution of current in the path itself (the current distribution through vias and around corners is not modelled exactly). Another type of discrepancy that can occur is when the segment lengths in the actual path are not commensurate with the segment length used in the model path. It could also represent that there are artifacts in the data, such as position noise. Finally, Fig. 4.2 (d) shows a side view of the reconstruction of the path. This was a very regular test pattern, so we knew the design of the path. Although most of the segments we reconstructed matched the design, there were some discrepancies right near the vias, where our reconstructed vias appear one segment before or after its location in the real sample.

4.3 Corner search algorithm

The corner search consists of two search algorithms which run one after the other or can be run independently. The first is a “clean-up” search which identifies specific situations where well known errors are made in wirization paths. These typically occur at “corners” in the path, *i.e.* places where an x , y or z segment is followed by a segment of a different type. It is quite common for example for a corner to appear too early in the path or too late, and therefore it is of interest for the search to be able to quickly get rid of these defects. Figure 4.3 (a) shows such an example. The x - y corner appears too early and should be moved by one grid spacing to the right of its current location. The corner search tests about a dozen

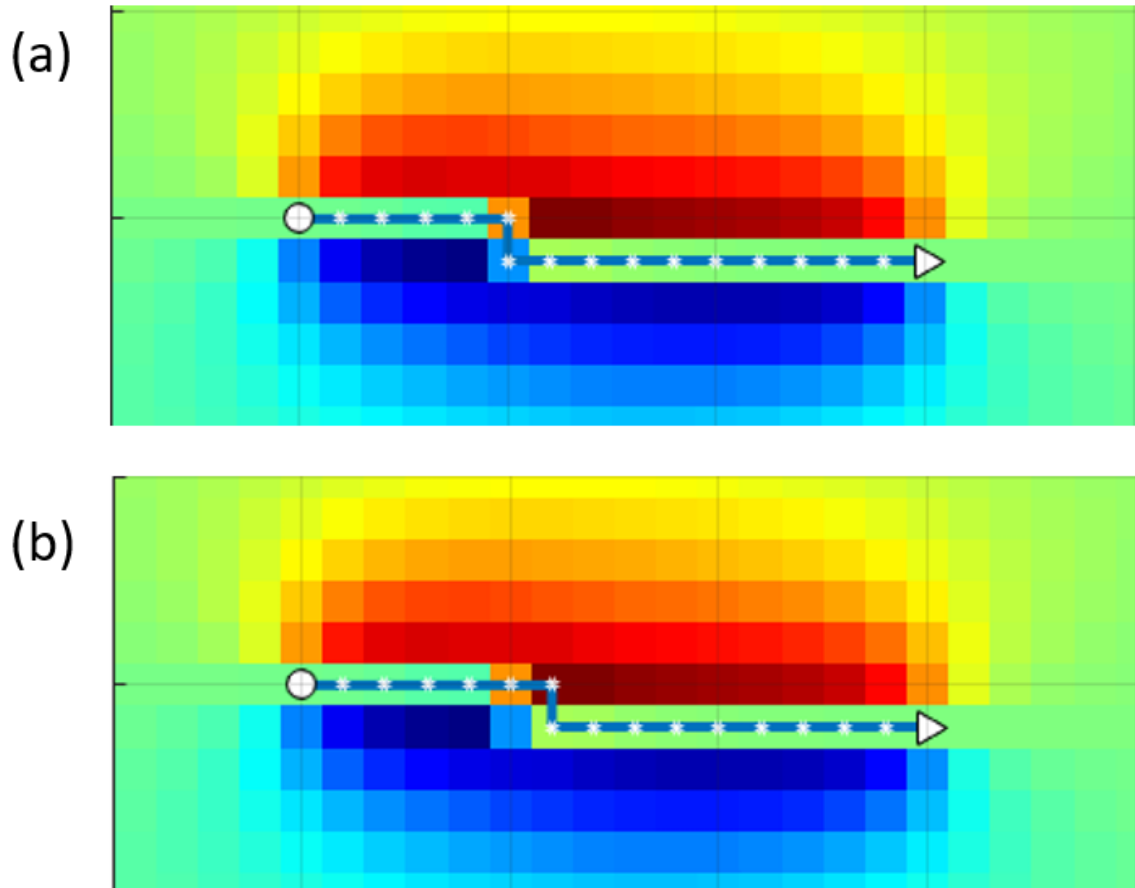


Fig. 4.3. The location of the x - y corner in paths (a) and (b) differ by one segment. This is a common error in paths. The corner search helps to quickly identify such patterns.

such patterns, which contain either one or two rings.

The second corner search algorithm is a more general path search algorithm similar to the z -search algorithm. Just like the z -search algorithm, it uses a correlation length input parameter n_r which specifies the number of rings to vary simultaneously. Rings within n_r of each other are varied simultaneously to ensure the search tries enough ring combinations, while rings further away are not varied together to limit the number of combinations searched. The algorithm for the corner search is as follows:

- (1) Load input parameters such as the area of the image to calculate the χ^2 over, the

segments to search over and the number of rings to vary simultaneously n_r .

(2) Identify all the x and y segments in the current wire being search. Note that unlike in the z search, the number of lateral segments will vary dynamically during the search and this must be taken into account.

(3) calculate the χ^2 of the current best fit magnetic image, χ_{test}^2 .

(4) Starting at the beginning of the path, the search calculates the field of every ring combination that can be added to the first n_r segments (*i.e.* lateral segments 1 to n_r). Note that unlike the z -search, each segment is not guaranteed to be able to move to the left or to the right because I do not allow the path to self-intersect. Therefore, there are a maximum of 3^{n_r} combinations but there could be fewer combinations as well. For each calculated ring combination, the routine adds the field generated to the current best fit magnetic image and computes the χ^2 , keeping track of the lowest computed χ^2 .

(5) At the end of step (4), the routine selects the path with the lowest computed χ^2 as the new best fit path. The set of segments to be varied increments by 1 (*i.e.* the new set of lateral segments are number 2 through $n_r + 1$).

(6) Steps (4) and (5) are repeated until the end of the wire is reached.

(7) If multiple wires are being searched on, the search (steps (1) through (6)) is executed on the next wire

(8) The search outputs the results to the main GUI interface.

In Figure 4.4 I provide an example of the capabilities of the corner search algorithm. Figure 4.4 (a) shows a simulated image of a 2-layer meandering path. To find a good approximation to this path, I first applied a wirization algorithm (see Section 5.4) and a parameter search. The resulting difference image between the signal and the field from the

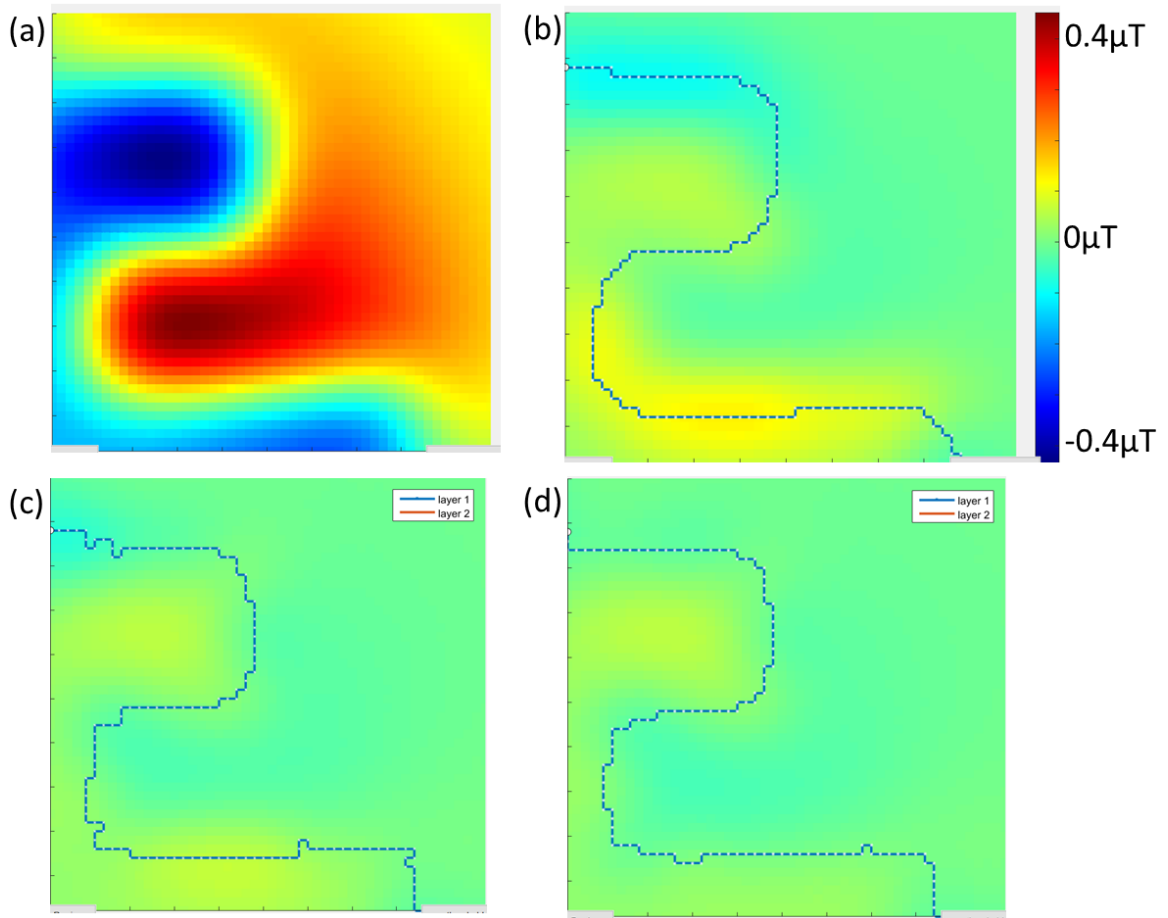


Fig. 4.4. (a) Magnetic data from simulated path. (b) $B_{fit} - B_{data}$ (difference between fit and data) after wirization and parameter search. $\chi^2 = 1.4 \times 10^8$. (c) $B_{fit} - B_{data}$ after one run of lateral search. $\chi^2 = 4.1 \times 10^7$. (d) After 3 runs through the entire path, the corner search algorithm has settled on a best path. The path is still incorrect because we have not done any vertical searches and the parameters are still approximate because they were searched based on the original wirization path. Improvements in the parameters used and z -searches are needed to improve the path further. $\chi^2 = 2.6 \times 10^7$. All images use the same color scale from the top right of the figure.

test path is shown in Fig. 4.4 (b). We can see that there are still significant discrepancies. Since these discrepancies look like they were due to lateral rings, I next applied the corner search algorithm. I did this over many steps, alternating with the parameter search. As we can see it was possible to reduce the discrepancies between the simulated and real magnetic images, although significant discrepancies remained (see Fig. 4.4 (c) and (d)). Using the z -search as well, this path can be completely resolved and since this was a simulation, we can check that we reconstructed the correct path.

4.4 Infeeds and outfeeds

One of the issues with real images is that the current leads, which are off of the current image, produce magnetic field in the image. Because of this, we must compensate for currents outside the image so that we obtain an image which only represents the currents inside the area of interest. This is important as all circuits have leads bringing the current in and out. We refer to these as the infeed and the outfeed currents. If these leads are vertical (*i.e.* supply the current vertically through the bottom of the chip), then they do not affect the magnetic field as vertical currents do not produce vertical magnetic fields. More likely, however, the leads are either horizontal, or some combination of both, for example due to a wirebond or a probe. Thus we need a routine to cancel out their fields.

Of course, users are not usually interested in the currents outside the image, so it is not critical to get the infeed and outfeed currents exactly right. They only need to be good enough to allow the path to be found inside the image. Additionally, infeeds and outfeeds are often completely straight to a considerable distance.

However, I should point out that it is usually critical to get rid of stray currents outside the scope of the image that produce magnetic fields that affect the magnetic image. Because of the lock-in method used to reduce magnetic noise, we only detect stray currents that are at the same frequency as our signal. However, those are precisely currents that may be connected to our infeed or outfeed leads. Therefore, care must be taken with the current path as it gets close to the sample.

We offer two ways to add infeeds. First, you can manually add segments going in any direction, because sometimes the operator knows what the infeeds look like because they have physically connected a probe to the chip being imaged. However, sometimes the infeed is actually a section contained within the chip and unknown to the operator. For example, if one is only imaging a small part of a chip, may be contained in the chip. Therefore, our second method is to use an automated infeed/outfeed algorithm, which adds segments to minimize the χ^2 . The algorithm will keep adding currents as long as the χ^2 decreases, but stops if the χ^2 starts increasing again. This way we hope to find roughly the correct length of the infeed. The algorithm only adds segments that are in the same direction as the first segment of the wire. That is, if the first segment is a $+x$ segment, then all segments added are also $+x$.

Finally, to guarantee that this algorithm terminates, we require that each step be at least a 0.1% improvement in the χ^2 . Otherwise some scans could generate unnecessarily long infeeds – notably, scans that have very long (effectively infinite) infeeds. This requirement means that the routine will stop adding infeeds if it makes the χ^2 worse, or if it simply doesn't make a difference.

Figure 4.5 (a) shows a simulation where we know the path on the image is correct

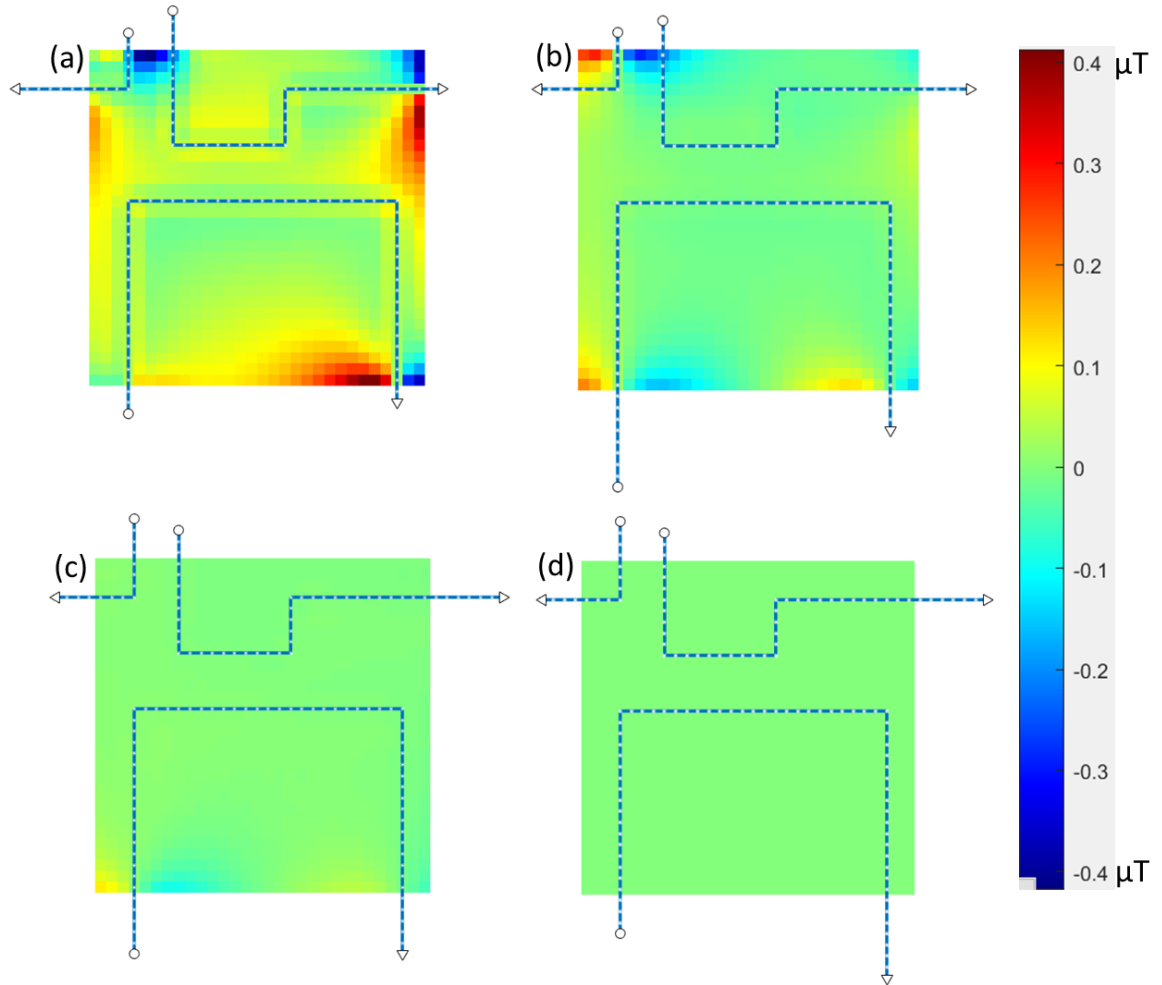


Fig. 4.5. (a) The path inside of image has been solved, but the infeeds are causing discrepancies. $\chi^2 = 1.8 \times 10^5$, $z = 10.2 \mu\text{m}$, $g = 0.362$. (b) After running auto infeed and outfeed once, $\chi^2 = 4 \times 10^4$, $z = 10.0366 \mu\text{m}$, $g = 0.35542$. Since the infeeds and outfeeds are correlated, we do not get perfect solution on the first try, but the χ^2 improves. We have also run the parameter search in between infeed searches. (c) After a second pass: $z = 9.986$, $g = 0.35298$, $\chi^2 = 4.05 \times 10^3$. (d) After two more runs, the χ^2 precipitously drops to 0.955, showing that we've reached the "true" solution. The difference image is entirely blank and would only show noise on an adjusted color scale. $z = 10 \mu\text{m}$, $g = 0.35355$. All images use the same color scale.

but the infeeds are of the wrong length. We use our simple automatic algorithm to try to find the lengths of the infeeds. The algorithm has to run multiple times because infeeds and outfeeds are correlated and these are also correlated with the parameters. After running the automated infeed routine once, we have lowered the χ^2 and improved the image, but there are still visible discrepancies. As we run the algorithm again (Fig. 4.5 (c)), the χ^2 drops and after 4 runs (Fig. 4.5 (d)), the χ^2 shows that we have reached the true solution.

4.5 Noise and goodness of fit

A critical step in the path search is knowing when the best fit path has been found and the search should be stopped. To determine how good the fit is, we use the χ^2 ,

$$\chi^2 = \frac{1}{\sigma_B^2} \sum_{i=1}^{N_m} [B_{z,i}^{data} - B_{z,i}^{fit}]^2, \quad (4.2)$$

where N_m is the number of pixels in the image and σ_B is the standard deviation of the noise in our image. The noise in our sensors obeys a normal distribution and our sensors are calibrated in a known field to obtain σ_B . Additionally, images often have regions with essentially no signal (far from any current source) and the noise in a scan can be found by taking the standard deviation of the data in this region. An even better approach is to find such a region in a difference image, where any background field has been removed and only noise remains. This is useful because the conditions and the sensors can change over time. Specifically, we've observed that the characteristics of the spin-valve sensors can drift significantly over the timespan of a month. Thus an image we are trying to analyze typically contains the information we need to estimate the sensor noise at the time the scan was acquired.

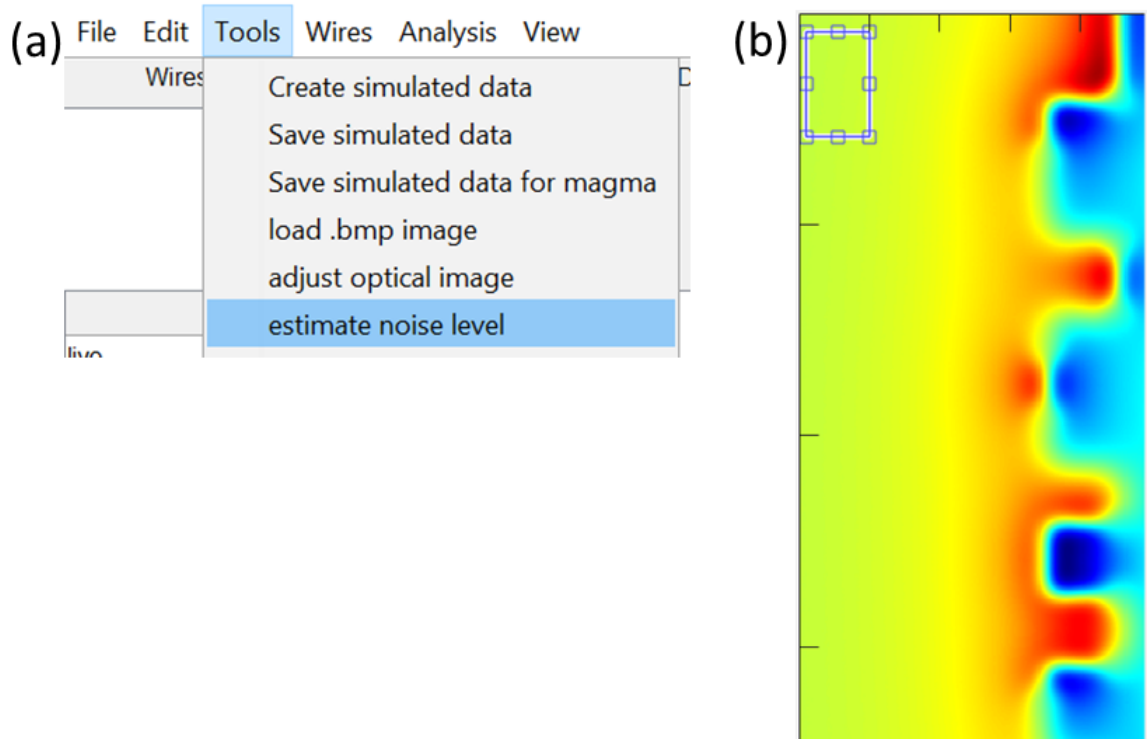


Fig. 4.6. (a) The “estimate noise level” tool in the 3D Solver GUI allows a user to select a square region in the scan image and the tool then outputs the standard deviation of the field in this region. (b) The region in the top left of the image has been selected. Estimated noise in this region was 193 pT per pixel, consistent with typical values for our SQUIDs.

To estimate the noise, I implemented a software tool that allows a user to manually select a region of the image to try to extract the noise in the image. Figure 4.6 (a) shows where the controls can be found in the 3D Solver GUI. In Fig. 4.6 (b), I have chosen a region in the top left of the image to extract the noise. Since our sensors have a normal noise distribution, we take the standard deviation of the data in this region to find the standard deviation of the noise. The estimated noise in Fig. 4.6 (b) was 193 pT, consistent with typical values for our SQUIDs.

As we improve the test path, we can take the standard deviation of the difference image. This allows us to improve the noise estimate, because we get rid of signal that was originally included in the noise estimate. If we can find a good solution for the test path, the difference image will just show random noise and the noise estimate will be quite accurate.

We then use this estimate to calculate the χ^2 . If our inverse is perfect, then χ^2 should simply be the number of pixels. Because scans can vary greatly in the number of pixels, in this thesis we use a reduced version of the χ^2 . Specifically, we divide the χ^2 value by the number of pixels. In this way, a χ^2 of 1 shows a statistically solved scan. A χ^2 greater than one shows that we have not yet resolved the scan. Unless otherwise noted I will use this convention throughout this thesis.

There are other types of noise we have encountered in our analysis, most notably position noise from the stages, and artifacts from the SQUID contact pads (see Chapter 6). We have also seen effects from thermal expansion of the MAGMA system. We have made considerable efforts to minimize these, but these sources must be evaluated on a case by case basis and they cannot be estimated using the included tool.

4.6 Parameter search

The parameter search I built for the 3D Solver allows us to search on scan and wire parameters. There are eight scan parameters one can search on: the sensor-to-sample distance z , the gain g , the data offset B_0 , the sensor tilts θ and ϕ , and three sample alignment parameters – the x sample offset, y sample offset and in-plane sample rotation. Each wire also has several parameters that can be searched on, namely the current I , the wire width b , and the layer-to-layer separations h_i . The goal of the parameter search is to find the combination of parameters which generates the lowest value for χ^2 . One critical consideration when designing the parameter search was to try to minimize its runtime. Early in the design process, it became apparent that different parameters require a different amount of computation. That is, varying the z or the h_i values requires re-calculating the field of the entire current path. On the other hand, searching over B_0 or g requires only a simple additive or multiplicative operation which executes much faster. I identified three levels of computational complexity depending on how time consuming the search was.

The first set of parameters require recalculating the field from each segment in the path. This set includes z , the h_i 's and the b 's and is the slowest set to search on. The second set of parameters are the sensor tilts, and the sample x and y offsets and in-plane rotation. Critically, none of these parameters require us to re-compute the field of each segment individually. Instead, the sensor tilts require a few operations on the sum of the field while the sample offsets and rotation require interpolation of the image. Finally, the fastest parameters to search on are the gain, the currents in the wire and the data offset. The

optimal value for these parameters can be found by a simple matrix inversion since

$$[B_z] = g * (I_1 * [B_1] + \dots + I_n * [B_n]) + B_0 \quad (4.3)$$

Where $[B_i]$ is the field from the i -th wire.

Because these three sets of parameters require vastly different amounts of time to be searched on, I decided to build the parameter search in three levels instead of treating each parameter equally. The first level includes the longest parameters to search on, the second level includes the parameters which take a moderate amount of time to search on, and the third level contains the fastest parameters to search on. For the top two levels, we use MATLAB's built-in `fminsearch` algorithm [76], which attempts to minimize the value of χ^2 by trying different values for the parameters. The `fminsearch` function is an implementation of the Nelder-Mead simplex algorithm [77]. This algorithm explores the phase-space of a multi-variable function and attempts to find a local minimum while making no assumptions about the gradient of the minimizing function. Each iteration of `fminsearch` recalculates the χ^2 for new values of the search parameters. In our three-level approach, for each iteration of level 1 parameters, we optimize level 2 and level 3 parameters completely. Similarly, each time a new set of level 2 parameters are tried, we optimize level 3 parameters. This allows us to minimize the number of search iterations computed over level 1 parameters and therefore minimize the number of times the field from the path is re-calculated from scratch. Parts of the parameter search code can be found in [Appendix A.3](#).

4.7 Multiple wires

One enhancement that I made to the 3D Solver was to enable it to reconstruct multiple current paths. In the original version of the 3D Solver, we assumed that there was only one continuous wire of current and used a double array to store the wire information. Later on, I created a wire object class in order to enable us to include multiple wires. The code defining the properties of the wire class can be found in [Appendix A.1](#). Each instance of the wire class contains information individualized to each wire, such as the number of segments, the segment coordinates, the segment lengths, the wire width, and the current through the wire. I also rewrote the 3D Solver functions to loop over instances of the wire class instead of assuming that there was only one wire in the image.

To test the multiwire capabilities, we created a set of simulated SQUID images of 2-layer multi-wire samples (see Figs. [4.7](#) and [4.8](#)). As with the multi-layer simulations, one purpose was to develop our own abilities to use the Solver on samples with more challenging characteristics. Another purpose was to demonstrate that the 3D Solver can obtain the exact 3D path in non-trivial case where there are multiple wires. For these initial test cases, the paths were relatively simple in that they only involved 2-layer patterns and the images had good but realistic levels of S/N . A challenging aspect was that, although the paths were not heavily corrugated, there were long sections with irregular steps in some of the wires. Note that the person who solved for the paths was not the person (K. Torkashvan) who created the simulated patterns and therefore had no prior information about the paths except that there were multiple wires present and that they meandered over two layers. Another quite challenging and realistic aspect of this exercise was that it was not known at the start if some

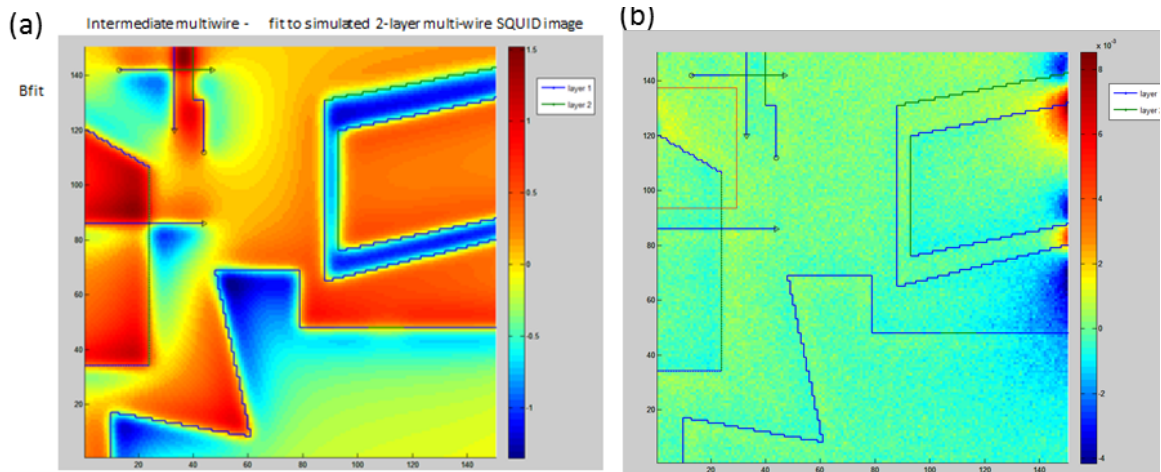


Fig. 4.7. (a) “Intermediate Mutli-wire” simulated SQUID magnetic field image of a 2-layer multi-wire sample. (b) Bfit-Bdata afer running the 3D Solver. The main discrepancies remaining are in the in-feed and out-feed lines on the right side of the image - all segments in the frame of the image appear to be correctly placed. The best fit path is shown supersposed on both images. Note that there are eight disconnected wires, some of which cross over others.

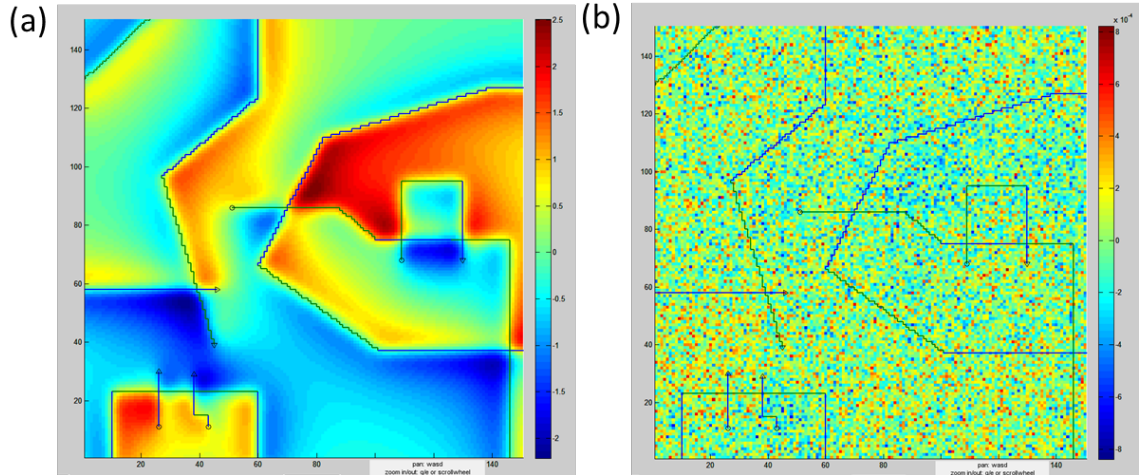


Fig. 4.8. (a) Simulated SQUID magnetic field image of a 2-layer multi-wire sample. (b) $B_{fit} - B_{data}$ after running the 3D Solver. All segments appear to be correctly placed and the residue is almost entirely random noise. The best fit path is shown superposed on both images. Note that there are eight disconnected wires, some of which cross over others. This image was created by Keyvan Torkashvan and solved by Fred Wellstood in a few hours, with no prior knowledge of the current path.

of the wires carried different currents than others (it turned out that some did) and it was not known at the start if the layer-to-layer separation was the same for all the wires (it turned out that one of the wires had a different layer-to-layer separation). Yet another challenging and realistic feature of the images was that they had multiple in-feed and out-feed lines, some of which headed off in a stair-case fashion well outside the images.

4.8 Cropping and region of interest searches

To speed up the path and parameter searches, I developed cropping tools that allow a user to restrict the search to a chosen region. The first tool is the “crop2” tool. This

restricts the region in which the χ^2 of the image is calculated. In Fig. 4.9 I show an example of applying a crop2 region to the lower left part of a magnetic scan (the crop2 region is shown in red). All of the 3D Solver search algorithms are based on minimizing the χ^2 , and so a crop2 region has two main effects. First, it can dramatically speed up the calculation. Imagine for example that in Fig. 4.9, we are only interested in working on fixing the discrepancies in the lower left part of the image. If we only want to vary segments in that part of the image, then it makes sense to restrict the χ^2 calculation to that part of the image as the field in the rest of the image will not change significantly, and calculating it would be a waste of time. Thus, the crop2 region can dramatically speed up the search routines by eliminating unnecessary calculations. Secondly, the crop2 region can be used when one knows that searching a particular region will give good parameter or segment information. For example, the crop2 region is often used on a long infeed or outfeed at the beginning of the search process. Since those sections are usually only affected by the z and g , limiting ourselves to a small region of the scan lets us acquire the z and g without being hampered by not knowing the path or other parameters such as the h_i 's.

I also developed another region of interest tool which is used for the segment searches. When we know that most of the path is well resolved, it dramatically speeds up the search to skip regions we know have the correct path to focus on areas where the path is incorrect. When this ROI tool is used, the search routines will only vary segments inside the ROI. This is used to speed up the path searches and has no effect on the parameter search.

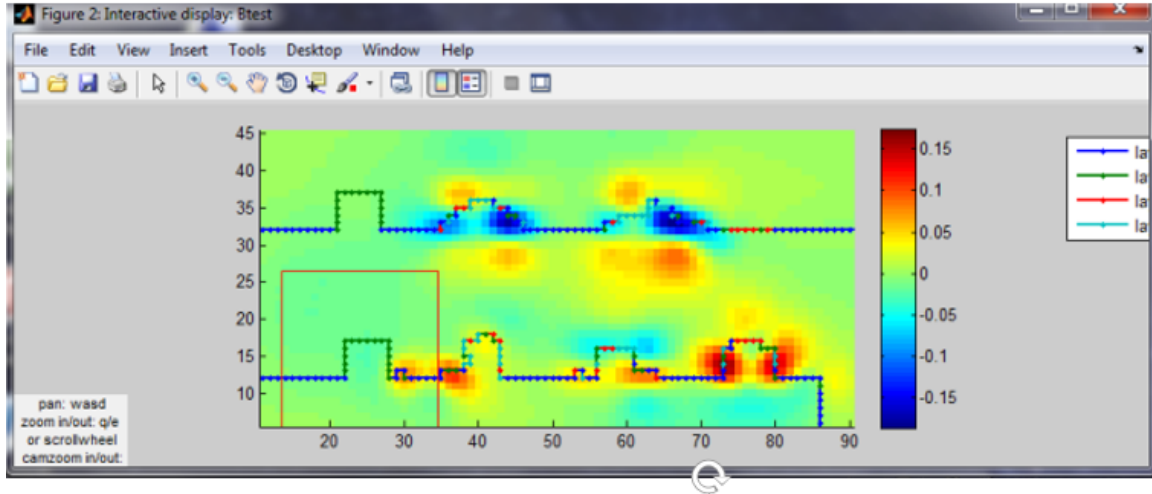


Fig. 4.9. Screenshot of the 3D Solver showing crop2 region in red. The crop2 region selects a part of the magnetic image on the lower left of the image. The path is varied to minimize χ^2 in this region.

4.9 Conclusions

In this chapter I discussed the major algorithms I developed to implement the 3D Solver. The most important of these are the corner search, the z -search, and the parameter search. The parameter search is composed of multiple subroutines but at its core is a multi-dimensional simplex search algorithm. The corner search allows one to search for lateral ring combinations, while the z -search searches for vertical patterns. I also discussed some of the other important algorithms we use in the 3D search, such as wirization routines and the infeed and outfeed routines. I discussed how I measured the sensor noise in a scan and determined the goodness of fit. Finally, I discussed how I implemented multiple wires, cropping, and region of interest searches. In the next chapter I present the GUI I created to use these algorithms, and discuss how to apply them to obtain good inversion results.

Chapter 5: Running the 3D Solver

5.1 Introduction

The 3D Solver inverse software is an analysis tool I developed in Matlab in collaboration with Neocera. The precursor of the 3D Solver were routines written in Mathematica code. These routines were later migrated to Matlab for speed and to take advantage of Matlab's more powerful object-oriented programming capabilities. Eventually, I wrote a graphical user interface (GUI) to make the inversion routines easier to use. In this chapter I'll describe how to use this GUI to run the 3D Solver and will also explain the decisions made in designing the GUI software.

Typically, there are many steps involved in inverting a magnetic image. To obtain an inverse using the 3D Solver it is important for a user to understand both how and why to apply certain commands, as well as what order the steps should be taken in.

5.2 Main graphical user interface

There are two main windows in the 3D Solver GUI, the Main Control Panel and the Interactive Plot. Figure [5.1](#) shows the main control panel after a scan has been loaded. Scans taken with the MAGMA imaging system and stored in files with a .dc or .ac extension can

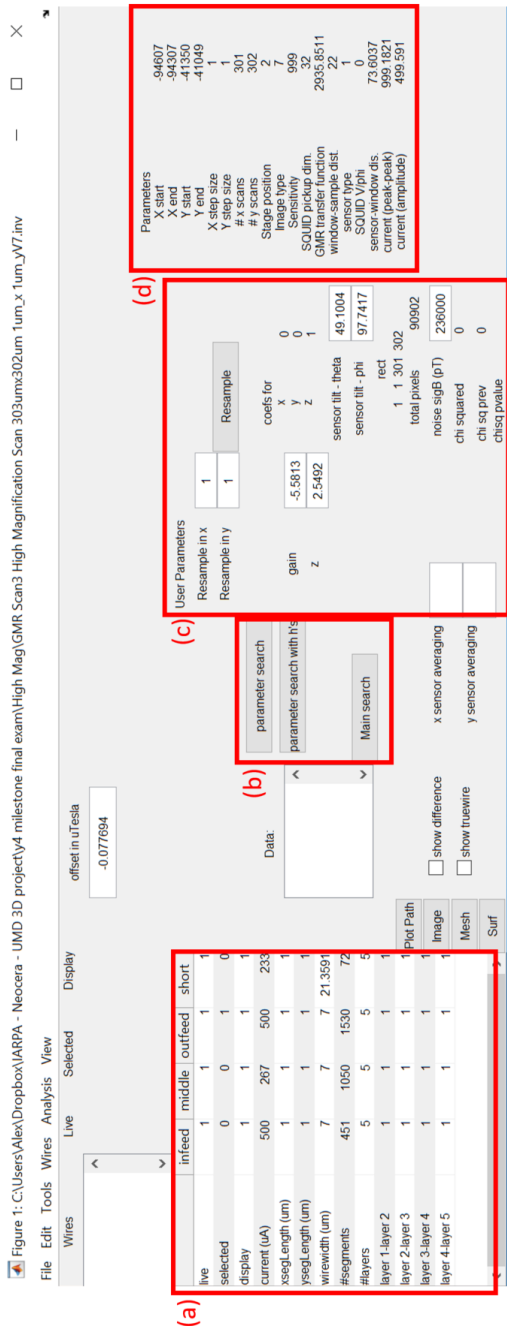


Fig. 5.1. The 3D Solver's GUI main control panel. (a) Wire parameters are listed in this section. They are entered manually by the user or found via a parameter search. (b) Buttons for the parameter search and main segment search. (c) Scan parameters fit by the user including gain, noise level and sensor angles. (d) Scan parameters set by MAGMA image acquisition software, including number of data points and scan resolution.

be opened in the 3D Solver by selecting Open under the File tab in the main control panel menu bar. When the scan is loaded, its file name appears in the Control Panel's title bar (see Fig. 5.1). The imaging parameters of the scan are loaded into a table on the right side of the GUI (see Fig. 5.1 (d)). These parameters include the scanning area size, the pixel-to-pixel distance in x and y , the type of sensor used and sensor calibration, the sensor-to-sample distance, and the current passed through the sample. These parameters are collected by the MAGMA imaging software when an image is acquired. Some of these parameters, such as the current through the sample and the sensor calibration, are automatically used by the inverse, while others, such as the estimated sensor-to-sample distance, are there for the user's reference.

Figure 5.1 (c) shows where a user can set many of the inversion parameters for the scan. These fields are automatically populated by default values but they are modifiable by the user. For example, while the default segment grid spacing is the same as the pixel-to-pixel spacing, the pixel-to-pixel spacing can be changed via pixel interpolation to draw segments on a different grid. Similarly, the gain, sensor tilts, and noise levels can also be set by the user.

Figure 5.1 (a) shows where the user can set wire parameters. In this example, there are four wires that I named "infeed," "middle," "outfeed" and "short." Each wire can have parameters independent from the other wires, such as the current through the wire, the number of layers, the layer separations, and the wire width. In this example, all the current (500 μA) is passing through the infeed and the outfeed wires. However the current is split between the "middle" wire and the "short" wire. The infeed, outfeed and middle wires have a wire width of 7 μm , corresponding to trace width of the manufactured sample. The

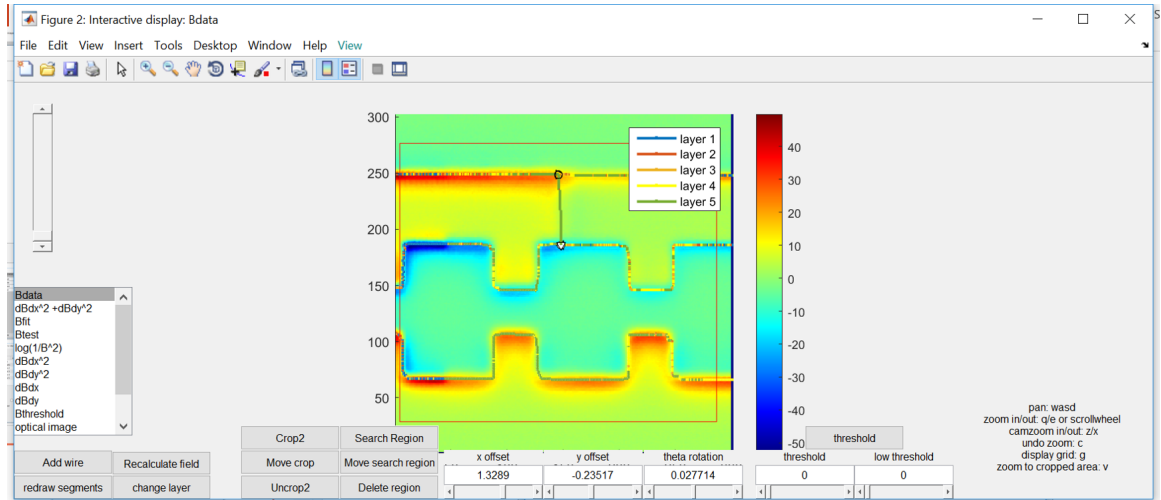


Fig. 5.2. Main 3D Solver interface showing the display panel for the interactive plot.

short, however, has a different width which was found via a parameter search that gave the best agreement between the measured magnetic field image and the simulation. All of the parameters in Fig. 5.1 (a) and (c) can be entered manually if known, or they can be found via a parameter search, as discussed in Section 4.6 and Section 5.6.

Finally Fig. 5.1 (b) shows the buttons on the main control panel for accessing the parameter search and main segment searches. Clicking on these buttons opens popup menus which allow the user to make choices for the parameter search and main segment search routines (see Figs. 5.3 and 5.4).

Figure 5.2 shows the display panel for the Interactive Plot. In this example a false color image of the magnetic field data is displayed in the center. As shown in the color bar scale to the right of the plot, red represents strong positive fields while blue represents strong negative fields. Overlaid on top of the image is the current best solution for the currents.

To the left of the main plot, a user can select a variety of different types of images that

will appear in the main plot region. The best fit current paths will be overlaid on top, also color coded by layer as shown by the layer labels. B_{data} shows the original data. B_{fit} shows the field corresponding to the current of the best fit path, and B_{test} shows $B_{fit} - B_{data}$. In this example, the data is being displayed. We can see that the wire called “short” is extending from the top of the image (“infeed” wire) to the middle. This is a good visual representation of the short in this sample. Other images of interest, such as the field derivatives, can also be displayed. These are helpful because they often give a rough idea of where the currents are, and are in fact used as a rough “inverse” [78]. This is because $\partial B_z/\partial x$ and $\partial B_z/\partial y$ tend to be maximum directly above a y or x current carrying wire, respectively.

The Neocera MAGMA system has an integrated optical/infrared camera to take pictures of the sample. Optical images taken with the integrated camera can be loaded into the 3D Solver and displayed in the interactive plot, with the path overlaid. These optical images of the sample can be aligned and superimposed with magnetic scans and the inverse solution. This helps a user guess locations of the current path and confirm the solution obtained with the inverse when the currents paths are visible at the top of the sample. Users can zoom in or out using the mouse scroll wheel, use the W, A, S and D keys to pan around the image, and switch from one type of image to the next while maintaining spatial scale (zoom) and registration. This way, potential anomalies in the magnetic data and the currents can be correlated to any anomalies in the optical image (*e.g.* surface debris).

Finally, the MAGMA software records both the in-phase and out of phase channels of the signal. Both channels can be displayed, and in fact any phase can be reconstructed from these two images. Most of the time we are only concerned with the in-phase signal. However in practice there can be signal in the out of phase channel, indicating capacitive

leakage or some other issue with the sample (see Fig. 8.10 for example).

Some of the most frequently used tools for manipulating the path can be accessed through buttons at the bottom of the interactive display panel (see Fig. 5.2). The “Add wire” button allows a user to manually add a new current path by drawing a wire on the image. The paths can be modified by using the “change layer” or “redraw wire” buttons. Finally, the field from the new path can be updated by pressing the “recalculate field” button which computes the field due to the currents in all path segments. This panel also has controls for the crop region and the path search region. The crop region, outlined by the red square in Fig. 5.2, is the part of the image that the 3D Solver considers when it is calculating the χ^2 or running a search. Segments in the entirety of the image are used to calculate the field, but the field is only calculated in the crop region, and only this field is used to calculate the χ^2 of the image. This is useful when one is only interested in inverting part of the image, or when a global parameter such as the sample-to-sensor separation z can be easily determined by analyzing a small portion of an image, or when one wants to speed up a search by limiting the area searched (which speeds up the field and χ^2 calculations). The Crop region can be controlled directly from the Crop2 buttons below the interactive plot. To the right of the Crop2 button are tools for defining a search region. If a search region is defined, the segment search algorithms will only try to vary segments within the region and leave others untouched.

Controls for lateral offsets and rotations of the data with respect to the simulation are located on the lower right of the interactive display panel. These let a user align the measured image to the x - y grid of the simulation. These controls allow subpixel to multi-pixel offsets in the data by generating an interpolated image from the data. Such sub-pixel

alignment is critical because pixel-sized errors in segment location would yield errors much larger than the typical noise in our data. Similarly, we expect manhattan geometry in our samples. The rotation option lets us make sure that the manhattan geometry of the sample is precisely aligned with the segment grid.

5.3 Order of operations

Searching for a best fit path in an efficient manner requires that the steps in the search process be conducted in a certain order. To begin using the GUI, go to the File tab and click open to load a .inv or .ac file. .ac files are original magnetic scan data files generated by the MAGMA system. .inv files are “inverse” files proprietary to the 3D Solver in which one can save results from the analysis. After selecting the .inv or .ac file, the interactive display shows a false color image of the magnetic field data (see Fig. 5.2). If one opens a .inv file, the display also shows a plot of the segmented wire path. The main control panel loads previously saved parameters as well as parameters relevant to the scanned image from the .ac file.

After loading a scan, I typically crop the image if I am only interested in a subsection of the scan. There is a “hard crop” option under Tools>Hard Crop (in the main control panel menu bar) which completely eliminates cropped parts of the scan. Next, if there is a very simple or known part of the path it is best to start by working on this section. To work on one region of a scan, the “soft crop” tool (Crop2) can be used to select a rectangular region where searches will be conducted. Unlike a hard crop, the crop2 keeps the rest of the image displayed and easily accessible for analysis. As the analysis progresses, the crop2 region

can be turned off or moved so that a different region can be analyzed. Next, I examine the image for rotation and adjust the image so that it is well aligned by setting the in-plane sample rotation (θ) in the interactive plot panel (see Fig. 5.2).

The next step is to add an initial path as described in Section 5.4. I select from one of the automatic or semi-automatic wirization routines included with the solver, or I manually draw a path on top of the magnetic data, an optical image, or another representation of the data. Initially I may only be able to accurately wirize a small part of the image – for example, an infeed or an outfeed section. That is enough to start with if I use the crop2 to indicate to the program that I focusing on this region for now. Generally, I try to use all available information and insight to create an accurate starting path because the entire process works much better if the starting path is closer to the true path.

The next step is to determine initial values for the global parameters for the scan. Critical parameters include the z , the gain g , the sensor angles θ and ϕ , and data voltage offset (if any). All of these parameters are critical to the search process and accurate values should be obtained as soon as possible and updated as the analysis proceeds. It is important to realize that since these parameters are global, in favorable cases I can get good estimates for them by analysis on a small portion of the scan where I have a good idea of what the path is, and these parameters should work for the entire scan. If one does not have good initial estimates from prior scans or other information, then a parameter search needs to be run. The parameter search requires initial “seed” values, and of course having seed values close to the true value makes the search more accurate and faster. For example, I usually expect the “gain” to be close to one and I use that as a default value before the first parameter search. Also whoever took the scan may have a reasonable guess for the z based

on whether the spin-valve sensor or the SQUID was used and the known characteristics of the sample that was imaged. Typically, it is best to start with a parameter search on the z and the gain g , because these are particularly critical to the fit. Next, one should search the other global parameters, including the sensor angles and data voltage offset. It's important to remember that in order to be sensitive to certain sensor angles, the pattern simulated must actually produce field in the x , y and z directions. Otherwise the angle just acts a global multiplicative factor, just like the gain. After initial values have been obtained, it is important to do simultaneous searches on the parameters, selecting all the parameters to be searched on at once.

Once global parameters are established, one can extend the path to the entire picture by wirizing or manually drawing, if only part of the image was wirized. If the starting path is close to the true path, one can now try to search for wire parameters if that has not been done yet. In particular, one can search for the layer-to-layer spacing, and the currents in each wire if the wires branch. The wirewidth parameter usually only produces a small effect and should only be searched on at the very end of the inversion. If the starting path is too rough, or it does not contain any segments beyond the top layer, then it will not be useful to search on the wire parameters at this point and best guesses should be entered for the wire parameters.

The next step is to begin varying the path to obtain better agreement between the simulated field and the data. Initially it may be best to use the drawing tools to make some obvious adjustments, but the major work involves using the main search tools to place segments to refine the lateral path of the wire and to place segments in the top or bottom layer. Figure 5.3 shows the interface for the main segment search. As can be

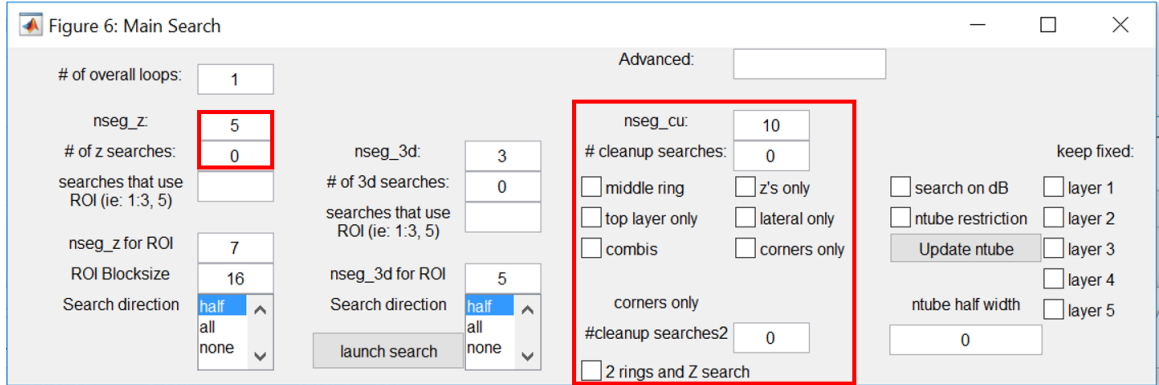


Fig. 5.3. GUI interface for calling the path search in the 3D Solver. The input text boxes I outline in red to the left red control the z search, specifically the number of times the algorithm runs and the correlation length (in segments). To the right I outline in red the corner search and cleanup searches, which have many options for the type of ring patterns that are searched for.

seen, it is quite complex as we have developed and tested many algorithms. However, the two main ones used are the z segment search and the corner search. These searches are indicated by the red boxes on Fig. 5.3. I can choose how many times each search will run (the default is 0 times for each search when first opening the window). For the z search, I can also input a correlation length in number of segments. The rule of thumb is to focus on larger discrepancies in the field and progressively work my way down to smaller and smaller discrepancies. I can identify areas of discrepancies by displaying the difference field, $B_{data} - B_{fit}$. Typically, lateral misplacements of the segments produce larger discrepancies than vertical misplacements. Therefore, I usually run the corner search several times before running the z search. I can recognize the difference between lateral and vertical displacements because vertical errors tend to produce dipole (+/-) patterns, while

lateral errors produce monopole patterns in the magnetic field. Errors in the parameters are also recognizable because they tend to affect the entire image rather than a localized area. As the path becomes more refined, one may need to offset the pixels or adjust the grid by interpolating the image, to make sure that the segment grid goes right through the middle of the actual segments in the real sample.

The search process is iterative. Each parameter or path search returns a χ^2 lower or equal to the previous one. I am usually required to run each search many times. For example, the z -search only moves segments by at most one layer each time it is run. For example, if a segment starts in the topmost layer but is in fact located in the 5th layer, I need to run the z -search algorithm at least 4 times to get the correct placement. Similarly, the corner search algorithm usually only modifies the path by one ring at a time and must be run several times to fully correct large discrepancies. Additionally, I typically use the crop2 tool extensively to focus on regions with large discrepancies one at a time. When the searches stop improving the χ^2 , I stop this process and re-evaluate my best fit path. Are there any glaring discrepancies left in the magnetic difference image? Are these discrepancies at the level of the noise, or much larger? What is causing these discrepancies? For example, there may be a faint current line indicating a leakage that was not visible before, but is made visible when most of the signal in the path is accounted for. In this case, I would add a new wire and continue the search process. Other times, we have discrepancies in our final image that are caused by factors that we know we are not modelling appropriately but cannot correctly account for. For example, we may know that we are not appropriately modelling the current in the TSVs in the sample, which is causing discrepancies in our magnetic field fit despite our current path being otherwise correct. Or, we may know that

there is significant position noise in the sample and that this noise is dominating our final best fit path.

5.4 Drawing and re-drawing paths

In order to run the 3D Solver search routines such as the parameter search or the path search, we need to create a starting path for the 3D Solver. We call finding the initial starting path the “wirization” process. The closer the starting path is to the true path, the faster a parameter search or a path search will converge on the right solution. There are three ways to create an initial path: one can use one of the automated wirization routines, draw the path manually, or import a path found from analysis of another scan of the same sample or from some other source of information.

5.4.1 Automatic routines

There are four automatic wirization routines we use: the LVC wirization, the derivatives wirization, the logarithmic wirization and the “weighed methods” wirization. These automatic wirization routines can be accessed in the main control panel menu bar under the “Wires” tab drop down menu. For samples that run from left to right without crossing back, the LVC wirization is a good option, as it should yield good results and is extremely robust. For more complicated samples, the other routines make use of the field derivatives and other transformations on the data to follow the path of the current through the scan. For clean magnetic field scans (low field noise and position noise) where the structure is relatively discernible simple and discernible, an automatic wirization option is a good choice. Note

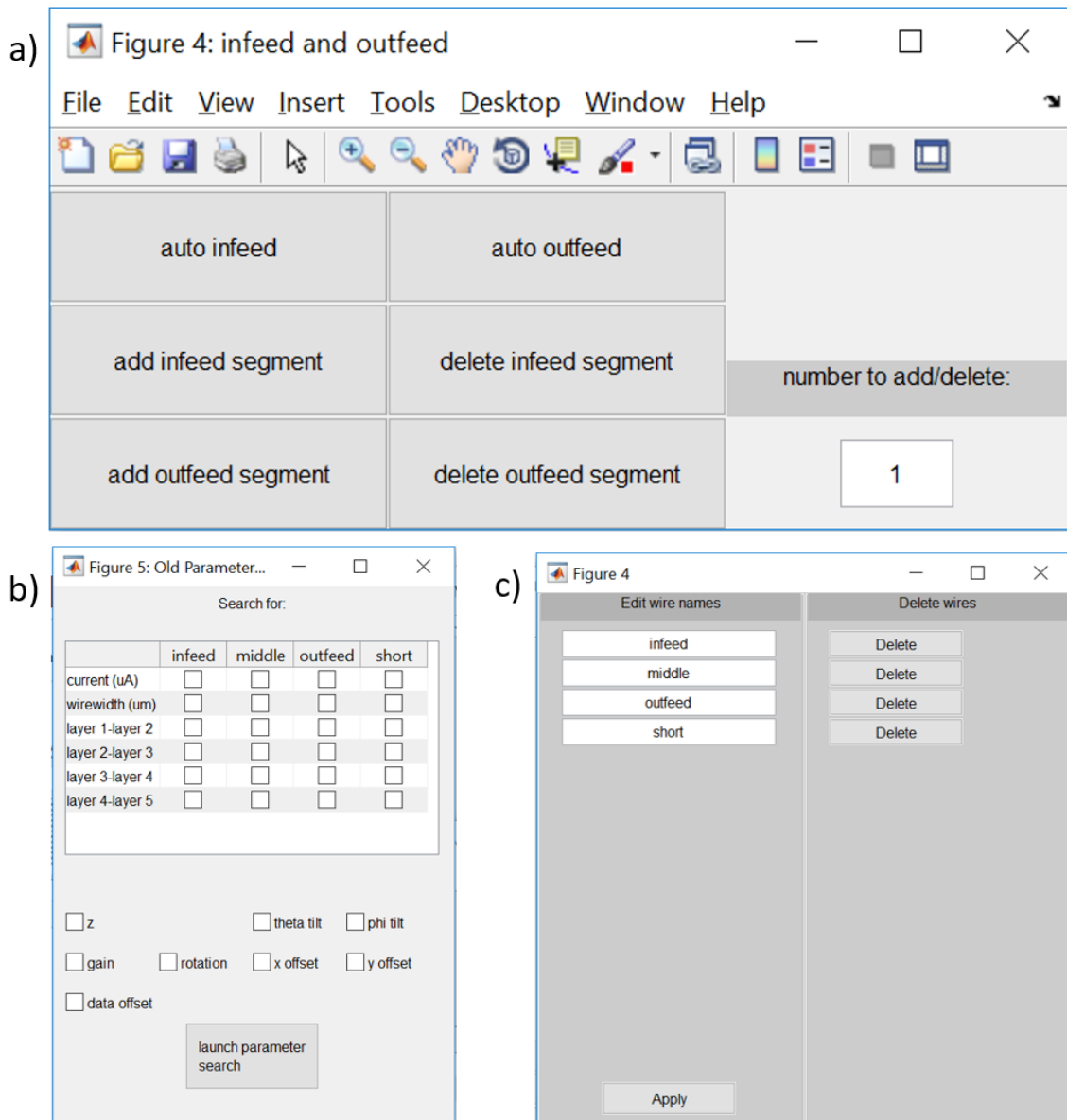


Fig. 5.4. Tools for creating and modifying the infeed and outfeed lines. (a) The automated infeed/outfeed creation routine is also run from this window. (b) To conduct a parameter search, the user must select each parameter that will be searched. The wire parameters are in the wire table at the top, while the scan parameters are listed at the bottom. (c) Control panel for deleting or renaming wires.

that the main goal of automatic wirization is to get an initial path that has good lateral position for the segments. In fact the wirization routines put everything into a single layer and getting vertical position for the segments is handled later in the process.

One difficulty and a remarkable feature of the wirization routines is that they must be robust to work using just the magnetic image and without taking into account any parameter values. This is essential because at the start of an analysis, the parameters are often not known. In particular the gain, z and current values from the MAGMA scanning software are not guaranteed to be accurate. Current leakage or sensor drifts can throw off the gain or current. The scanning software can tell the distance from the sensor (spin-valve) or the sensor window (SQUID) to the top of the sample but cannot tell the distance to the topmost current layer in samples where the layers are buried.

The LVC wirization technique takes advantage of the fact that on some samples there is a single path that more or less goes from left to right across the image (see Fig. 4.2 (a) for example). This certainly doesn't hold true for all samples, but when it does hold true the LVC wirization is very effective. If the sample has a path that goes from top to bottom instead, the routine can be employed after simply rotating the image by 90° .

I note that none of our automatic wirization techniques can automatically detect if the currents are going from right to left. But if the operator thinks this is likely, then the LVC is a good choice. The routine allows the path to meander in y but does not allow the path to cross back on itself in x , *i.e.* no $-x$ segments are allowed. This allows the routine to construct the path column by column. The algorithm of the LVC wirization works as follows. For each column the routine places a $+x$ segment at the maximum of $|\partial B_z/\partial y|$, and then connects these segments together with $\pm y$ segments. This simple approach can

give a remarkably good initial path in situations where the true path starts on the left side of the image and finishes on the right but without doubling back on itself. The automatic infeed and outfeed routines can then be used to add or remove segments at the start and end. For paths that double back, if the individual sections are discernible, the technique can be applied by first splitting the scan into different areas where the current doesn't go back on itself. This can be done by using the crop2 region, as the path will only be wirized in the crop2 region if one is selected. Code for the LVC wirization is included in [Appendix A.2](#).

Of course, currents don't always flow from left to right. In fact, it is common for samples to have infeed and outfeed leads right next to each other and to form a big loop (see [Fig. 5.5 \(a\)](#) for example). To automatically wirize such samples, I exploited two proxies to try to follow the path. The first proxy makes use of the fact that directly above a long straight wire in the xy plane, the gradient $(\partial B_z/\partial x, \partial B_z/\partial y)$ will be at a maximum (see [5.5 \(b\)](#)). In fact, $\partial B_z/\partial x$ and $\partial B_z/\partial y$ has been used directly for an inverse [\[74\]](#), and I used this in the "derivatives" wirization. Another useful indicator of a long straight wire location in the x - y plane is that B_z is positive on one (lateral) side of the wire and negative on the other, and goes through zero directly over the wire. If the wire bends, or other wires are present the zero may not be exactly over the wire. Still, in simple cases the zero roughly tracks the wire. [Figure 5.5 \(c\)](#) shows $1/(\log(B))^2$, which is meant to emphasize data points very close to zero. As we can see, this tracks what we could easily imagine are the currents in the image, albeit with some rounding of the corners where the current changes direction. While it is not perfect, it often helps follow the path. Finally, the weighed average wirization weighs the derivatives and the logarithmic wirization to wirize the image.

The derivatives, logarithmic and weighed wirizations used almost the same algorithm

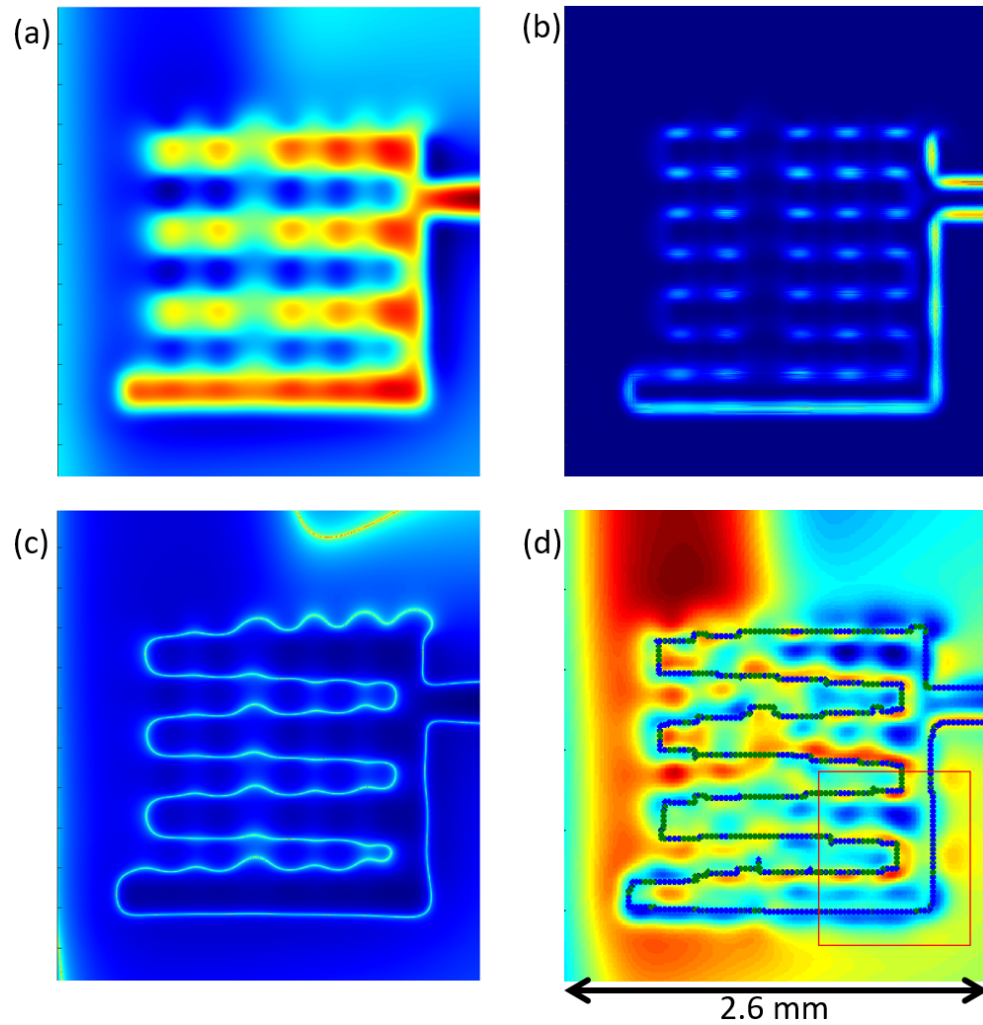


Fig. 5.5. (a) Scan of a CEA-LETI sample. This sample cannot be wirized using the LVC wirization. (b) $\partial^2 B_z / \partial x^2 + \partial^2 B_z / \partial y^2$ of the data. This is a good proxy for the currents in the image, however the lower layer segments are very weak in this image. (c) $1 / \log(B_z^2)$ of the data. This view emphasizes the areas of the scan where there is zero field, which we expect to be roughly above the currents in the image. (d) wirization using the “weighed methods” technique overlaid with the difference image. Some segments in the path have also been placed in the lower layer depending on the intensity of the field. The segment length has also been increased to $10 \mu\text{m}$ (from $2.5 \mu\text{m}$) which smoothes out the path.

to wirize the path, but with different filter functions.

(1) A starting point for the path was generated. I had the option to provide the starting point of the wirization manually by clicking on the image or automatically, by selecting the pixel with the highest value in the image.

(2) The value for the filter function was calculated for the four pixels adjacent the starting pixel. Whichever pixel had the highest value was the next vertex in the path.

(3) Step (2) was repeated until the path either reached the edge of the image or crossed itself, which is forbidden by our restrictions.

The filter function for the derivatives wirization is $F_d = \partial B_z/\partial x, \partial B_z/\partial y$. This wirization is especially useful because it carries a sign and therefore can follow the current in a particular direction. The logarithmic wirization has a filter function of $F_l = 1/(\log(B))^2$. One of the downsides of the logarithmic wirization is that it can tend to loop back onto itself, because it only looks at the magnitude of the signal and carries no information as to the direction of the currents. Finally, the weighed method used a filter function of $F_w = a_1 F_d + a_2 F_l$. a_1 and a_2 are adjustable but usually set around $a_1 = 1$ and $a_2 = 0.5$, which in practice has given the best results.

One of the difficulties for these algorithms is knowing where to start. Selecting the autostart option makes the wirization process start at the pixel with maximum $(\partial B_z/\partial x + \partial B_z/\partial y)^2$ the data. The idea is that the path surely goes through the point of greatest gradient in the field. From this point, the wirization continues all the way to the border of the image. This can often work well if the infeeds run off the image and the path can then be completed using the infeed/outfeed routines. In case where the current is fed in vertically in the middle of the image, infeed and outfeed routines can be used to

automatically delete extraneous segments that go too far outside the image. There is also an option for manually choosing where the routine starts the paths, instead of having the routine automatically select the starting point. In this case, the user deselects the “automatic start” option under the wire>wirization menu, and clicks on where they want to start in the image after selecting which wirization routine they want to run.

5.4.2 Drawing a path manually

Sometimes the wirization routines do not produce a good wirization. This may be the case when the signal is too weak or when multiple wires are preventing the wirization from creating a good starting path. If the initial path is clear and straightforward to the user, or the user has other information about where the current is in the sample, then a good option is for the user to draw in the path (thanks to Bill Vanderlin for suggesting this option).

Before drawing a path, the user needs to decide which interactive plot they want to draw on top of. A user can draw over any interactive plot, but I mostly draw over the raw data, an image of the derivatives, the optical image or Btest.

To start drawing on the interactive plot, click on the “add wire” button on the bottom left of the interactive plot (see Fig. 5.2). The algorithm then draws a straight line between two points where the user clicks, similar to drawing a line in Microsoft Paint or Photoshop. A modified version of the Bresenham algorithm [79] is used to convert that line into a rasterized, segmented version that lies on the grid. By right clicking, a user can also assign segments to the different layers. To draw a new wire path, I used the following procedure.

- (1) First, I clicked on the wirize button.

(2) I next left clicked on on a specific pixel in the interactive plot to set the starting wirization point.

(3) I then dragged the mouse. This causes the interactive plot to display a manhat-tanized preview path that hovers over the plot. It is important to keep in mind that the direction you choose to wirize from point A to point B determines the direction of the current. Right clicking clicking cycles through the possible layers that the wirized path will be placed on. When new paths are created, they have 2 layers by default. This can be changed in the wire parameter table on the left side of the main control window.

(4) I then left click again onto another pixel to set the first section of the path. I continued to left click on the image to draw sections of the path until done.

(5) To finalize the path, I click the middle mouse button over the pixel at the end of the desired path. After the path is drawn, the path parameters (such as the current or layer-to-layer spacings) can be adjusted. An example of a manual wirization can be seen in the additional materials video.

Once a wire exists, it can be manually modified at any point during the search process, or “redrawn.” Re-drawing paths works the same way as drawing paths. A user initiates re-drawing a path by clicking on the “redraw segments” button (instead of the “Add wire” button), and then clicks on the part of the path that is to be re-drawn. When the user is done redrawing, the previous version of that part of the path is deleted. The new segments that the user drew are inserted in the middle of the path, replacing the part that was cut out. At any point, wires that were drawn or wirized can be deleted individually via the main interface menu bar (under wires > rename/delete).

When performing a manual wirization, I typically just created a wire that mapped out

the top layer x - y lateral structure of path and used path search tools to move lower layer segments to the correct layers. It is important to emphasize here that you must have a trial path before any path search or parameter search can be done. Following wirization, you can use the “adjust optical image” tool to align your wirized path with the picture of your real sample. Although this has no impact on any of the automatic searches, it can be very useful in guiding path changes during manual redrawing, in guiding where to conduct a crop2 search, and in deciding if z -searches or lateral searches might be fruitful.

I note that when manually drawing a path, the routine does not allow the path to intersect itself. No vertex in the grid can be in the same wire path twice. Bad paths will give an error message and many of the functions will not work with bad paths. However, two separate wires may be drawn such that they intersect or overlap, and this can be useful in circuits with branching current paths as the branching point needs to be a part of each wire in the path.

Once a wire is created, the magnetic field it produces can be found using the “Recalculate field” button. This updates the simulated magnetic field (B_{fit}) to correspond to the wirized path. B_{fit} can be displayed by selecting B_{fit} in the list box in the interactive plot (see Fig. 5.2). The B_{test} plot, which is a plot of $B_{fit} - B_{data}$, is useful in deciding how to vary the path and match the original magnetic field data. In many cases the first wirization is good enough to allow a user to start searching for some of the parameters via the parameter search. Typically, I first try to pin down g , z and the field offset.

5.5 Using Wirization techniques

For a user who has just opened a .ac file for the first time, one of the first things to do is decide on how to wirize the sample. In particular, it is necessary to determine whether manual wirization or automatic wirization is the best approach to drawing an initial wire path. Looking at the different plots available on the interactive plot can help inform this decision. One can access automatic wirization techniques under the Tools tab, in the drop down menu click on “wirize LVC Alex” for a list of techniques.

For clean magnetic field scans (low noise and low saturation) where the structure is relatively discernible, an automatic wirization option is a good choice. There are a variety of wirization techniques that we use commonly, the two best general purpose techniques being weighed wirization and the LVC wirization. In many cases however, you may want to use manual wirization, which involves the wirize, redraw, and change layer push buttons. The automatic wirization algorithms I developed only draw the lateral shape of a path and place all the segments in the top layer. With manual wirization the user can assign layers as they draw the path.

Note that the wirization options all create a new wire for the path. This makes it easy to try several different wirization techniques and keep only the best result while deleting the other ones. To modify an existing path, I use the redraw option. The change layer tool modifies the existing path by moving individual segments to different layers. For preliminary manual wirization, I typically would draw a wire in the top layer that mapped out the x - y lateral structure of the path and use other tools to adjust which layer each segment is on, such as the z -search. After wirization it helps to adjust the optical image tool

to align your wirized path with the picture of your real sample if a picture was available.

After adding a path, one can use the “plot path” button on the main control panel (see Fig. 5.1) to create a 3D plot of the path. One can also display the fit field image by clicking on B_{fit} in the list of display images (see Fig. 5.2) and the recalculate button to view the magnetic field generated by the new path.

5.6 Parameter search

One of the main difficulties of the parameter search is that in order to obtain good parameters, one needs to perform the parameter search on a good path. But in order to obtain a good path from the path search, one needs good parameters. To obtain reasonable initial parameters, ideally one wants a starting path that includes as many known features and is as close to the true path as possible. Key path features include lateral structures, layer spacing, segment layer placement, infeed and outfeed wires, sample rotation and any other sample or sensor parameters that are already known. In practice, I have found that some key sample and scan parameters can often be obtained by working on just a small part of the image that is clear or well resolved. If a good trial path can be drawn in this region, the Crop2 tool can be used to run a parameter search on just this portion. This not only allowed me to accurately resolve key parameters but also made the parameter search considerably faster since the path was close to the true path and a smaller number of data points were fitted to. Even though these parameters were only resolved for part of the image, all the parameters, including the z , g and the sensor tilts are constant for the entire image.

To conduct a parameter search, one first inputs to the control panel the values for all

Table 5.1. Parameters that must be specified or found in the parameter search in order to obtain a simulated field image from a test path. There are 8 scan parameters, and each wire has a current parameter, a wire width, and layer-to-layer distances between each layer. Thus the total number of wire parameters will depend on the number of wires and the number of layers for each wire.

Scan parameters	Wire parameters
sensor to sample distance (z)	current (I)
gain (g)	wire width (w)
sample in-plane rotation	layer-to-layer spacing
sensor tilt (theta)	
sensor tilt (phi)	
lateral x offset	
lateral y offset	
data offset	

known parameters and best estimates or guesses for all the remaining parameters, *i.e.* the parameter search requires a starting value for every parameter. Table 5.1 shows all of the parameters that need to be determined. The actual number of parameters depends on the number of layers and the number of wires in the sample. It is important before beginning a parameter search to use all known information about the sample and sensor in order to quickly obtain reliable and accurate results from the search. For example, having accurate infeed and outfeed lines can be extremely important to obtain reasonable parameters.

For preliminary parameter searches I typically search z and g first because they are interrelated and can otherwise cause a parameter search to compensate one for the other. I found that parameter searches can be honed in little by little first starting with z and gain, then adding other parameters to the search. After running a parameter search, it is important to verify that the values you get are reasonable given what you expect from your sample. Having decent starting parameters helps the searches, but a rough starting path may lead the search to return unreasonable values. When this happened, I reset the parameters and worked some more on refining the path before running another parameter search. When using the 3D Solver, it was quite typical to alternate between running a parameter search and running path searches to refine segment layer assignments and to get more and more precise parameters.

I note that all parameter values can be entered manually by typing numerical values into designated boxes in the main control panel or interactive display panel. Also, sliders on the interactive panel (see Fig. 5.2) are used to perform manual rotational or linear transformations on the data as well as for thresholding. Slider changes are updated live on the interactive plot. (see the rotation, x -offset, y -offset sliders on Fig. 5.2), however to view

the effects of the changes on the B_{fit} and B_{test} plots, one must press the recalculate button.

Area averaging of the SQUID and spin-valve sensors are the only parameters that can't be searched on automatically, because I assume that the sensor sizes are well known. Of course, one can always conduct a manual search by entering in the values of a parameter by hand, recalculating, and noting whether the χ^2 has decreased.

One technique I used to speed up a search was to resample to a large segment length (w_x, w_y) which are set on the main control panel (see Fig. 5.1)). I found that this can save considerable computation time. The other advantage is that automatic wirization and cleanup searches will yield less corrugated paths. The use of excessively small segment lengths allows noise to overly influence the results of any cleanup or auto wirization routine. An image can also be resampled to larger pixel sizes to smooth out the signal and the noise. Since the noise has high spatial frequencies, resampling tends to work best with data that has been heavily over-sampled with respect to z , which sets the spatial scale of the signal.

To perform a parameter search, a user needs to take the following steps:

- (1) Adjust the sample and wire parameters to the best estimated or known values
- (2) Press the parameter search button, select the parameters that they want to search simultaneously, in one launch, and then click the launch parameter search button. Note that the search time increases exponentially with the number of parameters selected.

- (3) After the search, check that the parameters obtained are reasonable by looking at the B_{test} image (viewable by selecting B_{test} in the listbox to the left of the interactive display panel). One should also check how much the χ^2 has improved. Both the current and previous values of χ^2 are shown on the interactive control panel. Note that simultaneous parameter searches on more than one wire will generally take much longer given that all

permutations of wires and their parameters must be searched. After getting a preliminary top layer path and parameters, typically I would next run some cleanup searches or a z -search on the path. Another option is to use thresholding for a quick assignment on of lower layer segments (see Fig. 5.2). Sliders are used to perform rotational or linear transformations on the data as well as do thresholding; slider changes are updated live on the plot (See the rotation, x -offset, y -offset sliders in Fig. 5.2).

The parameter search currently uses the built in Matlab function `fminsearch` to minimize the χ^2 , which uses a simplex algorithm [80], as described in Section 4.6. This minimization technique relies heavily on initial input values and consequently the parameter space that is searched is localized. In some cases, the parameter search can get stuck in a local minimum, but it usually works well if the starting parameters are near enough to the true values. It is sometimes helpful to manually explore the parameter space and find reasonable starting values before using the automated parameter search.

5.7 Grid size

Typical images produced by the MAGMA system have a 1 μm by 1 μm pixel-to-pixel distance. However, other pixel sizes are common, for example if the user wants take a quick scan of a large area. Sometimes it is advantageous to resize the pixel-to-pixel distance in the x and y directions, w_x and w_y . Having less pixels can help make some calculations faster when the extra resolution isn't needed. On the other hand, w_x and w_y also set the minimum segment length, as the 3D Solver requires the x and y segment lengths to be a multiple of w_x and w_y respectively. The 3D Solver allows the pixel size in a data set to

be altered by interpolating from the measured image. To do this, I used a built-in Matlab interpolation function [76] that uses linear interpolation. These parameters are accessed in Fig. 5.1 (c). This is important because the pitch of a sample might be different from the image's pixel-to-pixel distance. For example, one might have a sample with a repeating sequence every 45 μm , but have an image with a resolution of 10 μm . In this case, one would want to resample at 5 μm or 11.25 μm so that the segments can be in sync with the sample *i.e.* so that the segment grid can match the sample.

5.8 Conclusions

In this chapter, I described how to use the 3D Solver, including its main tools and the type of output solution it produces. Needless to say, the 3D Solver is a complex piece of software to use and experience and understanding are needed to operate it. To get the most out of it, a user will need to be aware of how to access its different algorithms, how those algorithms work and when those algorithms should be applied. The 3D Solver is still “research” grade software. A few key tasks have been automated or greatly simplified and it is clear that many more tasks could be automated. The user interface should be significantly improved and then user-tested for commercial grade software.

Chapter 6: MAGMA System

6.1 Introduction

In this chapter I briefly describe the Neocera MAGMA system which we used to acquire magnetic scans. I first give an overview of the different parts of the system. I then describe the SQUID sensor (the spin-valve sensor is covered in detail in [Chapter 7](#)), the cryogenic system, the vacuum components, and the scanning stages. Finally, I discuss the software controls, and conclude.

6.2 Overview of the system

Neocera's magnetic imaging scanning microscope [81,82] uses two different magnetic sensors as well as an optical/infrared camera. One magnetic sensor is a SQUID that provides high sensitivity to magnetic fields and allows us to image very weak currents (in the nA range) or currents deeply buried in a sample. The second magnetic sensor is a spin-valve sensor that allows surface layers to be imaged with better spatial resolution than the SQUID, although its magnetic field sensitivity is about 2 to 3 orders of magnitude worse than the SQUID's.

Figure 6.1 shows a photograph of the Neocera MAGMA Magnetic Field Scanning

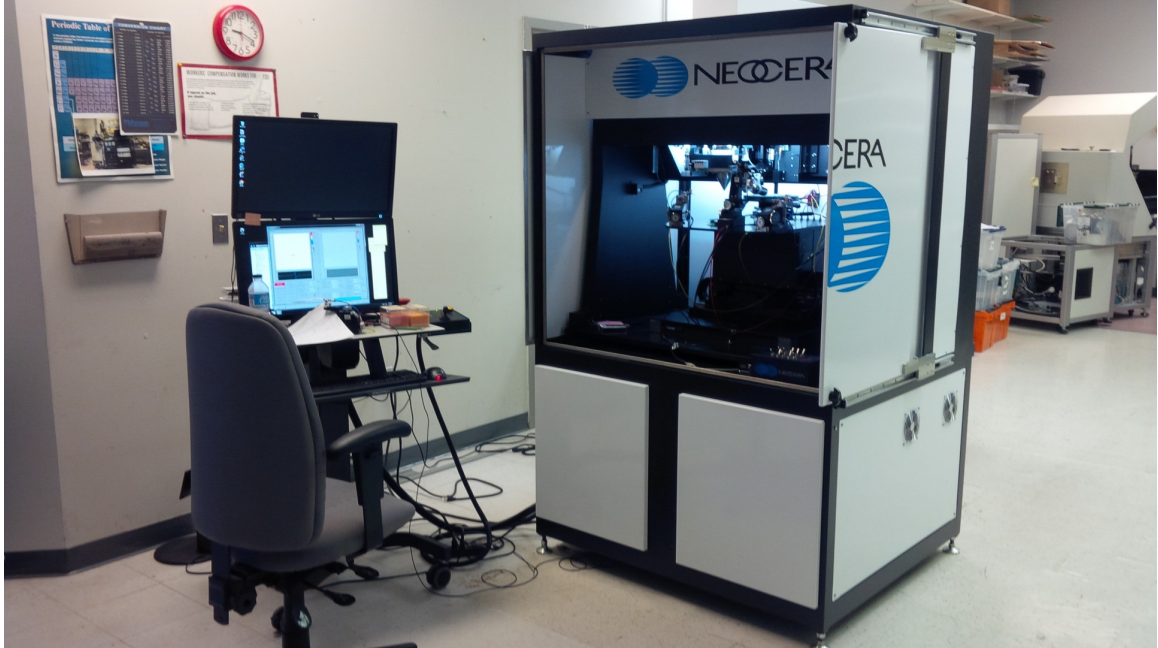


Fig. 6.1. Neocera MAGMA Magnetic Field Scanning System. To the left is the control computer and software. The scanning apparatus is enclosed in a cabinet to the right.

System that was developed for the 3D imaging project. On the left is a computer workstation that controls the system and on the right is a metal cabinet. The upper half of the cabinet houses the scanning tables, the sensors, and the cryogenic and vacuum parts of the apparatus. The base of the cabinet houses various pumps and other auxiliary equipment. During scanning the upper metal cabinet is usually closed to reduce rf interference from external sources and thermal drift due to heat and changes in air currents, as well as interference from bright light shining on the sample or on the parts of the system that can lead to thermal expansion and position drifts that are easily visible in a scan.

Figure 6.2 shows the xyz scanning stages and the sensors in more detail. The SQUID is mounted at the end of a sapphire rod that is enclosed in an aluminum cone-shaped vacuum chamber. The end of the cone is sealed with a 10 μm thick diamond window that separates

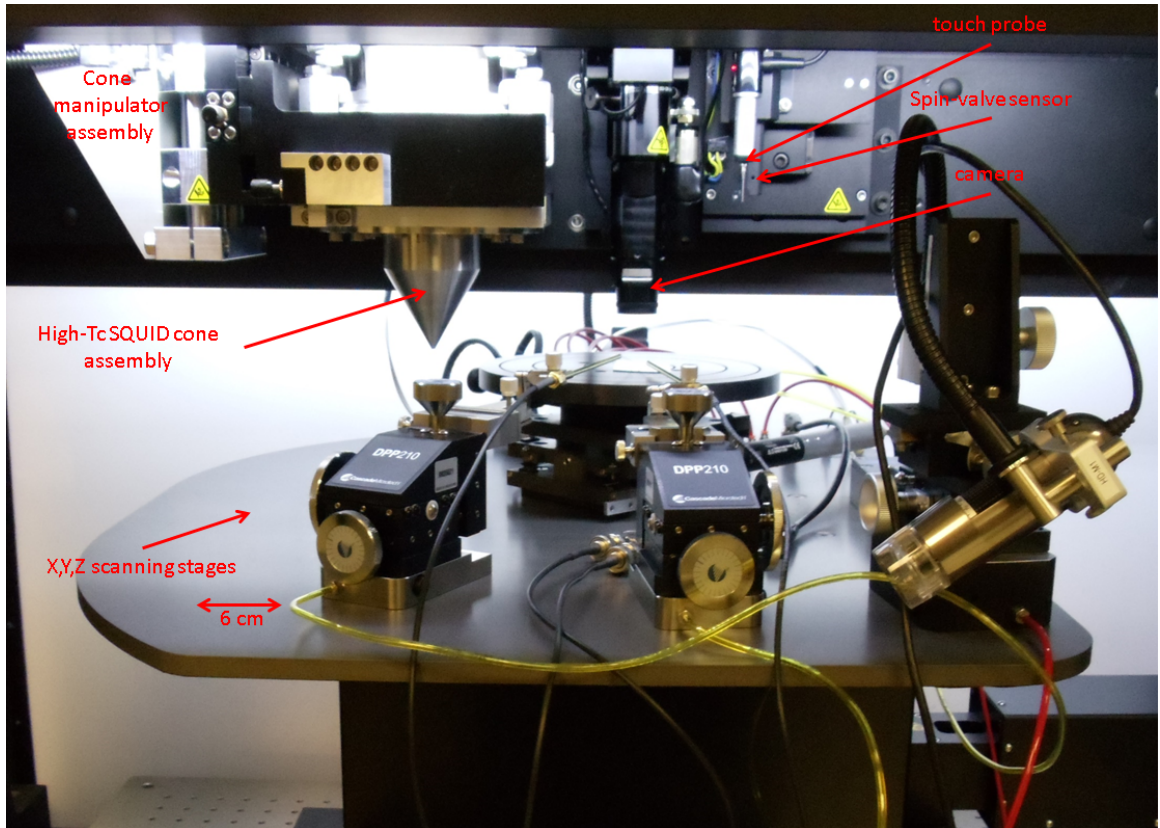


Fig. 6.2. Close up of the MAGMA system xyz scanning stages, sensors and sample staging area.

room temperature and air from the cryogenic vacuum environment. The SQUID itself is fixed relative to the system. However, the aluminum cone moves with respect to the SQUID. When the system is not scanning, the cone lowers so that the SQUID is kept far from the tip of the cone. When the SQUID sensor is scanning, the cone is raised by the cone manipulator assembly to bring the SQUID very close to the diamond window, so that it can be close to the sample which is on the other side of the window. The rod is cooled to about 77K. In Fig. 6.2, the SQUID cone is on the left above the sample stage. The camera, touch probe and spin-valve sensor are to the right of the SQUID cone. In Fig. 6.2 the sample is mounted on a sample holder, which is itself on the xyz motion stages. The scanning stages move the sample under a given sensor for imaging. The touch probe and spin-valve sensor can be retracted when not in use. That is, only one sensor (SQUID, spin-valve sensor or infrared/optical camera) can be used at a time. The xyz stage position is calibrated to within a few μm so that the same area can be imaged by different sensors. Also visible on Fig. 6.2 are probes that are used to connect power to the sample during scanning.

The xyz stages are quite large to allow correspondingly large ($\approx 12''$), wafer-sized samples to be scanned. The x stage has a large range, about 45 cm, to allow a sample to be moved under the different sensors. The stages are quite precise, with a position noise of about $\sigma_x \approx 200 \text{ nm}$ [83]. The position of the sensors (infrared camera, spin valve, squid, and touch probe) is calibrated so that the stages can bring a sample from under one sensor to the next, and the same area can be imaged by multiple sensors.

The MAGMA system uses a commercial Stirling cycle cryocooler to cool the sapphire SQUID tip to about 77 K. The system is relatively compact and low maintenance compared to Joule-Thompson based cryo-coolers used in the first MAGMA system [84].

During scanning, it is important that the the sample surface be parallel to the scanning plane. Otherwise, the SQUID will vary in height above the sample during the scan. More importantly, if the tilt is too extreme, the SQUID window will crash into the sample and potentially break. Before starting to scan a new sample, the touch probe is used to touch the sample surface in three areas to measure how level the sample is. If the sample is not level, the MAGMA software automatically calculates how the stage needs to be adjusted and the stages are then manually adjusted using three levelling screws on the sample mount.

During a scan, the x stage is continuously moving as the sensor is taking data. After each x -line of data is taken, the sample is moved away from the sensor (the separation z is increased), while the sample is repositioned in x and y for the start of the next line. If there is a need for tilt correction, the z stage also slowly moves during the scan to keep the sensor at the same height above the sample.

As the magnetic sensor scans over the sample in the x direction, a hardware or software lock-in amplifier continuously measures the in-phase and out-of-phase voltage from the sensor. The lockin's output is continuously recorded as a function of the sample's position, yielding the magnetic field image which can then be displayed using the MAGMA software or 3D Solver. The dc output from our sensor is also recorded. Although it does not typically contain signals from current paths, it is sensitive to magnetized regions in the sample and environmental disturbances, so it is useful as a diagnostic signal when problems are encountered.

Figure 6.3 shows a control panel for the MAGMA system software. This panel allows the user to apply the standard inverse described in Chapter 2 to a scan taken with the MAGMA system. In Figure 6.3, the magnetic scan is loaded in the top right of the image

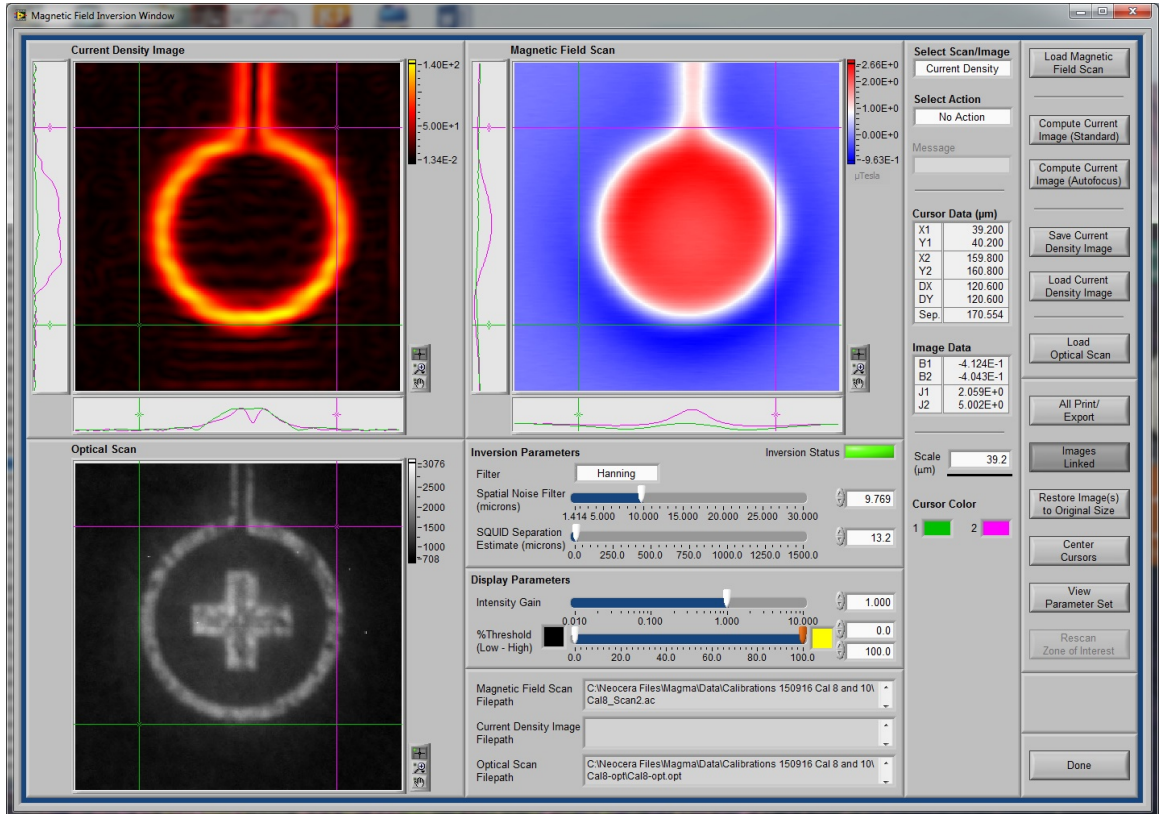


Fig. 6.3. MAGMA software control panel showing the Magnetic field inversion interface.

In this window, the magnetic data is loaded into the top right image. The results from the standard inverse are shown in the top left, and the MAGMA optical image is shown in the bottom left.

and displayed as a red/blue false color image. The optical image of the same area taken by the MAGMA system is displayed in the bottom left. The results of the standard inverse is displayed in the top left, which displays the square of the current density, $J^2 = J_x^2 + J_y^2$ as a false color image. The scan displayed in Fig. 6.3 contains no J_z currents and we can see that the MAGMA software does a good job reconstructing the currents and that those match the metallization which can be seen in the optical image. To the bottom right are the controls for the inverse process. Users of the software have several parameters they can fine-tune to obtain a better current reconstruction. The most important are the sensor-to-sample separation and the spatial noise filter (*i.e.* the k-space cutoff k_w). Users can also choose which type of k-space cutoff to apply. As we can see, this software is much simpler to use and much more polished than the 3D Solver software (compare to Figs. 5.1 and 5.2). Finally, more analysis tools are accessible by pressing the buttons on the right edge of the window.

6.3 SQUID sensor

The dc SQUID used in the MAGMA system is made from $\text{YBa}_2\text{Cu}_3\text{O}_{7-x}$ on a SrTiO_3 bi-crystal substrate [85]. The device has a square-washer shape with an inside diameter of about 20 μm , an outside diameter of about 40 μm and an effective area of about $(30 \mu\text{m})^2$ (see Fig. 6.7). It is mounted on the end of a tapered sapphire rod (the SQUID tip) [84] which in turn is attached to the cold stage of the Stirling cycle refrigerator. While in operation at 77K, the SQUID is maintained in a flux-locked loop [86] with a roughly 20 kHz bandwidth and the feedback flux is coupled to the SQUID via an on-chip line which is patterned next

to the SQUID (see Fig. 6.7). The SQUID chip is polished to less than 1 mm in diameter to allow it to be brought close to a 10 μm thick diamond window which separates air from vacuum at the end of the cone-shaped vacuum enclosure. An xyz window control assembly (see Fig. 6.2) is used to center the SQUID chip in the window and bring the window up to the SQUID – it can be as close as a few μm from the inner surface of the window without causing the SQUID to warm up.

The optimal SQUID sensor size is dependent on the distance between the sensor and samples. If too small of a SQUID sensor is used, the signal-to-noise ratio will be relatively low. However, if the SQUID area is too large, the image will be smeared out spatially and the resolution will be limited by the sensor size. Neither of these extremes is desirable, and this suggests there is an optimal choice for the sensor area. Thus, if the sample can be brought closer to the sensor, we would do better by using a smaller SQUID. Our analysis of this situation shows that for our current scanning distances of 40-200 μm , the optimal sensor diameter is $b = 0.89z$. The devices currently used by the MAGMA system have an effective diameter of about $b = 30 \mu\text{m}$. This was judged to be close enough to the optimal value that there was little to be gained by using devices with the optimum diameter, especially since small differences from the optimum lead to very small (second order) improvements. In addition, we wanted to achieve even closer separations z between the sensor and the sample. A SQUID with size $b = 30 \mu\text{m}$ should be optimal at $z = 34 \mu\text{m}$, which may well be achievable with the current setup.

As I discussed [Chapter 3](#), getting the SQUID close to the sample is critical to getting good spatial resolution. [Figure 6.4](#) gives some idea of just how close the SQUID window gets to the sample while scanning. In a series of tests, Neocera has demonstrated that the

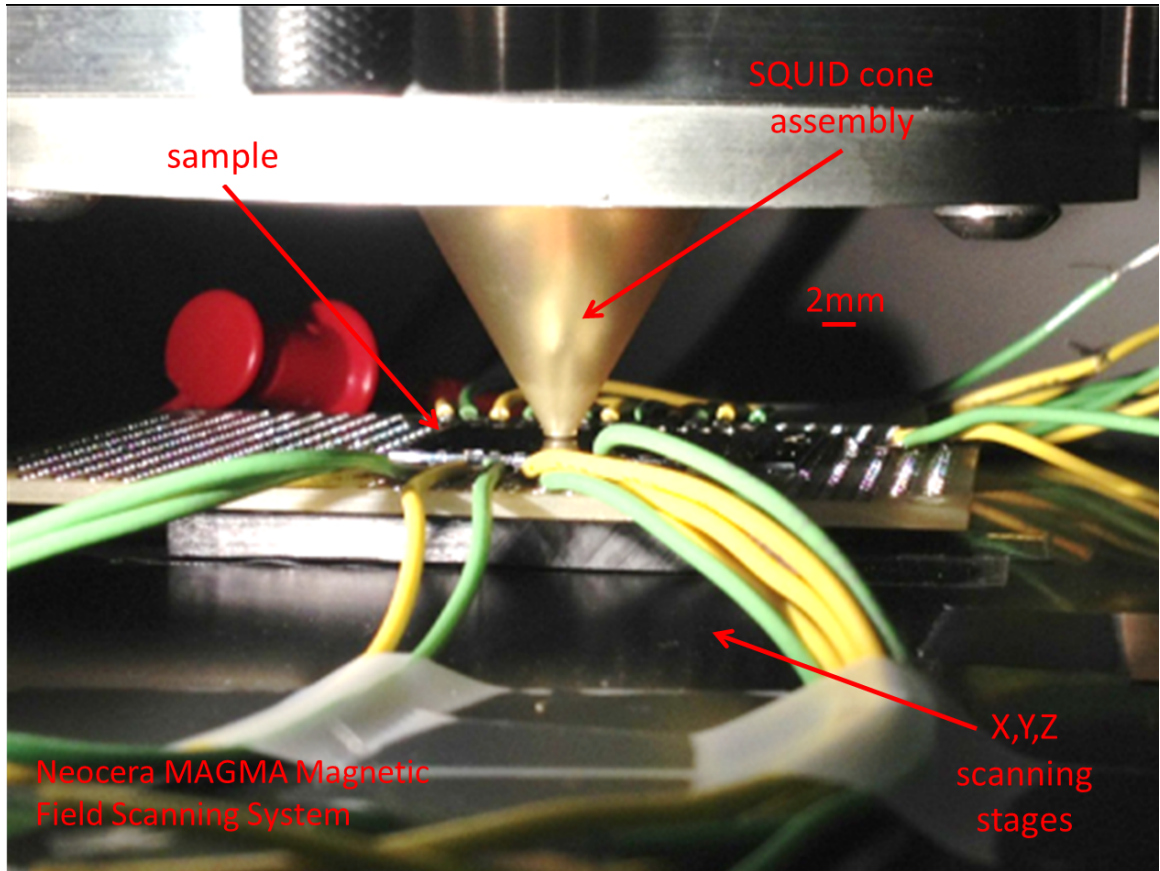


Fig. 6.4. Close up of the SQUID cone while imaging a sample.

SQUID can be brought as close as about $45\ \mu\text{m}$ to the surface of a sample. This is quite challenging, as the surface of the diamond window is about 2 mm in diameter (see Fig. 6.4). This means that window and sample surfaces must be extremely level. Also, the diamond window is $10\ \mu\text{m}$ thick, and space must be left between the SQUID and the window, and between the window and the sample. In order to achieve such tight tolerances, Neocera has developed an automatic levelling system. A touch probe is used to determine the location of the sample surface and the window. Three levelling screws are connected to motors that then level the surface of the diamond window with respect to the sample surface to guarantee it is parallel to the sample.

Averaging time is an important consideration for both the SQUID and spin-valve sensors. The settings are adjustable in the control software and the data is recorded at fine time intervals to allow for post-processing. Most of the scans I examined are taken with an averaging time between 5 ms and 20 ms. The x scanning stage is continuously moving during the scan, while the y scanning stage only moves as the sensor is coming back to the beginning of the next line. Typically, an ac current at a frequency of a few kHz is applied to the input/output leads of a sample. The software lockin is then used to extract the in-phase and out-of-phase signal from the ac magnetic field at the frequency of the applied current. The software lockin allows us to adjust the lockin frequency and roll off frequency or time constant to avoid aliasing effects. Suppose that the sensor is moving at 3 mm/s, and the averaging window is set at 20 ms. This means that each data point would be averaged over the field in a $60\ \mu\text{m}$ long section. Since the SQUID has an effective diameter of $30\ \mu\text{m}$, this section is actually $90\ \mu\text{m}$ long end-to-end. The choice of window is important because the accuracy with which we can determine the vertical position of currents in the sample can

be improved by decreasing the noise in the measured magnetic field. On the other hand, averaging of the magnetic field over the area degrades the spatial resolution and limits our ability to determine the depth of a current segment.

6.4 Comb contact pads

During the 3D Solver project we realized that the SQUIDs we were using produced images with small artifacts, or distortion. To get a clear picture of what was happening, we acquired images of the field produced by a long straight wire. We found that even these simple straight wire images revealed a small systematic discrepancy between the magnetic images and the expected image of a wire. The discrepancies were small (on the order of 1%) but systematic and much larger than the SQUID noise. This was an issue because unaccounted for distortion in the image can cause problems when using the 3D Solver to find the true path and the sample parameters.

Figure 6.5 (a) shows a line cut from a scan of a single straight wire taken using the MAGMA system. At first glance this line cut looks exactly like one would expect. For comparison, Fig. 6.5 (b) shows a line cut from the best fit path at that location, which looks like a very close match. However, Fig. 6.5 (c) shows that the difference between the data and the fit has unexpected features that do not look like random noise. We initially thought that these discrepancies might have been caused by averaging over the SQUID area, or by the wire width, or by changes in z due to a tilted scanning plane, or possibly an unknown problem with the lockin. However, we noticed that the anomaly was roughly 200 μm away from the center of the signal on each side, and realized that this was the same as the distance

between the SQUID and the contact pads. The superconducting contact pads did in fact turn out to be the cause of the problem. The pads were superconducting and, due to the Meissner effect, caused a perturbation of the magnetic field that the SQUID picked up. Figure 6.5 (d) shows the difference between the data and a fit that used this single model to account for the perturbation caused by the contact pads. We see that the discrepancies have been significantly lowered, suggesting that this is the cause. Finally, after also taking into account the SQUID area and the wire width, we see that the discrepancy was further lowered to the level of the noise, as shown in Fig. 6.5 (e).

The underlying cause for this problem is that magnetic fields are prevented from penetrating the pads due to currents that flow around the perimeter of the pads (see Fig. 6.6). Since the pads are made of superconducting YBCO, they are subject to the Meissner effect. These currents create a field that is picked up by the SQUID and this effect can be modelled by assuming that each pad adds a magnetic signal to the SQUID that is proportional to the field at the pad; it is as if there were a small pickup loop at each pad. To reduce the distortion, we designed a SQUID chip with “comb-shaped” contact pads (see Fig. 6.6 (b)). Each tooth has a width of 5 μm and a length of 180 μm . The space between the teeth in the combs allows magnetic fields to thread through, greatly reducing the edge currents in the pads. The perturbation detected by the SQUID is also reduced because opposing edge currents are closer together (separated by the width of a tooth), producing less field far away. Additionally, comb pads should tend to trap fewer magnetic vortices in the superconducting films that form the pads. This is important because trapped magnetic vortices can move around and cause magnetic noise in the SQUID, reducing its sensitivity. Even if a vortex is nevertheless trapped in the YBCO film, the narrow lines in the comb will

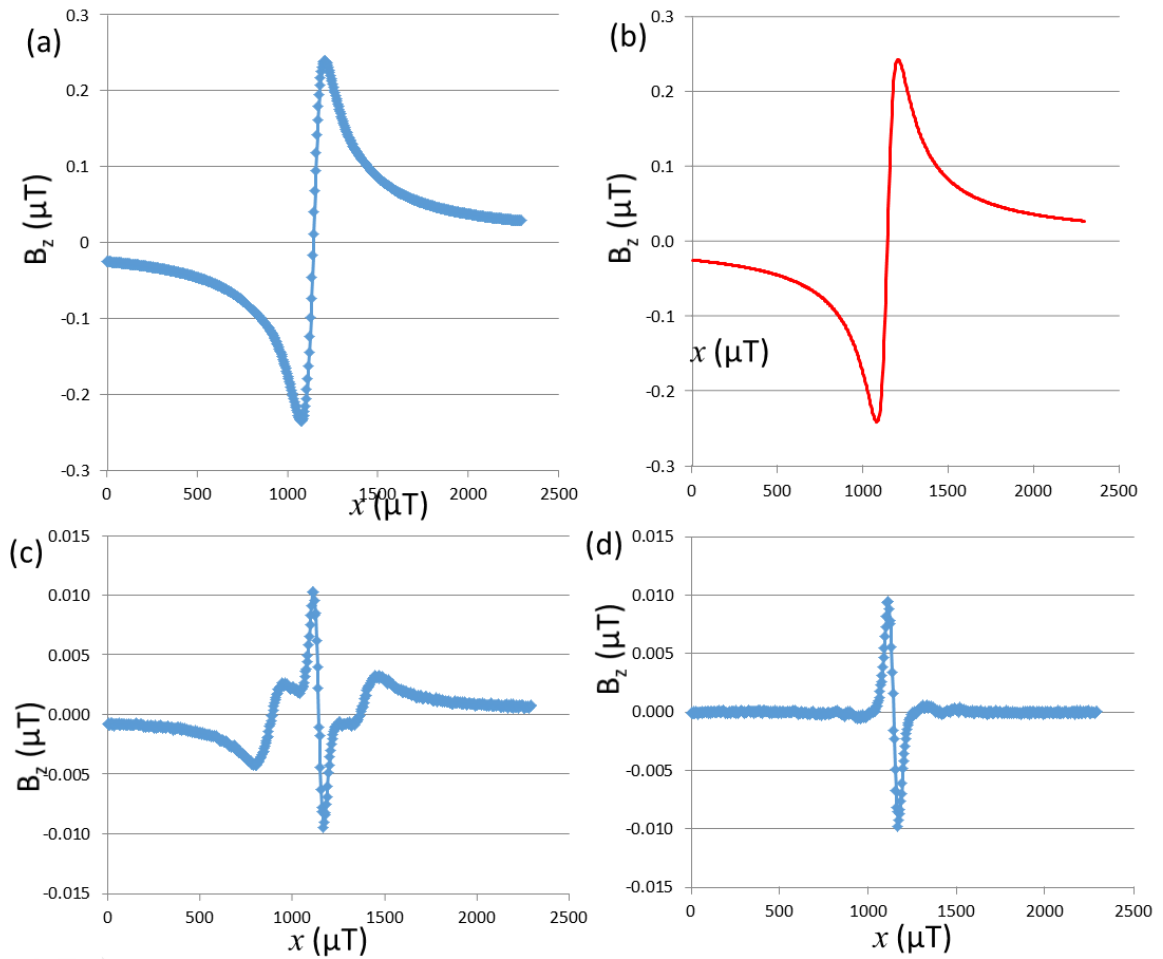


Fig. 6.5. (a) Measured magnetic field component B_z as a function of x taken using a high- T_c SQUID with conventional contact pads. Line cut from a scan of a single straight current carrying-wire looks as expected. (b) Magnetic field line cut showing field from best fit path with $z \approx 180 \mu\text{m}$. (c) Difference between the data (a) and the fit (b) reveals systematic artifacts in the image; *i.e.* the difference is not random noise. (d) Difference after accounting for the field perturbation due to the contact pads. Large anomalies about $200 \mu\text{m}$ away from wire are removed.

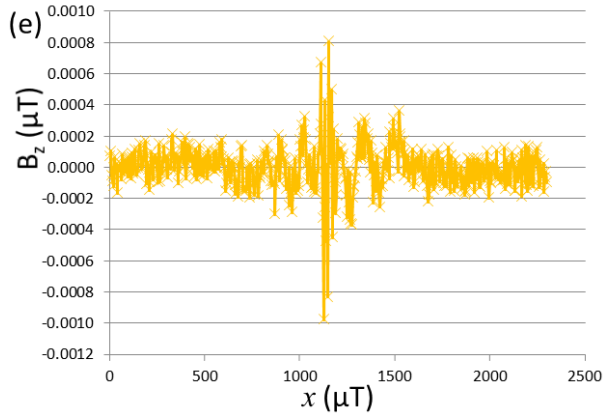


Fig. 6.5. (e) Difference after SQUID sensor size and wire width are also taken into account.

This last fit is at the level of the noise.

lead to less coupling of magnetic flux from the vortex into the SQUID. Finally, by exposing more ab-faces of the YBCO film the comb pads may reduce the contact resistance between the YBCO and Au metal pads.

Figure 6.6 shows the standard pad design side by side with the comb pad design. Figure 6.7 shows a completed SQUID chip with the comb pad design. For this chip, we also made a small change in the layout of the SQUID to reduce the width of the line used to define the SQUID body along one dimension to reduce field perturbation from the SQUID body itself. In figure 6.7 the pads are covered with a thin Au contact layer and the pad on the left has been partly broken during dicing.

To test the SQUID sensors with comb-shaped pads, we installed a device in a MAGMA test system. Analysis of noise in the images showed a level of about 165 pT. This was about 20% lower than the nominal SQUID noise level of 200 pT, but well within the typical range of noise seen in our SQUIDS.

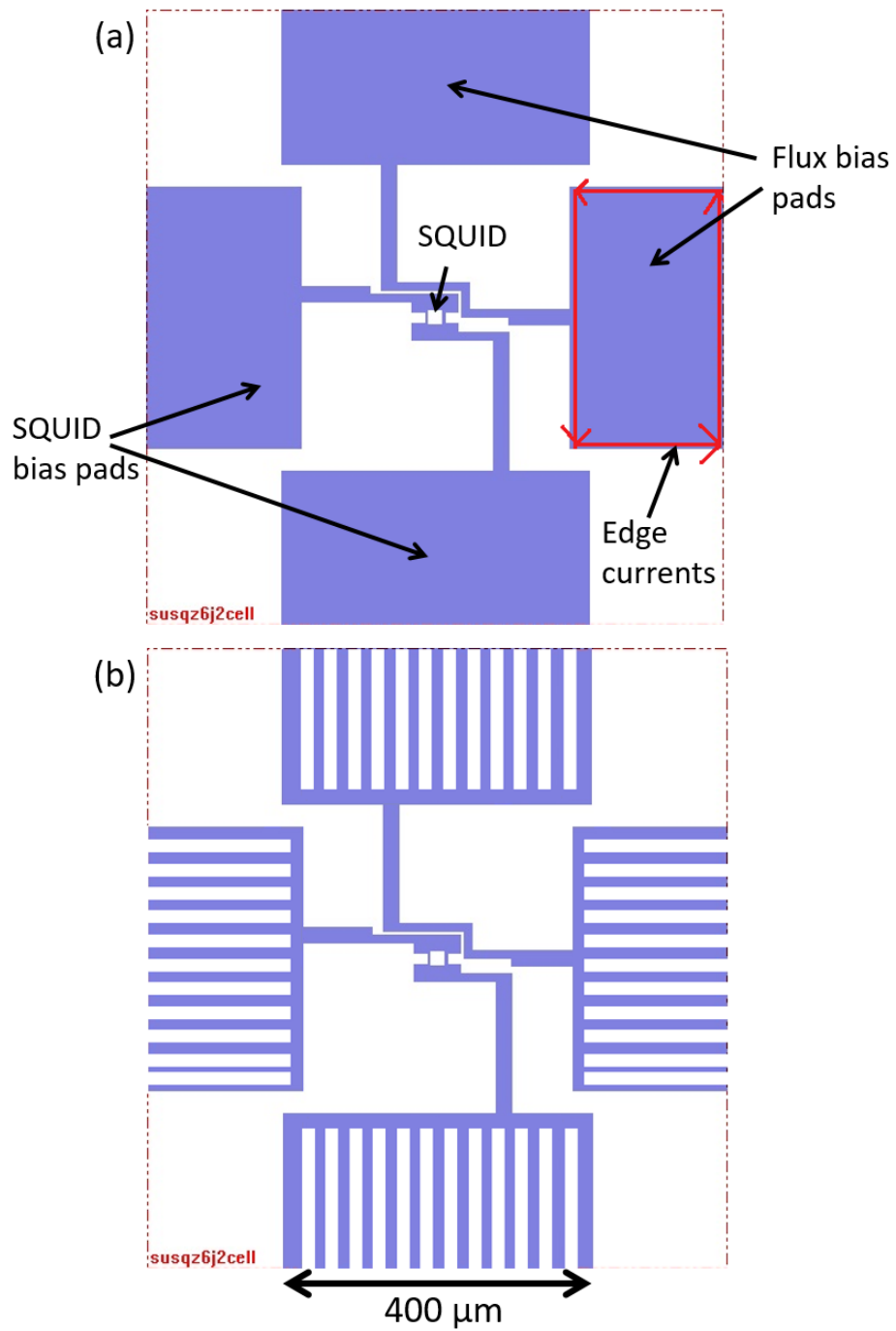


Fig. 6.6. (a) Conventional pad design for the high- T_c SQUID sensor. Blue regions are YBCO. Typical edge currents are shown in the right pad (red). The pads are 400 μm by 200 μm . (b) New pad design, which reduces pad area and edge currents.

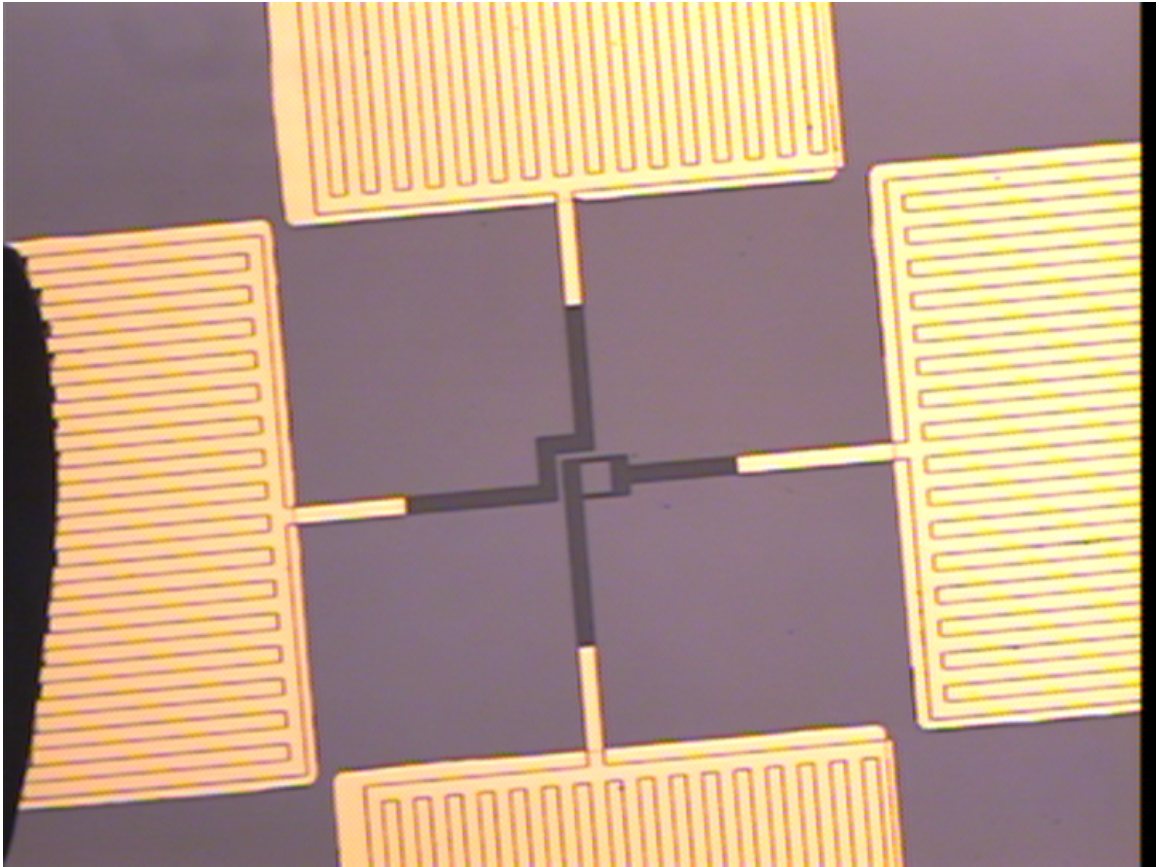


Fig. 6.7. Photograph of YBCO SQUID. The SQUID loop is the small black rectangle in the middle of the image and its center hole is about $30\ \mu\text{m}$ on a side. It is connected to two large contact pads which supply bias current to the SQUID and measure its voltage. The other two pads are connected to the flux feedback coil.

6.5 Magnetometer or gradiometer?

The Neocera MAGMA systems have exclusively used z -axis magnetic field sensors for the SQUIDs, meaning that the SQUID only measures the field perpendicular to the scanning plane. A natural question to consider is whether there is any advantage to measuring the magnetic field in the x or y directions [87] instead of the z direction. To answer this question we used simulations to evaluate depth capability obtainable from an x -SQUID (which measures B_x) and a 3-component xyz -SQUID. We also considered changing the orientation of the spin-valve sensor to measure B_x or B_y instead of B_z . Our simulations and analysis showed that there was no improvement in spatial resolution by having sensors measure different components of the magnetic field. The only improvement was from the relatively larger S/N due to using more sensors. It is possible that measuring B_x and B_y would reduce the computational complexity of the inverse, but more research is needed to show that this would be the case.

We also used simulations to evaluate whether a magnetic gradiometer [88] could be used to improve the spatial resolution of the path search technique. The key to improving the spatial resolution is to improve the signal-to-noise ratio (S/N) (see Chapter 3) since this is what determines the smallest grid size that can be used. Although using a properly designed gradiometer would have little effect on the intrinsic sensor noise, it might reduce the impact of position noise since the field difference would be taken at a fixed distance determined by the gradiometer layout. Since position noise in our system was the dominant noise in many real imaging situations [35], reducing the effect of position noise could potentially lead to substantial improvements in the performance we could achieve in practice.

To understand the S/N for a gradiometer, we consider a situation where position noise dominates the magnetic noise from the sensor. That is, the total effective rms magnetic noise σ_B in each pixel

$$\sigma_B = \sqrt{\left| \frac{\partial B}{\partial x} \right|^2 \sigma_x^2 + \left| \frac{\partial B}{\partial y} \right|^2 \sigma_y^2 + \sigma_{B_0}^2} \quad (6.1)$$

where σ_{B_0} is the intrinsic SQUID noise and σ_x and σ_y are the rms uncertainty in the position at which data B_z was acquired for the pixel due to positioning errors in the xy stages. For an N pixel magnetic image of a long straight wire along the x -axis we can write the signal-to-noise ratio as:

$$\left(\frac{S}{N} \right)_B = \sum_{i=1}^N \frac{B_i^2}{\sigma_{B_0}^2 + \left| \frac{\partial B}{\partial x} \right|^2 \sigma_x^2 + \left| \frac{\partial B}{\partial y} \right|^2 \sigma_y^2} \quad (6.2)$$

where B_i is the magnetic field acquired at location x_i . Since position noise is dominant ($\sigma_{B_0} \ll \sigma_B$), and we are imaging a long wire at a distance z , we can approximate this expression by:

$$\left(\frac{S}{N} \right)_B \approx \sum_{i=1}^{N'} \frac{B_i^2}{\left| \frac{\partial B}{\partial y} \right|_i^2 \sigma_y^2} \approx \sum_{i=1}^{N'} \frac{B_i^2}{\left| \frac{B_i}{z} \right|_i^2 \sigma_y^2} \approx \sum_{i=1}^{N'} \frac{B_i^2 z^2}{B_i^2 \sigma_y^2} \approx N' \frac{z^2}{\sigma_y^2} \quad (6.3)$$

where N' is the number of pixels in the region where the signal from the wire is significant.

We now compare this to the signal-to-noise ratio from measuring the gradient of the magnetic field. Again, we consider an N pixel image with position noise of a long straight wire along the x -axis. In this case we construct the gradient signal by taking difference in the field between two locations with a well-defined separation. Although the average location of the two measurements will vary because of positioning of the sensor and position noise, we assume that the separation between the two locations always has a precisely defined difference and for simplicity we will assume that this is the grid spacing

w . This corresponds to building two sensors which are rigidly separated by a distance w and then scanning this over a sample. We will suppose that the first sensor reports field B_{i1} at locations x_i and the second reports field B_{i2} at locations $x_i + w$, *i.e.* one grid spacing away from where B_{i1} was measured. We can now write the signal-to-noise ratio for a gradiometer that is dominated by position noise as:

$$\left(\frac{S}{N}\right)_{gradiometer} \approx \sum_{i=1}^N \frac{(B_{i2} - B_{i1})^2}{2\sigma_B^2 + \left|\frac{\partial(B_2-B_1)}{\partial x}\right|_i^2 \sigma_x^2 + \left|\frac{\partial(B_2-B_1)}{\partial y}\right|_i^2 \sigma_y^2} \quad (6.4)$$

Again assuming that position noise dominates sensor noise, and using the fact that we are imaging a long straight wire on the x-axis, we can write:

$$\left(\frac{S}{N}\right)_{gradiometer} \approx \sum_{i=1}^{N'} \frac{(B_{2i} - B_{1i})}{\left|\frac{\partial(B_2-B_1)}{\partial y}\right|_i^2 \sigma_y^2} \approx \sum_{i=1}^{N'} \frac{\left|\frac{\partial B}{\partial y} w\right|_i^2}{\left|\frac{\partial \frac{\partial B}{\partial y} w}{\partial y}\right|_i^2 \sigma_y^2} \approx \sum_{i=1}^{N'} \frac{\frac{B_i^2}{z^2} w^2}{\left|\frac{\partial^2 B}{\partial y^2} w\right|_i^2 \sigma_y^2} \approx N' \frac{z^2}{4\sigma_y^2} \quad (6.5)$$

Comparing the S/N of a gradiometer (Eq. (6.5)) to the S/N ratio for the standard case of magnetic imaging with position noise (see Eq. (6.3)), we see that the S/N ratio of the gradiometer is decreased by a factor of 4. This happens because the derivatives of B are even more sensitive to small positioning errors than the B field is. Thus, even though there is no error in the separation between the two sensors the average location of the two sensors leads to an effective position noise term in the gradient that is even more detrimental than for the magnetic field. Based on these considerations, we determined that the use of a gradiometer configuration does not allow us to reduce the impact of position noise.

6.6 Conclusions

In Chapter 6, I provided an overview of the MAGMA system, including the SQUID, the cryogenic system, the software lock-in, and the MAGMA scanning software.

Chapter 7: Spin-Valve Sensor Fabrication and Characterization

7.1 Introduction

The MAGMA system has two magnetic imaging sensors, a SQUID and a thin-film spin-valve sensor (SV) [45, 89, 90]. In this chapter I examine the fabrication and characterization of the spin-valve sensor. I first go over the basic physics of the spin-valve sensor and then discuss sensor fabrication. I next discuss the sensor's sensitivity and noise performance, and follow with a discussion of the trade-offs between spin-valve sensors and SQUIDs. I then discuss how the sensor is physically fastened to the system via a cantilever, and finally conclude.

7.2 Theory

The spin-valve sensor is a thin-film device that is built from several layers [91]. The three critical layers are the pinned layer, the conducting layer, and the free layer, as shown in Fig. 7.1 (b). Most of the current flows through the 2 nm thick Cu conductive layer. For zero applied magnetic field, the magnetic polarization of the CoFe pinned layer and the free layer (CoFe/NiFe bilayer) are orthogonal; the magnetization of the pinned layer is fixed by the pinning layer in the vertical $+z$ direction while the magnetization of the free

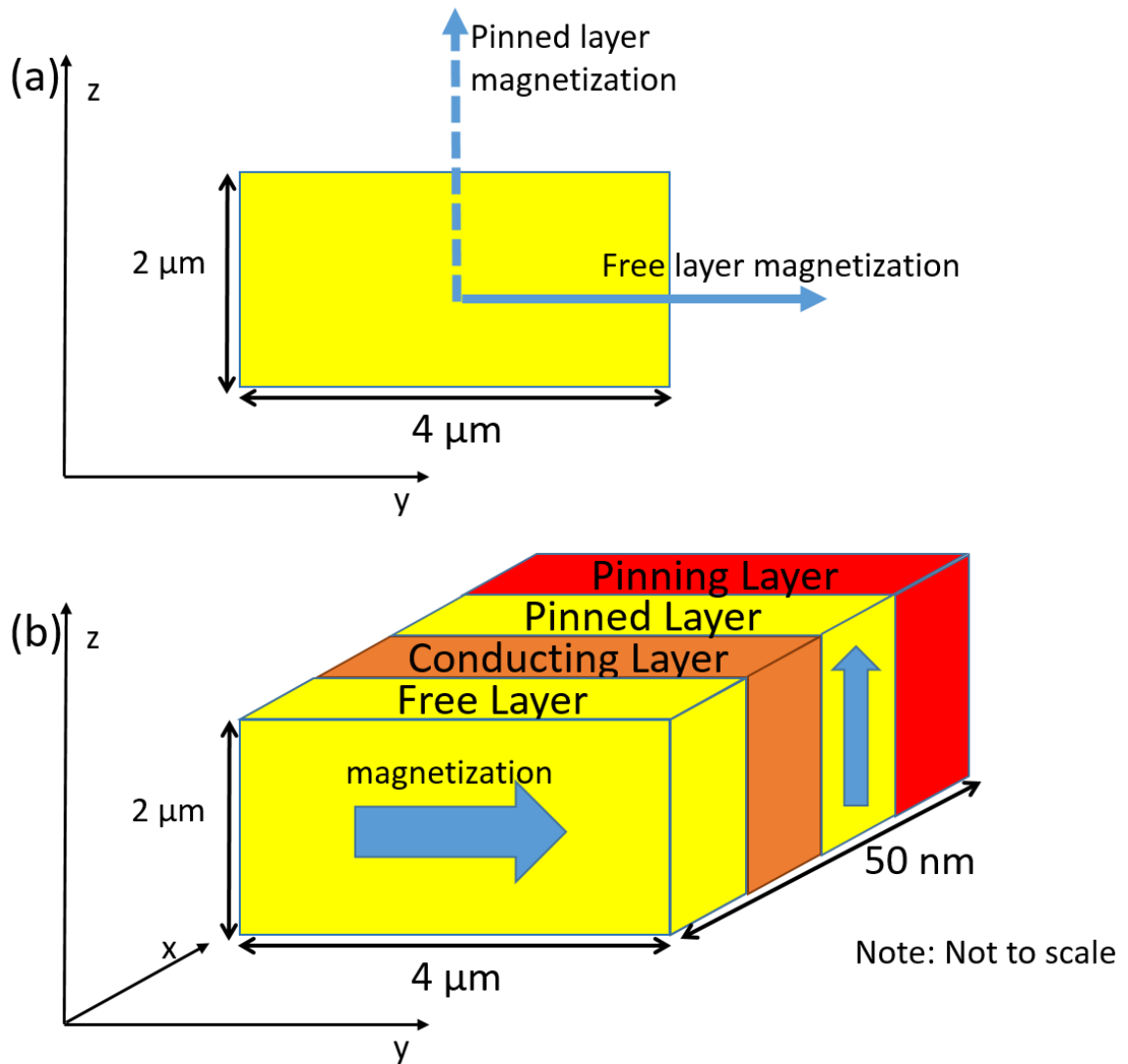


Fig. 7.1. (a) The resistance of the spin-valve sensor is determined by the orientation of the pinned layer and free layer magnetization. By design, when no external field is applied the two layers are magnetized perpendicular to each other. (b) Schematic showing the key layers in the spin-valve sensor. The current passes through the conducting layer, which is sandwiched between the free layer and the pinned layer. The sheet resistance of the conducting layer changes according to the direction of the free layer magnetization due to spin-dependent scattering.

layer is oriented along the y axis (see Fig. 7.1 (a)). If an external magnetic field is applied in the direction parallel to the pinned layer, the free layer magnetization rotates. As the magnetization of the free layer changes, the resistance of the Cu conducting layer changes due to spin-dependent scattering of electrons off of the free and pinned layers [92]. When the free layer and pinned layer magnetization are pointing in the same direction, the sensor is at its least resistive. When the free layer and pinned layer are pointing in opposite directions, the sensor is at its most resistive due to spin-flip scattering off of the interface. Thus by measuring the resistance of the sensor, one detects the strength of the applied magnetic field along the direction of the pinned layer magnetization.

Figure 7.2 shows a magnetoresistance curve of a spin-valve sensor that is $70\ \mu\text{m}$ long and $10\ \mu\text{m}$ wide. I built this device at INESC [93] using the same process, tools and materials typically used for the smaller Neocera spin-valve sensors, but this device was much larger than the $4\ \mu\text{m}$ by $2\ \mu\text{m}$ sensors used in the MAGMA system. The red curve shows the resistance versus the applied magnetic field that I measured for this device. From this curve, we can see that the sensor has a very linear response from $-10\ \text{G}$ to about $+20\ \text{G}$. The blue dotted line is a fit to this linear region which shows a sensor response of $1.5\ \Omega/\text{G}$. Above $\pm 50\ \text{G}$, the sensor has fully saturated. The magnetic layers are already parallel or antiparallel and the sensor is no longer sensitive to changes in the external magnetic field. The sensor has a coercivity field of about $1.7\ \text{Oe}$, showing very little hysteresis and the overall resistance of about $820\ \Omega$ varies by about 5% over the full field range shown.

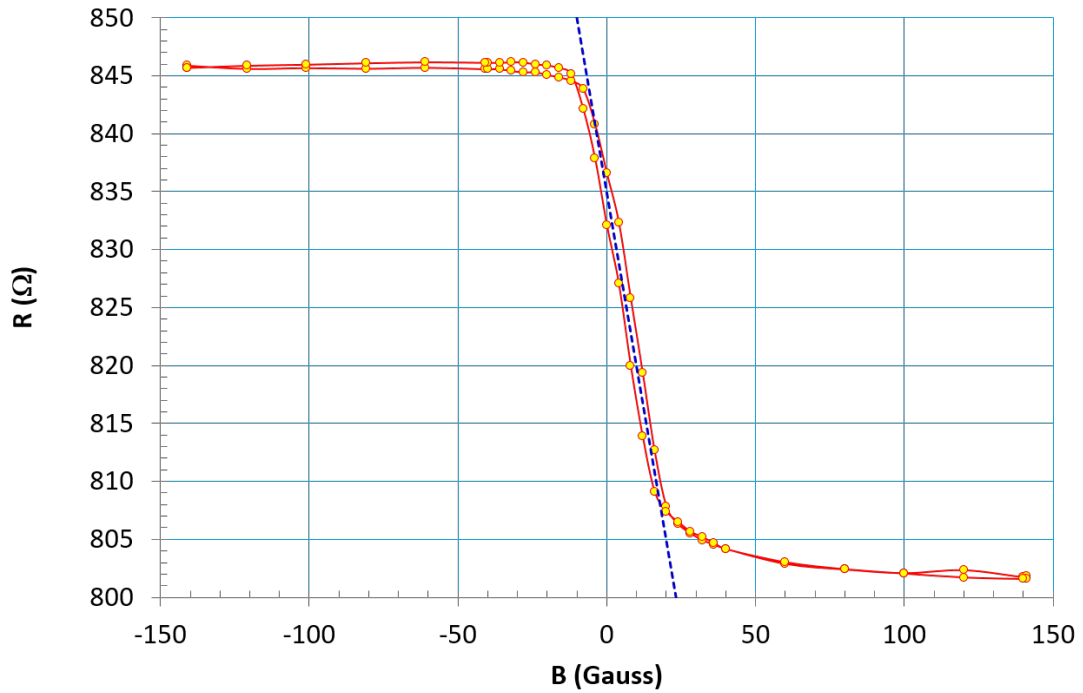


Fig. 7.2. The yellow points and red curve show resistance versus applied magnetic field for a 70 μm long spin-valve sensor I fabricated at INESC. The sensor shows little hysteresis (coercivity of 1.7 Oe) and the operating region near $B = 0$ is very linear. The maximum response is 1.5 Ω/G (blue dotted line) for an overall magneto-resistance ($\Delta R/R_{min}$) of 5.6%.

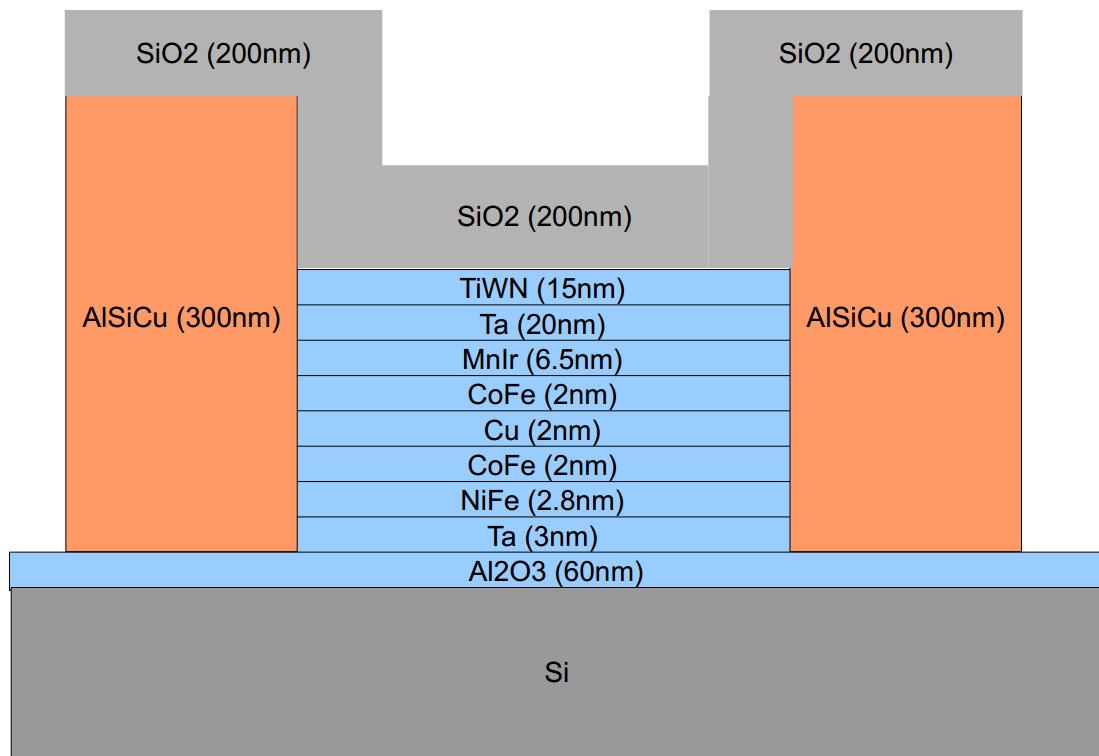


Fig. 7.3. Thin-film structure of the INESC spin-valve sensors. The AlSiCu layers on both sides of the stack are the conducting pads that electrically connect the spin-valve sensor to its bias leads. The blue layers in the middle show the spin-valve stack and different layer thicknesses. Note: note to scale.

7.3 Sensor stack and fabrication

The spin valve sensors we used were produced at the Instituto de Engenharia de Sistemas e Computadores (INESC) in Lisbon, Portugal. The custom built sensors they made for Neocera have a $2\ \mu\text{m}$ by $4\ \mu\text{m}$ surface area and are made from a complex stack of thin films (see Fig. 7.3). In order from the top to bottom (Si substrate), the stack is formed from a 200 nm passivation layer of silicon dioxide, 15 nm of TiWN, 20 nm of Ta, 6.5 nm of MnIr, 2.0 nm of CoFe, 2.0 nm of Cu, 2.0 nm of CoFe, 2.8 nm of NiFe, 3.0 nm of Ta, and 60 nm of Al_2O_3 on a Si substrate. The tantalum is used as a protective capping layer on the top and bottom of the sensor. The MnIr layer is the antiferromagnetic pinning layer. It is coupled to an adjacent CoFe layer, the pinned layer. The MnIr pinning layer forces the pinned layer to keep the same magnetic polarization regardless of the external magnetic field. The other key layers are the “free layer” formed by the CoFe/NiFe bilayer and the Cu conducting layer which is sandwiched between the free layer and the pinned layer. Because the signal comes from a change in the polarization direction of the free layer, the sensor is sensitive to fields along the axis that is both in the plane of the sensor and perpendicular to the free layer polarization.

Figure 7.4 shows three spin-valve sensors out of 100 that I fabricated on a 3 inch diameter glass substrate. While these sensors are larger than the ones we used in the MAGMA system ($70\ \mu\text{m}$ versus $4\ \mu\text{m}$ long), they are made with the same materials, in the same facility, and with the same layer profiles as the MAGMA sensors. As shown in Fig. 7.3, we used a current in plane (CIP) design, with the AlSiCu blocks acting as current pads.

[Appendix C](#) shows the run sheet I used for making spin-valves at INESC. I first did

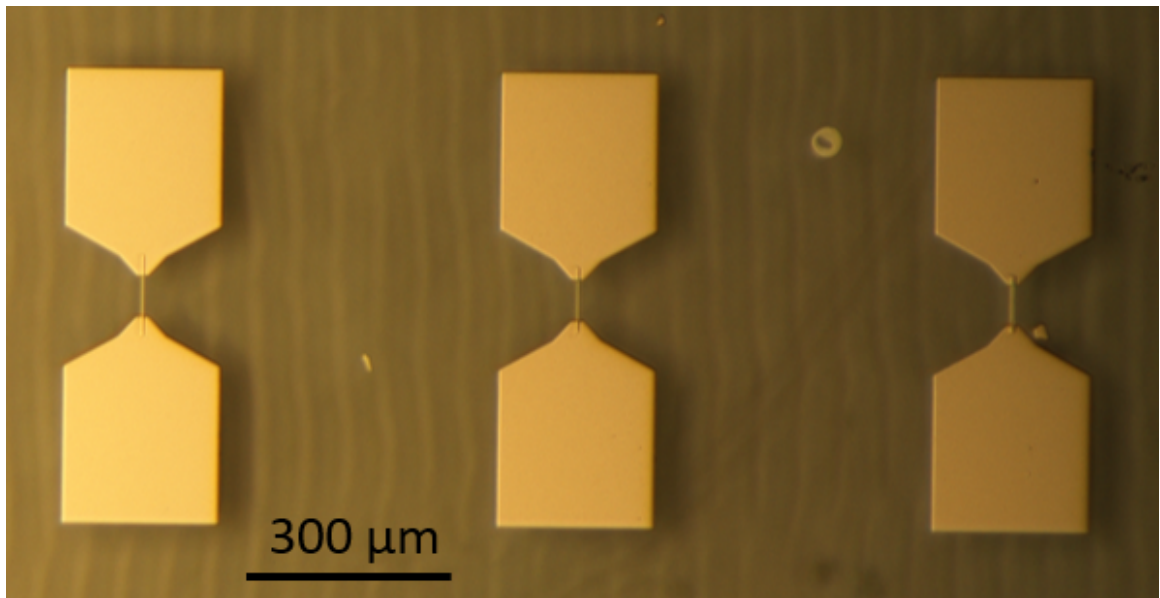


Fig. 7.4. Photograph of three spin-valve sensors I built at INESC. The sensors are 70 μm long and range in width from 10 μm to 25 μm . These devices were built on a glass substrate and are connected to large pads at the top and bottom.

a cleaning step on the substrate using an Alconox solvent bath and applying ultrasound for 30 minutes. The second step was a multi-layer deposition in a Nordiko 3000 ion beam deposition system [94]. The Nordiko 3000 deposited the entire 7-layer spin-valve stack without breaking vacuum. This allowed the sensor stack to be as contamination free as possible. During the deposition I applied a field of 50 Oe to induce magnetization anisotropy in the pinning, pinned and free layers. In the third step I coated the wafer with HMDS photoresist using a vapor priming technique [95]. In the fourth step I determined the shape of the spin valve sensors (70 μm long and widths between 10 and 25 μm) via photolithography using a Heidelberg DWLii direct write laser lithography machine [96]. Fifth, I etched the sensors using a Nordiko 3600 ion beam deposition machine. At 1 \AA per second, I etched about 300 \AA in two steps to avoid overheating. In step 6, I stripped the remaining photoresist. At this point in the process the spin-valve sensors are complete but I still have to create contact pads to be able to test them.

In step 7, I deposited HMDS as a negative resist, then used a second photolithographic exposure in the Heidelberg laser lithography tool to define the contact pads. I then deposited 300 nm of Al and used a liftoff process in Microstrip 3001 [97] at 50° C and ultrasound to remove the unwanted material. After a final cleaning step using isopropanol, the process was complete.

Table 7.1 shows ΔR values I measured for the sensors I made (see Appendix C for more details). All of the sensors had $MR \approx 5\%$, and resistances between 300 and 800 Ω for sensors with widths ranging from 10 to 25 μm .

While the process I used was similar to that used for the MAGMA sensors, the MAGMA sensors are two orders of magnitude smaller in area, just 2 μm by 4 μm , giving

Table 7.1. Magnetoresistance values for some of the spin-valve sensors I built at INESC are between 4 and 6%.

Spin-valve ID	R_{\min}	R_{\max}	ΔR (Ω)	MR (%)
A3	801.6	846.2	44.6	5.56
C3	578.1	608.7	30.6	5.29
E3	450.5	474.6	24.2	5.37
I3	321.2	339.0	17.8	5.53
J3	298.9	315.3	16.5	5.23
A1 (s1)	827.1	874.5	47.5	5.74
A4 (s1)	828.6	878.5	50.0	6.03
B3 (s1)	658.4	696.0	37.6	5.71
E3 (s1)	471.0	494.3	23.2	4.93
G3 (s1)	378.6	399.5	21.0	5.54
I1 (s1)	399.3	415.4	16.1	4.03

them 50Ω impedance, and they are built on Si rather than glass. The length to width ratio (2:1) of the MAGMA sensor is rather small considering that shape anisotropy [98] is used to make sure the free layer is oriented along the y axis in zero field. The advantage of the smaller design is that a smaller sensor leads to less area averaging and better spatial resolution. In practice the MAGMA spin-valve sensors can resolve currents to submicron resolution if they can be brought in close contact with a sample.

7.4 Sensor characterization

Figure 7.5 shows a magnetoresistance curve measured at Neocera for a $2 \mu\text{m}$ by $4 \mu\text{m}$ MAGMA spin-valve sensor. The resistance of the sensor is typically designed to be about 50Ω to enable a wideband frequency response, from dc to GHz. This sensor showed a maximum magneto-resistance ($\Delta R/R_{\min}$) $\approx 10\%$, although this required applying fields of

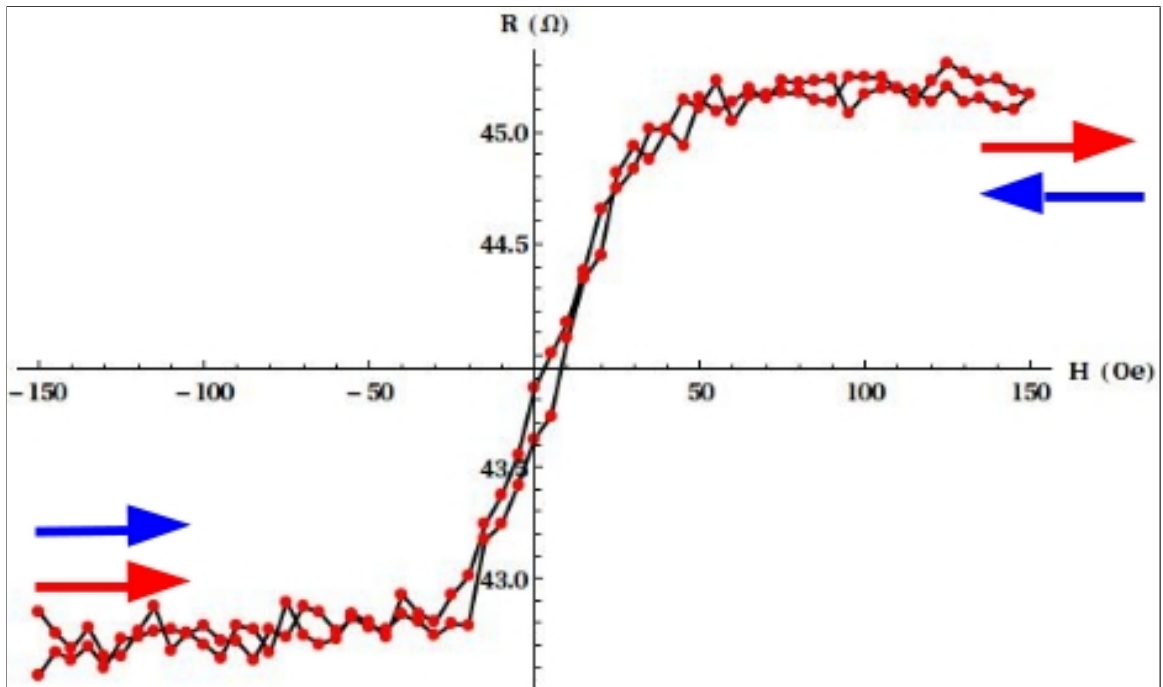


Fig. 7.5. Magnetoresistance characterization used to compute the transfer function for the spin-valve sensor. This particular sensor shows an average sensor resistance of 43.9Ω and a magnetoresistance of 5.5% .

a few tens of Gauss, well above the range of magnetic field that are typically imaged.

From Fig. 7.5 I can also determine the sensor's responsivity in its linear regime and find $dR/dB \approx 47.5 \text{ m}\Omega/\text{G}$ before amplification. When running the MAGMA system, we current bias the sensor and measure the voltage. To get the strongest signal possible $\Delta V = I\Delta R$, it is to our advantage to pass the maximum current possible. Typically we use 1 mA, and Neocera reports that the use of higher currents reduces the sensor lifetime. This gives a response of $0.475 \mu\text{V}/\mu\text{T}$ before amplification.

At low frequencies, $1/f$ resistance fluctuations dominate the noise in the spin-valve sensors. The Nyquist noise has a voltage noise power spectral density of $S_v(f) = 4k_bTR$,

where T is the temperature and R is the sensor's resistance. Given the sensor resistance of about 45Ω , $T = 300 \text{ K}$ and an imaging time of $\tau = 20 \text{ ms}$ per pixel, this results in noise of about

$$\sigma_B = \frac{\sqrt{4k_B T R (1/\tau)}}{I \partial R / \partial B} \approx 13 \text{ nT} \quad (7.1)$$

per pixel in a magnetic image. Our sensors have noise of about $\approx 120 \text{ nT}$ per pixel. It is possible that some of the remaining noise is coming from the spin-valve pre-amplifier and $1/f$ noise.

7.5 Spin-valve advantages and disadvantages compared to a SQUID

A spin-valve sensor has several advantages compared to a SQUID. A spin-valve sensor is operated in air at room temperature and can run in contact with the sample. This allows for a high spatial resolution (better than $1 \mu\text{m}$) for current-carrying layers near the surface of the sample. In practice, when we run scans in contact the sensor is $1\text{-}2 \mu\text{m}$ away from the surface of the sample because it is difficult to get the sensor closer than that to the edge of its substrate. Out of contact scans can typically be as close as $5\text{-}10 \mu\text{m}$ away. Also, the spin-valve sensors are smaller than the SQUIDS we use (2 by $4 \mu\text{m}$ rather than $30 \mu\text{m}$ by $30 \mu\text{m}$), so the effective pickup area and averaging are appropriately small for the scanning distance.

The main disadvantage of our spin-valve sensors is that they have much higher noise than a SQUID. As discussed above, the noise in our typical sensors is about $100\text{--}200 \text{ nT/pixel}$ given our scanning conditions (see Fig. 7.6). In contrast, the SQUID sensor has 150 pT/pixel noise. In order to get better performance we would have to increase the

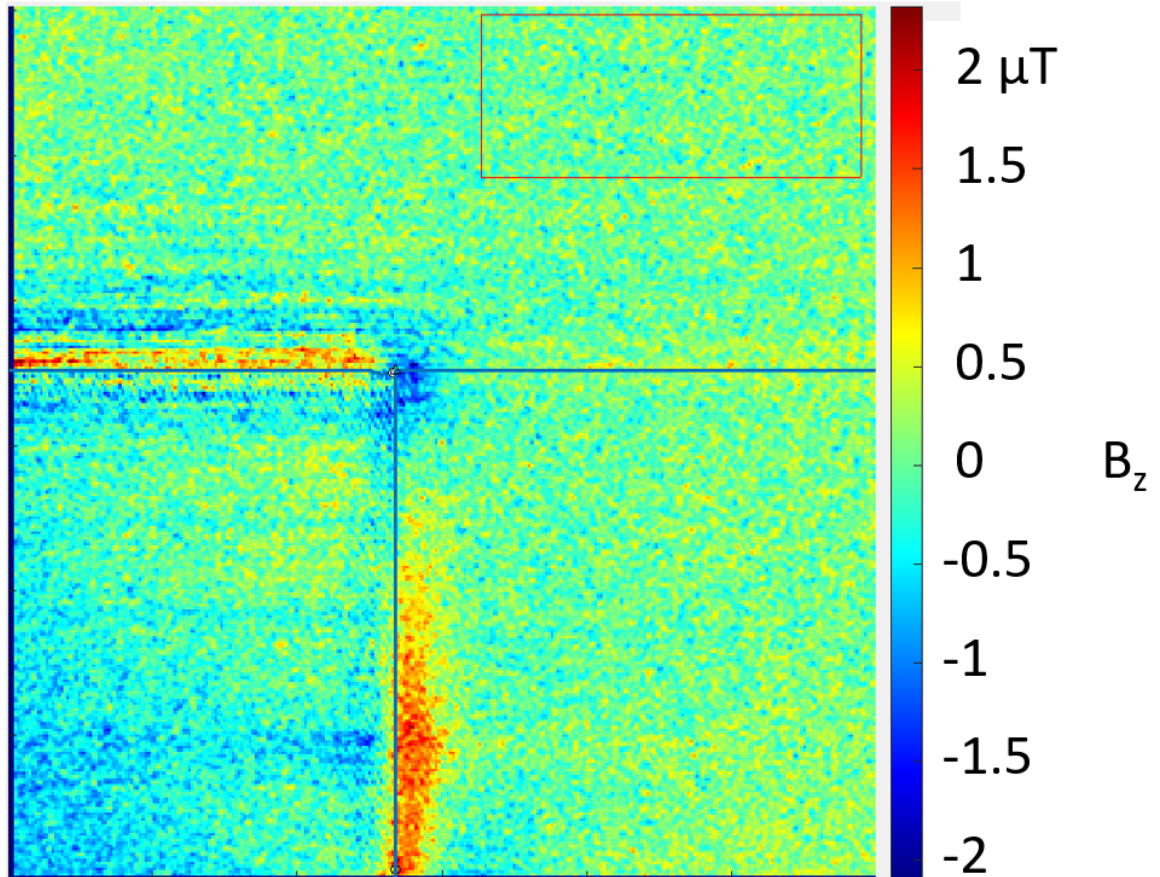


Fig. 7.6. $B_{data} - B_{fit}$ for L-shaped single scan # 21. The total noise from the spin-valve sensor was found by looking at the difference between the measured field and the simulated best fit field, in a region where the fit is good. The noise in the red box in the top right was found to be about 120 nT by taking the standard deviation of the difference field in that region. This is comparable to the value found from the sensor alone.

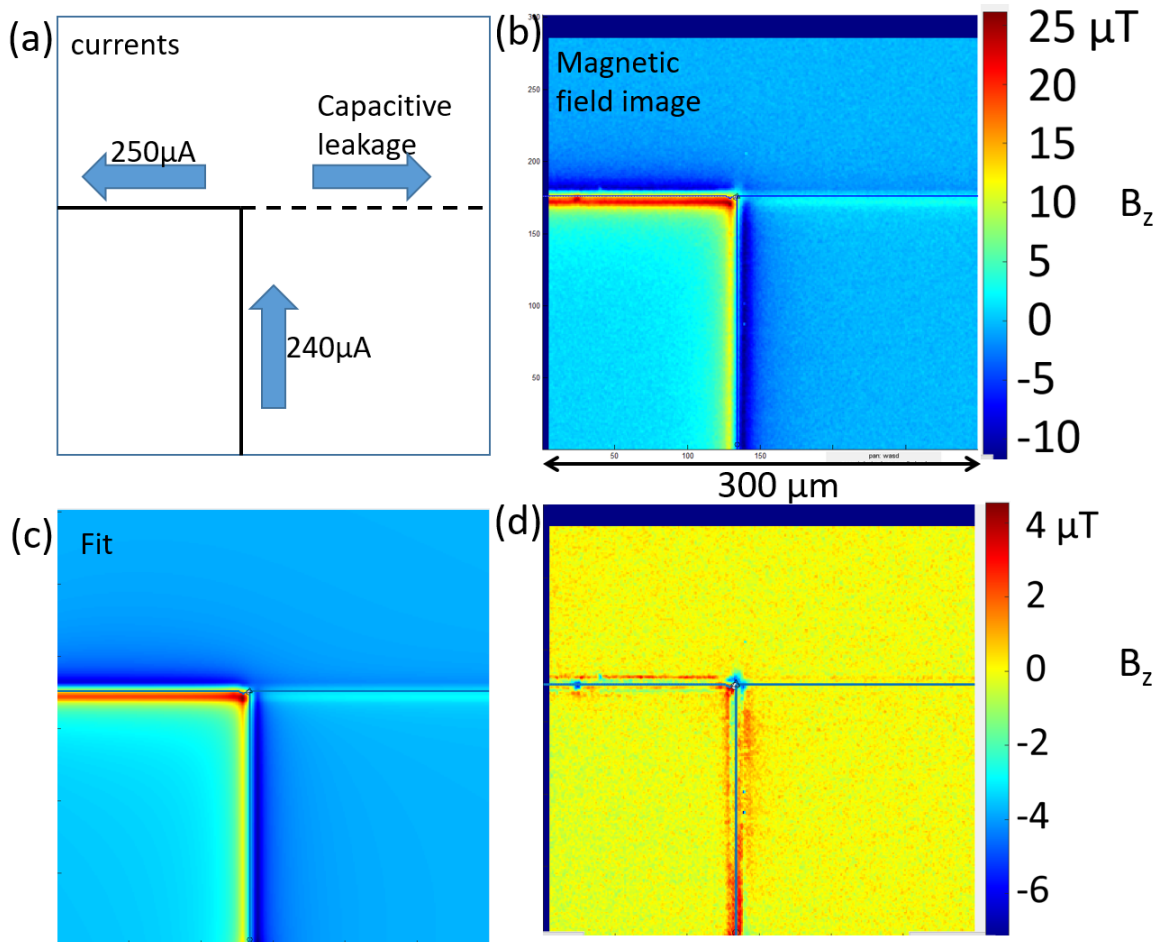


Fig. 7.7. Tilt scans show that the measurement direction of the spin-valve sensor isn't in the z direction. (a) Schematic of currents in the sample. Design gives strong field components in many directions, allowing extraction of sensor tilt parameters. (b) Magnetic field image # 24 collected with the spin-valve sensor during a series of 24 scans. (c) Best fit simulated magnetic field image created using 3D Solver software. Overall, the fit image is in good agreement with the measured magnetic image, indicating that both the parameters and the path are well resolved. (d) Difference image between the data and the fit.

sensitivity $\partial R/\partial B$ or increase the maximum current we can use to bias the device. In addition, position noise [35] can significantly degrade the noise performance, especially for in-contact scans.

While the SQUID is much more sensitive, it has its own challenges. The SQUID must be cooled to cryogenic temperatures and kept in vacuum while the samples are in air at room temperature. This significantly increases the system cost, footprint and amount of engineering required to use the SQUID. The need for a cryogenic system and vacuum pumps can also generate mechanical and electrical noise and these need to be dealt with to ensure that the system performance is not compromised.

To maintain cryogenic conditions, the SQUID is kept behind a 2 mm diameter 10 μm thick diamond window. The SQUID sensor cannot touch the window, nor can the window be in contact with the sample during a scan. This increases the distance from the sensor to the sample. In practice we have imaged with the SQUID as close as 44 μm away from the sample, and bringing it closer in the present setup is challenging. The reason that the window is 2 mm in diameter is that the face of the SQUID chip is about 0.8 mm on a side and some space is needed for clearance and sealing the window to the aluminum cone. In practice, it is difficult to get mm size surfaces parallel enough to bring them much closer than a few μm apart. If the SQUID chip touches the window it can cause the window and cone to cool, leading to thermal contraction and to the SQUID point pushing through the window.

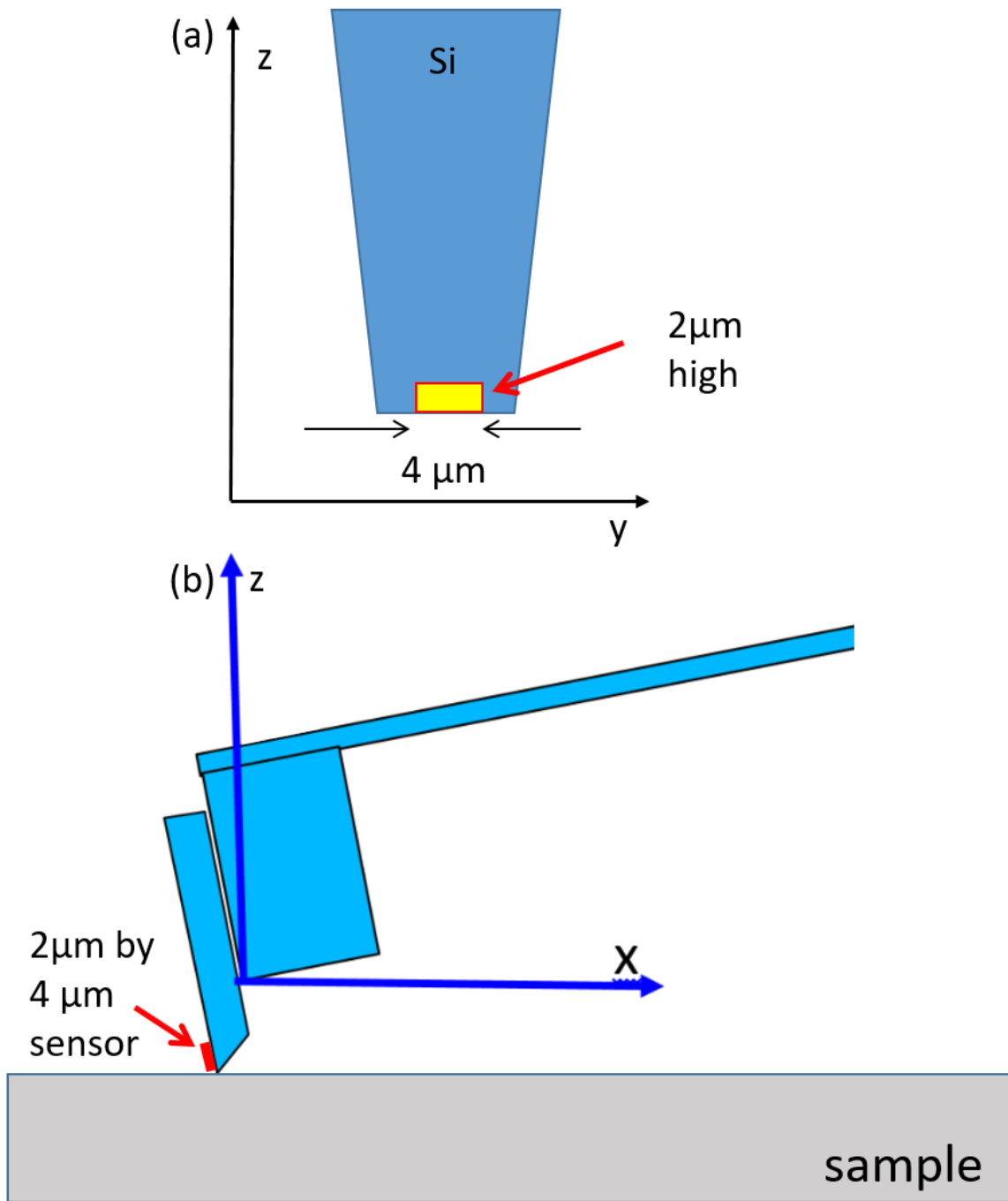


Fig. 7.8. The spin-valve sensor is mounted on a cantilever in order to scan in contact with the sample. (a) Front view. (b) Side view.

7.6 Sensor integration into the MAGMA system

The spin-valve sensor used in the MAGMA system is fabricated on a Si wafer. The wafer is diced into chips and each chip is then cut and polished to produce a tapered shape with the sensor within a few μm or less from the edge of the chip (see Fig. 7.8 (a)). The chip is mounted on a small aluminum block and attached to the end of a flexible cantilever. The cantilever allows the sensor to be brought into gentle contact with the surface of a sample and allows the sensor to follow the surface topography during a raster scan (see Figure 7.8 (b)).

One issue we found with this arrangement was that it caused deviations in the position of the sensor when scans were made in contact with the sample. If the sample surface was not flat, changes in the cantilever position and orientation would contribute position and tilt noise to the final image. However, we also found tilt and position variations while imaging flat samples. As part of a series of scans examining the sensor tilt, we took repeated images of an L-shaped sample (see Fig. 7.7 (a)). These images were then analyzed using the 3D Solver to extract the best path (see Fig. 7.7) and best fit parameters, including the sensor gain g , the sensor tilts θ and ϕ , the sensor-to-sample separation z , the line width w and noise σ_B , as well as other sample and imaging parameters. Table 7.2 summarizes the best fit results for key parameters from these scans. Scans 17 through 21 were taken out of contact, with the others taken in contact. As Figs. 7.9 and 7.10 (a) show, scans 17-21 showed much more stable values for the sensor polar and azimuthal angles θ and ϕ . Thus, even in flat samples, in-contact scanning produces additional noise, likely due to variations in the cantilever orientation and sample-to-sensor contact separation. In fact this problem

Table 7.2. Table of parameters for the series of 24 tilt scans of an L-shaped test sample.

n (data set number)	θ (degrees)	Φ (degrees)	g	σ_B (nT)	z (μm)
1	34.77	89.82	2.326	112.3	1.63
2	34.70	95.83	2.429	111.0	1.77
3	35.66	91.61	2.338	108.8	1.96
4	34.75	91.08	2.294	111.5	2.50
5	33.72	94.46	2.306	112.6	2.54
6	36.62	95.92	2.272	123.1	1.54
8	36.55	98.85	2.347	112.0	1.68
9	38.52	91.44	2.364	115.7	1.66
10	38.38	96.59	2.345	166.3	1.84
12	35.17	101.22	2.335	122.3	1.79
13	38.73	96.53	2.292	125.2	1.71
14	41.13	95.57	2.398	118.5	1.84
16	36.16	92.56	2.250	126.1	1.83
17	34.63	93.27	2.355	110.8	2.53
18	32.77	95.24	2.351	113.5	5.78
19	35.42	92.87	2.488	102.2	8.55
20	32.60	92.16	2.358	104.8	11.23
21	32.71	92.49	2.388	106.2	13.53
22	35.13	101.24	2.390	106.9	1.80
23	35.56	96.91	2.358	108.9	1.63
24	33.45	85.17	2.248	112.2	1.42

is readily visible in Fig. 7.6 as a relatively large line-to-line discrepancy when the sensor is near the current path (see upper left part of image near pad in Fig. 7.6). More work is needed to improve the cantiliver design and operation to achieve repeatability of scanning in contact with the spin-valve sensor.

7.7 Spin-valve sensor tilt

The MAGMA spin-valve sensors were designed to measure the z (vertical) component of the magnetic field. During our analysis of scans, we noticed that many images had an “imbalance” in the maximum positive vs. negative field. Figure 7.7 shows an example from our set of L-scan images. For an image of the z -component of the magnetic field from a straight wire in the x - y plane, we would expect to see positive and negative regions of equal strength near the wire. Analysis of these images using the 3D Solver revealed that the spin-valve sensors were not picking up the z component, but a component tilted significantly away from the z -axis. Specifically, we use two angles θ and ϕ to describe the direction of the field component that the sensor is measuring. Following typical spherical coordinates convention, ϕ is the azimuthal angle (angle from the x -axis) and θ is the polar angle (angle from the z -axis, see Fig. 2.1). While ϕ was near 90° , as expected, we were surprised to find $\theta \approx 45^\circ$ (see Table 7.2). If we were measuring along the z axis, we would expect $\theta = 0^\circ$.

The simple L-shaped pattern (see Fig. 7.7 (a)) was chosen because the geometry of its currents is simple, so it would be easy to get a good fit, and because this pattern generates a field along each axis in different locations, so the fits were sensitive to the sensor tilts.

While we had suspected the sensor was tilted for quite some time, it was often ambiguous in a scan because many current layouts don't generate fields with all three components or generate very complicated patterns.

Fig. 7.7 (b) shows image # 24 from this set. Using the 3D Solver software, we obtained the best-fit magnetic field fit (see Fig. 7.7 (c)). The difference image between the data and the fit is shown in Fig. 7.7 (d), and overall this shows a reasonably good fit, although clearly some discrepancies remain. Specifically, we were most interested in the global parameters of the scans including the detection direction. The strongest discrepancies are located at places where it is difficult to model the currents (*i.e.* the corner) – these discrepancies do not overly affect the tilt angles.

From Fig. 7.7 (b) we extracted parameters, and found that the sensor was rotated by $\theta = 35^\circ$ from the z axis. In contrast, the angle ϕ was near 90° , as expected. Figure 7.10 (a) shows the angle θ from the z -axis for each of the scans we took of the L-shaped sample. These results show that the sensor angle is varying but generally tilted from the z -axis by $30\text{-}40^\circ$, even when the cantilever was not in contact with the sample.

These results naturally raise the question of why the sensor detection angle of the spin-valve sensor is tilted so far from the vertical. Observation of the cantilever during a scan reveals only small physical tilting of the sensor during scans. Thus we conclude that the tilt is due to the in-plane magnetization of the free layer pointing away from the horizontal direction (see Fig. 7.11). The most likely cause is the low shape anisotropy of the $2\ \mu\text{m}$ by $4\ \mu\text{m}$ sensors leading to the magnetization being off from the z axis. We note that the tilt angle is close to the corner-to-corner diagonal direction of the sensor, which is $\arctan(1/2) = 26^\circ$.

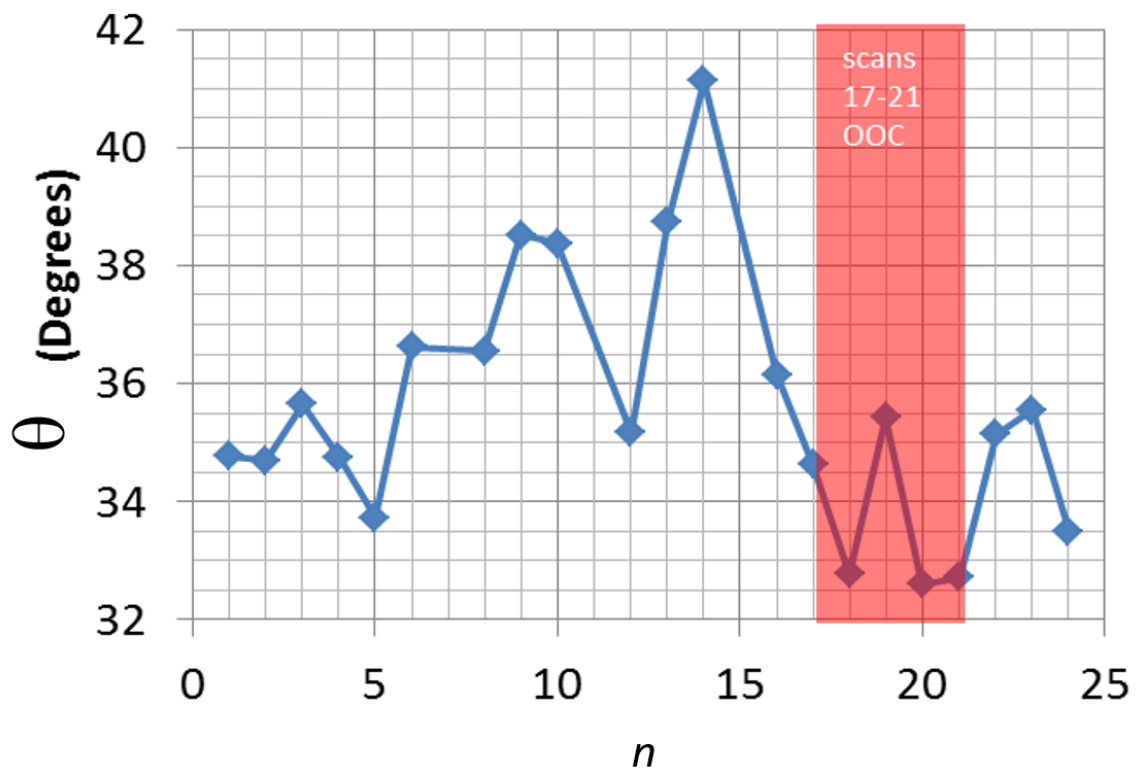


Fig. 7.9. Plot of the best fit sensor detection angle θ versus data set number n from an analysis of the tilt images of the L-shaped sample. The scans #18 to 21 (red band) were taken out-of-contact while the other scans were taken in-contact with the sample. The sensor tilt and variations in the sensor tilt appear to be larger when the sensor is run in-contact.

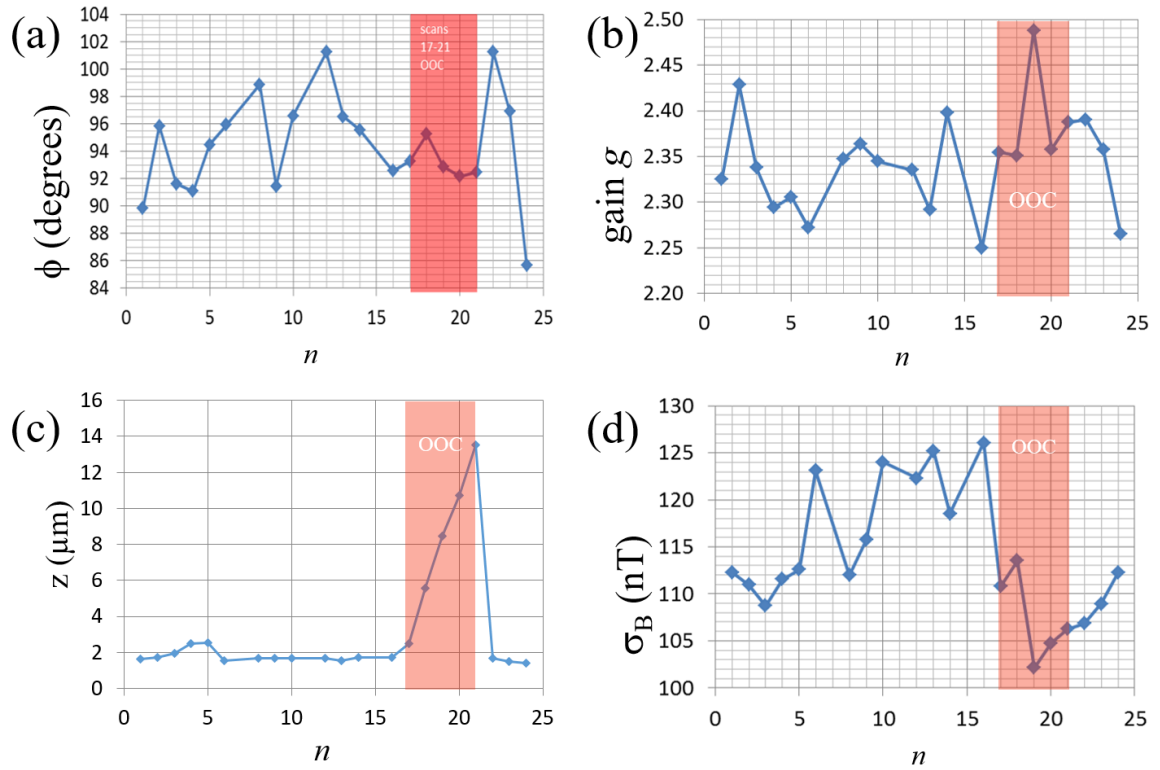


Fig. 7.10. (a) Plot of the sensor angle ϕ versus data set number n . (b) Plot of the gain g versus data set number n . (c) Plot of the sensor-sample distance z versus data set number n . (d) Plot of the noise standard deviation σ_B versus data set number n . These parameters are from an analysis of the tilt images of the L-shaped sample. Scans #18 to 21 (red band) were taken out-of-contact while the other scans were taken in-contact with the sample.

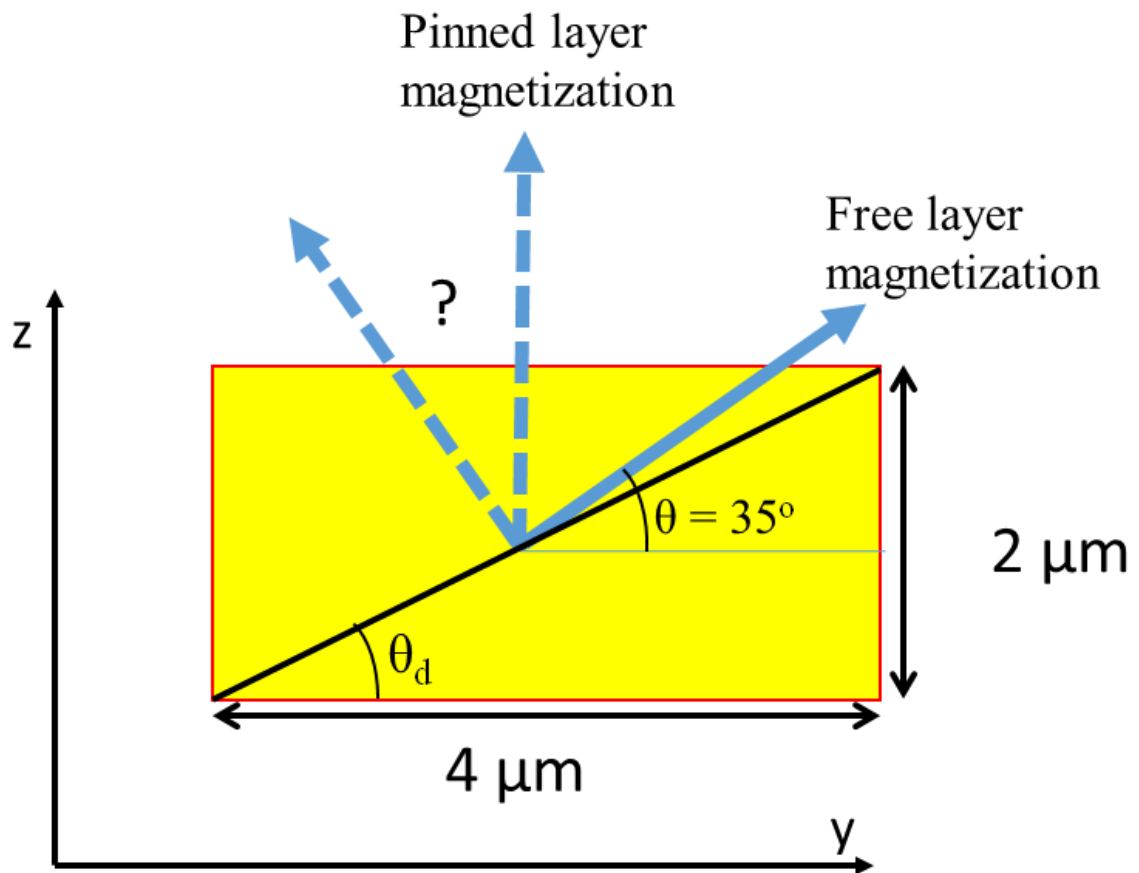


Fig. 7.11. Model of the spin-valve sensor in which the free layer's magnetization is tilted by 35° from the y-axis. Since the sensor is most sensitive to the magnetic field perpendicular to the magnetization of the free layer and in the plane of the free layer, this device detects the component of the field 35° from the z-axis. It is unclear whether or not the pinned layer is also rotated. Note that $\theta_d = \arctan(2/4) = 26^\circ$.

7.8 Conclusion

In Chapter 7 discussed the layout, fabrication and operation of our spin-valve sensors. I also discussed the noise of the sensors and compared the advantages and disadvantages of spin-valves and SQUIDs. I discussed some unexpected behavior we observed in the spin-valve sensors – they are detecting a field at a tilt from what they were designed to do – and the possible cause of this behavior.

Chapter 8: Select Magnetic Images

8.1 Introduction

Over the course of this project we acquired hundreds of scans of a wide variety of samples. In this chapter I present a few scans in order to demonstrate the capabilities of the 3D Solver for analyzing magnetic images from the MAGMA system. The first example is an image of a simple 3-layer linear via chain. The second image is of a more challenging path, a five-layer meander sample. I next discuss two examples of modified samples which demonstrate how this system can be used to identify the location of a short. Finally, I present a large area scan of a sample containing tens of thousands of TSVs. This last example demonstrates how the system is useful even without running the inversion, and in particular demonstrates the importance of in-phase and out-of-phase information.

8.2 SU8 three-layer sample

Figure 8.1 shows a summary of some key results from sample 1. Sample 1 had three distinct wiring layers with a 10 μm layer-to-layer separation, with the different layers being connected by 10 μm by 10 μm square vias. The wire was 5 μm wide, with a slightly larger infeed/outfeed metal trace of 7 μm . The metal was gold and the 10 μm thick insulation

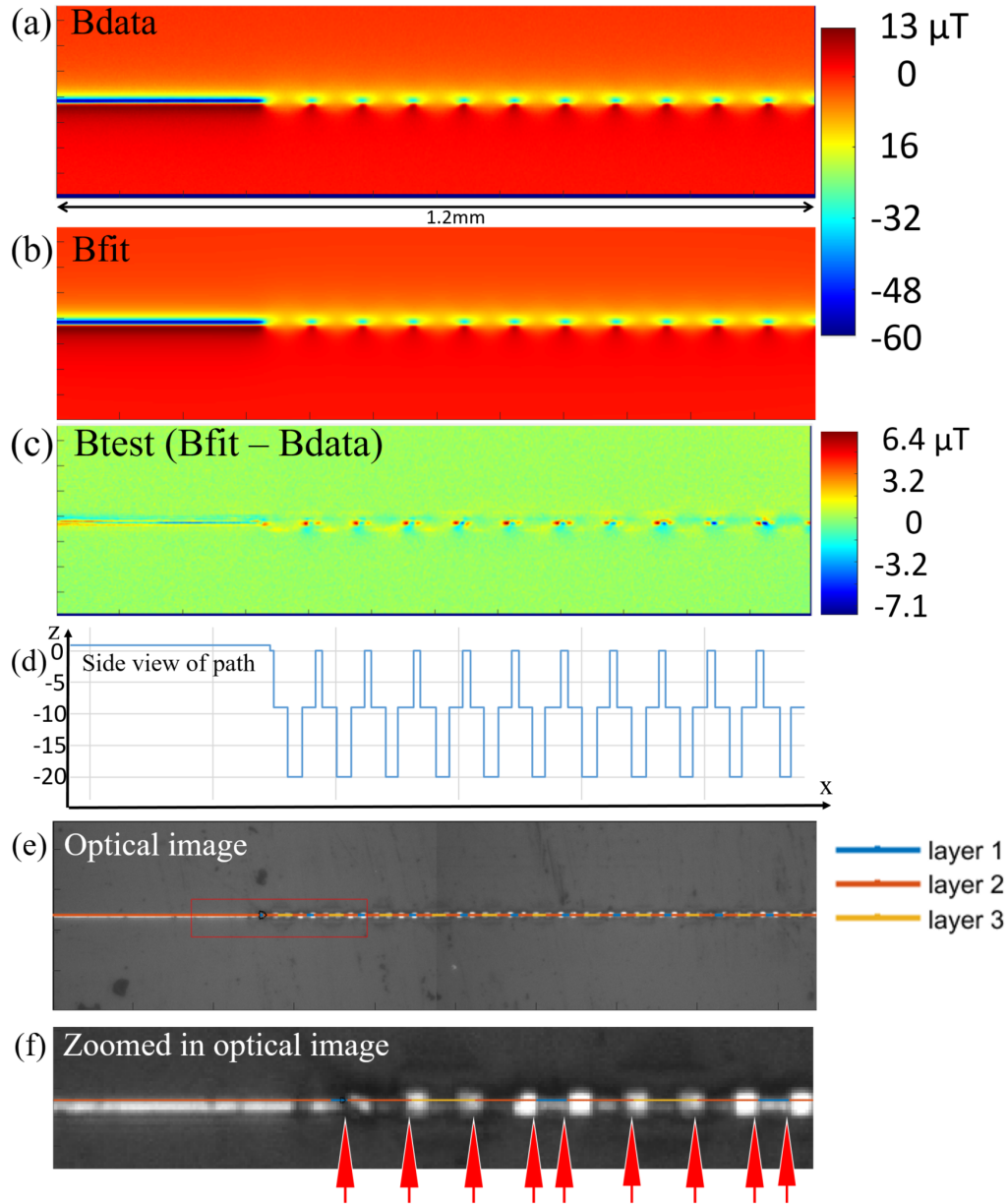


Fig. 8.1. Results from sample 1, a three layer sample in SU8. (a) Magnetic data (B_{data}) acquired with the spin-valve sensor. (b) Reconstructed magnetic image (B_{fit}) based on best fit current path and best fit parameters. (c) Magnetic difference image ($B_{fit} - B_{data}$) shows areas of discrepancies near the vias. (d) Side view of best fit path. (e) Optical image from MAGMA system of entire scan area. (f) Zoomed in optical image shows good agreement with superimposed path. Vias in best fit path (marked by red arrows) fall within metallization of vias in optical image.

layers were made from SU8 (a clear plastic printed on an Si substrate). In this sample, the current path goes up and down over three layers as it goes from left to right across the sample. Figure 8.1 shows the image measured by the spin-valve sensor. It covers an area of 1200 μm by 300 μm , has a pixel size of 2 μm by 2 μm and took about 22 minutes to acquire. For this scan, the spin-valve sensor was scanned in contact with the sample.

In Fig. 8.1 (a) we see that the linear via chain goes along the center of the image from left to right. Notice also that the left hand side of the image contains a long straight section of wire that is in the top layer – this part of the image is very useful for extracting global scan parameters such as the sensor to top layer separation z , the gain g , and the sensor tilts ϕ and θ . To analyze this image, I drew a straight line starting path across the image, adjusted the sample tilt so that my path would line up with the magnetic field, and then used the parameter search to find the global scan parameters from the left part of the image. I then alternated z -searches and parameter searches, generally working on a small part of the path at any time by defining a crop2 search region. The corner search was not necessary since the path does not meander in the y direction. It was necessary to do a careful search of the sample rotation, and apply an x and y offset so that my path was well-aligned with the image. The field from the infeed and outfeed wires to the sample affects the final image and it was necessary to take them into account. I used the automated infeed and outfeed routine, which extended the infeed and outfeed about 200 μm straight out from on the left and the right of the image. Beyond that distance, the infeeds have no measurable effect on the χ^2 . Figure 8.1 (b) shows the magnetic field corresponding to the best fit path. By eye, this image looks indiscernible from that shown in 8.1 (a), however they are slightly different. This is visible in Fig. 8.1 (c), which shows the difference image of the magnetic fit and data

$(B_{fit} - B_{data})$. Note that the scale on the difference images goes from $-7.1 \mu\text{T}$ to $6.4 \mu\text{T}$, whereas the data originally ranged from $-60 \mu\text{T}$ to $13 \mu\text{T}$. Thus there are still significant discrepancies in the reconstructed image, but the reconstruction has captured much of the signal. A closer look shows that the most significant discrepancies are all located near the vias. This is not surprising since if the grid spacing is not exactly commensurate with the via-to-via spacing, the path will differ from the true path at the vias. Also, the vias in the sample are square and $10 \mu\text{m}$ by $10 \mu\text{m}$, while we are modeling the current through the vias as an infinitely thin wire. Since our imaging distance is only $z = 3.6 \mu\text{m}$ to the top layer, this effect is noticeable in the data. The rest of the image fits remarkably well.

Despite the differences, the reconstructed best fit path (see Fig. 8.1 (d)) is close to the path seen in the optical image. Fig. 8.1 (e) shows a top view of the optical image for the entire scan area with the best fit path overlaid. The via positions on the right side appear to be well-aligned with the optical image, while the via positions on the left side appear to be slightly misaligned. One possible cause is that the grid spacing ($10 \mu\text{m}$) is not commensurate with the via-to-via spacing in the image. For example, a small error in the optical image scale could cause such a discrepancy. Figure 8.1 (f) shows a top view of a zoomed-in portion of the optical image with the best fit path overlaid. In this image we can see the relatively large ($10 \mu\text{m}$ by $10 \mu\text{m}$) square pads of the vias, which are significantly wider than the horizontal metal traces. For the most part the vias in our best fit path correspond with the location of the vias as seen on the optical image. However, while my best fit path vias all fall within the metallization (see red arrows in Fig. 8.1 (f)), my best fit path tends to shorten the top layer sections as compared to the bottom layer and middle layer sections. There are a few reasons why this might be the case. First, it could be that

Table 8.1. Best fit parameters obtained for scan of sample 1 (3 layer LVC) shown in Fig.

8.1 (a).

MAGMA parameters		fit scan parameters	fit value	nominal values
image x length (μm)	1196	z (μm)	3.6156	2
image y length (μm)	300	ϕ (sensor)	85.0319°	90°
x step size (μm)	2	θ (sensor)	-46.477°	0°
y step size (μm)	2	g	-309.5839	1
# x pixels	599	σ_B (μT)	39	0.2
# y pixels	151	xoffset (μm)	0.71803	0
sensor type	spin-valve	yoffset (μm)	-2.5373	0
θ (sample)	0.061107°			
χ^2	1.25E+06			1.00E+05
Wire parameters				
Name	LVC	Infeed		
I (μA)	1211.3253	1211.3253		1200
w_x (μm)	1	4		-
w_y (μm)	4	4		-
b (μm)	6.9	5.9		5
# of segments	1044	124		-
# of layers	3	3		-
h_{1-2} (μm)	9.1224	-0.65723		10
h_{1-2} (μm)	11.2606	-1		10

our fitted z distance is slightly too small, and the path search is compensating by putting segments on the edge of the top section in the middle layer instead. Or, it could be that our path is doing its best to model the currents in the vias on the manhattan grid. Putting the via currents in the middle layer would produce a smaller error than putting them in the top layer because the field from top layer segments is very strong. It is likely that to improve my model I need to have a more detailed model of the currents in the vias.

Table 8.1 shows the best fit and other parameters I obtained for this particular scan and the nominal values from the design. In the Table's top left are the scanning parameters set and measured by the MAGMA system software before the scan is acquired. In the top middle I list scan parameters fit to and extracted via iterative parameter searches on the magnetic image. At the bottom left are parameters describing the wires, which are also found by a best fit search. These wire parameters include the layer-to-layer separation, the wire widths, and the current through each wire. Note that this path was modelled with two wires as the infeed section of the path had a wider wire width than the linear via chain section. This also allowed us to take into account a very slight height discrepancy between the infeed section of the scan and the meander.

To the right of Table 8.1 are the nominal design values for sample 1. The biggest discrepancy between the expected (nominal) values and our best fit parameters is the θ sensor tilt. Our sensor is tilted 45° from the z axis, instead of being parallel to the z axis. The sample parameters are in very good agreement. The nominal layer-to-layer separation is $10\ \mu\text{m}$ and we are about $1\ \mu\text{m}$ from this value. While $h_{1=2} = 11.2\ \mu\text{m}$, keep in mind that $h_{1-3} = 20.38\ \mu\text{m}$ which is very close to the design spec. In other words, errors in h_{2-3} may be compensating for errors in h_{1-2} , and h_{1-3} is only $300\ \mu\text{m}$ from the design value.

8.3 3DiS five-layer sample

Over the course of this project, we received several samples built to our specifications by 3DiS technologies [99] that used copper electroplating [100] to deposit conducting paths on insulating 3D surfaces formed using a laser deposition technique. While this method does not produce TSVs, these samples could be made with our desired dimensions (1 to 10 μm layer-to-layer separations) and the resulting paths are completely visible optically or with an SEM. This means that we can evaluate the 3D Solver by comparing a path reconstructed with the 3D Solver directly to an SEM or optical image. This is not possible with more traditional TSV samples without de-processing the sample because the lower layers are buried under Si.

Sample 2 is a meander produced by 3DiS. Figure 8.2 shows an SEM image of a sample with similar layout but with a 10 μm layer-to-layer separation. Sample 2 has 5 layers with nominal 1 μm vertical layer-to-layer separations, and a nominal wire width of $b = 7 \mu\text{m}$. Note that one challenge presented by 3DiS's samples is that the metallization pattern is deposited on the "built up" surface of the sample (see Fig 8.5). Unlike many other samples we imaged, the 3DiS samples have relief on their surface. This makes it more challenging to bring the spin-valve close to the sample surface, for fear of knocking the sensor into the protrusions on the surface of the sample. Similarly, running with the sensor in contact with the sample would produce large z variations and the resulting data would not be a fair representation of an image from "buried" paths, nor could it be analyzed with the present version of the 3D Solver since the 3D Solver requires a constant z . For the image I present here, the MAGMA system was run with the sensor out of contact about 5 μm above the top

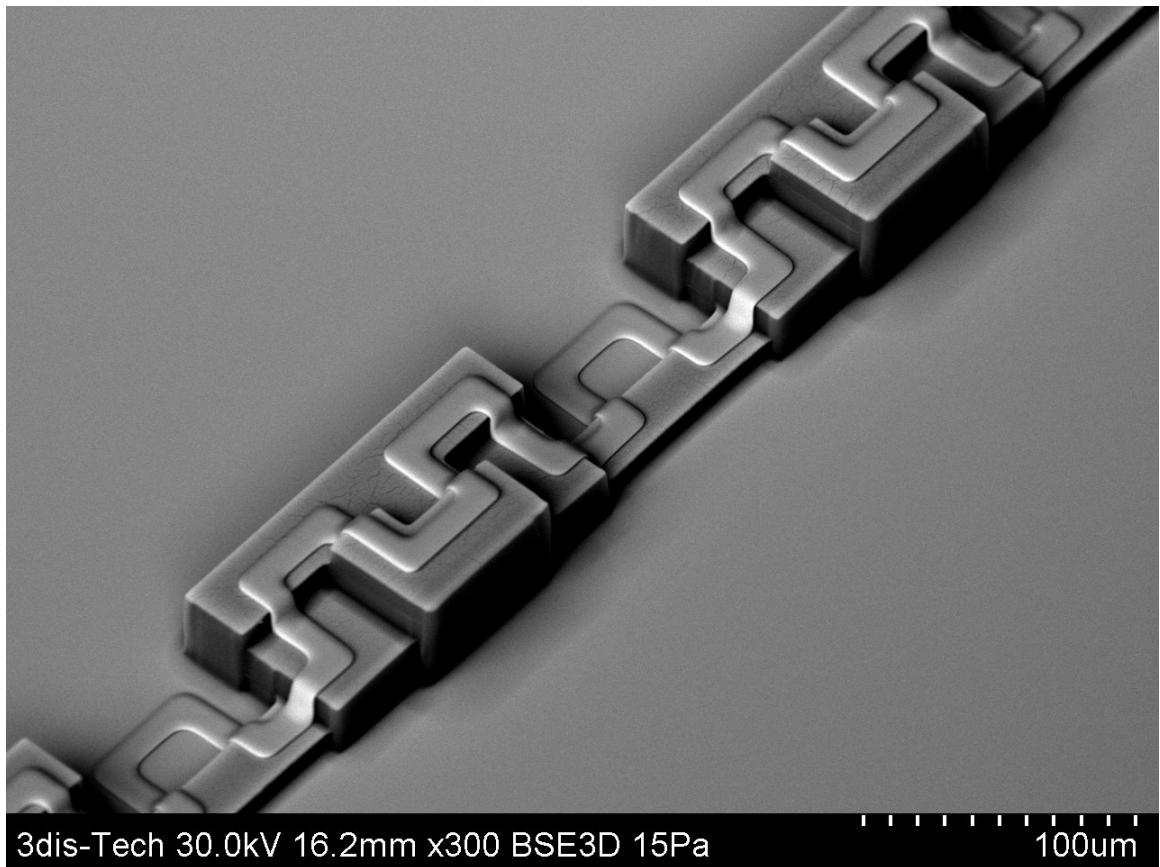


Fig. 8.2. SEM image of sample 2, a 5-layer meander. This sample has 10 μm nominal layer-to-layer separation.

layer.

Figure 8.3 shows results from the 3D Solver analysis performed on sample 2. Figure 8.3 (a) shows the false color magnetic image acquired using the spin-valve sensor, with red representing strong positive fields and blue representing strong negative fields. In this image the magnetic field strength ranges from $-30 \mu\text{T}$ to $+8 \mu\text{T}$, with this asymmetry suggesting a substantial sensor tilt. As in sample 1, this scan presents a long, straight infeed section to the left, with a more complicated and interesting pattern occurring on the right side of the image. As we will see, two complications of the infeed are that it is on the lowest layer (layer 5) and that its width is different from the width of the rest of the pattern. The overall area of the scan is 1.3 mm by 0.3 mm, with a pixel step size of $2 \mu\text{m}$ in the x and y directions.

Figure 8.3 (b) shows the reconstructed magnetic field corresponding to the best fit path. This image is very similar to the measured magnetic image. Figure 8.3 (c) shows that there are still some discrepancies remaining in the difference between the data and the fit. Some of the segments are assigned to incorrect layers. Figure 8.3 (d) shows the corresponding optical image from the MAGMA system. In this image, the building blocks on which the metallization is deposited are visible, allowing us to easily identify the layout of the true path for comparison with the path found from the magnetic scan. In Fig. 8.4 (a), I have enlarged Fig. 8.3 (d) and superposed the true path with color coded layers. This allows easy comparison to the best fit path shown in Fig. 8.4 (b).

To find this path, I first wirized the sample using the LVC wirization. Then, I set the crop2 region to the long infeed located on the left of the image. This allowed us to get a good value for g and z and the sensor tilts. One complication is that because the infeed is in the

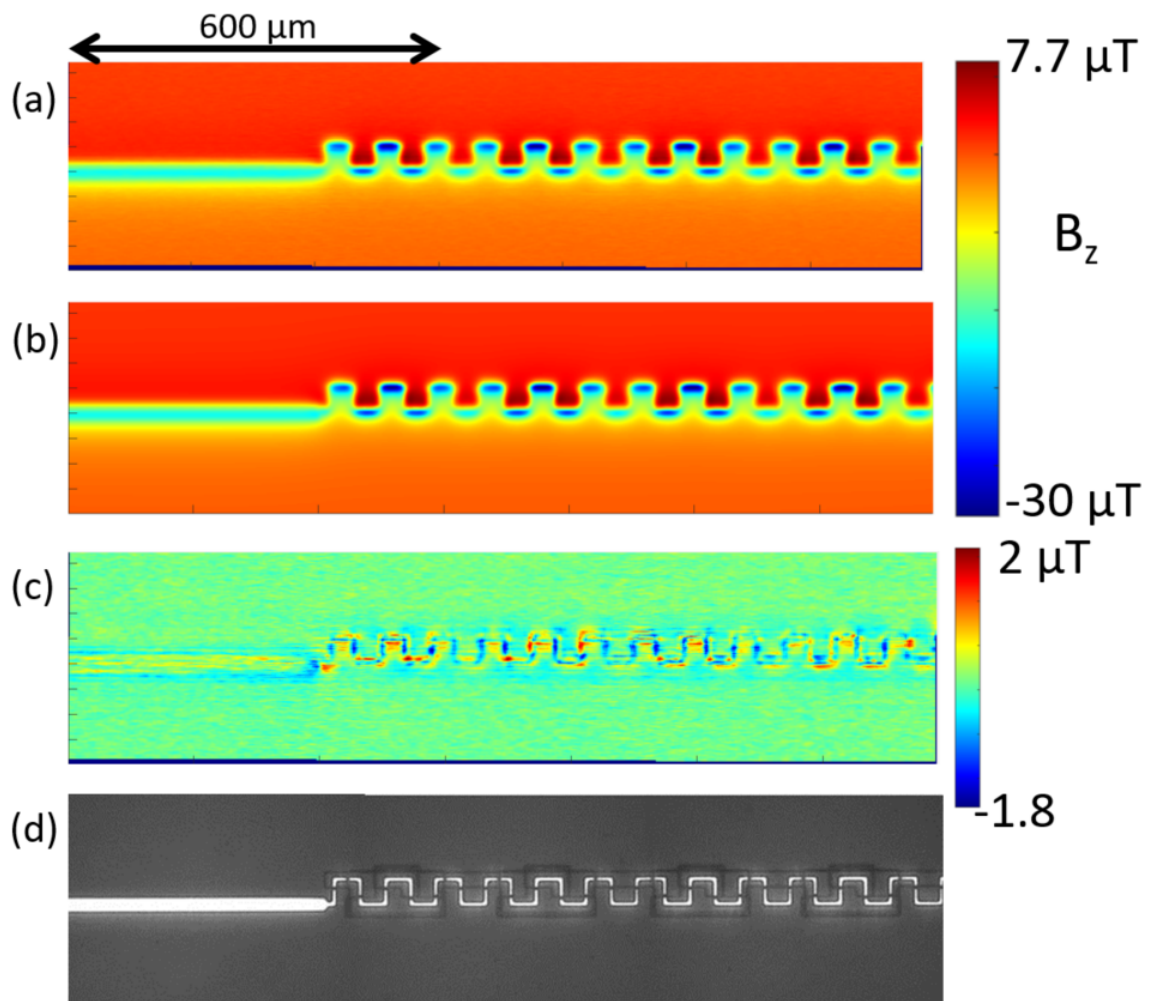


Fig. 8.3. (a) 1378 by 330 μm magnetic image of sample 2 acquired with MAGMA system spin-valve sensor. (b) Best fit magnetic image. (c) Magnetic difference image ($B_{fit} - B_{data}$) shows some discrepancies. The best fit path is close to the design path, but some segments are assigned to incorrect layers, particularly on the lower layers. (d) Optical image from MAGMA system.

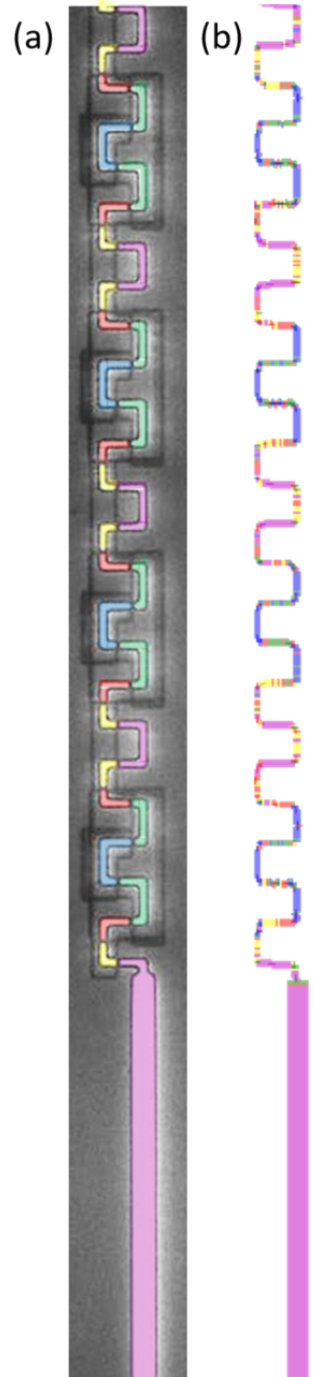


Fig. 8.4. (a) Design path overlaid on top of MAGMA system optical image. The edges of surface relief supporting the metallization is clearly visible. (b) Best fit current path. Note: image is 1378 μm by 330 μm . layer 1 = blue, layer 2 = green, layer 3 = red, layer 4 = yellow, layer 5 = purple.

Table 8.2. Sample and imaging parameters for sample 2 image in Fig. 8.3 (a), a spin-valve magnetic scan of a 5-layer meandering 3DiS sample with 1 μm layer-to-layer separations.

MAGMA parameters		fit scan parameters		nominal values
image x length (μm)	1378.00	z (μm)	6.74	5
image y length (μm)	334.00	ϕ (sensor)	92.24	90
x step size (μm)	2.00	θ (sensor)	55.81	0
y step size (μm)	2.00	g	7.99	1
# x pixels	690	σ_B (nT)	937.51	200
# y pixels	168	xoffset (μm)	0.05	0
sensor type	spin-valve	yoffset (μm)	-2.45	0
		θ (sample)	0.21	0
		χ^2	3.32E+05	115920
Wire parameters				
Name	meander	infeed		
I (μA)	1088.53	1088.53		1000
w_x (μm)	2.00	2.00		-
w_y (μm)	2.00	2.00		-
b (μm)	7.20	21.96		5
# of segments	2003.00	408.00		-
# of layers	5.00	5.00		5
h_{1-2} (μm)	1.30	1.00		1
h_{2-3} (μm)	0.83	1.00		1
h_{3-4} (μm)	0.91	1.00		1
h_{4-5} (μm)	1.29	0.90		1

lowest layer, we are actually fitting to the value $z + h_{1-2} + h_{2-3} + h_{3-4} + h_{4-5}$, which makes the actual location of the top layer somewhat more uncertain than in samples where the infeed is in the top layer. After wirizing and conducting a first parameter search, I started using the corner search to improve the path. I then alternated between corner searches, z searches and parameter searches. In this case, I did not modify the segment length w from the default segment length which is equal to the pixel-to-pixel distance. Since the pixel-to-pixel distance is quite small in this case (1 μm), but the features of the path are quite a bit larger, I should have used a larger segment length, which likely would have produced much better results. It is rather counter-intuitive that my individual segments are 1 μm long but 7 μm wide. In part because of this, we can see many of the segments are placed in the wrong layers, as they introduce transitions that do not fit with the optical image. The nominal design layer-to-layer spacing in sample 2 was 1 μm , which made it challenging to determine between adjacent layers, especially between layers 4 and 5. By visual inspection we can see that top layer segments are much more accurately placed than the lower layer segments. This is unsurprising since we expect much more signal from the top layer than from the bottom layer. In general, even when segments are misplaced, they are usually not more than one layer away from their correct layer. For example, segments that should be in the top layer (blue) can be found in the 2nd layer (green) in my best fit path, but rarely in a layer lower than the 2nd layer. Overall, the field from the reconstructed path is capturing 99.82% of the signal power in the image and the lateral placement of segments is very good.

In Table 8.2, I summarize the parameters extracted from the analysis of 8.3 (a). Note that we have used different wires for the infeed and the outfeed, as the infeed has a larger wire trace than the meander section, as can be seen in Fig. 8.3 (d). Our layer-to-layer

separations match well with the design values from 3DiS, as the largest difference is a 0.30 μm difference from the nominal value. Note that the infeed has no lower layers and that those values were not searched on – only the h_i of the meander section of the path were optimized. In terms of imaging parameters, our values are in line with our expectation. The only anomalous parameters are the spin-valve tilt, fit to 55° and the noise, which was unexpectedly high in this scan at $\sigma_B \approx 1 \mu\text{T}$ per pixel.

8.4 Modified 3DiS five-layer samples

As part of the evaluation of the 3D Solver technique we wanted to test our ability to identify and locate shorts in multi-layer samples. In order to do so, we designed samples 3 and 4 as meandering via chains with 1 μm and 10 μm layer-to-layer separations, respectively. Subsequently, a group at Sandia National Laboratory used a focused ion beam to modify the samples and induce shorts in unknown locations. Our goal was to identify the location and specifically the layer in which the short was located. Of course, the short would have been visible in optical images of the sample, but we were prevented from viewing the sample optically for this exercise. In fact, prior to imaging we were not even certain whether a short had in fact been added or some other modification had been made. This exercise was part of an evaluation our team had to take while being observed by the managing team from IARPA. Figure 8.5 shows SEM images taken by 3DiS before the samples were modified. I note that samples 3 and 4 shared the same layout, with the only differences being that they had nominal layer-to-layer separations of 1 μm and 10 μm , respectively, and different trace widths of 7 μm and 10 μm , respectively. Each scan presented in this section took about 20

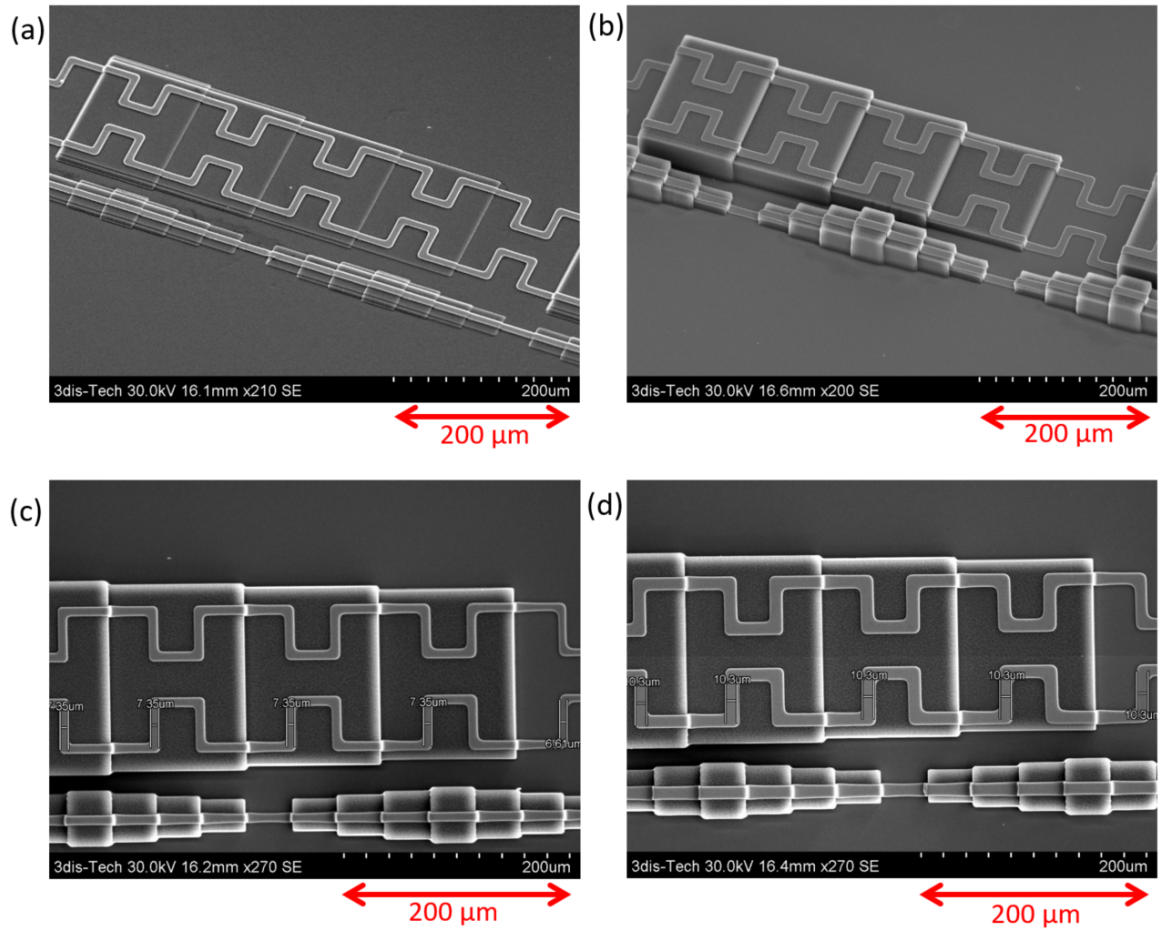


Fig. 8.5. SEM images of 3DiS samples 3 and 4 (images courtesy of 3DiS). (a) Angled view of sample 3 (1 μm layer-to-layer). (b) Angled view of sample 4 (10 μm layer-to-layer). (c) Top view of sample 3. (d) Top view of sample 4.

minutes to acquire.

Figures 8.6 and 8.7 summarize our results on sample 3, the 3DiS short-induced sample with 1 μm layer-to-layer separation and an added short. Figure 8.6 (a) shows a magnetic field image taken of the entire area of sample 3. This SQUID scan covers an area of 10.17 mm by 0.5 mm with a 16 μm by 8 μm pixel step size and the total scan time was about 22 minutes. Here red corresponds to 0.4 μT (out of the page), and blue corresponds to -0.4 μT (into the page). As we did not know where or how the Sandia group had edited the circuit, we took this low resolution large area scan first to see if we could identify obvious regions of interest that were worth examining at high resolution.

Although we did not know how sample 3 had been modified, we did know what the unmodified sample was designed to look like, and this was crucial to identifying the location of the short. Figure 8.5 (c) shows a top-view SEM image of a small section of sample 3. In the original design, the path entered from the top left, went horizontally across the sample from left to right while meandering up and down on five layers and in the x - y plane. The path then went back from right to left, and then from left to right one more time before exiting the sample on the right. Examining the raw large-scale SQUID image in Fig. 8.6 (a) we see that about 1.6 mm from the left edge of the image the horizontal meandering section signal suddenly grows weaker, and a weak path continues to the right before it wraps around and rejoins a strong section of the path on the left side of the sample. This behavior suggests the presence of an additional current path connecting the upper and lower meandering sections. In other words, the scan reveals an induced short in the structure. The magnetic field to the right of the short is weaker as some of the current in the structure is diverted through the short.

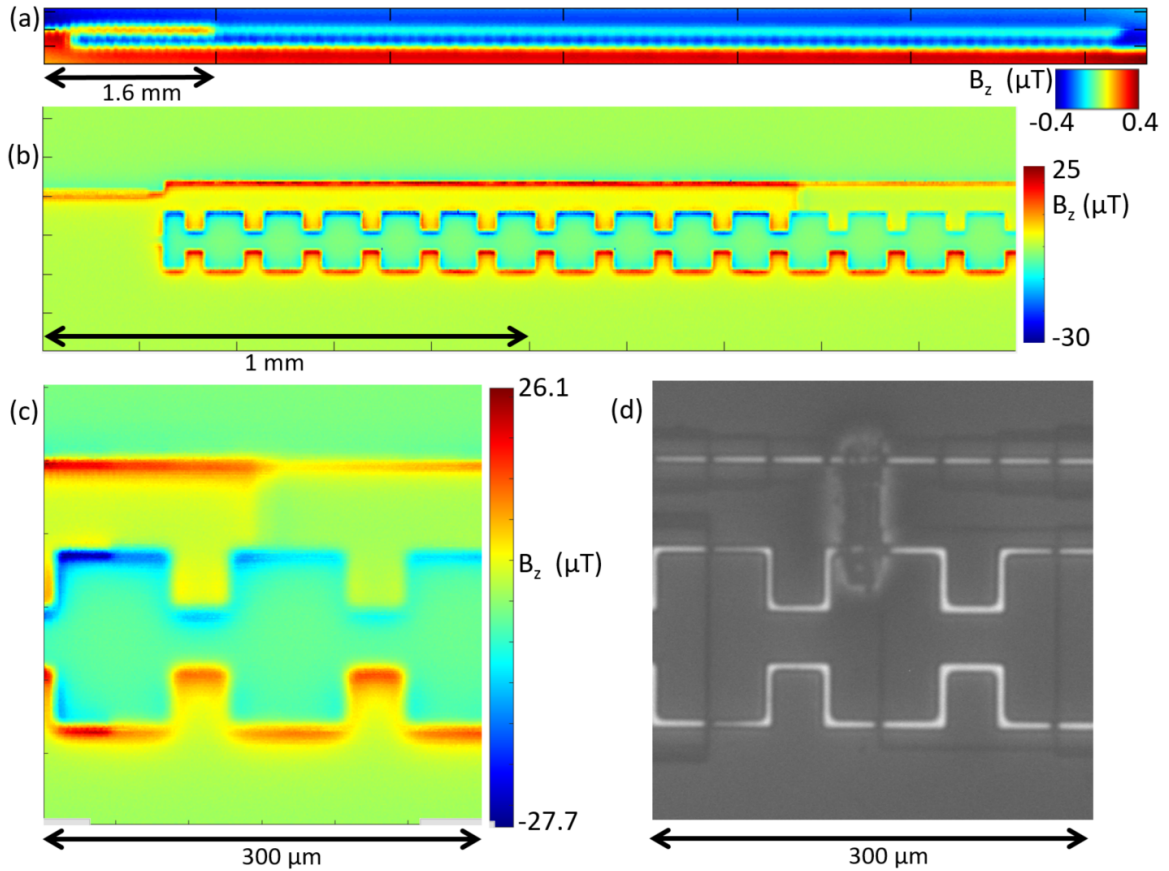


Fig. 8.6. (a) A coarse SQUID scan of sample 3 quickly pinpointed the problem region, 1.6 mm from the left edge. The pixel size was 16 μm by 8 μm and the total area was 10.1 mm by 500 μm . (b) In contact spin-valve scan of a smaller region around the short. Resolution of 2 μm by 4 μm , total area of 2 mm by 500 μm . (c) In contact high resolution scan (1 μm pixel-to-pixel distance) of the shorted area. (d) Optical image from the MAGMA system showing the short created using FIB.

Subsequent images of sample 3 were taken with the spin-valve sensor. Figure 8.6 (b) shows a second image with a medium level zoom (2 μm by 4 μm pixels), and Fig. 8.6 (c) shows an even smaller region centered on the short's location and acquired with high 1 μm by 1 μm pixel size. Each of these images took about 15-20 minutes to acquire. At this point in the process, the lateral position of the short was very well resolved, and all that was left was identifying the vertical layer in which the short was located. Considering the CAD layout of the sample and the lateral location of the short deduced from the magnetic image, it was likely that the short was on the lowest layer. Nonetheless, I applied the 3D Solver technique to get confirmation of the short's layer, as in general the lateral location of a short would not be enough to deduce its depth.

Figure 8.7 shows the results from the 3D Solver analysis which was performed on the scan in Fig. 8.7 (a). This spin-valve scan covered a 300 by 300 μm area around the short. Figure 8.7 (b) shows the reconstructed magnetic field from the best fit path. To find this path, a starting path was drawn by hand by following then obvious currents. We then iteratively applied the parameter search, z search and corner search until the test path had correctly captured most of the image. Comparing Fig. 8.7 (a) (the data) and Fig. 8.7 (b) (the fit) we see that they are very similar. As expected, the best fit path had the short in the lowest layer (layer 5). We also found the best fit wire width b for the short was about 21 μm , substantially wider than the 7 μm width of the rest of the path. Figure 8.7 (c) shows $B_{fit} - B_{data}$, the difference between the field from the best fit path and the data. The difference is typically small, with the larger discrepancies tending to be horizontal streaks likely due to position or tilt noise from the sensor. Figure 8.7 (d) shows the reconstructed path superposed on the MAGMA optical image. As we can see, our reconstructed path

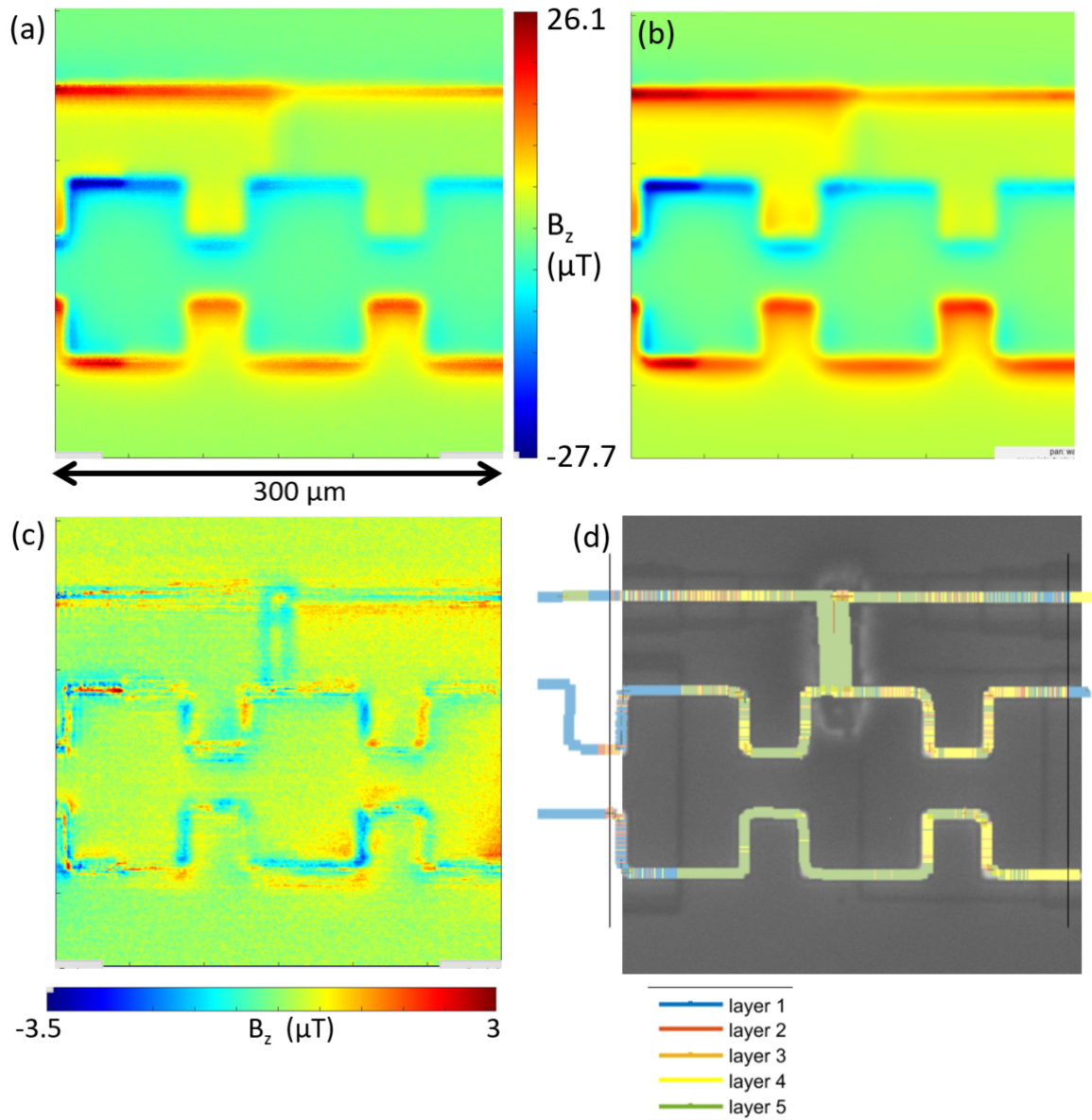


Fig. 8.7. (a) High resolution ($1 \mu\text{m}$ by $1 \mu\text{m}$) magnetic scan of $300 \mu\text{m}$ by $300 \mu\text{m}$ area around the short in sample 3. The current is split between the vertical short and the branch going to the right. (b) Simulated magnetic image created from best fit path and parameters. (c) Difference magnetic field image between measured image and reconstruction from best fit path. (d) Best fit path superposed on optical image from MAGMA system. The location of the short in the reconstructed path matched that in the optical image.

lines up very well with the circuit visible on the optical image, including the induced short. The short was on the indeed on the lowest layer and the width of the short as seen on the optical image compares well with the best fit value of 21 μm (see Table 8.3).

This example provided a very realistic test of the 3D Solver. The magnetic images were obtained by one member of our team, who could see optical images of the sample, but the magnetic images were analyzed by members of our team who did not view the optical images and had limited time of a few hours to complete the analysis. Needless to say, all this made the inversion more challenging than would have been the case otherwise. The 3D Solver had some difficulties placing segments in the middle layers in their correct layers (see Fig. 8.7 (d)), however it did a good job with segments in the top and bottom-most layers and if we had used a longer segment length for the reconstruction the resulting path would have been much cleaner. We found that the short was located in the bottom-most layer, and this was later confirmed by the team at Sandia. In the end we “passed” the evaluation and these results established the viability of detecting and localizing an unknown circuit modification in a 5-layer 3D test sample.

The best fit parameters for sample 3 are summarized in Table 8.3. Note that on top of a good match with the nominal layer-to-layer separations, the actual layer-to-layer separations were later measured via FIB. We found a very good match between the layer-to-layer separations measured via the MAGMA system and FIB. In particular, the four nominal layer-to-layer separations on this sample were 1 μm and the 3D solver was able to extract these separations to a few percent. Finally, I note that the SQUID and spin-valve images were all of high quality and largely free from artifacts and distortion.

A similar analysis was performed on sample 4 which also had 5 layers but with a

Table 8.3. Best fit parameters for sample 3 – modified 5-layer 3DiS sample with added short and 1 μm layer-to-layer separation.

MAGMA parameters		fit scan parameters		fit value	nominal values
image x length (μm)	300	z (μm)	2.55	2	
image y length (μm)	301	ϕ (sensor)	97.74	90	
x step size (μm)	1	θ (sensor)	49.10	0	
y step size (μm)	1	g	-1.97	1	
# x pixels	301	σ_B (nT)	236.00	200	
# y pixels	302	xoffset (μm)	1.33	0	
sensor type	7	yoffset (μm)	-0.24	0	
		θ (sample)	0.03	0	
		χ^2	8.27E+05	9.00E+04	
Wire parameters					
Name	infeed	middle	outfeed	short	
I (μA)	500	267	500	233	
w_x (μm)	1	1	1	1	
w_y (μm)	1	1	1	1	
b (μm)	7	7	7	21.3591	
# of segments	451	1050	1530	72	
# of layers	5	5	5	5	
h_{1-2} (μm)	1.04	1.04	1.04	1.04	
h_{2-3} (μm)	1.01	1.01	1.01	1.01	
h_{3-4} (μm)	0.96	0.96	0.96	0.96	
h_{4-5} (μm)	0.9	0.9	0.9	0.9	

layer separations	nominal	best fit	measured by FIB	% difference	absolute difference
h_{1-2} (μm)	1	1.04	1.11	6.51%	0.07
h_{2-3} (μm)	1	1.01	1.05	3.88%	0.04
h_{3-4} (μm)	1	0.96	1.13	16.27%	0.17
h_{4-5} (μm)	1	0.9	0.92	2.20%	0.02

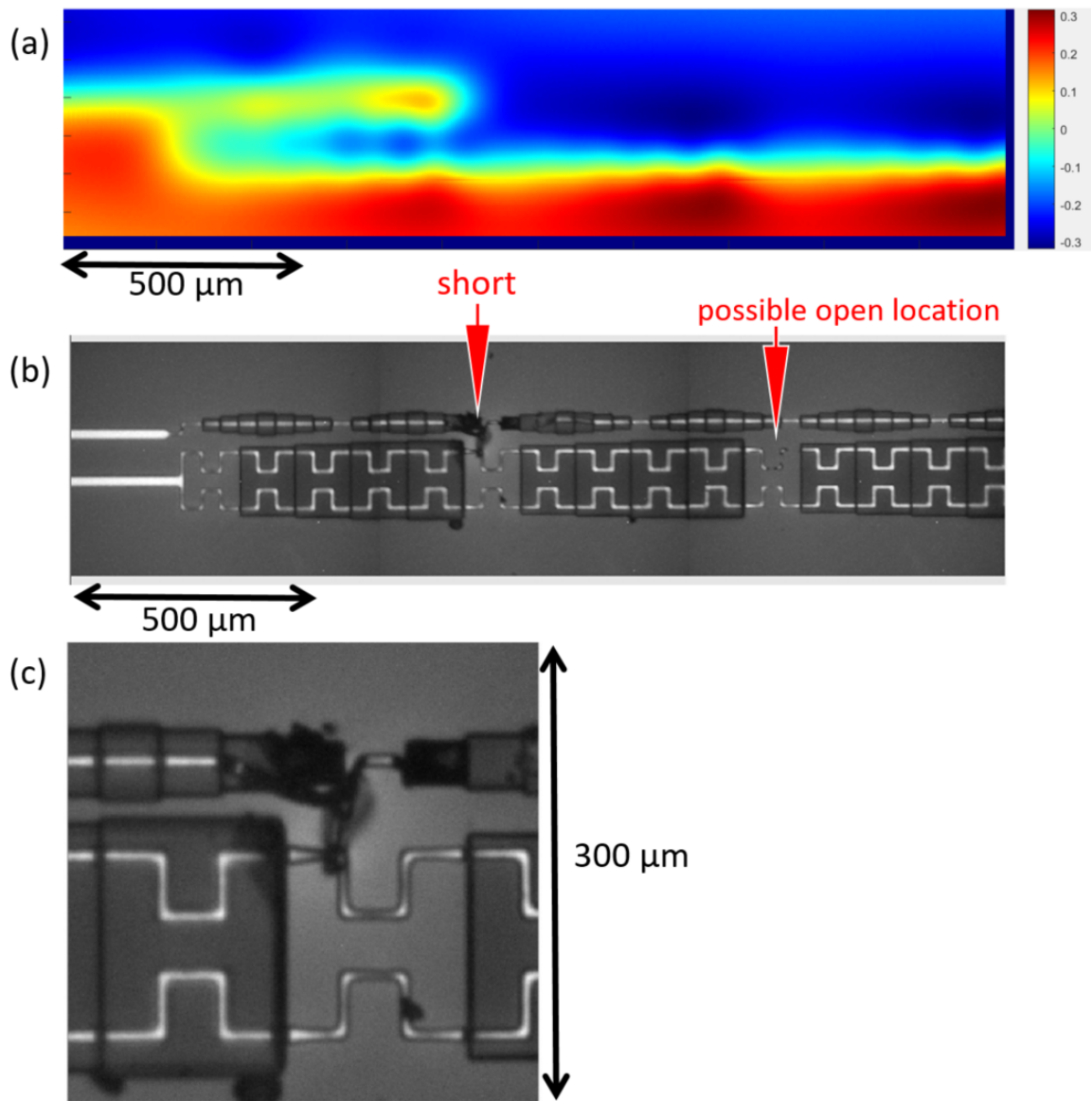


Fig. 8.8. (a) Medium area SQUID scan shows that the current does not follow the metal-
 lization in sample 4 as designed. A short connects across the designed path about 300 μm
 from the left edge of the scan. False color scale in μm . (b) Optical image from MAGMA
 system shows the location of the short and confirms the location found from the SQUID
 scan. (c) Optical image from MAGMA software shows the short and nearby sections of the
 path.

nominal 10 μm layer-to-layer separation. Figure 8.8 (a) shows an initial SQUID scan of the left half of sample 4. This reveals that the current in the sample did not follow the left-right-left-right path designed for this sample. Instead, the path abruptly changes course about 800 μm from the left edge of Fig. 8.8 (a). This suggests that a short has been added at that location and this short connected the upper horizontal section of the meandering path to the middle horizontal section. Figure 8.8 (b) shows an optical image of the sample. The induced short is clearly visible and its location matches with that suggested by the magnetic image. Figure 8.8 (c) shows an optical image of the short in more detail. As in the analysis of sample 3, the optical images of sample 4 were not available to the analysis team until after we had completed the analysis.

I note that, unlike sample 3, in the magnetic image of sample 4 there did not appear to be any field detected in the bypassed section of the path to the right of the short. This suggested that there was an open on the bypassed section of the path, or that this section had a very high resistance so that all the current went through the short. It is likely that this open was created when the modification to the sample was made, but its location was not revealed by the magnetic scans. To pin down the location of the open from a magnetic scan, one would have to use an opens detection technique such as Neocera's high frequency magnetic imaging technique [101], but this was outside the scope of this evaluation.

Once the location of the short was identified from the large scale magnetic image shown in Fig. 8.8 (a), we used the spin-valve sensor to acquire a high resolution (1 μm by 1 μm) image of a 300 μm by 300 μm area around the short (see Fig. 8.9 (a)). Table 8.4 summarizes the parameters for this scan. Although the designed path was similar to that in sample 3, as the Sandia team chose to edit both samples in a similar location, there were

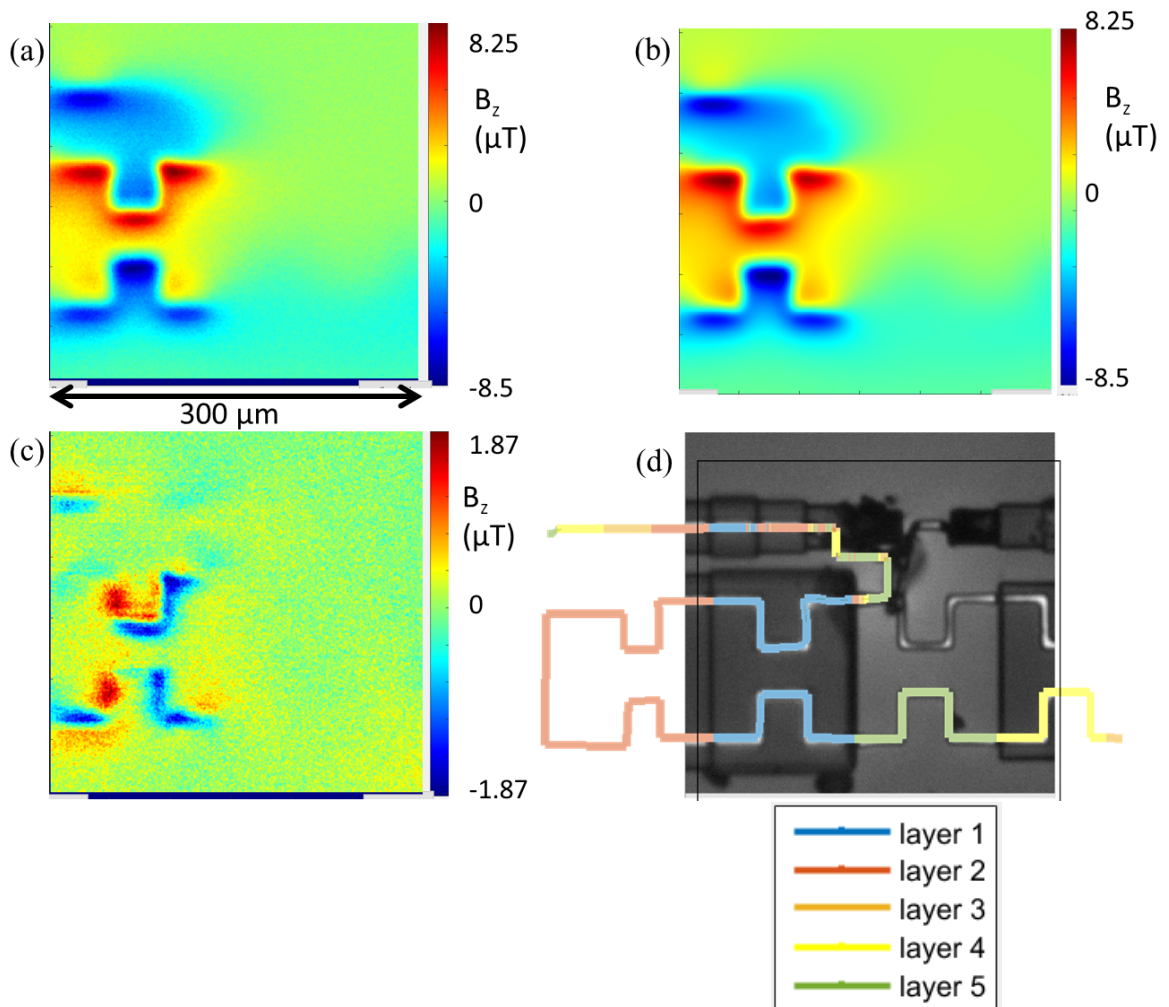


Fig. 8.9. (a) High resolution ($1\ \mu\text{m}$ by $1\ \mu\text{m}$ pixels) magnetic scan of $300\ \mu\text{m}$ by $300\ \mu\text{m}$ area of sample 4. All the current appears to be diverted to the short, which suggests that the section of path to the right of the short has an open somewhere. (b) Magnetic image created from best fit path and parameters. (c) Difference between measured field and that reconstructed from best fit path. (d) Best fit path overlaid on top of optical image from MAGMA system with color indicating the layer depth.

several obvious differences. First, there was no split current branching off to the right side of the image. This makes the analysis considerably easier, as I only needed to deal with one continuous current rather than a branching current path. Indeed, I only used a single wire in the inverse for sample 4, as opposed to four wires in the inverse of sample 3. Second, the layer-to-layer spacing was 10 μm in sample 4 as opposed to 1 μm in sample 3. This made it much easier to distinguish the top layer segments, but more difficult to see the bottom layers as they were 40 μm away.

To invert this scan, I first wirized the image by drawing the suspected path by hand. From the larger area scans I had an idea of the path layout outside of the scan area and I already knew that there was no current through the normal metallization path that normally goes off to the top right of the image. I then iteratively applied corner searches, parameter searches, and the z search algorithm. I focused the z search algorithm around the region of the short since this was the region we were most interested in. Unlike in sample 3, I did not use a separate wire for the short. This meant that I could not adjust the wire width b of the short independently from the wire width of the normal metallization, and the inverse likely suffered from this. If I were to redo the analysis I would include a separate wire for the short in order to be able to adjust its wire width.

Since this analysis was part of our final report to IARPA, I kept track of the analysis time, which was about 5 hours on this sample. The best fit path produced the magnetic image shown in Fig. 8.9 (b). Figure 8.9 (c) shows the resulting difference image ($B_{fit} - B_{data}$). Significant differences remain but the path has clearly captured most of the signal and most of the difference image appears to be noise. Given the time constraints, the fit was judged to be good enough to locate the short, which was the goal of the inversion. With more

Table 8.4. Best fit parameters for sample 4 – modified 10 μm sample with added short.

MAGMA parameters		fit scan parameters	fit value	nominal values
image x length (μm)	307	z (μm)	10.12	2
image y length (μm)	302	ϕ (sensor)	81.97	90
x step size (μm)	1	θ (sensor)	43.63	0
y step size (μm)	1	g	1.89	1
# x pixels	308	σ_B (nT)	200	200
# y pixels	303	xoffset (μm)	-0.373	0
sensor type	Spin-valve	yoffset (μm)	-5.58	0
		θ (sample)	0	0
		χ^2	6E+05	9E+04

Wire parameters	
Name	wire1
I (μA)	499.776
w_x (μm)	1
w_y (μm)	1
b (μm)	7
# of segments	1747
# of layers	5

layer separations	nominal	best fit	measured by FIB	% difference	absolute difference
h_{1-2} (μm)	10	11.94	11.39	4.71%	0.55
h_{2-3} (μm)	10	10.04	10.46	4.10%	0.42
h_{3-4} (μm)	10	10.54	10.13	3.97%	0.41
h_{4-5} (μm)	10	10.5	10.63	1.23%	0.13

time, I could likely have obtained a better fit around the top to bottom layer via, which fits poorly and produces a large blue (negative) discrepancy. Finally, Fig. 8.9 (d) shows the best path we obtained overlaid on the optical image. Evidently, the path matches the optical image very well, including the location of the short added by the Sandia team. We also found layer-to-layer separations close to the FIB measured values for the sample. Our largest difference with the FIB measured values was $0.55\ \mu\text{m}$, which is quite good.

The analysis I performed on images of samples 3 and 4 show that both the spin-valve sensor and SQUID were able to identify the location of shorts and discern key parameters on a 5-layer path. Of course, to identify what is part of the intended circuit and what is an unintended short, the original layout must be known. The analysis of samples 3 and 4 also shows that for practical applications, a full inversion and a completely converged current map may not be necessary to identify the location of a short. Indeed, commercial users would likely be most interested in obtaining the location and depth of a short. In favorable situations, it is possible that they could get this information without going through the trouble of a full 3D inversion. For example, we did not fully invert the currents in the entire scans of the sample (Figs. 8.6 (a) and 8.8 (a)). Instead, we chose to invert the currents in a smaller region around the short (Figs. 8.6 (c) and 8.9 (a)). This made the analysis considerably easier and it is likely that a full inversion of the large-scale images would not have provided significant additional information about the short. Nevertheless, comparison of the best fit parameters to the known sample parameters provides a powerful check on the integrity of the image and the path obtained from the inverse.

8.5 Fraunhofer sample

Sample 5 is a 3-layer sample made by the Fraunhofer Institute to test its TSV manufacturing repeatability in a single sample. Sample 5 covers a relatively large area (about 1 cm^2) and contains roughly 70,000 TSVs connected in series. The TSVs in this sample are created using a microbump technique [102] which connects the 3 dies together. Our analysis of sample 5 provided insight on how the phase of the magnetic signal can be an important factor in the imaging process, and showed how the MAGMA system can be used to troubleshoot large area structures.

Figure 8.10 shows a large area (1 cm^2) scan of sample 5 with 500,000 pixels. In this sample the current is fed in through a vertical infeed which connects to the bottom left in Fig. 8.10. The current exits through a vertical outfeed at the top right of the sample. This scan reveals some interesting behavior. I note that the MAGMA system automatically collects both x and y -channel measurements when it scans. The x -channel is the signal in phase with the AC current powering the sample, while the y -channel represents the magnetic signal 90° out of phase with the current. Thus, the x -channel from the SQUID or spin-valve sensor usually carries all of the signal, and the (y -channel) which is 90° out-of-phase with respect to the drive signal is pure noise. In this case, however, we found there was a large signal in both channels.

The x -channel (Fig. 8.10) image shows the regular pattern expected for the TSV meanders. However, a closer examination reveals that the upper part of the image is slightly bluer (*i.e.* negative) than the bottom portion of the image. At the same time, the y -channel (Fig. 8.11) shows a broad, diffuse blue-red dipolar background, as well as the fine-scale

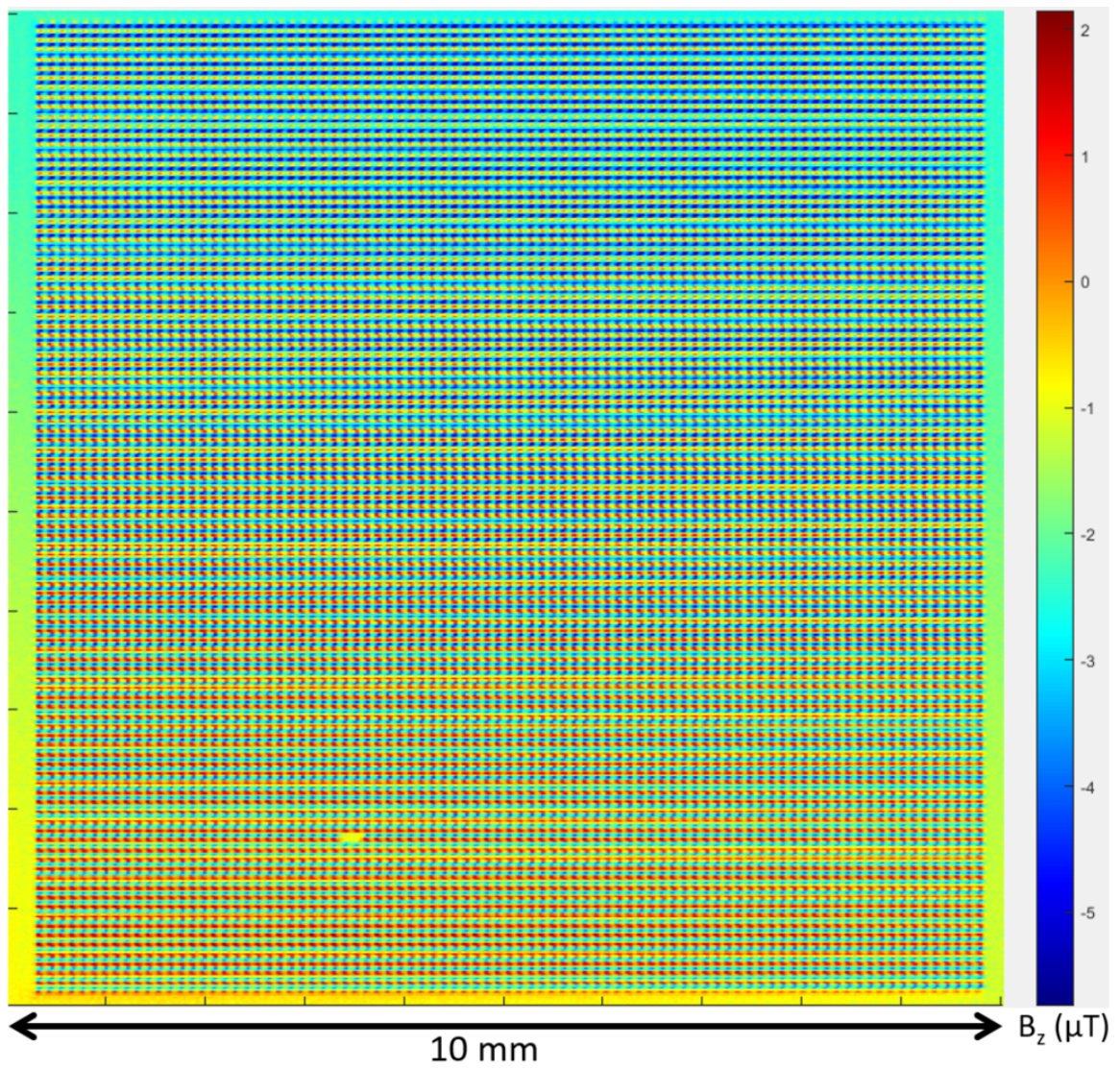


Fig. 8.10. x -channel of magnetic scan of sample 5 (spin-valve scan).

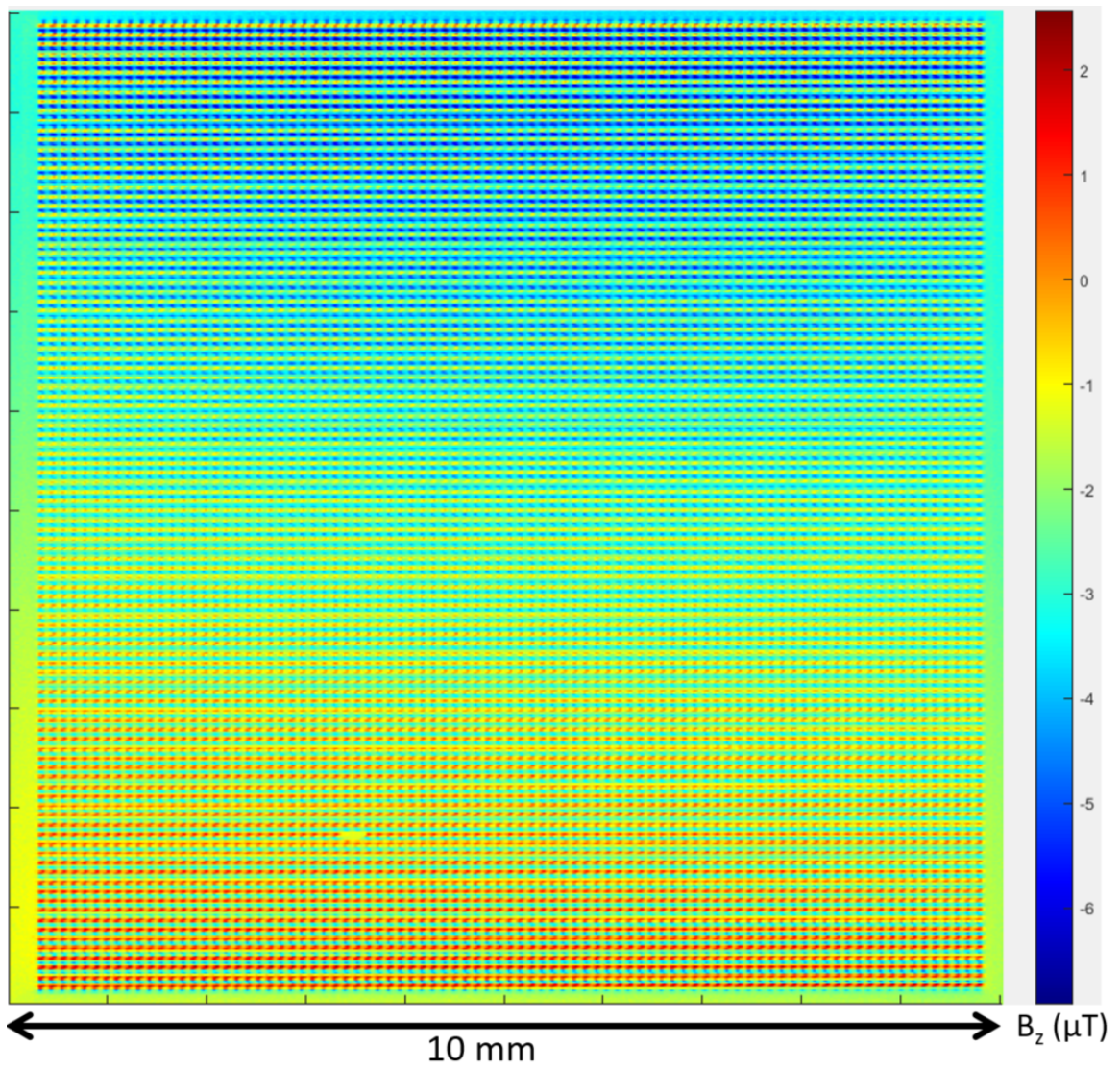


Fig. 8.11. y -channel of magnetic scan of sample 5. The x -channel should be the magnetic signal from currents running in the TSVs. The y -channel should just be noise, but instead there is a significant blue-red background in addition to some fine-scale contribution from the TSVs.

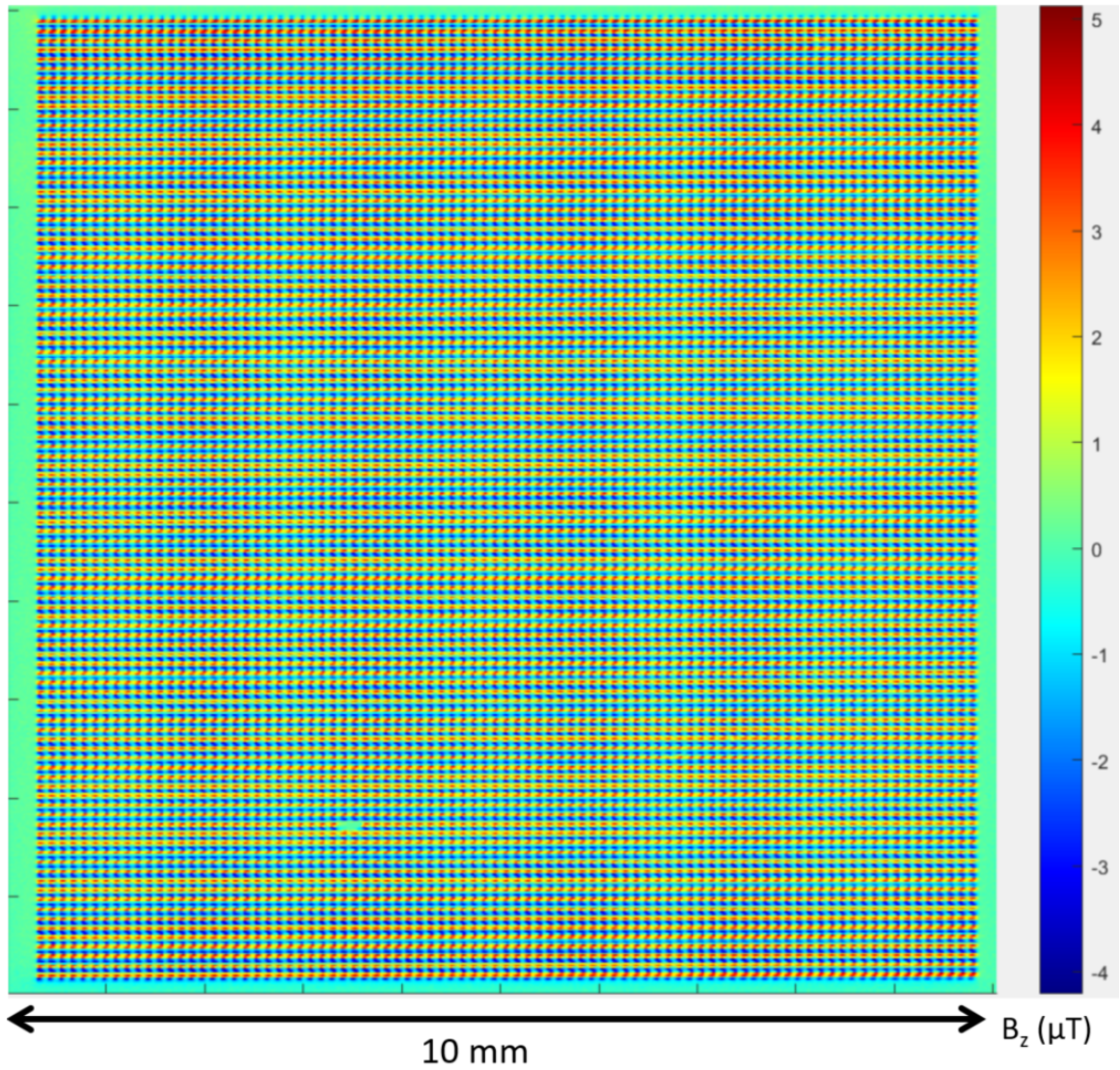


Fig. 8.12. Spin-valve signal -25° out of phase. This phase best represents the sample and gets rid of background contributions.

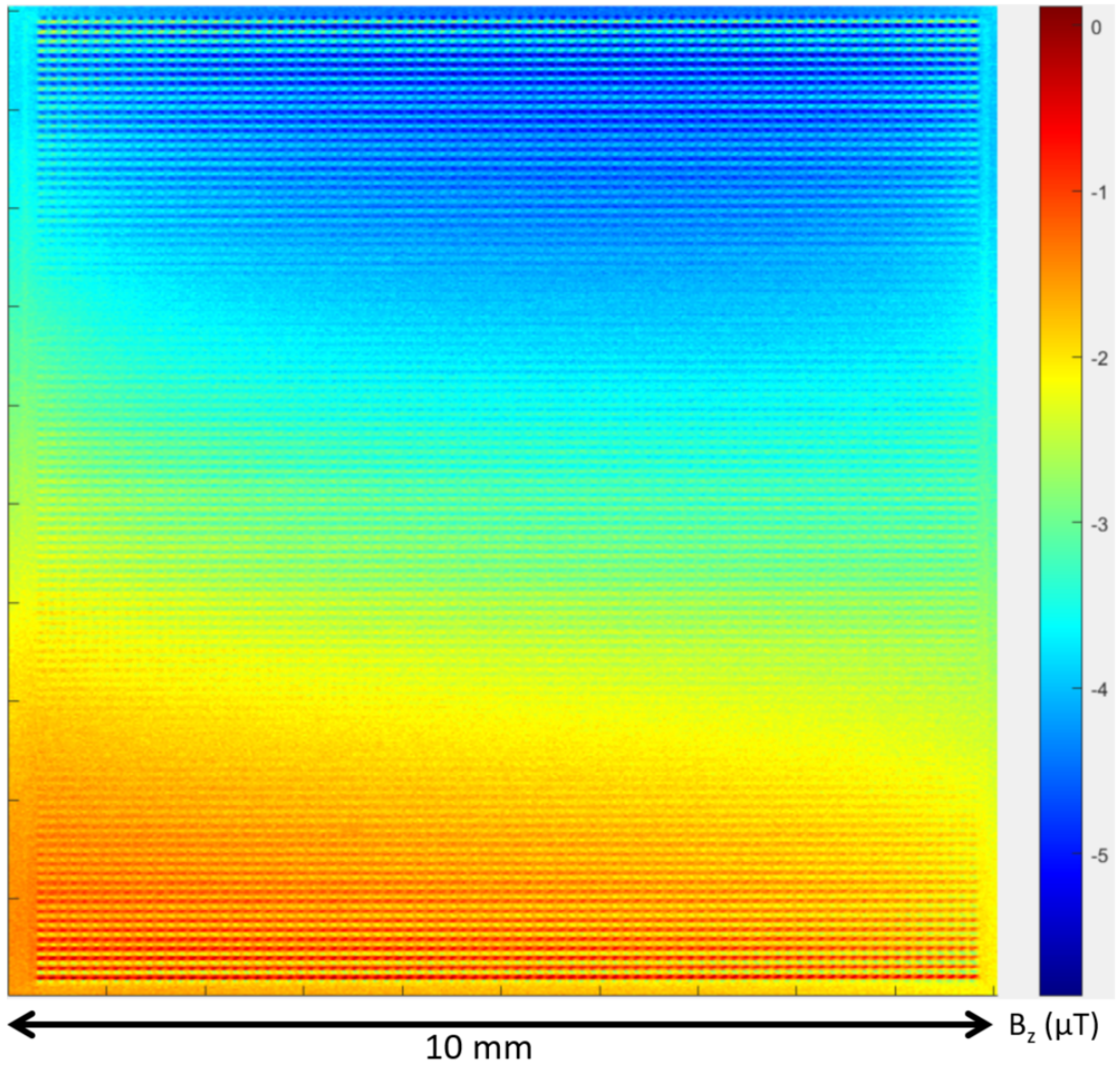


Fig. 8.13. Spin-valve signal 65° out-of-phase captures out-of-phase signal, possibly due to dielectric or capacitive leakage.

pattern due to the TSVs. The fact that there is a fine-scale pattern from the TSVs in both the x and y channels may just be due to there being a phase-difference between the drive and the current in the sample. The measurements were made at 9 kHz and the meander path is actually several meters long if you were to unfold it, and the resulting RC time constants may be contributing a significant phase shift. However, this would lead to a constant phase shift between the source voltage and field, but not a spatially varying background and cannot account for the broad red/blue dipolar background. Because this background is out of phase with the rest of the scan, it also cannot be explained by infeed or outfeed currents in the image. Two possibilities are that it is dielectric leakage or that the spin-valve is picking up a capacitive (voltage) signal.

One feature I built into the 3D Solver was the ability to take in two magnetic images for both the x and y channels and combine them to produce an image at a user-defined phase. In this case, choosing a phase of -25° from the x -channel gave the best result (Fig. 8.12). The -25° image was much cleaner and more uniform than the original AC image and the dipolar background was removed to first order. Note in particular that the background in Fig. 8.12 is uniform and shows no sign of the gradient present in Fig. 8.10. Figure 8.13 shows the image formed at $+65^\circ$ out-of-phase, where the expected TSV signal is minimized and the dipolar signal is maximized.

Getting the correct phase information is important for two reasons. First, a dipolar background introduce artifacts in the inversion process and cause problems with the fitting if we try to apply the 3D solver. The fact that the dipolar signal is out-of-phase with respect to the drive suggests that it is not a magnetic signal, or at least not due to the magnetic field produced by the current flow in the wire. To faithfully reconstruct the wire path from the

magnetic image, we need to be able to remove this out-of-phase artifact. Thus, to obtain the current path through the TSVs one should perform an inverse on the image shown in Fig. 8.12 at a phase of -25° because the dipolar component has been minimized. Second, this dipolar signal carries additional information and may be interesting for failure analysis. A significant out-of-phase signal can be due to a non-magnetic signal. One possibility is that the spin-valve sensor is acting as a capacitive pickup, which could produce a signal that is out-of-phase with respect to the magnetic field. With the relatively high resistance of the sample ($2\text{k}\Omega$), we needed to apply a 1.5 V amplitude signal to drive $750\ \mu\text{A}$ through the sample. This is a relatively large voltage, and would give a relatively large capacitive signal compared to other samples discussed here. Voltage detection could be useful for detecting the location of breaks in an open circuit. Further work is needed to understand the underlying cause of the out-of-phase signal in this sample and how it can be used.

From an analysis perspective, this sample contains about 70,000 vias. These vias are stacked in pairs (see Fig. 8.14 (b)) and therefore the minimum number of individual segments required to invert the entire image would be about 70,000, which is computationally challenging for the current version of the 3D Solver. Of course, inverting a small portion of the image would be easier except for the field produced by the path outside the region. Had a particular section of the image been of considerable interest, we could have looked at powering up just that section and imaging it in a tighter region as we did with samples 3 and 4. However this magnetic scan still gives a lot of information about the sample. Since sample 5 has a highly repetitive structure, a full inverse is not necessary to get good information about the quality of the vias.

In the magnetic scan shown in Fig. 8.12, each dipole (red and blue dot pair) corre-

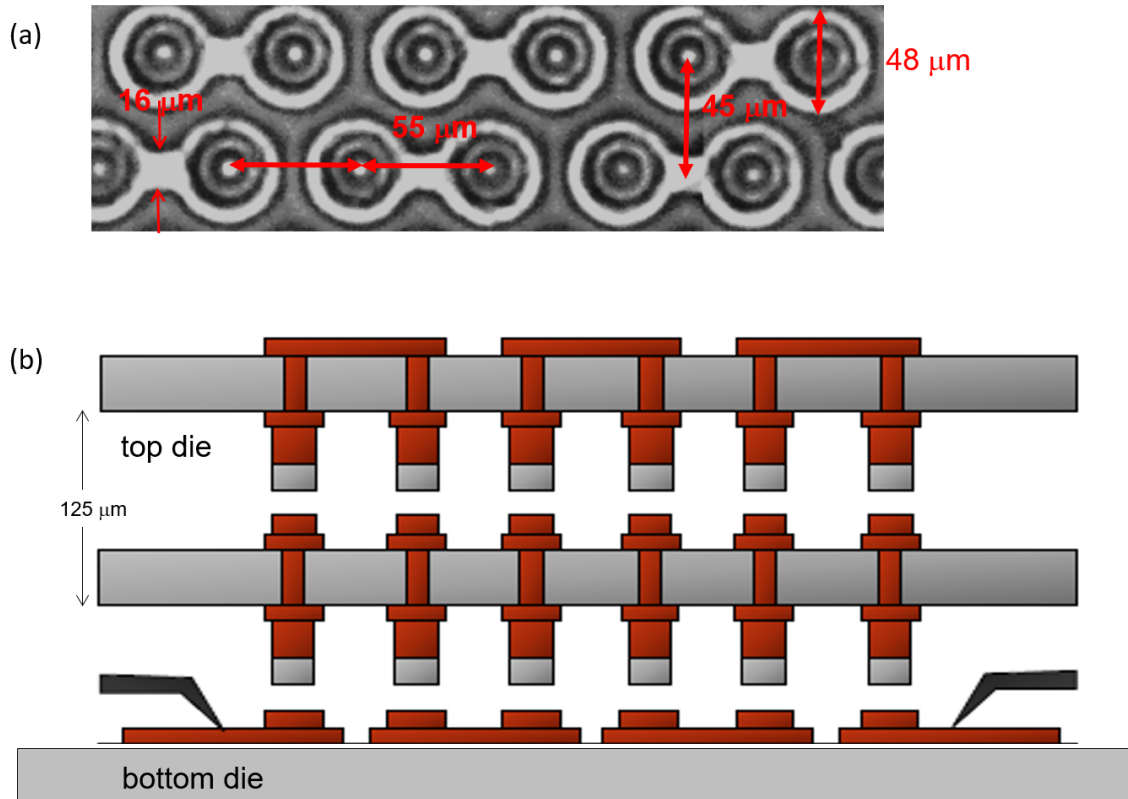


Fig. 8.14. (a) Top view optical image of sample 5. TSVs and top layer connections between adjacent TSVs are visible, while bottom layer connections between TSVs are not visible. (b) Side view schematic of metallization in sample 5 from [103]. The vias are arranged in series so there is a single continuous current path through the entire sample. The current path meanders between the top and bottom layers and passes through each of the roughly 70,000 TSVs.

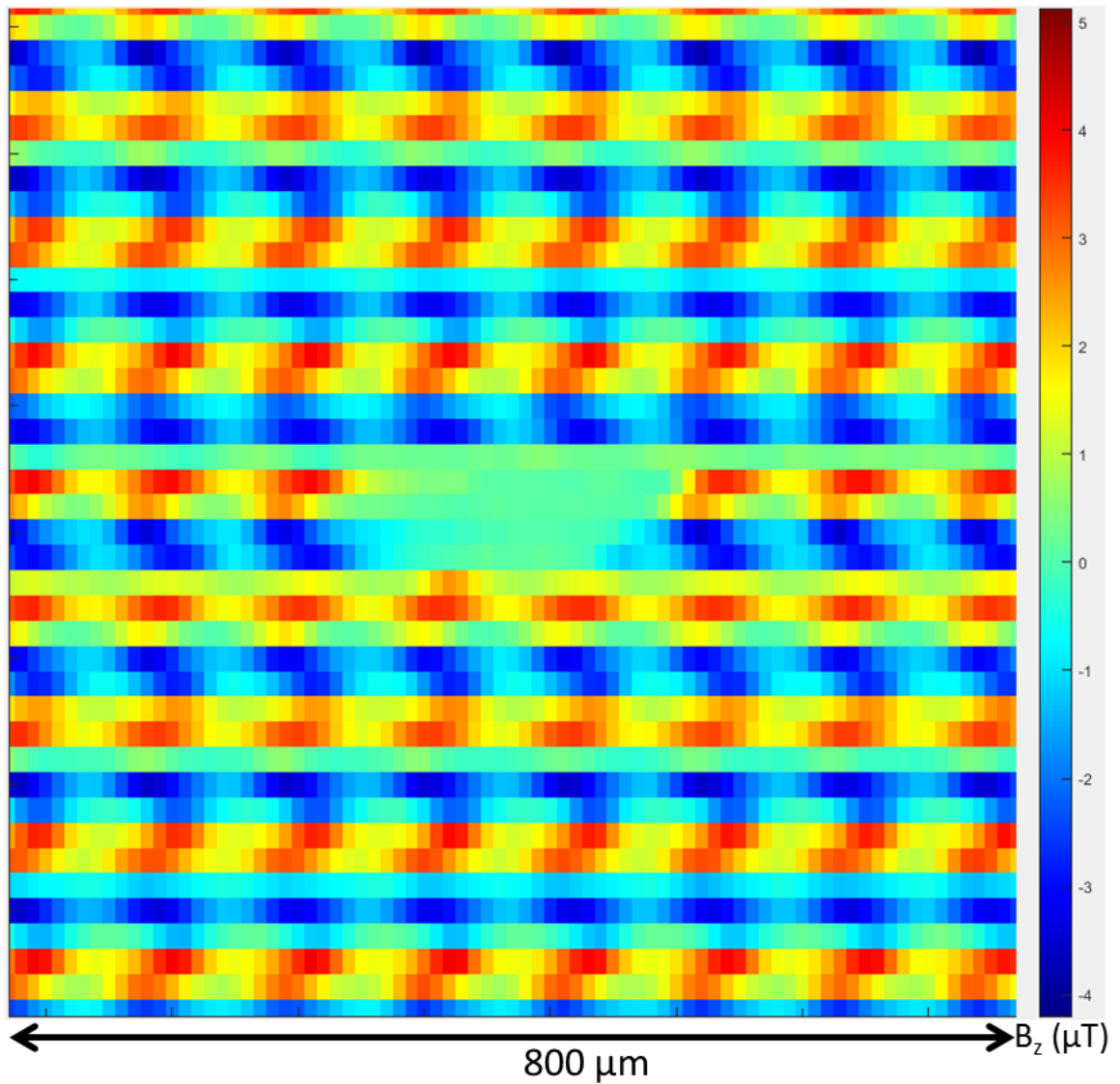


Fig. 8.15. Zoom in of small region in the bottom left of sample 5. The signal from two top-layer segments is missing, suggesting that there was a short in the lower layer at that location or that the sensor did not pick up signal in that region

sponds to a lateral segment in the top layer of the sample, which connects two TSVs (see Fig. 8.14). Close examination reveals that the entire sample is connected and the signal is spread uniformly throughout the whole die. Examining the repeatability of these dipoles, I note that there is a small region in the lower left part of the image that appears to be missing 2 top layer segments (see detailed view in Fig. 8.15). In this case, it is unclear if there a short on the lower section bypassing a few vias entirely, or if there was a problem with the scan itself rather than the vias. To find out, we could re-image the sample. If the new image contained the missing top segments, this would indicate that the problem was with the original scan rather than the vias. A more quantitative analysis could also be done using the solver. One could also fit each dipole to a model of the magnetic field or measure any deviations from the mean dipole signal. Having identified the location of potentially defective vias, one can then use a tool such as an FIB to cross-section the sample at that location and understand the precise nature of the defect.

8.6 Conclusions

In this chapter I presented five multi-layer samples with scans taken using SQUID and spin-valve sensors, and discussed the analysis of their images using the 3D Solver. In particular, I demonstrated the use of the 3D Solver search routines on magnetic scans of these samples, and used the solver to reconstruct the 3D current paths that produced the field and to determine key sample parameters such as the layer-to-layer separations. My analysis showed that the MAGMA system and the 3D Solver are effective tools to analyze samples with lateral pitches on the order of a few μm , and with layer-to-layer separations

between 1 and 10 μm , which is a technologically interesting size scale. I showed in blind tests that the 3D Solver is an effective tool for finding shorts in a sample provided you have a reference for what the original, undamaged circuit looks like. I also showed that magnetic imaging is an effective tool for large area analysis of tens of thousands of TSVs.

Chapter 9: Future Work and Conclusions

9.1 Future work

Magnetic imaging has proven to be a useful tool for Fault Isolation/Failure Analysis and this application will likely continue to drive the development of the MAGMA platform. Here, I briefly discuss some possible next steps in this development.

One major change that would significantly improve the microscope's performance would be to use sensor arrays. A cellphone camera sensor typically has about 10^7 pixels. In contrast, the MAGMA system uses a single SQUID or a single spin-valve sensor to image a sample. With a single sensor, images which usually take about 15 minutes to acquire. This imaging time was chosen as a compromise between noise performance and the maximum time that a busy engineer might think is reasonable. Using an array of sensors has the potential to make the scanning time as fast as taking a picture. Alternatively, if scanning time is plentiful, then the extra time can be used for improved resolution or lower noise. A sufficiently closely packed array of sensors would allow one to forego scanning completely. This would greatly reduce the position noise of the scanning stages, which is a significant noise source in our present system [35]. Sensor arrays may also be the key to scanning at submicron resolutions as spin-valve sensors are about 50 nm thick. Using an array would potentially allow high resolution on large areas.

Making arrays of spin-valve sensors or SQUIDs is not particularly difficult. In fact such sensors are already made in large batches using standard photolithographic processes [104, 105]. The main challenges lie in developing an effective multi-sensor read-out system and a robust positioning mechanism for getting the sensors close to a sample and minimizing position noise. Unlike CCDs, where charge accumulates and to be read out in a sequential fashion [106], readout in a SQUID or spin-valve array must be continuous to be able to take full advantage of the sensors' low noise. At present, individual sensors are read-out using what is effectively a hardware or software lock-in amplifier. While the use of a software lockin should simplify readout of multiple devices, ultimately this read-out method is not obviously scalable cheaply to thousands of sensors, and a new scalable approach would be desirable.

Another major area where more work is needed is on the inverse problem. We now have at our disposal two partial inverses. The "standard inverse" allows us to quickly invert currents constrained to a single layer. The 3D Solver inverse allows us to invert currents that are constrained to a Manhattan grid geometry. Some natural questions to ask are: what other partial inverses can we use? Is there a choice better suited to failure analysis? Are there advantages to combining these different approaches?

We have partial answers to these questions. The set of current distributions in a finite volume can be thought of mathematically as a group [107]. The operation on this "current" group is adding current distributions together. Its identity element is the zero current distribution. Similarly, the set of all possible magnetic field measurements in the plane of the sensor also forms a group. The addition of magnetic fields is the operation on the "image" group and the identity element is zero magnetic field.

There are some things we can understand about these groups. The Biot-Savart law is a linear operation, that is $B(J_1 + J_2) = B(J_1) + B(J_2)$. Thus it defines a homomorphism [107] between the current group and the image group. This homomorphism is surjective and its kernel is not trivial. The kernel \mathcal{K}_{BS} of the Biot-Savart law homomorphism is the set of current distributions that produce no magnetic field in the imaging plane.

Finding \mathcal{K}_{BS} , and using it in combination with any one partial inverse would essentially fully solve the magnetic inverse problem. To see this, suppose J_{sol} is the solution to a magnetic measurement B_{data} . Then $\forall J_k \in \mathcal{K}_{BS}, J = J_{sol} + J_k$ is also a solution. Conversely, if J is also a solution, then $J = J_{sol} + J_k$ for some $J_k \in \mathcal{K}_{BS}$. Thus one could use \mathcal{K}_{BS} along with any one partial inverse to find all the possible solutions to a particular magnetic measurement, as having the kernel allows you to go from any one solution to any other.

Other incremental modifications could also be implemented to improve the system. On the hardware side, many small improvements can be made to the SQUID-associated parts of the detector system. In practice, the main limitation to the SQUID resolution is its distance to the sample rather than its sensitivity. Therefore improvements should mainly be aimed at bringing the SQUID closer to the sample by reducing the SQUID-to-window distance.

One way to bring the SQUID closer to the sample would be to have a smaller SQUID chip. Currently the SQUID chip is about 1 mm by 1 mm. This is a relatively large surface and getting it tens of μm or less away from the window requires extremely precise levelling. A smaller chip would not need as precise a level. In contrast, the SQUID itself is only 30 μm on a side. The most space consuming part of the SQUID chip are the contact pads; there are four of them and they are each about 0.1 mm by 0.1 mm (see Fig. 6.7). The pads

are so large because we need to get a low resistance contact between the SQUID and its bias leads so that we do not lose output signal from the SQUID. If the contact resistance could be lowered through better fabrication or if it was possible to move the pads to the sides of the tip, we could make a drastically smaller chip, and more easily bring the SQUID close to the window. We could also then use a thinner, smaller window. Unfortunately, getting good YBCO to grow over the edge of the chip is difficult due to the need to have the YBCO grow with the correct crystalline lattice structure in order for it to be superconducting at 77K. Another approach that allows the contacts to be moved out of the way is to use an “x-SQUID” [87], which would involve placing the SQUID on the side of the tip instead of on its face.

Additionally, because the SQUID in the MAGMA system is housed inside an aluminum cone that holds the thin window, it is hard to determine precisely how close the SQUID is to the window. In order to better measure and control the window, one could add a wire to the window and use this as a window locator. By passing current through the wire, and then scanning the window with respect to the SQUID by using the x and y window control assembly, one could image the field from the wire. Fits to the resulting data would reveal the distance between the SQUID and the window. While scanning samples, no current would be applied to the window wire and it should not affect sample scans. We did some proof-of-principle tests of this idea and found that we should be able to achieve an accuracy of around 1 μm for the window-to-SQUID separation, and this accuracy can likely be improved. This approach could also be used to calibrate the SQUID gain and check the window level. This could potentially allow us to break the 45 μm barrier in SQUID-to-sample distance and simplify the set-up and operation of the window control.

Another factor that limits the SQUID-to-window distance in practice is debris that falls onto the window. Debris can prevent us from bringing the SQUID close to the window and requires warming up the system to remove, which is a relatively time consuming process. Incorporating a “dust catcher” into the tip or cone walls could reduce the amount of debris falling onto the window, thereby allowing closer proximity between the window and the SQUID and letting the system run at consistently tighter SQUID-to-window distances.

While sensor-to-sample distance is a major limitation for the SQUID, the situation is quite different for spin-valve sensors. Since we are already able to bring spin-valve sensors 1-2 μm away from the samples (see [Chapter 7](#)) and our magnetic inverse further sharpens the resolution of the current path, reducing the separation is not a major issue provided we don't need significantly better resolution. Instead, our spin-valve sensors would significantly benefit from better signal-to-noise performance.

If resolution better than 1-2 μm is needed, smaller spin-valves would help. The sensors we use are between 2 and 6 microns long. We believe that the current design would scale down to sensors about 500 nm in length, but more work is needed to see how much current can be applied without destroying the device and how the resulting S/N scales.

It is interesting to note that for the standard inverse, improvements in sensitivity only yield logarithmic improvements in resolution (see Eq. (2.60)). However, scaling of the resolution with the S/N is much more favorable for the 3D inverse (see [Section 3.7](#)), and sensitivity gains are worth pursuing. One limitation to the sensitivity of the spin-valve sensors is the amount of current that can be passed through them. Passing more current through the sensors would increase our signal. Unfortunately, Neocera has found that passing more than 1 mA can reduce the life of the sensor [[108](#)]. We need to gain a better

understanding of how sensor breakdown is happening. If heating is the issue, then placing a heat-sink on the sensor might allow us to increase the current and the sensitivity.

Another way to get more sensitivity is to use a larger sensor. However since sensor size limits spatial resolution, there are real trade-offs. One way to avoid this trade-off is to use a dual sensor approach. With a small sensor and a large sensor on the same chip, one can get both high sensitivity and high spatial resolution. In this scheme, the spin-valve chip would have a small spin-valve sensor as close as possible to the sample, giving good spatial resolution, while also having a larger, secondary spin-valve sensor for good sensitivity. SQUID and spin-valve dual scans can be useful, but we have yet to demonstrate similar benefits can be achieved for dual spin-valve sensor scans.

There were some other issues with the spin-valve sensors. As discovered in the course of the project, field detection using spin-valve sensors is not as straightforward as with SQUIDs. Specifically, we need to better understand why the spin-valve sensor measurement direction is tilted and somewhat unstable. A complete field detection study, and tests such as torque magnetometry [109] could help us better understand what is going on and devise a fix. In addition, the flexibility of the cantilever that holds the sensor introduces tilt noise, which together with position noise results in a significant increase in the sensor noise.

On the analysis side, many improvements can be made. The software for the current 3D Solver is a prototype of what a commercial tool could look like. While it has good scientific capabilities, the user interface needs more development to make it truly usable to FA engineers. Right now, many manual steps are required, which increase the difficulty and effort needed to do analysis. Many of these steps can be automated. Full automation

of the 3D Solver would require more research; although most of the individual steps can be automated, the order of operations matters and it appears to be very challenging to develop a fully automated package.

More effort could also be put to speeding up the calculations. Achieving reasonable run-time has been a major limitation of the more ambitious path searching algorithms of the solver. Improving the efficiency of the algorithms and using more powerful computers to run the inverse are obvious ways to shorten the time to find a solution.

It would also be useful to develop the capability to search multiple scans simultaneously. Right now we analyze scans independently, but it is possible to run the parameter search and path search algorithms on multiple scans simultaneously (*i.e.* optimizing the combined χ^2 from two or more scans at the same time). The way to do this is straightforward, but it would require significant modifications of the existing software.

Another interesting idea is to link the inversion software with the scanning software. For example, a noisy low resolution preliminary image could be quickly acquired and analyzed to identify interesting areas that would be worth scanning at higher resolution. This would help by resulting in lower noise in parts of the image that matter, while keeping the total imaging time reasonable. Figuring out how to do this in a methodical and automated way would allow us to optimize the total scanning time.

It would also be interesting to try to extend the 3D Solver technique to open circuit failure localization [101], and incorporate information from Space Domain Reflectometry [110], an open-failure detection technique.

Another interesting avenue is to focus less on inverting the currents and more on finding defects, which is subtly not the same thing. In many cases, it is not actually

important to get a full current map, as the user may already have the CAD design. Rather, what is important is to precisely locate a defect. Using available CAD information to generate an accurate “model” magnetic field could allow one to find the location of defects without inverting the field. Similarly, a “correlation” technique where one powers different pins, all of which have a shorting path in common, can reveal the short location while leaving out signal from non-shortened paths.

Finally, while our work shows proof-of-principle applications of 3D magnetic imaging, commercial acceptance of 3D magnetic imaging remains to be demonstrated. Commercial testing is ongoing, and time will tell if 3D magnetic imaging becomes a widely used technique for failure analysis.

9.2 Conclusions

In this thesis I discussed the development of a technique for obtaining 3D currents from 2D magnetic images of samples with wires that connected multiple layers. I demonstrated the viability and performance of my 3D Solver by using it to analyze multi-layer test samples and samples containing through silicon vias. I found that it is a practical method and this approach is being tested by Neocera for Failure Analysis of multi-layer test samples and 3D integrated circuits.

In [Chapter 2](#) I discussed the “standard inverse,” which was the state of the art of the field before I started on this project. I also showed how the Fourier inverse can be modified to account for sensor tilts. In [Chapter 3](#) I discuss the theoretical underpinnings of our new inverse technique, including noise considerations and the spatial resolution. In particular,

I found that the spatial resolution could be substantially better than is possible with the standard inverse.

The “standard inverse” requires the assumption that all currents are in a single plane. My new technique relaxes that assumption, and allows us to invert 3D currents. However, it introduces new assumptions, in particular the use of a Manhattan grid and discrete segments, wires, and layers. Implementing these constraints requires the use of a search algorithm instead of a closed-form expression. I used path search algorithms to reconstruct the currents in the sample, mainly the lateral search, vertical search and corner searches. Parameter searches are also critical to find the correct current paths. These algorithms are detailed in [Chapter 4](#).

In [Chapter 5](#) I introduced the 3D Solver, a matlab GUI that allows one to use all the software tools we built in one convenient place. Because the order in which the different search routines are applied is sample dependent, the routines need to be selected by an experienced operator. The 3D Solver is a prototype for what a real world solving software might look like.

As described in [Chapter 6](#), we used the Neocera MAGMA system to scan samples and obtain magnetic data. Neocera, in collaboration with my group at UMD, performed significant work to upgrade the MAGMA system to obtain the resolution, noise performance, and sensor-to-sample distance necessary to reconstruct 3D currents. Indeed, we are able to scan with the spin-valve sensor about 1.5 μm away from a sample, and the SQUID sensor 44 μm away. We are routinely able to scan at 1 μm pixel step size and 0.5 μm position accuracy [108]. Our SQUID sensors show a flux variation of 10-20 $\mu\phi_0/\sqrt{\text{Hz}}$, which corresponds to a magnetic field root mean square noise of 20-40 $\text{pT}/\sqrt{\text{Hz}}$. For typical scans

with 5-20 ms spent per data point, this translates into a 150-200 pT rms noise level in each pixel. Our spin-valve sensors show about 1000 times more noise, with a noise level of 100-200 nT/pixel.

In [Chapter 7](#), I showed that the spin-valve sensors we were using for some of the images did not pick up the magnetic field in the z direction as expected, but were consistently rotated in the in-plane direction by up to 40° . I also looked at the advantages and disadvantages of spin-valve sensors and SQUIDs for practical imaging applications. Both sensors show strengths and weaknesses. The spin-valve sensors are significantly easier to work with, and can give very high resolution results. The SQUIDs are much more sensitive and are ideal for very weak signals. The SQUIDs allow us to image more deeply buried layers because of their exceptionally low noise. The spin-valve sensors allow us to image at room temperature conditions, and let us get much closer to our sample. With both SQUIDs and spin-valve sensors, the present MAGMA imaging system can make use of the advantages of both sensors.

In [Chapter 8](#) I presented some magnetic images and their analysis with the 3D Solver. Over the course of this work, we acquired and analyzed hundreds of magnetic scans to understand how different samples and parameters affect the 3D inverse technique. I presented some representative scans and results on samples with up to 5 layers. I showed that I could resolve layer-to-layer spacings to the sub-micron level and independently resolved layers that were about $1 \mu\text{m}$ apart. I also demonstrated the ability to identify the location of shorts and defects in unknown samples.

Finally, in this chapter I briefly discussed some possible future directions for research and summarized my main results.

Appendix A: 3D Solver code

A.1 Wire class

```
1 classdef wire
2     properties
3
4         layerdepths = [0 10]%depth in microns of specific layers wrt top
           layer
5         coordSystemOrigin = [0 0]%gives the origin of the frame of reference
6         % the wire coordinates are calculated from. This value coincides
7         % with the bottom left corner of the magma scan the wire was first
8         % drawn in.
9
10        xsegmentlength
11        ysegmentlength
12
13        xpos %x, y, z positions in terms of magnetic field grid positions
14        ypos
15        zpos
16        name
17        testfield
18        wirewidth
19        wirelength %length of vectors xpos,ypos, zpos, as well as
           xcoordinates, ycoordinates, zcoordinates
20        isLive
21        isSelected
22        isDisplayed = 1;
23        identifier
24        current %current through wire in microAmps
25
26    end %properties
27    properties(Dependent)
28        totalNumOfSeg
29        layerSeparations
30        nlayer
31        xcoordinates%x, y, z positions in real microns with respect to
           startPoint
32        ycoordinates %all 3 are row vectors.
33        zcoordinates
```

```

34     longCoordinates %coordinates specified in the format x,y,z,
        segLength, segType
35     %for example: x,y, z -micron coordinates from bottom left of image
36     %segLength - micron length of segment
37     %segType: 1 =x, 2 = y, 3 = z
38     end

```

A.2 Wirization Schemes: LVC wirization

```

1  function wirizeLVC_cb(~, ~)%rename wirize_xy_meander?
2
3     [topy, topx ] = size(B_active1);
4
5     newWire = wire;
6     newWire = setNewWire(newWire);
7     newWire = newWire.old2newWire(parameters, userpar);
8     if ishandle(hcroprect)%needs to deal with optical image!!%*crop
9         pos1 = get(hcroprect, 'position');
10        pos1(3:4) = round(pos1(1:2)+pos1(3:4)-0.5);
11        pos1(1:2) = round(pos1(1:2)+0.5);
12        if previousplot == 2;%if optical image
13            xcoef = newWire.xsegmentlength/(parameters(2) - parameters(1))*((
                size(opt_image,2)-1));
14            ycoef = newWire.ysegmentlength/(parameters(4) - parameters(3))*((
                size(opt_image,1)-1));
15
16            pos1(1) = pos1(1)/xcoef - rect(1)+1;pos1(3) = pos1(3)/xcoef- rect(1)
                +1;
17            pos1(2) = pos1(2)/ycoef - rect(2)+1;pos1(4) = pos1(4)/ycoef- rect(2)
                +1;
18            pos1 = round(pos1);
19        end
20    else
21        pos1(1:2) = 1;
22        pos1(3:4) = [ topx topy];
23    end
24
25    if pos1(1) <1;
26        pos1(1) = 1;
27    end
28    if pos1(3) > topx
29        pos1(3) = topx;
30    end
31    wirexy = {};
32
33    ppsx = newWire.xsegmentlength/userpar(1);
34    ppsy = newWire.ysegmentlength/userpar(2);

```

```

35
36 [ ~, ycoord] = max(dBdy2);%gives value and index(row#) assoc. w/ max val.
    in col.
37 ycoord = round(ycoord/ppsx);
38 pos1(1) = round(pos1(1)/ppsx); pos1(3) = round(pos1(3)/ppsx);
39 %by convention we start at 1
40 for i=pos1(1):pos1(3)-1%need (-) to match the ycoord(i+1) dimensions
41     if(ycoord((i+1)*ppsx)==ycoord(i*ppsx))
42         wirexy = [wirexy {[i ycoord(i*ppsx) 0]}];% do +1 everywhere to prev.
            implementation...HK code started at 0
43     elseif(abs(ycoord((i+1)*ppsx)-ycoord(i*ppsx))==1)
44         wirexy = [wirexy {[i ycoord(i*ppsx) 0]}];
45         wirexy = [wirexy {[i+1 ycoord(i*ppsx) 0]}];
46     elseif(ycoord((i+1)*ppsx)>(ycoord(i*ppsx)+1))
47         wirexy = [wirexy {[i ycoord(i*ppsx) 0]}];
48         wirexy = [wirexy {[i+1 ycoord(i*ppsx) 0]}];
49
50         for n=1:(ycoord((i+1)*ppsx)-ycoord(i*ppsx)-1)
51             wirexy = [wirexy {[i+1 ycoord(i*ppsx)+n 0]}];
52         end
53     elseif(ycoord((i+1)*ppsx)<(ycoord(i*ppsx)-1))
54         wirexy = [wirexy {[i ycoord(i*ppsx) 0]}];
55         wirexy = [wirexy {[i+1 ycoord(i*ppsx) 0]}];
56
57         for n=1:(ycoord(i*ppsx)-ycoord((i+1)*ppsx)-1)
58             wirexy = [wirexy {[i+1 ycoord(i*ppsx)-n 0]}];
59         end
60     end
61 end
62
63 wirexy = [wirexy {[pos1(3) ycoord(pos1(3)*ppsx) 0]}];%add last endpt seg at
    outfeed
64 xwirize2 = zeros(size(wirexy));ywirize2 = zeros(size(wirexy));zwirize2 =
    zeros(size(wirexy));
65 for i = 1:size(wirexy,2)
66     xwirize2(i) = wirexy{i}(1); ywirize2(i) = wirexy{i}(2);
67 end
68 %wirearray = wire;
69     newWire = newWire.old2newWire(parameters, userpar, xwirize2, ywirize2,
        zwirize2);
70     newWire = thresholdWire(newWire);
71     wirearray = [wirearray, newWire];
72
73     updateWireControlPanel;
74     chooseplot_cb(hchooseplot);
75     %and accordingly sticks them in top or bottom layer.
76 end

```

A.3 Parameter Search

```
1 function [wireParameterSearchResults, scanParameterSearchResults] = ...
2     parameterSearchNew(scanParametersToSearchOn,
3         wireParametersToSearchOn,...
4         userpar, parameters, angle1, rect, Bdata, B_active1
5         , ...
6         data_offset, isCropped2, area_averaging, wirearray,
7         xOffset,...
8         yOffset,pos1)
9 %parameterSearchNew arguments:
10 % - scanParametersToSearchOn: structure array of logicals with the
11     following fields:
12 % z, thetaSensorRotation, phiSensorRotation, gain, dataOffset, xOffset,
13 % yOffset, sampleRotation. Each field contains a logical, either 1 or 0.
14 %
15 % - wireParametersToSearchOn: structure array of logicals with the
16     following fields:
17 % current, layerSeparations, wireWidth. the fields "current" and
18 % "wireWidth" are m x 1 arrays, where m is the # of wires in wirearray.
19 % layerSeparations is an m x n array, where n is the # of layerSeps in the
20 % wire with the most layers.
21 %* describe rest of input variables
22 %*make it so that fields that you want to search on only have to exist. ie
23 %have a section here that fills fields that aren't there.
24
25
26 %declare variables spanning nested function scopes
27 %level1Parameters %results from each search level.
28 %level2Parameters
29 %level3Parameters
30
31 numOfWires = length(wirearray);
32 numOfDataPoints = size(B_active1,1)*size(B_active1,2);%check what B_active1
33     looks like
34 B_active1_init = zeros(size(B_active1));
35 Bfit = zeros(numOfDataPoints,numOfWires);
36 Bfitx = Bfit;
37 Bfity = Bfit;
38 Bfitz = Bfit;
39 %% fill in empty slots for scanParametersToSearchOn and
40     wireParametersToSearchOn
41
42 if ~isfield(scanParametersToSearchOn,'z')
43     scanParametersToSearchOn.z = 0;
44 end
45 if ~isfield(scanParametersToSearchOn,'gain')
```

```

39     scanParametersToSearchOn.gain = 0;
40 end
41 if ~isfield(scanParametersToSearchOn,'thetaSensorRotation')
42     scanParametersToSearchOn.thetaSensorRotation = 0;
43 end
44 if ~isfield(scanParametersToSearchOn,'phiSensorRotation')
45     scanParametersToSearchOn.phiSensorRotation = 0;
46 end
47 if ~isfield(scanParametersToSearchOn,'dataOffset')
48     scanParametersToSearchOn.dataOffset = 0;
49 end
50 if ~isfield(scanParametersToSearchOn,'xOffset')
51     scanParametersToSearchOn.xOffset = 0;
52 end
53 if ~isfield(scanParametersToSearchOn,'yOffset')
54     scanParametersToSearchOn.yOffset = 0;
55 end
56 if ~isfield(scanParametersToSearchOn,'sampleRotation')
57     scanParametersToSearchOn.sampleRotation = 0;
58 end
59
60
61 if ~isfield(wireParametersToSearchOn,'current')
62     wireParametersToSearchOn.current = zeros(numOfWires,1);
63 end
64 if ~isfield(wireParametersToSearchOn,'wireWidth')
65     wireParametersToSearchOn.wireWidth = zeros(numOfWires,1);
66 end
67 if ~isfield(wireParametersToSearchOn,'layerSeparations')
68     wireParametersToSearchOn.layerSeparations = zeros(numOfWires,1);
69 end%*problem with # of layers
70
71 %% calculate # of level 3 Parameters
72
73 nWireCurrentsSearchedOn = 0;
74 for p = 1:numOfWires
75     if wireParametersToSearchOn.current(p) == 1
76         nWireCurrentsSearchedOn = nWireCurrentsSearchedOn + 1;
77     end
78 end
79
80 numOfLevel3Parameters = nWireCurrentsSearchedOn;
81 if scanParametersToSearchOn.gain == 1
82     numOfLevel3Parameters = numOfLevel3Parameters + 1;
83 end
84 if scanParametersToSearchOn.dataOffset == 1
85     numOfLevel3Parameters = numOfLevel3Parameters + 1;

```

```

86 end
87
88 %initialize matrix for level 3 search before the loop.
89 Bmatrix = zeros(numOfDataPoints, numOfLevel3Parameters);
90
91 %% search level 1 starts here
92 %unpacking variables for search level 1: z, layerdepths, wirewidth
93
94 x = []; %vector to contain all search variables for level 1 search
95
96 if scanParametersToSearchOn.z == 1
97     x = [x userpar(5)];
98 end
99
100 for m = 1:length(wirearray)
101     if wireParametersToSearchOn.wireWidth(m) == 1
102         x = [x wirearray(m).wirewidth]; %#ok<AGROW>
103     end
104
105     for n = 1:size(wireParametersToSearchOn.layerSeparations, 2);
106         if wireParametersToSearchOn.layerSeparations(m,n) == 1
107             x = [x, wirearray(m).layerSeparations(n)]; %#ok<AGROW>
108         end
109     end
110 end
111
112 if isempty(x)
113     recalc2(x)
114     level1Parameters = [];
115 else
116     level1Parameters = fminsearch(@(x) recalc2(x), x);
117 end
118
119 %% reconstruct answer here, not in other functions. keep it nice and tight.
120
121 %*initialize wireParameterSearchresults and scanParameterSearchResults. for
122 %variable parameter size (ie wireParameterSearchResults.current), make sure
123 %they are the right size.
124
125 scanParameterSearchResults = scanParametersToSearchOn;
126 wireParameterSearchResults = wireParametersToSearchOn;
127
128 %levelParameters: z, wireWidths, layerSeparations
129 q = 1;
130 if scanParametersToSearchOn.z == 1
131     scanParameterSearchResults.z = level1Parameters(q);
132     q = q + 1;

```

```

133 end
134
135 for m = 1:length(wirearray)
136     if wireParametersToSearchOn.wireWidth(m) == 1
137         wireParameterSearchResults.wireWidth(m) = level1Parameters(q);
138         q = q + 1;
139     end
140
141     for n = 1:size(wireParametersToSearchOn.layerSeparations, 2);
142         if wireParametersToSearchOn.layerSeparations(m,n) == 1
143             wireParameterSearchResults.layerSeparations(m,n) =
144                 level1Parameters(q);
145             q = q + 1;
146         end
147     end
148
149 %level2Parameters angle1; xOffset; yOffset; userpar(8); userpar(9) (sensor
150 %angle rotations)
151
152 n = 1;
153 if scanParametersToSearchOn.sampleRotation == 1
154     scanParameterSearchResults.sampleRotation = level2Parameters(n);
155     n = n + 1;
156 end
157
158 if scanParametersToSearchOn.xOffset == 1
159     scanParameterSearchResults.xOffset = level2Parameters(n);
160     n = n + 1;
161 end
162
163 if scanParametersToSearchOn.yOffset == 1
164     scanParameterSearchResults.yOffset = level2Parameters(n);
165     n = n + 1;
166 end
167
168 if scanParametersToSearchOn.thetaSensorRotation == 1
169     scanParameterSearchResults.thetaSensorRotation = level2Parameters(n);
170     n = n + 1;
171 end
172
173 if scanParametersToSearchOn.phiSensorRotation == 1
174     scanParameterSearchResults.phiSensorRotation = level2Parameters(n);
175     %n = n + 1; %no other parameter after this
176 end
177
178 %level3Parameters: gain, data_offset, currents

```

```

179
180 m = 1;
181 if scanParametersToSearchOn.gain == 1
182     scanParameterSearchResults.gain = level3Parameters(m);
183     m = m + 1;
184 end
185
186 if scanParametersToSearchOn.dataOffset == 1
187     scanParameterSearchResults.dataOffset = level3Parameters(m);
188     m = m + 1;
189 end
190
191 for p = 1:numOfWires
192     if wireParametersToSearchOn.current(p) == 1
193         wireParameterSearchResults.current(p) = wirearray(p).current*
194             level3Parameters(m);
195         %since answer just gives us a multiplicative factor to the current
196         m = m + 1;
197     end
198 end
199 %% Nested function definitions
200
201 function chi = recalc2(x2)
    [Redacted code optimizes level 2 parameters and calls level 3 parameter search.]
    1     if isempty(x3)
    2         chi = recalc3(x3);
    3         level2Parameters = [];
    4     else
    5         [level2Parameters, chi] = fminsearch(@(x3) recalc3(x3), x3);
    6     end
    7     %level2Parameterers doesn't need to be passed since scope spans
    8     %entire file
    9     end
10
11     function chi = recalc3(x4)
    [Redacted code optimizes level 3 parameters.]
    1
    2     end %recalc3
    3 end %parameterSearchNew

```

Appendix B: Ultimate limits on spatial resolution, J. Matthew *et. al.*

Ultimate Limits to Magnetic Field Imaging using SQUIDS

John Matthews* and F. C. Wellstood†

*Center for Nanophysics and Advanced Materials, Department of Physics,
University of Maryland, College Park, MD 20742*

(Dated: April 29, 2010)

Abstract

Without using magnetic flux guides, the best spatial resolution that has been achieved with SQUID microscopes is presently about $20\ \mu\text{m}$ when imaging room temperature objects with a $100\ \mu\text{m}$ standoff. The standoff distance z between the room temperature sample and the SQUID loop, the signal-to-noise ratio, and the inversion techniques which map the magnetic field image back to the source current density, are the main factors that limit the spatial resolution. We analyze magnetic imaging processes in general and find the ultimate limit to the spatial resolution for a given standoff z and signal-to-noise ratio. In the process, we develop a general formulation that can be applied to other near-field imaging techniques, and find that existing SQUID microscopes operating at $100\ \mu\text{m}$ standoff have an ultimate spatial resolution of about $0.5\ \mu\text{m}$ for typical sample imaging parameters, two orders of magnitude better than is currently being achieved.

PACS numbers: 85.25.Dq, 87.57.Ce, 07.55.-w

*Electronic address: jmatthews@poc.com; Current address: Physical Optics Corporation, 20600 Gramercy Place, Torrance, CA 90501

†Electronic address: well@squid.umd.edu

I. INTRODUCTION

In scanning SQUID microscopy [1–9], the output from a small flux-locked Superconducting Quantum Interference Device (SQUID) [10, 11] is recorded by a computer as a sample is scanned back and forth under the SQUID. The resulting data can be used to construct a false-color "image" of magnetic fields from the sample. For such a near-field system, one might expect the spatial resolution to be about equal to the sensor-to-sample separation z . In fact, for images of the z -component of magnetic field from current-carrying wires the spatial resolution is much worse, being almost five times the sample-to-SQUID separation [12]. For practical applications involving circuits, however, one often prefers a map of the current-carrying wires that are producing the fields rather than the fields themselves. This can be found by applying a Fourier-based magnetic inverse transformation to the magnetic field data [13]. Remarkably, such images of source currents can show a spatial resolution that is not only finer than that in the original magnetic field image, but also smaller than the SQUID-to-sample separation [12].

In this article, we begin with a brief review of the standard magnetic inverse technique and how it determines spatial resolution. Although the inversion technique is well-known, the spatial resolution that can be obtained from the inversion has only recently been found [12]. We next discuss, in principle, how the inverse technique could be "improved" by taking into account additional information that might be known about a sample [14]. We then explore how much improvement is possible in the spatial resolution by developing a general theory for the minimum measurable value of a small parameter λ from a magnetic image. We then apply this theory to find the minimum resolvable separation between different types of identical sources (e.g. wires, magnetic dipoles), and finish with a few concluding remarks.

A. Magnetic Inverse Technique

The standard magnetic inverse technique has been widely used in SQUID NDE and microscopy and has been described in detail by B. J. Roth *et al.* [13]. The main result is that if a magnetic field is generated by currents that are confined to a thin sheet of thickness d that is a distance z from the SQUID, and d is much smaller than z , then it is possible to uniquely determine the location and strength of the source currents from knowledge of just

the magnetic field.

For the standard inverse, Chatrathorn et al. [12] showed that the spatial resolution s is linear in z , and is related to all other parameters approximately logarithmically, by the implicit relation:

$$\frac{z}{s} = \frac{1}{2a} \ln \left[\frac{(2/\pi) \{a\mu_0 I / (\Delta x \sigma_B)\}^2 (z/s)^2 - 1}{2a(z/s) - 1} \right]. \quad (1)$$

where Δx is the length of a pixel in the magnetic field image, I is the current flowing in a wire being imaged, and σ_B is the rms magnetic field noise in each pixel. The parameter a is determined by the shape of the Fourier-space filter used to filter out noise at high spatial frequency; for a hard cut-off filter, $a = 2.783$. This result assumes that the only source of noise σ_B is magnetic field noise from the sensor, and not position noise [15], noise in the source currents, or other spatially dependent noise. Images obtained on several samples using a SQUID microscope have shown good agreement with this result, with z/s up to 4.5 being achieved at separations of 50 – 500 μm . [4, 12].

B. Defining the ultimate limit

Equation [1] gives the spatial resolution in a current density image formed using the standard magnetic inverse technique. To arrive at this result, two broad assumptions needed to be made: (1) current was confined to a two-dimensional plane whose thickness is small compared to the resolution of the microscope, and (2) current is conserved in this 2D plane. While these assumptions may seem restrictive, and will not be true for all samples, in practice one often knows much more about a sample. For example, in many integrated circuits the currents flow in wires that are thin enough to be considered as line sources, and these line currents may also be arranged according to Manhattan geometry. Further consideration suggests that if such information about a sample could be incorporated into an inversion technique, one could reduce the noise and improve the spatial resolution in the resultant current image. Use of “Manhattan filters” on scanning SQUID images of circuits bears this out [12].

A key question now becomes apparent: if by adding more information one can improve the spatial resolution, what is the ultimate limit to the spatial resolution? Of course, if one knows *all* information about a sample, then by definition even the smallest feature is

resolved, and the resolution $s = 0$. Instead, we may ask the penultimate question: *what is the spatial resolution if one incorporates all information about a sample, except one unknown parameter?*

For example, suppose that the sample consists of two parallel wires (long, straight, infinitesimally thin), each carrying known current $I/2$, separated by an unknown distance w and arranged as in Fig. 1. The idea is that if we can reliably determine the one unknown parameter w from the measured magnetic imaging data, then we will have resolved the wires. In the following section we develop this idea in detail for any parameter.

II. THEORY

To determine the ultimate limit to the spatial resolution we assume we have N magnetic field measurements B_i^m , and that each measurement has an uncorrelated random error drawn from a normal distribution with standard deviation σ_{B_i} . In addition, we will suppose we have a theory for constructing values B_i^{th} . Let $B^{th}(\vec{x}, \lambda)$ be the theoretical value of the field, where $\vec{x} = \{x_1, x_2, \dots\}$ are the known parameters of the problem, and λ is the one unknown parameter. From the data, the uncertainties, and the theory, we can construct the statistical quantity χ^2 as a function of λ [16]. The best estimate of λ is that which minimizes χ^2 . From $\chi^2(\lambda)$ we can also find an analytical expression for σ_λ , the uncertainty in λ , in terms of the σ_{B_i} .

For the application to magnetic field due to current flow in a wire, the components of \vec{x} could be for example the cartesian coordinates x, y, z where each measurement is made, the current I flowing in the wire, and the direction and position of the wire. λ will be an unknown parameter of the problem, and we assume that it can be written in dimensionless form, such that $\lambda \ll 1$. This condition is appropriate for finding the smallest resolvable λ - we will consider some specific examples below. Taylor expanding about $\lambda = 0$, we find:

$$B^{th}(\vec{x}, \lambda) = B^{th}(\vec{x}, 0) + \lambda \left. \frac{\partial B^{th}}{\partial \lambda} \right|_{\lambda=0} + \frac{\lambda^2}{2} \left. \frac{\partial^2 B^{th}}{\partial \lambda^2} \right|_{\lambda=0} + \dots \quad (2)$$

We now define:

$$\chi^2 = \sum_{i=1}^N \left(\frac{B_i^m - B_i^{th}}{\sigma_{B_i}} \right)^2. \quad (3)$$

Substituting [2] into [3] and rearranging, we find:

$$\chi^2 = \sum_{i=1}^N \frac{b_{0i}^2 - 2\lambda b_{0i}b_{1i} + \lambda^2 (b_{1i}^2 - b_{0i}b_{2i})}{\sigma_{Bi}^2} + \mathcal{O}(\lambda^3), \quad (4)$$

where

$$b_{0i} \equiv B_i^m - B^{th}(\vec{x}_i, \lambda = 0), \quad (5)$$

$$b_{1i} \equiv \left. \frac{\partial B^{th}(\vec{x}_i, \lambda)}{\partial \lambda} \right|_{\lambda=0}, \quad (6)$$

$$b_{2i} \equiv \left. \frac{\partial^2 B^{th}(\vec{x}_i, \lambda)}{\partial \lambda^2} \right|_{\lambda=0}. \quad (7)$$

Neglecting terms of order λ^3 and higher, and minimizing Eq. 4 with respect to λ , we find:

$$\lambda = \frac{\sum_{i=1}^N (b_{0i}b_{1i}) / (\sigma_{Bi})^2}{\sum_{i=1}^N (b_{1i}^2 - b_{0i}b_{2i}) / (\sigma_{Bi})^2}. \quad (8)$$

We now introduce a weak assumption about the noise σ_{Bi} , which simplifies the problem considerably. Since in a real experiment we can typically reduce the noise by increasing the measurement averaging time t_i at each point i , we rewrite σ_{Bi} in terms of t_i . Assuming a constant spectral density, we have

$$\sigma_{Bi} = \sigma_B \sqrt{\frac{T}{Nt_i}}. \quad (9)$$

Here $T = \sum_{i=1}^N t_i$ is the total time spent measuring all N points, and σ_B is the rms field noise if equal times T/N were spent at each point. Substituting Eq. 9 into Eq. 8 we find the best estimate for λ :

$$\lambda = \frac{\sum_{i=1}^N t_i b_{0i} b_{1i}}{\sum_{i=1}^N t_i (b_{1i}^2 - b_{0i} b_{2i})} \equiv \frac{\Sigma_A}{\Sigma_B}. \quad (10)$$

We next consider how well known λ is, i.e. what is the uncertainty σ_λ in λ . Since all parameters, other than λ , are assumed to be known exactly, the only contribution to σ_λ comes from the data B_i^{da} , which have uncertainties σ_{Bi} given by Eq. 9. Propagation of errors on Eq. 10 then yields:

$$\sigma_\lambda = \sigma_B \sqrt{\frac{T}{N} \sum_{i=1}^N \frac{1}{t_i} \left(\frac{\partial \lambda}{\partial B_i^{da}} \right)^2}, \quad (11)$$

where

$$\frac{\partial \lambda}{\partial B_i^{da}} = \frac{\partial \lambda}{\partial b_{0i}} = \frac{t_i}{\Sigma_B} (b_{1i} + \lambda b_{2i}) , \quad (12)$$

and thus

$$\sigma_\lambda = \sigma_B \sqrt{\frac{T}{N \Sigma_B^2} \sum_{i=1}^N t_i (b_{1i} + \lambda b_{2i})^2} . \quad (13)$$

Since the t_i are completely arbitrary, we can now choose them to minimize σ_λ . In this simplified picture, averaging for an infinitely long time would reduce σ_B and σ_λ indefinitely. However, in practice only a finite amount of time will be available, so we should minimize σ_λ with respect to the t_i subject to the constraint $\sum t_i = T$.

Using the method of Lagrange multipliers, we define the constraint as

$$G \equiv \sum_{i=1}^N t_i - T = 0 . \quad (14)$$

We next introduce the undetermined Lagrange multiplier, μ , and define a new function F :

$$F \equiv (\sigma_\lambda)^2 - \mu G \quad (15)$$

We then minimize the function F with respect to each t_i ; setting $\partial F / \partial t_i = 0$ we find:

$$\frac{\partial (\sigma_\lambda)^2}{\partial t_i} - \mu = 0 . \quad (16)$$

Evaluating the partial derivatives, we find:

$$\begin{aligned} \frac{\partial (\sigma_\lambda)^2}{\partial t_i} = & \frac{(\sigma_B)^2 T}{N \Sigma_B^2} \left\{ (b_{1i} + \lambda b_{2i})^2 - \right. \\ & - \frac{2}{\Sigma_B} \frac{\partial \Sigma_B}{\partial t_i} \sum_{j=1}^N t_j (b_{1j} + \lambda b_{2j})^2 + \\ & \left. + 2 \frac{\partial \lambda}{\partial t_i} \sum_{j=1}^N t_j b_{2j} (b_{1j} + \lambda b_{2j}) \right\} . \end{aligned} \quad (17)$$

Using Eq. 10 we then find, for each i :

$$\begin{aligned} \mu = & \frac{(\sigma_B)^2 T}{N \Sigma_B^3} \left[\Sigma_B (b_{1i} + \lambda b_{2i})^2 - \right. \\ & - 2 \Sigma_C (b_{1i}^2 - b_{0i} b_{2i}) + \\ & \left. + 2 \Sigma_D \{ b_{0i} b_{1i} - \lambda (b_{1i}^2 - b_{0i} b_{2i}) \} \right] , \end{aligned} \quad (18)$$

where

$$\Sigma_C \equiv \sum_{j=1}^N t_j (b_{1j} + \lambda b_{2j})^2, \quad (19)$$

and

$$\Sigma_D \equiv \sum_{j=1}^N t_j b_{2j} (b_{1j} + \lambda b_{2j}). \quad (20)$$

Note that Eq. 18 must hold for *all* i , but the only free parameters dependent on i are the t_i , since the b_i are fixed by the particular $B(\vec{x}, \lambda)$. However, the t_i only enter into Eq. 18 via the sums in Σ_C and Σ_D in Eqs. 19 and 20. Therefore the only way in general to satisfy Eq. 18 for all i would be if $N = 1$ or if the b_i are independent of i . Either way, this implies that the minimum σ_λ will be obtained by collecting all data at a single point, either by making a single long measurement, or N repeated measurements at one location.

This result allows us to greatly simplify Eqs. 8 and 13, since for the optimum choice of t_i there will only be one term in the sum, so that for all i we have $b_{0i} = b_0$, $b_{1i} = b_1$, and $b_{2i} = b_2$. We find the optimum:

$$\lambda = \frac{b_0 b_1}{b_1^2 - b_0 b_2}, \quad (21)$$

$$\sigma_\lambda = \frac{\sigma_B |b_1|^3}{(b_1^2 - b_0 b_2)^2}. \quad (22)$$

Using Eq. 21 to eliminate b_0 , we find:

$$\sigma_\lambda = \frac{\sigma_B}{|b_1|} \left(1 + \lambda \frac{b_2}{b_1} \right)^2. \quad (23)$$

We now impose the criterion that the minimum λ we will be able to resolve is when the uncertainty in λ equals λ , i.e. $\lambda = \sigma_\lambda = \lambda_{min}$. Applying this condition to Eq. 23 leads to a quadratic in λ_{min} , with solutions:

$$\lambda_{min} = \frac{1}{2} \frac{|b_1|}{\sigma_B} \left(\frac{b_1}{b_2} \right)^2 - \frac{b_1}{b_2} \pm \frac{1}{2} \frac{|b_1|}{\sigma_B} \left(\frac{b_1}{b_2} \right)^2 \sqrt{1 - \frac{4b_2 \sigma_B}{b_1 |b_1|}}. \quad (24)$$

In the limit of small noise,

$$\sigma_B \ll \frac{b_1^2}{4b_2}, \quad (25)$$

one can expand the square root in Eq. 24. In this limit, only the minus sign yields a physical solution, and one arrives at the naively expected result

$$\lambda_{min} \approx \frac{\sigma_B}{|b_1|}. \quad (26)$$

Eq. 26 turns out to be a very good approximation to Eq. 24 for many practical situations, as we will see in Section III. Finally, we note that Eq. 26 implies that the measurement is best made where $|b_1| = |\partial B/\partial \lambda|$ is a maximum.

III. MINIMUM RESOLVABLE SEPARATION OF TWO MAGNETIC FIELD SOURCES

To determine the ultimate limit to the spatial resolution in magnetic imaging, we consider the resolvability of two identical sources.

Let $B_1(x, y, z)$ be a component of the B -field from a single source, centered on the origin. The field from two such identical sources that are separated along the x -axis by $\pm w/2$ from the origin can then be written as:

$$B(x, y, z; w) = B_1(x + w/2, y, z) + B_1(x - w/2, y, z) . \quad (27)$$

The idea is to find the smallest w that can be resolved. From Section II, this suggests that we choose w to be our small parameter λ . However, one finds:

$$b_1 = \left. \frac{\partial B}{\partial w} \right|_{w=0} = \frac{1}{2} \left(\frac{\partial B_1}{\partial x} - \frac{\partial B_1}{\partial x} \right) = 0 . \quad (28)$$

Thus we cannot assign $\lambda = w$ and apply Eq. 26 since this requires $|b_1| > 0$. In fact, due to the $\pm w$ symmetry, all odd powers of w in the Taylor expansion vanish. Since only even powers of w enter, this suggests that we choose $\lambda = w^2$, in which case b_1 becomes

$$\begin{aligned} b_1 &= \left. \frac{\partial B}{\partial (w^2)} \right|_{w^2=0} = \frac{1}{2} \left. \frac{\partial^2 B}{\partial w^2} \right|_{w=0} \\ &= \frac{1}{8} \left(\frac{\partial^2 B_1}{\partial x^2} + \frac{\partial^2 B_1}{\partial x^2} \right) = \frac{1}{4} \frac{\partial^2 B_1}{\partial x^2} , \end{aligned} \quad (29)$$

which is non-zero.

A. Resolving Current-Carrying Wires

We now consider the case of two parallel, infinitely long, current-carrying wires, and determine the minimum resolvable separation w_{min} (see Fig. 1).

The z -component of the magnetic field B_{1z} due to a single wire carrying a current $I/2$ along the y -axis in the negative y -direction is

$$B_{1z} = \frac{\mu_0 I}{4\pi} \frac{x}{x^2 + z^2} = \frac{\mu_0 I}{4\pi z} \frac{u}{1 + u^2} , \quad (30)$$

where $u \equiv x/z$. From Eq. 29 we find:

$$b_1 = \frac{\partial B}{\partial(w^2)} = \frac{1}{4} \frac{\partial^2 B_{1z}}{\partial x^2} = \frac{1}{4z^2} \frac{\partial^2 B_{1z}}{\partial u^2}, \quad (31)$$

and Eq. 26 yields

$$w_{min}^2 = \left(\frac{4\pi\sigma_B}{\mu_0 I} \right) \frac{2(1+u^2)^3}{u(u^2-3)} z^3. \quad (32)$$

This function is a minimum at $u = \sqrt{2} - 1$. Substituting for u and taking the square root of Eq. 32 yields

$$w_{min} = 4(\sqrt{2} - 1)\alpha^{-1/2} z^{3/2}, \quad (33)$$

where

$$\alpha = \left(\frac{\mu_0 I}{4\pi\sigma_B} \right). \quad (34)$$

We note that α has dimensions of length, and is related to the signal-to-noise ratio.

The thick solid line in Fig. 2 shows w_{min} vs. z from Eq. 33. The dashed line shows the spatial resolution of the standard magnetic inverse from Eq. 1. For these plots we used typical parameters for scanning SQUID microscopes ($I = 100\mu\text{A}$, 15 minute scan at $30 \text{ pT}/\sqrt{\text{Hz}}$). Note that for $z = 100\mu\text{m}$ the ultimate limit to the spatial resolution (w_{min}) is about $0.5 \mu\text{m}$, whereas the standard inverse yields $s = 20 \mu\text{m}$. The implication is that there are almost two orders of magnitude to be gained by adding information into the inversion routines.

We next consider the case of two parallel wires of finite length L , each carrying a current $I/2$, separated by a distance w in the x -direction. From the Biot-Savart law, the z -component of the magnetic field from a single wire, centered at $x = 0, z = 0$, with ends at $y = y_2$ and $y = y_1$, carrying current $I/2$ in the negative y -direction is:

$$B_{1z} = \frac{\mu_0 I x}{8\pi(x^2 + z^2)} \left\{ \frac{y_2 - y}{\sqrt{x^2 + (y_2 - y)^2 + z^2}} - \frac{y_1 - y}{\sqrt{x^2 + (y_1 - y)^2 + z^2}} \right\} \quad (35)$$

Intuitively we expect that we will obtain the best spatial resolution if we take data along the midpoint of the wire ($y = 0$), and indeed this can be shown to be the case. Setting $y = 0, y_2 = L/2$ and $y_1 = -L/2$, and introducing the dimensionless variables $u \equiv x/z$ and $\ell \equiv L/2z$, we can write:

$$B_{1z} = \frac{\mu_0 I \ell}{4\pi z} \frac{u}{(1+u^2)\sqrt{1+u^2+\ell^2}}. \quad (36)$$

To find the best resolution we must measure at the value of $u = x/z$ which minimizes σ_{w^2} . This optimal value of u will depend on the length L of the wires, and must be solved numerically. We can now evaluate the minimum measurable w^2 from Eqs. 26 and 29. The results for w_{min} are plotted in Fig. 2 for some representative values of L , using the full expression for λ given in Eq. 24.

A similar analysis can be made for the x -component of the magnetic field from two parallel wires of length L . In this case the field from a single wire centered on the origin is

$$B_{1x} = \frac{\mu_0 I \ell}{4\pi z} \frac{1}{(1+u^2)\sqrt{1+u^2+\ell^2}} \quad (37)$$

and the optimum value of $x/z = 0$ for all values of L . w_{min} can then be expressed in analytical form

$$w_{min} = \sqrt{\left(\frac{4\pi\sigma_B}{\mu_0 I}\right) \frac{4z^3(1+\ell^2)^{5/2}}{\ell(3+2\ell^2)(1+\ell^2)}}. \quad (38)$$

For two parallel wires carrying opposing current, Eq. 27 is modified to

$$B(x, y, z; w) = B_1(x + w/2, y, z) - B_1(x - w/2, y, z), \quad (39)$$

and b_1 is then given by

$$b_1 = \left. \frac{\partial B}{\partial w} \right|_{w=0} = \frac{1}{2} \left(\frac{\partial B_1}{\partial x} + \frac{\partial B_1}{\partial x} \right) = \frac{\partial B_1}{\partial x}. \quad (40)$$

and

$$w_{min} = \left(\frac{4\pi\sigma_B}{\mu_0 I}\right) z^2 \frac{(1+\ell^2)^{1/2}}{\ell}, \quad (41)$$

measured at the origin. Figure 2 again shows w_{min} vs. z for this case (see dotted curves). The resolution is better for the anti-parallel wires than for parallel.

To better understand these results, we consider two limiting cases: infinitely long wires ($L \gg z$, or equivalently $\ell \gg 1$), and infinitesimally short wires ($L \ll z$). Evaluating these limits for B_x or B_z , and for parallel or antiparallel wires leads to a total of eight possible cases (see Table I). In these limits, there is no ℓ -dependence, so w_{min} reduces to a simple power of z . The fourth column in Table I gives an expression for w_{min} . For the first item in the list (two long, parallel wires, B_z measured), we recover Eq. 33, for example.

Some general conclusions can be drawn from Table I. First, the z -dependence in every case is a power larger than 1. This indicates that it is beneficial for resolution to reduce z as far as possible, which is to be expected. Second, if we compare the results for B_x and

B_z , we find the same dependencies on z , I , and σ_B . The numerical coefficients are slightly different - w_{min} is marginally lower for B_x in the parallel cases, whereas in the antiparallel cases, B_z yields a slightly lower value for w_{min} . However, a word of caution is necessary here - since we are discussing ultimate limits for idealized situations, these small differences are likely to be swamped in practice by other effects.

Lastly, we find that I and σ_B always occur in the combination $\mu_0 I / 4\pi \sigma_B$, which we denote as α . This quantity, which has dimensions of length, is a measure of the signal to noise ratio, since increasing the current, or decreasing the magnetic field noise both lead to an increase in signal-to-noise. From Table I we also see that the effect of α and z is stronger for the antiparallel configuration than for the parallel configuration.

B. Resolving Magnetic Dipoles

We next consider the minimum resolvable separation w_{min} between two magnetic dipoles of magnitude m . There are many interesting physical phenomena which produce magnetic dipole fields, ranging from the microscopic level, such as sub-micron ferromagnetic particles used in recordable magnetic media [17], to magnetotactic bacteria [6, 18], up to the truly macroscopic scale of geophysical [19] or astrophysical fields, for example due to the Earth or sun.

We begin with the field at \vec{r} due to a single dipole $\vec{m} = m\hat{z}$ located at the origin,

$$\vec{B}_1(\vec{r}) = \frac{\mu_0}{4\pi} \frac{3\vec{r}(\vec{r} \cdot \vec{m}) - r^2\vec{m}}{r^5}. \quad (42)$$

The z and x components of the magnetic field are then, respectively,

$$B_{1z} = \frac{\mu_0}{4\pi} \frac{m(3z^2 - r^2)}{r^5}, \quad (43)$$

and

$$B_{1x} = \frac{\mu_0}{4\pi} \frac{3mxz}{r^5}, \quad (44)$$

where $r = \sqrt{x^2 + y^2 + z^2}$.

We proceed as before and set $\lambda = w$ (or $\lambda = w^2$ if the w -term vanishes, as in Eq. 27), $u = x/z$, and $y = 0$, due to the symmetry of the problem. We then evaluate the first and second order derivatives with respect to u , which yields b_1 , w_{min} , and the value of u that minimizes w_{min} , for the antiparallel and parallel cases, respectively. The results are summarized in

Table II; column 3 gives an expression for w_{min} , for example $w_{min} = 0.3646z^4/\beta$ for two antiparallel magnetic dipoles, with B_z being measured. Here $\beta \equiv \mu_0 m/4\pi\sigma_B$ is the relevant signal-to-noise parameter, which has dimensions of (length)³.

If we assume $\sigma_B = 1$ pT, which is a reasonable number for a SQUID sensor, and $m = 10^{-15}$ Am² for an individual magnetic domain or a magnetotactic bacterium, we obtain $\beta = 10^{-10}$ m³. To resolve neighboring magnetic domains/bacteria separated by about 0.1 μ m would require z to be no greater than about 70 μ m (assuming antiparallel alignment of neighboring moments). This is well above the minimum z of about 20 μ m of many existing scanning SQUID microscopes that image room-temperature samples. Fig. 3 shows plots of w_{min} vs. z for various cases.

C. Resolvability of $1/r^n$ Fields

The above results can be generalized to cover any field which decays as $1/r^n$, for $n > 0$. In such a case we can always make a transformation to dimensionless variables e.g. $u \equiv x/z$. The field from a single source then becomes

$$B_1 = \frac{f(u)}{z^n}. \quad (45)$$

If the field from two sources separated by a distance w is symmetric in w , then it will depend only on w^2 , so

$$w_{min}^2 \approx \frac{\sigma_B}{b_1}, \quad (46)$$

where

$$b_1 = \frac{\partial B}{\partial w^2} = \frac{1}{4z^{2+n}} \frac{\partial^2 f}{\partial u^2}. \quad (47)$$

This then leads to

$$w_{min} \approx \left(\frac{4\sigma_B}{\partial^2 f / \partial u^2} \right)^{1/2} z^{1+n/2}. \quad (48)$$

If the field is antisymmetric in w (as for antiparallel wires), one finds

$$w_{min} \approx \left(\frac{\sigma_B}{\partial f / \partial u} \right) z^{1+n}, \quad (49)$$

consistent with the low- z behavior of w_{min} for the examples discussed above.

To understand the high- z behavior, which is linear in the examples above, we note that

$$b_1 = \frac{f_2}{4z^{2+n}}, \quad (50)$$

and

$$b_2 = \frac{f_4}{96z^{4+n}}. \quad (51)$$

where $f_j = \partial^j f / \partial w^j$. If a value of u exists for which $f_2/f_4 < 0$, then the dominant term in an expansion of Eq. 24 at high z is b_1/b_2 , which is independent of σ_B , and has the same dimensionality as λ_{min} . For example, if we set $\lambda = w^2$, b_1/b_2 will be proportional to z^2 , whereas if we set $\lambda = w$, b_1/b_2 will be proportional to z , thereby w_{min} is always linear in z at high z .

For the symmetric case

$$w_{min} \approx 24 \sqrt{\left| \frac{f_2}{f_4} \right|} z. \quad (52)$$

For the antisymmetric case $b_2 = 0$, so we must repeat some of the analysis from Sec. II to order w^3 , and include the third derivative b_3 . This leads to:

$$\lambda_{min} = -\frac{b_1^2}{2b_3\sigma_B} + \sqrt{\left(\frac{b_1^2}{2b_3\sigma_B}\right)^2 - \frac{b_1}{b_3}}. \quad (53)$$

In the low- z limit, we recover Eq. 26, as expected. In the high- z limit, the b_1/b_3 term dominates, and for the $1/r^n$ field

$$w_{min} \approx 2 \sqrt{\left| \frac{f_1}{f_3} \right|} z. \quad (54)$$

IV. SUMMARY AND CONCLUSIONS

The theory for the spatial resolution s obtained by the magnetic inverse technique, given by Eq. 1, shows that $s \propto z$. However, the magnetic inverse technique contains relatively few assumptions about the sample, giving it broad applicability but sub-optimal resolution. If, instead, we could place greater restrictions on the possible solutions, then we could increase the ability of the inverse to resolve smaller features.

In an effort to understand the potential gain in spatial resolution that may be obtained by adding known information about a sample into a magnetic inversion algorithm, we have determined analytical expressions for the ultimate limit to the spatial resolution. In order to do this, we have developed a formulation for determining the minimum measurable value of a single parameter, when all other parameters of a theory are known exactly. We applied this theory to several specific, relatively simple examples, in which the unknown parameter

is identified with the spatial resolution. As an aside, we note that this single-parameter formulation is very general, and can in principle be applied to analysis of other types of data with a single unknown parameter.

Since in this paper we are primarily concerned with scanning SQUID microscopy, the examples we have considered are simple approximations of typical systems measured experimentally. We find that to a good approximation, the minimum separation w_{min} scales as a power law with the standoff distance z . For small z the exponent of the power law is greater than 1, indicating that there is a significant advantage to reducing z as much as possible. In every case, at large z the minimum separation becomes linear with z , agreeing with the standard near-field limit, where the spatial resolution is roughly the standoff z . It is also interesting to note that the ultimate limit to the spatial resolution scales as a power law in the number of measurements (or S/N or σ_B), as compared to the standard magnetic inverse, which scales logarithmically. [12] Finally, at small z , we find that existing SQUID microscopes are achieving spatial resolutions that are about two orders of magnitude from the ultimate limit. If additional information about a sample could be incorporated into the imaging process, then it should be possible to obtain substantial improvements in spatial resolution even at relatively large stand-off distances.

Acknowledgments

We acknowledge the support of this work by the Center for Superconductivity Research (now the Center for Nanophysics and Advanced Materials), Neocera, Inc., the Maryland Industrial Partnership Program (MIPS), and the Air Force Office of Scientific Research (AFOSR). We thank Lee Knauss and Antonio Orozco for many useful discussions.

-
- [1] A. Mathai, D. Song, Y. Gim, and F. C. Wellstood, *Appl. Phys. Lett.* **61**, 598 (1992).
 - [2] J. R. Kirtley and J. P. Wikswo, *Ann. Rev. Mat. Sci.* **29**, 117 (1999).
 - [3] S. Chatrathorn, E. F. Fleet, F. C. Wellstood, L. A. Knauss, and T. M. Eiles, *Appl. Phys. Lett.* **76**, 2304 (2000).
 - [4] E. F. Fleet, S. Chatrathorn, F. C. Wellstood, L. A. Knauss, and S. M. Green, *Rev. Sci. Instrum.* **72**, 3281 (2001).

- [5] Magma-C1TM Scanning HTS SQUID Microscope, Neocera, Inc., US Patent No. 5491411.
- [6] H. L. Grossman, W. R. Myers, V. J. Vreeland, R. Bruehl, M. D. Alper, C. R. Bertozzi, and J. Clarke, Proc. Natl. Acad. Sci. **101**(1), 129 (2004).
- [7] C. Veauvy and K. Hasselbach, Phys. Rev. B **70**, 214513 (2004).
- [8] S. M. Frolov, M. J. A. Stoutimore, T. A. Crane, D. J. V. Harlingen, V. A. Oboznov, V. V. Ryazanov, A. Ruosi, C. Granata, and M. Russo, Nature Physics **4**, 32 (2008).
- [9] M. E. Huber, N. C. Koshnick, H. Bluhm, L. J. Archuleta, T. Azua, P. G. Bjornsson, B. W. Gardner, S. T. Halloran, E. A. Lucero, and K. A. Moler, Rev. of Sci. Instrum. **79**, 053704 (2008).
- [10] J. Clarke, in *SQUID Sensors: Fundamentals, Fabrication and Applications*, edited by H. Weinstock (Kluwer Academic Publishers, Dordrecht, The Netherlands, 1996), pp. 1–62.
- [11] J. Clarke and A. I. Braginski, *The SQUID Handbook* (Wiley-VCH, Weinheim, 2004), 1st ed.
- [12] S. Chatrathorn, E. F. Fleet, and F. C. Wellstood, Jour. Appl. Phys. **92**, 4731 (2002).
- [13] B. J. Roth, N. G. Sepulveda, and J. J. P. Wikswo, J. Appl. Phys. **65**, 361 (1989).
- [14] F. C. Wellstood, J. Matthews, and S. Chatrathorn, IEEE Trans. Appl. Supercond. **13**, 258 (2003).
- [15] S. Y. Lee, J. Matthews, and F. C. Wellstood, Appl. Phys. Lett. **84**, 5001 (2004).
- [16] P. R. Bevington and D. K. Robinson, eds., *Data Reduction and Error Analysis for the Physical Sciences* (McGraw-Hill, New York, 1992), 2nd ed.
- [17] M. P. Sharrock, IEEE Trans. Magn. **25**, 4374 (1989).
- [18] A. S. Bahaj, P. A. B. James, and F. D. Moeschler, IEEE Trans. Magn. **32**, 5133 (1996).
- [19] J. B. Lee, R. J. Turner, M. A. Downey, A. Maddever, D. L. Dart, C. P. Foley, R. Binks, C. Lewis, W. Murray, G. Pankovic, et al., Exploration Geophysics **32**, 9 (2001).

Tables

TABLE I: Summary of the minimum resolvable separation w_{min} for two parallel/antiparallel (P/A) wires of length L separated by a distance w . Each wire carries a current $I/2$; the signal-to-noise is contained within the quantity $\alpha = \mu_0 I / 4\pi\sigma_B$, where σ_B is the uncertainty in the measured magnetic field. The long (L) and short (S) wire limits correspond to $L \gg z$ and $L \ll z$, respectively. x_{opt}/z is the location at which the measurement should be made for optimum resolution.

B_z/B_x	P/A	L/S	w_{min}	x_{opt}/z
B_z	P	L	$1.6569z^{3/2}\alpha^{-1/2}$	0.4142
B_x	P	L	$1.4142z^{3/2}\alpha^{-1/2}$	0
B_z	P	S	$2.0347z^2\alpha^{-1/2}L^{-1/2}$	0.3615
B_x	P	S	$1.6330z^2\alpha^{-1/2}L^{-1/2}$	0
B_z	A	L	$z^2\alpha^{-1}$	0
B_x	A	L	$1.5396z^2\alpha^{-1}$	0.5774
B_z	A	S	$2z^3\alpha^{-1}L^{-1}$	0
B_x	A	S	$2.3292z^3\alpha^{-1}L^{-1}$	0.5

TABLE II: Summary of the minimum resolvable separation w_{min} for two parallel/antiparallel (P/A) magnetic dipoles $\vec{m} = m\hat{z}$ separated by a distance w . The signal-to-noise is contained within the quantity $\beta = \mu_0 m / 4\pi\sigma_B$, where σ_B is the uncertainty in the measured magnetic field. C is a dimensionless numerical coefficient, e.g. $w_{min} = Cz^{5/2}\beta^{-1/2}$ for two parallel magnetic dipoles (B_z). x/z is the location at which the measurement should be made for optimum resolution.

B_z/B_x	P/A	w_{min}	x/z
B_z	P	$(1/3\sqrt{2})z^{5/2}\beta^{-1/2}$	0
B_x	P	$0.7044z^{5/2}\beta^{-1/2}$	0.27594
B_z	A	$0.3646z^4\beta^{-1}$	0.38295
B_x	A	$(4/3)z^4\beta^{-1}$	0

Figure Captions

FIG. 1. Two current-carrying parallel wires centered on the origin, separated by a distance w .

FIG. 2. Minimum resolvable wire separation $w_{min}(z)$ for B_z due to two parallel (solid line) or antiparallel (dotted line) current-carrying wires. The thick lines show the result for infinitely long wires, the three thin lines show the results for 1 mm, 100 μm , and 10 μm -long wires (from right to left). We assume a current of 100 μA , $\sigma_B = 1$ pT, equivalent to averaging for 15 mins at 30 pT/ $\sqrt{\text{Hz}}$. The dashed line shows the spatial resolution of the standard magnetic inverse, as given by Eq. 1; we have chosen the pixel size to scale with z ($\Delta x = z/100$).

FIG. 3. $w_{min}(z)$ for B_z due to two parallel (solid line) or antiparallel (dotted line) magnetic dipoles $\vec{m} = m\hat{z}$, with $\beta = \mu_0 m / 4\pi\sigma_B = 10^{-10}$, 10^{-8} and 10^{-6} . The arrow indicates the direction of increasing β . A value of $\beta = 10^{-10}$ corresponds to a dipole strength $m = 10^{-15}$ Am² for magnetic field noise $\sigma_B = 1$ pT, which is equivalent to counting for 15 mins at 30 pT/ $\sqrt{\text{Hz}}$. Eq. 24 was used to generate the curves, note the change to a linear dependence on z at high z . The shaded area maps out the region that is inaccessible by varying z and β .

Figures

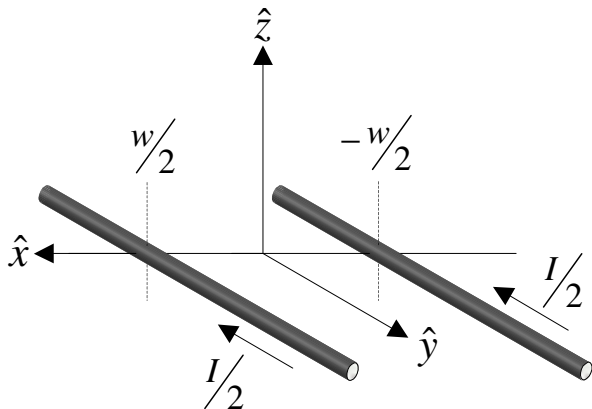


FIG. 1: Two current-carrying parallel wires centered on the origin, separated by a distance w .

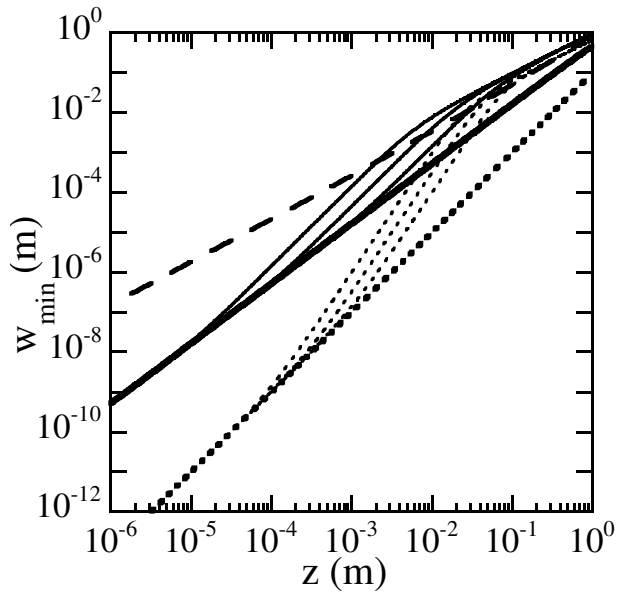


FIG. 2: Minimum resolvable wire separation $w_{min}(z)$ for B_z due to two parallel (solid line) or antiparallel (dotted line) current-carrying wires. The thick lines show the result for infinitely long wires, the three thin lines show the results for 1 mm, 100 μm , and 10 μm -long wires (from right to left). We assume a current of 100 μA , $\sigma_B = 1$ pT, equivalent to averaging for 15 mins at 30 pT/ $\sqrt{\text{Hz}}$. The dashed line shows the spatial resolution of the standard magnetic inverse, as given by Eq. 1; we have chosen the pixel size to scale with z ($\Delta x = z/100$).

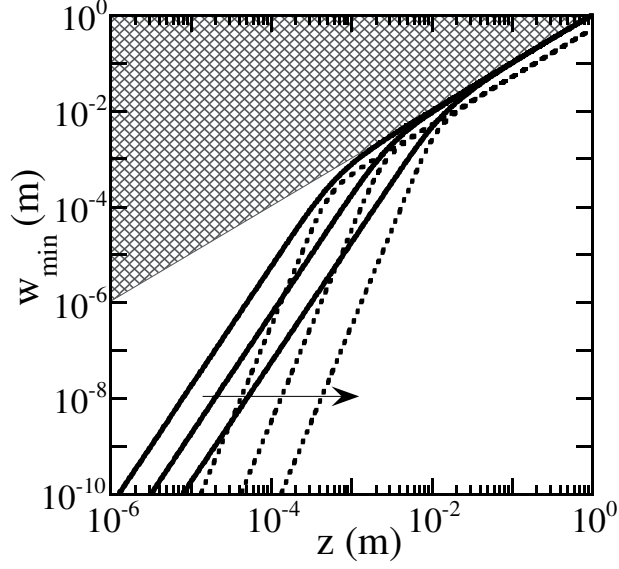


FIG. 3: $w_{min}(z)$ for B_z due to two parallel (solid line) or antiparallel (dotted line) magnetic dipoles $\vec{m} = m\hat{z}$, with $\beta = \mu_0 m / 4\pi\sigma_B = 10^{-10}$, 10^{-8} and 10^{-6} . The arrow indicates the direction of increasing β . A value of $\beta = 10^{-10}$ corresponds to a dipole strength $m = 10^{-15}$ Am² for magnetic field noise $\sigma_B = 1$ pT, which is equivalent to counting for 15 mins at 30 pT/ $\sqrt{\text{Hz}}$. Eq. 24 was used to generate the curves, note the change to a linear dependence on z at high z . The shaded area maps out the region that is inaccessible by varying z and β .

Appendix C: Run sheet detailing steps for spin-valve sensor fabrication

Run Sheet - Spin Valve sensor

Responsible: Alex JEFFERS

Sample ID:

STEP 1: Substrate preparation - Glass substrate

Date: 5/28/2014

Operator: Lu Guang

Machine: Wet Bench (Ultrasounds)

Date: __/__/__

Conditions: Clean for 30 minutes in Alconox solution with ultrasounds;
Clean with DI water and blow dry with compressed air gun.

Done by Lu Guang beforehand to save time

STEP 2: Spin-valve Deposition in Nordiko 3000

Date:

Operator: Susana Freitas

Pre-Treatment: No

Lu Guang

Conditions:

Read

Chamber pressure before deposition: $3.4e^{-7}$ Torr

Chamber pressure during deposition: $7.69-7.6e^{-5}$ Torr

Subst Rotn: 30 rpm

Batch: Top pinned Spin-valve

Glass/ Ta₂₀/NiFe₂₈/CoFe₂₃/Cu₂₀/CoFe₃₃/MnIr₂₀/Ta₁₀₀

Observations - test sample (glass)

Test files: SV1752 and _____

MR = 5.67 % Hf = - 19.86 Oe

Hex 200 Oe Hc (MR) = 587 Oe

Read conditions during deposition:

RF FWD: 110-113 W

RF REF: 0 W

Pos Grid: 1000 V Pos. Grid current: 24.5 μ A

~~Avg Grid: 24.5 V~~

Neg. Grid: 291.3 V

Xe Flow: 2.9 sccm

Applied: 50 e

STEP 4: SV sensors definition

Date: 5/28/2014

Operator: Jose Bernardo
Lu Guang

Coating conditions:

Vapour - prime (5min HDMS) @130 °C (program 0) Total time: 30 min
 Coater 6/2 speed = 1.5 μm
 coater arm that applies PR not working properly
 (shaking back & forth), Bernardo Fixed it ("old & bad bearings")
 step 1: 800 rpm for 5 min
 step 2: 2500 rpm for 30s

Exposing Conditions:

Map	Mask	85 E	Q F	10 min/die 20 total	X ₀ , Y ₀ (nm)	Die dimensions (μm)
LINFO2	Sensor_100um Sensor_200um	270m	1301	1.5h	Não temos cruze alinhamento na 1ª layer	15400x15400 61207 x 18068 (21862 x 17868)

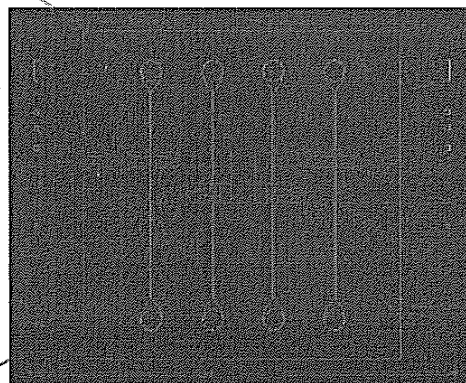
need to adjust these parameters to my samples

5/28/2014

Development: recipe 6/2 Time: 10 min total

Conditions: ~~Robotic arm~~ Robotic arm from water tray to baking platform
 dropped wafer at wrong time - water had to be adjusted manually
 sensoresv100 canais pequenos + contacto comum.dwg

See attached image



Die area: 20975*17657

Easy axis

need to replace this drawing by my mask, but only for layer 1 (spinvalve sensor)

Observations: Optical inspection at microscope, to confirm if the resist is where we expected (that is: with the shape of the sensors), and also measure the dimension of the sensor elements) SV sensors looked very good, clean & correct dimensions.

STEP 5: Spin-valve Etch in Nordiko 3600 (IBD)

Date: 5/28/2014

Operator: Diana

Conditions:

B.P.: $6.3e^{-7}$ Torr

Batch: junction etch 60 deg

during process: $1.3e^{-4}$
Setpoint Assist Gun: 105 mA, 735V/-350V, 10 sccm Ar
Subst Rotn: 30 rpm Subs Pan : 60 °

Read Assist Gun :
Assist Neutraliser:

~1 Å/s

Observations: etched thickness 304 Å ⇒ required time: 400 sec (for safety margin)

Comments: write down the physical/chemical technique used for this etch step.

ion milling, 200 seconds

cd down to avoid burning the resist

ion milling, 200s.

eye test + resistance: good.

NFAWD: 191W
RF REP: 2W
Vt : 723.8V
curr: 104 mA
V- : -344V
cur: 3 mA

Ar: 10 sccm

profile-meter: thickness remaining: 1.4 μm. see attachment

STEP 6: Resist Stripping in Wet Bench

Date: 5/28/2014

Operator: Beat Alex

Conditions: Microstrip 3001 @ 80°C + ultrasounds
65°C 30 minutes

Cleaning: IPA cleaning + DI water + blow dry with compressed air.

Alex draps sample in isopropanol

Observations:

See under microscope if resist is clean near the sensor area

Only one small area still had PR

STEP 7: Contact leads definition

Date: 5/29/2014

Operator: Jose Bernardo

Coating conditions:Vapour - prime (5min HDMS) @130 °C (program 0) No vapor +
Coater 6/2 speed = 1.5 μm

Coating Arm works fine this morning

Conditions:

Map	Mask	E	F	Time	X ₀ :Y ₀ (μm)	Die dimensions (μm)
LINFO2	paint on 5V-2 Sensor 100um L2 Sensor 200um L2	70	0 50	1H20 13 min/ die	168 1887:1323 54	21202 x 18068

[need to replace this drawing by my mask, but only for layer 2 (contact leads)]

Development: recipe: 6/2 Time: 10 min total.**Observations:** 1st loading arm still not loading well.**STEP 8: Al 3000 Å Deposition**

Date: 5/29/2014

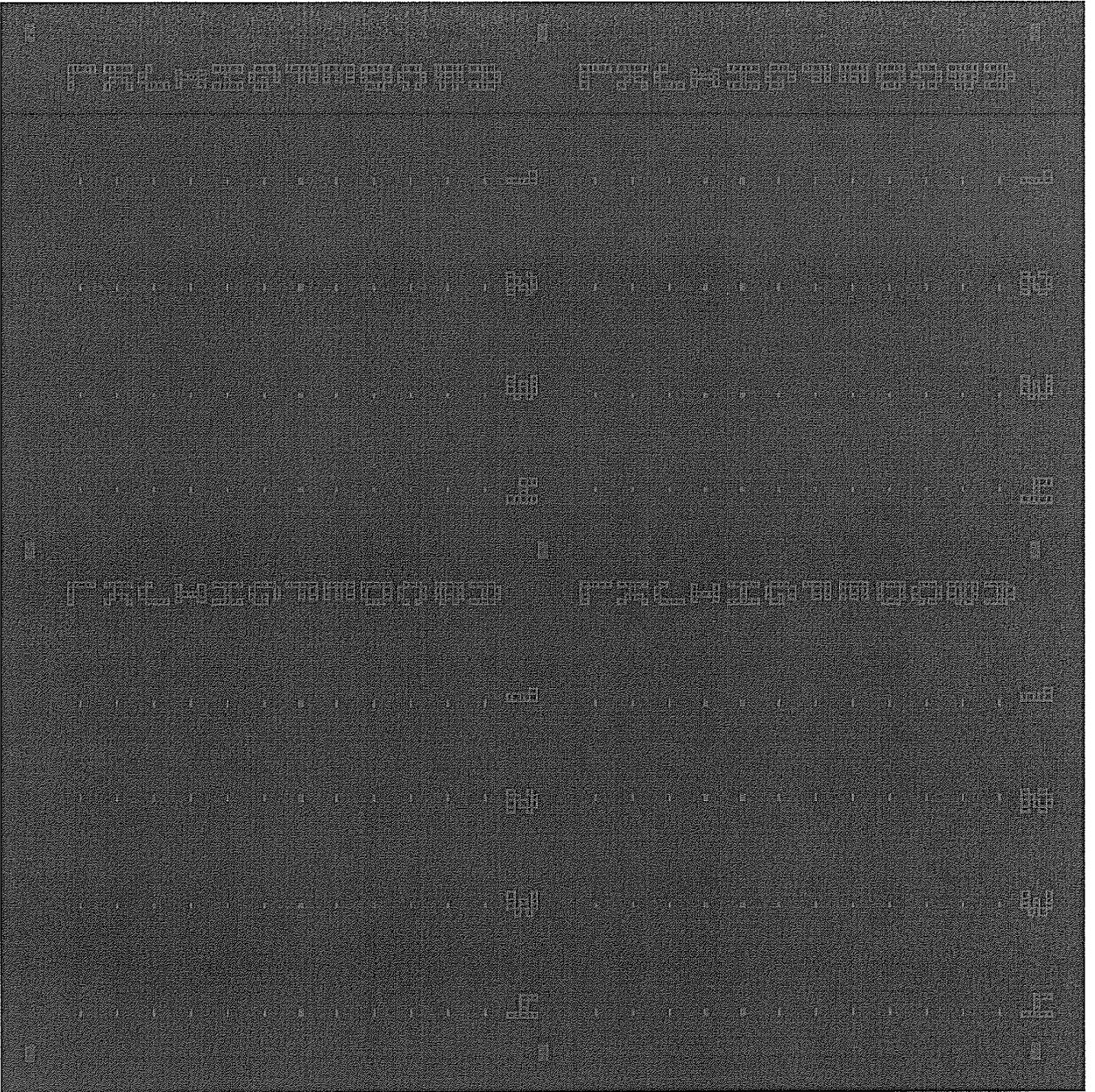
Operator: Lu Guang
~~Fernando Silva~~**Pre-Treatment:** Etch 60 seconds**Conditions:**Magnetron sputtering B.P.: 2.4e-6T, work P: 3.1mT
t = 78s.**Observations:** Deposit TiW passivation: t = 31s, B.P.: 1.3e-6T, work P: 3.1mT**STEP 9: Al Liftoff in Wet Bench**

Date: 5/29/2014 Started: 12:47pm

Operator: Bea + Alex

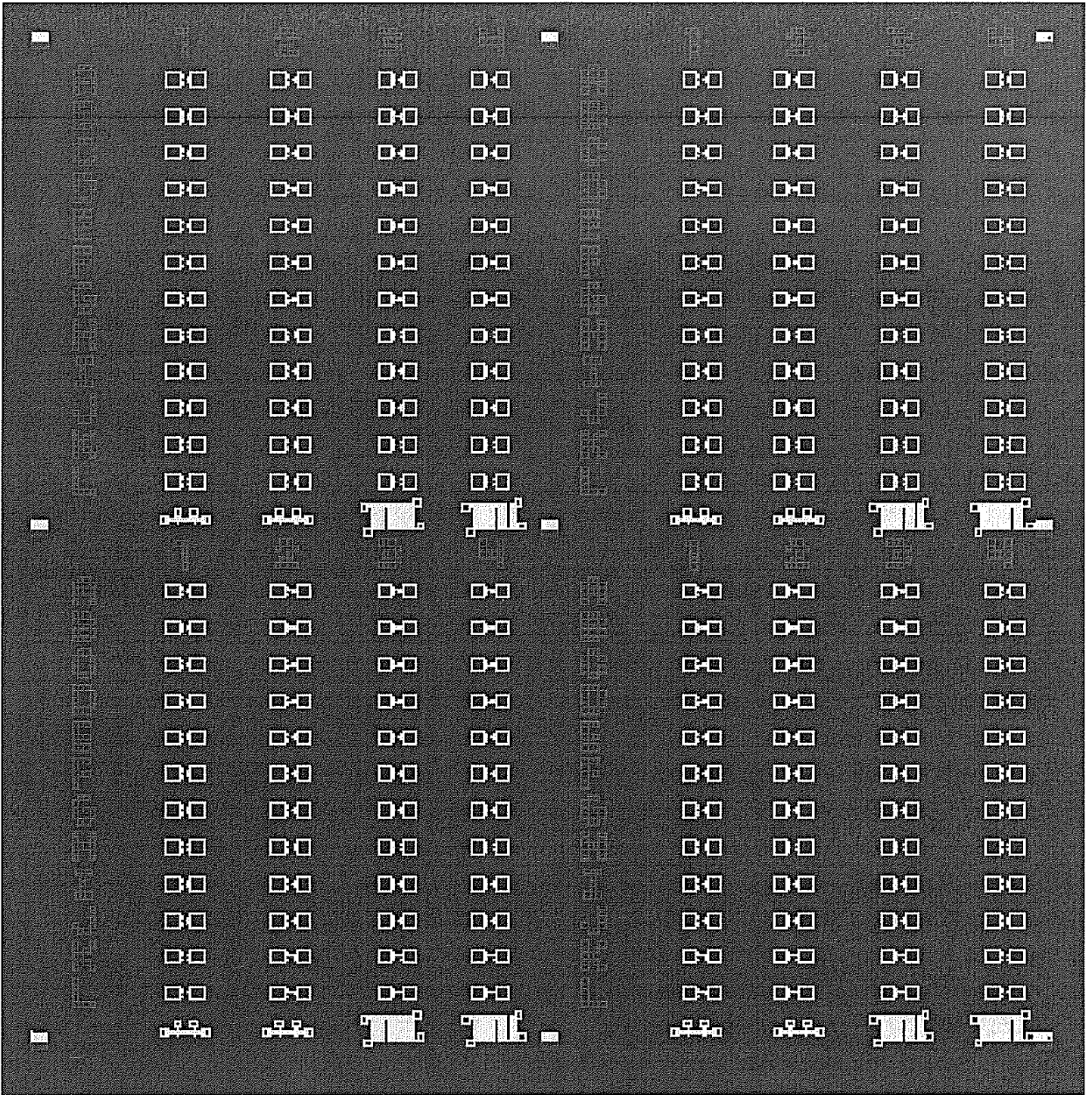
Pre-Treatment: No**Conditions:** Microstrip 2001 @ 80°C + ultrasounds**Observations:** 51
Dropped sample in isopropanol againdrop sample on floor & shatter it
Some water got into beaker w/ microstrip & S
sample was removed from bath.samples looked good under microscope.
named sample a little dirty.

easy axis \uparrow
step 4
pauli_sv_1



↑ easy axis

pauli-sv-2



STEP 13: Wafer Dicing in Disco DAD 321

Date:

Operator: Susana Freitas

Pre-Treatment: No

Conditions:

photoresist protecting the wafer (coater 6/2)

Recipe #201

Work thickness = 0,68 mm

Tape thickness = 0,150 mm

Blade height = 50 μm

Speed = 20 mm/s

Kerf width = 400 μm

index

CH1 = 9,2 mm

CH2 = 9,2 mm

Observations:

STEP 20: Measurement of SV

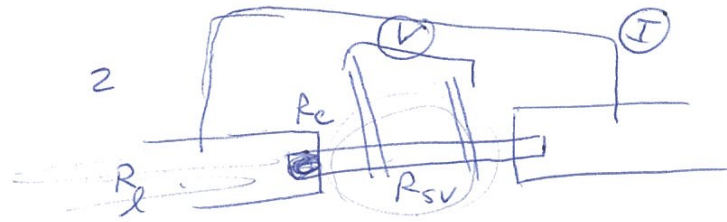
Manual test with the probes

Results:

SV number	Rmin (Ohm)	MR (%)	Linear range	
#1	801.5	5.56	40 (-2020)	3A TL
#2	578	5.29		3C TL
#3	450	5.37		3E TL
#4	321	5.53		3I TR
#5	315	5.23		3J TR
#6	820	6.03		4A BR
#7	827	5.74		1A TR
#8	658	5.71		3B BR
#9	471	4.93		3E BR
#10	378	5.54		3G BR
	<u>399</u>	4.03		1I BR

(h)
2 μm
2.5 μm
3 μm

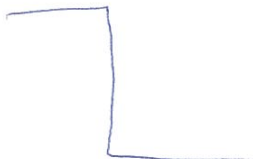
Process Time : 2 days

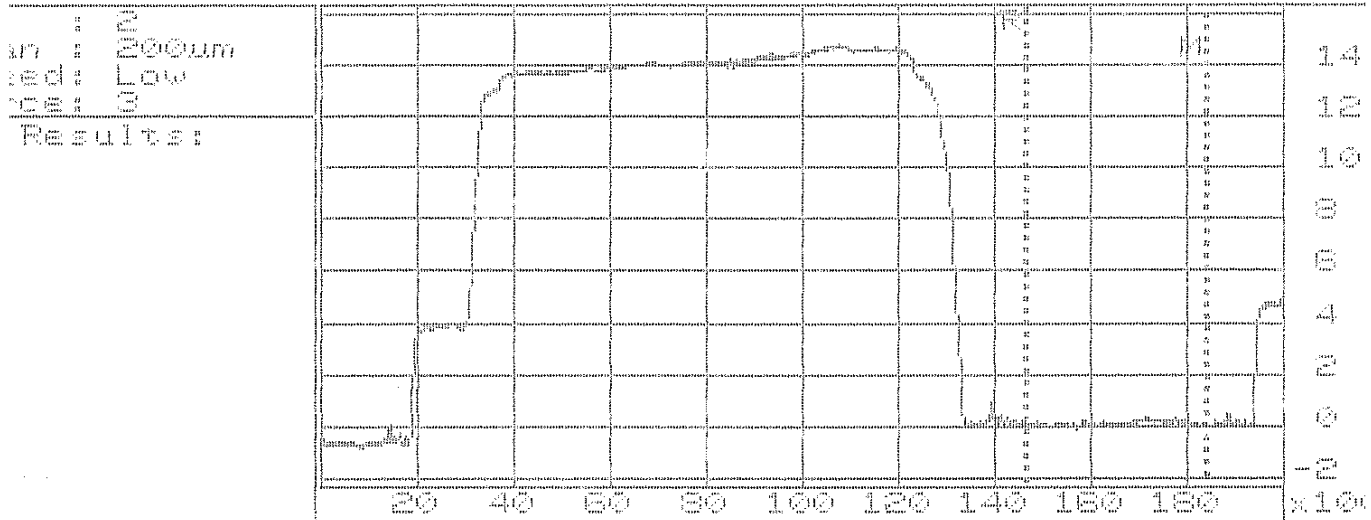


$$\rightarrow R_{TOTAL} = R_{sv} + 2R_e + 2R_{pad}$$

$$\rightarrow \Delta R = \Delta R_{sv}$$

$$\Rightarrow MR = \frac{\Delta R}{R_{TOTAL}} = \frac{\Delta R}{R_{sv} + 2R_e}$$





Programming:	Cursors:	*Vert/A	Horiz/um
	M:	0	0184
	R:	0	0146
	Δ:	0	33
	Resolution:	High	

Bibliography

- [1] Anna W Topol, DC La Tulipe, Leathen Shi, David J Frank, Kerry Bernstein, Steven E Steen, Arvind Kumar, Gilbert U Singco, Albert M Young, Kathryn W Guarini, et al. Three-dimensional integrated circuits. *IBM Journal of Research and Development*, 50(4.5):491–506, 2006.
- [2] T. P. Moffat and D. Josell. Extreme bottom-up superfilling of through-silicon-vias by damascene processing: suppressor disruption, positive feedback and turing patterns. *J. of The Electrochem. Soc.*, 159, 2012.
- [3] R. S. Patti. Three-dimensional integrated circuits and the future of system-on-chip designs. *Proceedings of the IEEE*, 94, 2006.
- [4] P. Garrou, C. Bower, and P. Ramm. *Handbook of 3D Integration: Volume 1 - Technology and Applications of 3D Integrated Circuits*. John Wiley & Sons, 2011.
- [5] G. Katti, M. Stucchi, K. De Meyer, and W. Dehaene. Electrical modeling and characterization of through silicon via for three-dimensional ics. *IEEE Trans. on Elec. Dev.*, 57, 2010.
- [6] Timothy L Jackson and Tim E Murphy. Methods of fabrication of semiconductor dice having back side redistribution layer accessed using through-silicon vias and assemblies thereof, November 8 2005. US Patent 6,962,867.
- [7] L. A. Knauss, B. M. Frazier, H. M. Christen, S. D. Silliman, K. S. Harshavardhan, E. F. Fleet, F. C. Wellstood, M. Mahanpour, and A. Ghaemmaghmi. Detecting power shorts from front and backside of ic packages using scanning squid microscopy. *Proc 25th International Symposium for Testing and Failure Analysis*, 1999.
- [8] F. Infante, P. Perdu, and D. Lewis. Magnetic microscopy for 3d devices: Defect localization with high resolution and long working distance on complex system in package. *European Symp. on Reliability of Electron Devices*, 49, 2009.
- [9] LA Knauss, SI Woods, and A Orozco. Current imaging using magnetic field sensors. *Microelectronics Failure Analysis Desk Reference*, 5:303–311, 2004.

- [10] S Chatrathorn, EF Fleet, FC Wellstood, LA Knauss, and TM Eiles. Scanning squid microscopy of integrated circuits. *Applied physics letters*, 76(16):2304–2306, 2000.
- [11] Randall C Black and Frederick C Wellstood. Measurements of magnetism and magnetic properties of matter. *The SQUID Handbook*, 2:391–440, 2006.
- [12] John H Lau, Cheng Kuo Lee, CS Premachandran, and A Yu. *Advanced MEMS packaging*. Citeseer, 2010.
- [13] Guruprasad Katti, Michele Stucchi, Kristin De Meyer, and Wim Dehaene. Electrical modeling and characterization of through silicon via for three-dimensional ics. *IEEE Transactions on Electron Devices*, 57(1):256–262, 2010.
- [14] Perry L Martin. *Electronic failure analysis handbook: techniques and applications for electronic and electrical packages, components, and assemblies*. McGraw-Hill Professional Publishing, 1999.
- [15] EDFAS Desk Reference Committee et al. *Microelectronics Failure Analysis: Desk Reference*. Asm International, 2011.
- [16] LA Bradshaw, RS Wijesinghe, and JP Wikswo Jr. Spatial filter approach for comparison of the forward and inverse problems of electroencephalography and magnetoencephalography. *Annals of biomedical engineering*, 29(3):214–226, 2001.
- [17] JP Wikswo Jr. The magnetic inverse problem for nde. In *SQUID Sensors: Fundamentals, fabrication and applications*, pages 629–695. Springer, 1996. See for example.
- [18] Eduardo Andrade Lima, Andrei Irimia, and John P Wikswo. The magnetic inverse problem. *The SQUID Handbook: Applications of SQUIDs and SQUID Systems, Volume II*, pages 139–267, 2006. See page 192.
- [19] L Knauss. Detecting power shorts from front and backside of ic packages using scanning squid microscopy. In *ISTFA 1999: 25 th International Symposium for Testing and Failure Analysis*, pages 11–16, 1999.
- [20] LA Knauss, A Orozco, SI Woods, and AB Cawthorne. Advances in scanning squid microscopy for die-level and package-level fault isolation. *Microelectronics Reliability*, 43(9):1657–1662, 2003.
- [21] J Clarke and AI Braginski. *The squid handbook: Applications of squids and squid systems*. vol. 2, 2006.
- [22] Bradley J Roth, Nestor G Sepulveda, and John P Wikswo Jr. Using a magnetometer to image a two-dimensional current distribution. *Journal of applied physics*, 65(1):361–372, 1989.
- [23] Paul C Lauterbur. Image formation by induced local interactions: examples employing nuclear magnetic resonance. 1973.

- [24] Zhi-Pei Liang and Paul C Lauterbur. *Principles of magnetic resonance imaging: a signal processing perspective*. The Institute of Electrical and Electronics Engineers Press, 2000.
- [25] David Cohen et al. Magnetoencephalography: evidence of magnetic fields produced by alpha-rhythm currents. *Science*, 161(3843):784–786, 1968.
- [26] Matti Hämäläinen, Riitta Hari, Risto J Ilmoniemi, Jukka Knuutila, and Olli V Lounasmaa. Magnetoencephalography—theory, instrumentation, and applications to non-invasive studies of the working human brain. *Reviews of modern Physics*, 65(2):413, 1993.
- [27] Gerhard Baule and Richard McFee. Detection of the magnetic field of the heart. *American Heart Journal*, 66(1):95–96, 1963.
- [28] David Cohen. Magnetic fields around the torso: production by electrical activity of the human heart. *Science*, 156(3775):652–654, 1967.
- [29] David Cohen, Edgar A Edelsack, and James E Zimmerman. Magnetocardiograms taken inside a shielded room with a superconducting point-contact magnetometer. *Applied Physics Letters*, 16(7):278–280, 1970.
- [30] Hans Koch. Recent advances in magnetocardiography. *Journal of electrocardiology*, 37:117–122, 2004.
- [31] A Mathai, D Song, Y Gim, and FC Wellstood. One-dimensional magnetic flux microscope based on the dc superconducting quantum interference device. *Applied physics letters*, 61(5):598–600, 1992.
- [32] A Mathai, D Song, Y Gim, and FC Wellstood. High resolution magnetic microscopy using a dc squid. *IEEE transactions on applied superconductivity*, 3(1):2609–2612, 1993.
- [33] G Panaitov, H-J Krause, and Y Zhang. Pulsed eddy current transient technique with hts squid magnetometer for non-destructive evaluation. *Physica C: Superconductivity*, 372:278–281, 2002.
- [34] Tae-Kyu Lee, JW Morris Jr, Seungkyun Lee, and John Clarke. Detection of fatigue damage prior to crack initiation with scanning squid microscopy. *Lawrence Berkeley National Laboratory*, 2005.
- [35] Su-Young Lee. Multi-channel scanning squid microscopy. 2004.
- [36] CC Tsuei, JR Kirtley, CC Chi, Lock See Yu-Jahnes, A Gupta, T Shaw, JZ Sun, and MB Ketchen. Pairing symmetry and flux quantization in a tricrystal superconducting ring of $\text{YBa}_2\text{Cu}_3\text{O}_7$. *Physical Review Letters*, 73:593–593, 1994.
- [37] LN Vu, MS Wistrom, and DJ Van Harlingen. Imaging of magnetic vortices in superconducting networks and clusters by scanning squid microscopy. *Applied physics letters*, 63(12):1693–1695, 1993.

- [38] A Mathai, Y Gim, RC Black, A Amar, and FC Wellstood. Experimental proof of a time-reversal-invariant order parameter with a π shift in $\text{YBa}_2\text{Cu}_3\text{O}_{7-\delta}$. *Physical review letters*, 74(22):4523, 1995.
- [39] Reinhold Kleiner, Dieter Koelle, Frank Ludwig, and John Clarke. Superconducting quantum interference devices: State of the art and applications. *Proceedings of the IEEE*, 92(10):1534–1548, 2004.
- [40] Quantum Design. *MPMS MultiVu Application User’s Manual*. Quantum Design, 2004.
- [41] Andrew P Roberts. High-resolution magnetic analysis of sediment cores: strengths, limitations and strategies for maximizing the value of long-core magnetic data. *Physics of the Earth and Planetary Interiors*, 156(3):162–178, 2006.
- [42] Phillip Schmidt, David Clark, Keith Leslie, Marcel Bick, David Tilbrook, and Cathy Foley. Getmag’s squid magnetic tensor gradiometer for mineral and oil exploration. *Exploration Geophysics*, 35(4):297–305, 2004.
- [43] CP Foley, KE Leslie, R Binks, C Lewis, W Murray, GJ Sloggett, S Lam, B Sankrithyan, N Savvides, A Katzaros, et al. Field trials using hts squid magnetometers for ground-based and airborne geophysical applications. *IEEE transactions on applied superconductivity*, 9(2):3786–3792, 1999.
- [44] M Bick, G Panaitov, N Wolters, Y Zhang, H Bousack, AI Braginski, U Kalberkamp, H Burkhardt, and U Matzander. A hts rf squid vector magnetometer for geophysical exploration. *IEEE transactions on applied superconductivity*, 9(2):3780–3785, 1999.
- [45] Ching Tsang, Robert E Fontana, Tsann Lin, David E Heim, Virgil S Speriosu, Bruce A Gurney, and Mason L Williams. Design, fabrication and testing of spin-valve read heads for high density recording. *IEEE Transactions on Magnetics*, 30(6):3801–3806, 1994.
- [46] IK Kominis, TW Kornack, JC Allred, and MV Romalis. A subfemtotesla multichannel atomic magnetometer. *Nature*, 422(6932):596–599, 2003.
- [47] HJ Mamin, M Kim, MH Sherwood, CT Rettner, K Ohno, DD Awschalom, and D Rugar. Nanoscale nuclear magnetic resonance with a nitrogen-vacancy spin sensor. *Science*, 339(6119):557–560, 2013.
- [48] Linh My Pham, David Le Sage, Paul L Stanwix, Tsun Kwan Yeung, D Glenn, Alexei Trifonov, Paola Cappellaro, PR Hemmer, Mikhail D Lukin, Hongkun Park, et al. Magnetic field imaging with nitrogen-vacancy ensembles. *New Journal of Physics*, 13(4):045021, 2011.
- [49] Max Born and Emil Wolf. *Principles of optics: electromagnetic theory of propagation, interference and diffraction of light*. CUP Archive, 2000.

- [50] Joseph Goldstein, Dale E Newbury, Patrick Echlin, David C Joy, Alton D Romig Jr, Charles E Lyman, Charles Fiori, and Eric Lifshin. *Scanning electron microscopy and X-ray microanalysis: a text for biologists, materials scientists, and geologists*. Springer Science & Business Media, 2012.
- [51] Lucille A Giannuzzi et al. *Introduction to focused ion beams: instrumentation, theory, techniques and practice*. Springer Science & Business Media, 2006.
- [52] John W Reeds. Wafer alignment and positioning apparatus for chip testing by voltage contrast electron microscopy, September 20 1988. US Patent 4,772,846.
- [53] Jon C Lee, CH Chen, David Su, and JH Chuang. Investigation of sensitivity improvement on passive voltage contrast for defect isolation. *Microelectronics Reliability*, 42(9):1707–1710, 2002.
- [54] GBM Fiege, V Feige, JCH Phang, M Maywald, S Gorlich, and LJ Balk. Failure analysis of integrated devices by scanning thermal microscopy (sthm). *Microelectronics Reliability*, 38(6):957–961, 1998.
- [55] HD Lambilly and Helmut O Keser. Failure analysis of power modules: a look at the packaging and reliability of large igbts. *IEEE transactions on components, hybrids, and manufacturing technology*, 16(4):412–417, 1993.
- [56] C Schmidt, F Altmann, C Grosse, A Lindner, and V Gottschalk. Lock-in-thermography for 3-dimensional localization of electrical defects inside complex packaged devices. In *Proc 34th int symp for testing and failure analysis*, pages 102–7, 2008.
- [57] Kannu Wadhwa, Rudolf Schlangen, Joy Liao, Tung Ton, and Howard Marks. Failure analysis of low-ohmic shorts using lock-in thermography. In *Proceedings of the 21th International Symposium on the Physical and Failure Analysis of Integrated Circuits (IPFA)*, 2014.
- [58] EF Fleet, S Chatraphorn, FC Wellstood, LA Knauss, and SM Green. Closed-cycle refrigerator-cooled scanning squid microscope for room-temperature samples. *Review of Scientific Instruments*, 72:3281–3290, 2001.
- [59] Sojiphong Chatraphorn. *Room-temperature magnetic microscopy using a high- T_c SQUID*, chapter 6, pages 99–130. 2000. Ph.D. dissertation:.
- [60] John David Jackson. *Classical electrodynamics*. Wiley, 1999.
- [61] FC Wellstood, Y Gim, A Amar, RC Black, and A Mathai. Magnetic microscopy using squids. *Applied Superconductivity, IEEE Transactions on*, 7(2):3134–3138, 1997.
- [62] William H Press. *Numerical recipes 3rd edition: The art of scientific computing*, chapter 12. Cambridge university press, 2007.

- [63] EF Fleet, S Chatrathorn, FC Wellstood, and LA Knauss. Hts scanning squid microscopy of active circuits. *Applied Superconductivity, IEEE Transactions on*, 9(2):4103–4106, 1999.
- [64] J Clarke and AI Braginski. *The SQUID Handbook: Applications of SQUIDS and SQUID Systems. Vol. 2*, chapter 10. New York: Wiley, 2006.
- [65] David Jeffrey Griffiths and Reed College. *Introduction to electrodynamics*, volume 3. prentice Hall Upper Saddle River, NJ, 1999.
- [66] Yitzhak Katznelson. *An introduction to harmonic analysis*. Cambridge University Press, 2004.
- [67] Sojiphong Chatrathorn. *Room-temperature magnetic microscopy using a high- T_c SQUID*, chapter 6, pages 132–134. 2000. Ph.D. dissertation:.
- [68] Sojiphong Chatrathorn. *Room-temperature magnetic microscopy using a high- T_c SQUID*, chapter 7, pages 131–145. 2000. Ph.D. dissertation:.
- [69] Gregory K Wallace. The jpeg still picture compression standard. *Consumer Electronics, IEEE Transactions on*, 38(1):xviii–xxxiv, 1992.
- [70] Karlheinz Brandenburg. Mp3 and aac explained. In *Audio Engineering Society Conference: 17th International Conference: High-Quality Audio Coding*, Aug 1999. <http://www.aes.org/e-lib/browse.cfm?elib=8079>.
- [71] E. F. Fleet. *Design and applications of a cryo-cooled scanning SQUID microscope*. PhD thesis, University of Maryland, College Park, October 2000.
- [72] AJ Blodgett and Donald R Barbour. Thermal conduction module: A high-performance multilayer ceramic package. *IBM Journal of Research and Development*, 26(1):30–36, 1982.
- [73] S Oktay and HC Kammerer. A conduction-cooled module for high-performance lsi devices. *IBM Journal of Research and Development*, 26(1):55–66, 1982.
- [74] David Cohen and Hidehiro Hosaka. Part ii magnetic field produced by a current dipole. *Journal of electrocardiology*, 9(4):409–417, 1976.
- [75] S Chatrathorn, EF Fleet, and FC Wellstood. Relationship between spatial resolution and noise in scanning superconducting quantum interference device microscopy. *Journal of applied physics*, 92(8):4731–4740, 2002.
- [76] MATLAB. Matlab documentation for fminsearch function, 2016. <https://www.mathworks.com/help/matlab/ref/fminsearch.html>, retrieved 2016-09-29.
- [77] Jeffrey C Lagarias, James A Reeds, Margaret H Wright, and Paul E Wright. Convergence properties of the nelder–mead simplex method in low dimensions. *SIAM Journal on optimization*, 9(1):112–147, 1998.

- [78] Hidehiro Hosaka and David Cohen. Part iv visual determination of generators of the magnetocardiogram. *Journal of electrocardiology*, 9(4):426–432, 1976.
- [79] Jack E Bresenham. Algorithm for computer control of a digital plotter. *IBM Systems journal*, 4(1):25–30, 1965.
- [80] George B Dantzig and Mukund N Thapa. *Linear programming 1: introduction*. Springer Science & Business Media, 2006.
- [81] LLC. Neocera. 10000 Virginia Manor Road Ste 300, Beltsville, MD 20705, USA, <http://neocera.com>, retrieved 2016-09-29.
- [82] A Orozco, NE Gagliolo, C Rowlett, E Wong, A Moghe, J Gaudestad, V Talanov, A Jeffers, K Torkashvan, FC Wellstood, et al. 3d ic/stacked device fault isolation using 3d magnetic field imaging. In *ISTFA 2014: Conference Proceedings from the 40th International Symposium for Testing and Failure Analysis*, page 33. ASM International, 2014.
- [83] Reliant systems Inc. stages x-y specifications, internal documentation.
- [84] E. F. Fleet. *Design and applications of a cryo-cooled scanning SQUID microscope*. PhD thesis, University of Maryland, College Park, October 2000.
- [85] Star Cryoelectronics. 25-A Bisbee Court, Santa Fe, NM 87508-1338, USA, <http://starcryo.com/>, retrieved 2016-09-29.
- [86] John Clarke and Alex I Braginski. *The squid handbook*. 2004.
- [87] J Matthews, SY Lee, FC Wellstood, AF Gilbertson, GE Moore, and S Chatrathorn. Multi channel high-t c scanning squid microscope. *IEEE transactions on applied superconductivity*, 13(2):219–222, 2003.
- [88] JE Zimmerman and Nolan V Frederick. Miniature ultrasensitive superconducting magnetic gradiometer and its use in cardiology and other applications. *Applied Physics Letters*, 19(1):16–19, 1971.
- [89] Bernard Dieny, Virgil S Speriosu, Stuart SP Parkin, Bruce A Gurney, Dennis R Wilhoit, and Daniele Mauri. Giant magnetoresistive in soft ferromagnetic multilayers. *Physical Review B*, 43(1):1297, 1991.
- [90] PP Freitas, F Silva, NJ Oliveira, LV Melo, L Costa, and N Almeida. Spin valve sensors. *Sensors and Actuators A: Physical*, 81(1):2–8, 2000.
- [91] DC Leitão, J Borme, A Orozco, S Cardoso, and PP Freitas. Magnetoresistive sensors for surface scanning. In *Giant Magnetoresistance (GMR) Sensors*, pages 275–299. Springer, 2013.
- [92] Robert L White. Giant magnetoresistance: a primer. *Magnetics, IEEE Transactions on*, 28(5):2482–2487, 1992.

- [93] Instituto de Engenharia de Sistemas e Computadores. Rua Alves Redol, 9, 1000-029, Lisboa, Portugal.
- [94] Véronique Gehanno, Paula P Freitas, Anabela Veloso, J Ferrira, Bernard Almeida, JB Soasa, A Kling, JC Soares, and MF Da Silva. Ion beam deposition of mn-ir spin valves. *Magnetics, IEEE Transactions on*, 35(5):4361–4367, 1999.
- [95] Marc J Madou. *Fundamentals of microfabrication: the science of miniaturization*. CRC press, 2002.
- [96] Heidelberg Instruments. Heidelberg Instruments GmbH, Tullastrasse 2, D-69126 Heidelberg, www.himt.de, retrieved 2016-09-29.
- [97] Fujifilm. Microstrip 3001 technical product information sheet. <https://www.fujifilmusa.com/shared/bin/MS%203001%20rev2.pdf>, retrieved 2016-09-29.
- [98] B Dieny. Giant magnetoresistance in spin-valve multilayers. *Journal of Magnetism and Magnetic Materials*, 136(3):335–359, 1994.
- [99] 3DiS Technologies. 478 Rue de la Decouverte, CS 67624, 31676 Labege, France.
- [100] Panayotis C Andricacos, Cyprian Uzoh, John O Dukovic, Jean Horkans, and Hariklia Deligianni. Damascene copper electroplating for chip interconnections. *IBM Journal of Research and Development*, 42(5):567–574, 1998.
- [101] S Hsiung, KV Tan, AJ Komrowski, DJD Sullivan, J Gaudestad, A Orozco, E Talanova, and LA Knauss. Failure analysis on resistive opens with scanning squid microscopy. In *Reliability Physics Symposium Proceedings, 2004. 42nd Annual. 2004 IEEE International*, pages 611–612. IEEE, 2004.
- [102] Seung Wook Yoon, Jae Hoon Ku, Nathapong Suthiwongsunthorn, Pandi Chelvam Marimuthu, and Flynn Carson. Fabrication and packaging of microbump interconnections for 3d tsv. In *3D System Integration, 2009. 3DIC 2009. IEEE International Conference on*, pages 1–5. IEEE, 2009.
- [103] All Silicon System Integration Dresden (ASSID). http://www.izm.fraunhofer.de/en/abteilungen/high_density_interconnectwaferlevel_packaging/ausstattung/all_silicon_systemintegrationdresdenassid.html, retrieved 2016-09-29.
- [104] HA Ferreira, DL Graham, PP Freitas, and JMS Cabral. Biodetection using magnetically labeled biomolecules and arrays of spin valve sensors. *Journal of Applied Physics*, 93(10):7281–7286, 2003.
- [105] Guanxiong Li, Shouheng Sun, Robert J Wilson, Robert L White, Nader Pourmand, and Shan X Wang. Spin valve sensors for ultrasensitive detection of superparamagnetic nanoparticles for biological applications. *Sensors and Actuators A: Physical*, 126(1):98–106, 2006.

- [106] James R Janesick. *Scientific charge-coupled devices*, volume 117. SPIE press Bellingham, Washington, 2001.
- [107] David Steven Dummit and Richard M Foote. *Abstract algebra*, volume 3. Wiley Hoboken, 2004.
- [108] Antonio Orozco. personal communication.
- [109] C Rossel, P Bauer, D Zech, J Hofer, M Willemin, and H Keller. Active microlevers as miniature torque magnetometers. *Journal of applied physics*, 79(11):8166–8173, 1996.
- [110] Jan Gaudestad, Vladimir Talanov, Nicolas Gagliolo, and Antonio Orozco. Space domain reflectometry for open failure localization. In *Physical and Failure Analysis of Integrated Circuits (IPFA), 2012 19th IEEE International Symposium on the*, pages 1–5. IEEE, 2012.